On prediction of residual stresses for additive manufacturing of Ti-6Al-4V

by

Vincenzo Brachetta

A thesis submitted for the degree of
Doctor of Philosophy

School of Metallurgy and Materials
College of Engineering and Physical Sciences
University of Birmingham
April 2024

Contents

Abstract

The study of mechanical performance of laser additive manufacturing components poses several difficulties, primarily due to the various variables introduced by the manufacturing process and the diverse parameters that can be adjusted during production. A significant factor contributing to these challenges is the presence of high thermal gradients created by the laser heat source, which lead to the formation of residual stresses – permanent stresses that remain even after the initial cause has been eliminated. The importance of addressing residual stresses lies in their potential to constitute a considerable portion of the stresses experienced during operational conditions and thus their negative contribution to failure. As demonstrated in this study, tensile residual stresses can adversely affect the fatigue life of mechanical components and, under opportune hypotheses and approximations, this reduction can be quantified.

Starting from the analogy of the additive process with welding, a versatile process model for laser-powder bed fusion of Ti-6Al-4V, based on finite element analyses, is presented, studied, and utilised to predict residual stresses. Through high-performance computing, the magnitude of residual stresses in a reduced geometrical domain can be estimated in the common process window for Ti-6Al-4V, which includes a laser speed of 200-1600 mm/s and a hatch spacing of 40-120 µm. The finite element model incorporates all the necessary temperature-dependant thermo-physical parameters, such as mass density, specific heat capacity, thermal conductivity, linear thermal expansion, Young's modulus, Poisson's ratio. These

parameters are interpolated from the literature, when possible, and some of them are presented for the first time, starting from the concept that a variable porosity at different temperatures can describe the aggregation of powder particles dispersed in the powder bed. Using this approach, all the physical quantities are separated between the substrate and the powder layer. The material mechanical behaviour is described through a recent thermo-viscoplastic constitutive model, which incorporates also the most relevant microstructural features, such as the martensitic thickness and spacing to predict an evolving dislocation density during deformation. This allows for a distinction to be made between the material responses of the substrate and the powder layer, wherein the martensitic phase produced by the rapid cooling rates results in an increased dislocation density. An accurate analysis of the heat transfer coefficient also leads to differentiate between the emissivity in the substrate and in the powder layer. Emissivity for the powder layer is calibrated with data available in the literature. All the calculations are performed taking into account the different laser speeds and hatch spacing values as well as one deposition layer of 40 µm and two deposition layers of 40 µm, following a bi-directional, double pass of laser beam, 90° rotation scan vector between layers.

The predicted residual stresses are in the range of 300-1000 MPa for speeds in the range 200-1400 mm/s and they are in agreement with several independent studies already published in the literature for laser-powder bed fusion of the same material and under similar processing conditions. In particular, the numerical studies presented here confirm that residual stresses can be significantly reduced from 1000 to 300–600 MPa by increasing the laser speed from 200 to 800 mm/s and that hatch spacing has little effect on residual stresses magnitude.

Additional considerations and metallurgical characterisation of the martensitic phase, present as by-product of the process, is presented. The experimental programme was based on the same idea of analogy of the additive process with

welding, and thus seven pairs of laser tracks were imprinted on the surface of a Ti-6Al-4V sheet, with gradually decreasing hatch spacing values. Therefore, the microstructure was analysed using optical and scanning electron microscopy, and geometrical data were extracted from the micrographs to statistically quantify the most important geometrical parameters for the size of the laths and for their dispersion at different locations of the melt pool. This quantification include statistical analysis of martensitic thickness, spacing, volume fractions, major-axis and minor-axis lengths, angle of growth. In addition, a martensitic model present in the literature which predicts the martensite thickness is extended from welding to a double laser pass with varying hatch spacing, showing that the former model is accurate and that the thickness does not vary significantly in the melt pool region for Ti-6Al-4V.

The numerical results obtained are validated using the Carlsson-Larsson theory with its most recent integrations, and through comparison with published literature. This shows that the theory can be used to predict residual stresses in agreement with finite element modelling, with a discrepancy of approximately 200 MPa. Finally, a fatigue analysis incorporating residual stresses, surface roughness and lath martensite width, is presented, showing a drop of about 200 MPa in the stress amplitude for very high loading cycles, when the tensile residual stress is 400 MPa.

Statement of original authorship

This thesis is submitted in fulfilment of the requirements for the degree of Doctor of Philosophy (PhD).

The research was carried out by Mr. Vincenzo Brachetta at the School of Metallurgy and Materials, College of Engineering and Physical Sciences, University of Birmingham, United Kingdom, from April 2019 to March 2024, first under the supervision of Prof. Hector Basoalto and later under the supervision of Prof. Paul Bowen.

The work is original and no part has been submitted for another degree at any other university. Wherever other researchers' work has been drawn from or cited, this is acknowledged in the text and the references are listed.

The author has strived to be as accurate and complete as possible in the creation of this dissertation and all attempts have been made to verify the informations provided in this work as best as possible.

Acknowledgements

First and foremost, the author would like to thank God: *You are worthy, our Lord and God, to receive glory and honour and power, for you created all things, and by your will they existed and were created.*

These years have been a unique opportunity for learning and for personal growth, and it has been a pleasure to come into contact with some of the people involved in both research and teaching. Therefore, for the forward-looking decision to invest in research and for the financial support given to this project, the author wishes to acknowledge the Defence Science and Technology Laboratory (DSTL), Ministry of Defence of the United Kingdom. Sincere gratitude goes to Prof. Hector Basoalto, for having given the author initial confidence, allowing him to begin this ambitious project, and for his good advises. The author wishes to thank his supervisor Prof. Paul Bowen for his extremely crucial support during the most critical phases of this research project. His high level of professionalism and his humanity were both fundamental to overcome the most difficult steps, both technical and practical, that arose during this project. Sincere thanks also go to Dr. Richard Turner, who is not only an excellent research advisor, but also a friend and the right person to trust in case of need, who provided his highly professional, committed, and selfless help throughout the duration of the research project. Thanks also go to Prof. Moataz Attallah (Director of AMPLab, the Advanced Materials Processing Laboratory, University of Birmingham), whose laboratory he heads turned out to be not only a space where investigate the pro-

cessing of materials and their characterisation, but also a fantastic place where share ideas and curiosities. Among the people who daily work or have worked in this laboratory, the author wishes to thank the professionalism, seriousness, and dedication of Dr. Stano Imbrogno and Mr. Francesco Careri. Their full support, suggestions, and dedication during the experimental stage of the present work were simply exceptional.

Other people collaborated indirectly to this project, enabling activities that provided additional insights and inspiration to the author, which inevitably reflected on the project improvement. During the work as Postgraduate Teaching Assistant (PGTA), it was also a pleasure to help Prof. Alessandro Mottura, who always demonstrated excellent teaching skills and showed immediate trust in the author. It was also a pleasure to be involved with the teaching activities and lecture preparation supervised by Dr. Austin Tomlinson, whose attention in establishing good teaching practices for the benefit of the students is admirable.

One cannot then forget those who are always behind the scenes, but who do equally fundamental work for the success of research, including people in the administration offices, all the technicians, and all the cleaners, whose precious work, carried out silently, is often underestimated. Thanks also go to Mrs. Dana Vasiljevic for her exceptional diligence, punctuality and precision with the administrative matters. For the same reasons, thanks go also to the people working at the University of Birmingham IT service and, in particular to the Birmingham Environment for Academic Research (BEAR) team, for constantly updating and maintaining the computational resources in an excellent state. Without the excellent calculation capabilities of BlueBEAR, the University of Birmingham supercomputer, the implementation and completion of the numerical simulations presented in this work would not have been possible. Sincere thanks also go to the staff of the university libraries, who dedicate themselves daily to provide a consistently excellent service. It is also thanks to their work that the Main Library

has often been a resource of inspiration for the author. Thanks to the choice to keep the shelves completely accessible, this inspiration has often followed paths other than those initially imagined.

Finally, to the author's family goes his eternal gratitude for teaching him the importance of knowledge, granting him all their love, confidence, and freedom, and supporting him through every difficulty in life. Special thanks also go to the daily and tireless support of my wife Federica Bucci, who has never lacked her love and for whose recognition these few words are not enough.

List of symbols

$b, \lvert b \rvert$	Burgers vector, magnitude of the Burgers vector;
c_p	specific heat capacity (at constant pressure);
$d_{\alpha'}$	martensite α' lath spacing;
$d_{\alpha,1}$	martensite lath minor-axis length;
$d_{\alpha,2}$	martensite lath major-axis length;
D	thermal diffusivity;
D_α	α-grain size;
E	Young's modulus;
h	hatch spacing / heat transfer coefficient;
h_r	radiation heat transfer coefficient;
h_c	convection heat transfer coefficient;
$h_{\alpha'}$	martensite α' lath length;
h_V	Vicker's hardness indentation depth;
H_V	Vicker's hardness number;
k	thermal conductivity;
k_B	Boltzmann constant;
t	time;
T	temperature;
T_b	boiling temperature;
$\dot{T}_c$	martensite critical cooling rate;
T_m	melting temperature;
$T_{m,f}$	martensite finishing temperature;
$T_{m,s}$	martensite starting temperature;

T_p	pre-heating temperature;
T_r	room / radiance temperature;
T_s	surface / substrate temperature;
T_β	β-transus temperature;
$T_{\beta,s}$	β-transus starting temperature;
V_α	α phase volume fraction;
$V_{\alpha'}$	α'-martensite volume fraction;
V_β	β-phase volume fraction;
$w_{\alpha'}$	martensite α' lath thickness;
α	linear thermal expansion;
ϵ	strain;
δ	elongation at yield;
$\dot{\epsilon}$	strain rate;
$\theta_{\alpha'}$	martensite α' lath angle;
μ	shear modulus;
ν	Poisson's ratio;
χ	martensite transformation coefficient;
ρ	mass density / dislocation density;
ρ_0	initial dislocation density;
σ	stress / Stefan-Boltzmann constant;
σ_M	von Mises stress;
σ_u	ultimate tensile stress;
$\sigma_{y,X}$	yield stress of the phase X;

List of abbreviations

ALM	Additive Layer Manufacturing;
DMD	Direct Metal Deposition;
DLED	Direct Laser Energy Deposition;
DMLM	Direct Metal Laser Melting;
DMLS	Direct Metal Laser Sintering;
EBM	Electron Beam Melting;
LBM	Laser Beam Melting;
LPBF	Laser Powder-Bed Fusion;
SLM	Selective Laser Melting;
SLS	Selective Laser Sintering;
WAAM	Wire and Arc Additive Manufacturing;
ASTM	American Society for Testing and Materials;
BCC	Body-Centered Cubic;
BSE	BackScattered Electrons;
CSV	Comma-Separated Value;
EBSD	Electron BackScatter Diffraction;
FEM	Finite Element Method;
HCP	Hexagonal Close-Packed;
HPC	High-Performance Computing;
ODB	Output DataBase;
OM	Optical Microscope;
SE	Secondary Electrons;
SEM	Scanning Electron Microscope;
TEM	Transmission Electron Microscope.

List of Figures

List of Tables

Chapter 1

Introduction

1.1 Objectives, significance, and purpose of the present study

Any manufacturing process inevitably introduces a number of variabilities to the final component. This has an impact on the mechanical properties of the material. Some of those variabilities arise due to the microstructure of the material, or residual stresses. Microstructural inhomogeneities and residual stresses can lead to premature failure, since microstructure influences mechanical properties and residual stresses can contribute to the stresses caused by applied loads on the fabricated part during in-service conditions. Therefore, the final component performance is highly dependent on its microstructure and on the residual stresses which, if unknown, can potentially lead to catastrophic failure. The processing parameters of a manufacturing process, such as those in welding (such as laser power and speed) or additive manufacturing (such as hatch spacing, laser power and speed, geometry), have a profound effect on the resulting microstructure and the residual stresses.

The main objective of this study has been to investigate the relationships be-

tween certain key processing parameters and changes in stress and microstructure during laser pass. The understanding of these factors is fundamental in evaluating their impact on mechanical properties, especially in delivering a guidance for engineers when estimating the residual stresses in laser manufactured components. In particular, the main focus of this study is on residual stresses and hatch spacing influence on the microstructure, with special attention on the martensitic α'-phase of the titanium alloy Ti-6Al-4V, during thermo-mechanical processing generated by a laser source scanning process.

The general approach of this investigation allows one to focus more on aspects of the microstructure and residual stresses, and so derive general conclusions, rather than looking into the specifics of every individual manufacturing process. However, since hatch spacing and laser speed are two fundamental variables of the additive manufacturing process, the majority of this study has been undoubtedly influenced by this focus, which, with its complexity, is considered a challenging field to predict inhomogeneities in a coupled thermal-mechanical-metallurgical fashion.

1.1.1 Industrial relevance of the problem

Nowadays, some parts in the compressors of advanced gas turbine engines, like the bladed disks in aero-engines – so-called BLISKs (BLade-Integrated diSKs) – are fabricated using expensive conventional techniques, such as the solid-state joining processes called *linear friction welding* and *electro-chemical machining* [1, 2]. These components are mainly made using titanium alloys and they are subject to severe mechanical stresses and vibrations [3]. This relatively new production technology aims to completely replace classic blade disc systems, in which the blades are attached in a second stage, with a new component, the BLISK, in which the blades and disc are produced together as a single part. The main advantage of using BLISKs is the elimination of contact stresses at the

attachment point, which benefits fatigue life [3]. Their position within an aircraft engine is represented in Figure 1.1. Titanium alloys found also application in low pressure turbine blades, which are made by *investment casting* and subsequently machined. However, the plan is to use additive manufacturing to produce these blades [4]. Despite the initial high cost, titanium and titanium alloys are generally preferred in aerospace for their light weight, high strength and stiffness, which help to improve aircraft fuel efficiency [4, 5].

Whilst linear friction welding has seen a limited industrial implementation other than BLISKs manufacture [2], additive manufacturing is definitely more flexible in terms of geometries of the parts that can be designed and built. Moreover, additive manufacturing is rapidly overtaking current technologies not only for its versatility, but also thanks to the possibility of repairing damaged components, as the BLISK repair illustrated in Figure 1.4. The interest in remanufacturing, which includes repair and restoration, is emerging as appropriate approach for reusing a component in a sustainable economy [6].

Broadening the field of application to other components and not necessarily only to the BLISKs, additive manufacturing permits to use less material during the fabrication process, since the waste in terms of the materials has been estimated around 70% for the conventional manufacturing processes [1]. Therefore, since a component can be repaired or manufactured with less material, the industrial relevance of the present study lies to the possible mitigation of the environmental issues arising from the reduction of excessive use of material resources and energy, instead of being completely discarded and manufactured from the beginning. A better understanding of additive manufacturing and its influence on the mechanical properties of the fabricated part, will permit manufacturers in the forthcoming future to improve current manufacturing processes. The hope is that this could lead to more environmentally-friendly, cost-effective and efficient use of the limited raw material resources available.

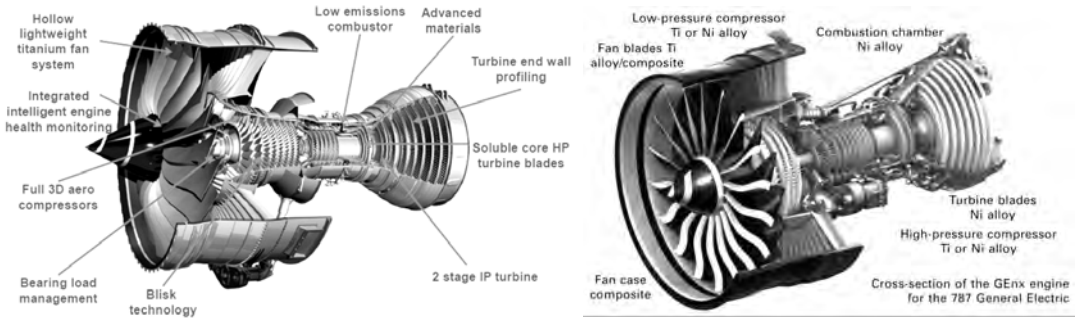

(a) Image reproduced from [7, p. 7, fig. 4].

(b) Image reproduced from [8, p. 20, fig. 6].

FIGURE 1.1: Nomenclature and material used in the manufacturing of an aircraft engine.

1.2 Aim of the study

The aim of the present study is to investigate the residual stress formation and the aspects related to the microstructural changes in titanium alloy Ti-6Al-4V, arising as a consequence of a laser melting process and rapid cooling associated with the hatch spacing, which is the distance between two consecutive laser scans. However, the hatch spacing is not the only process variable involved in the layer-by-layer building, so a more realistic study should take into account the overall effect of additional variables, for example, considering the combined effect of laser speed with hatch spacing. An additional objective is formulating an improvement in the understanding of the development of residual stresses in any manufacturing process by making use of the finite element method combined with experimental work. To achieve this goal, a numerical framework to model a laser source scan can be used to establish some relationships between the processing conditions and the distribution and magnitude of residual deformation and stresses, arising from the extreme conditions to which the material is subjected.

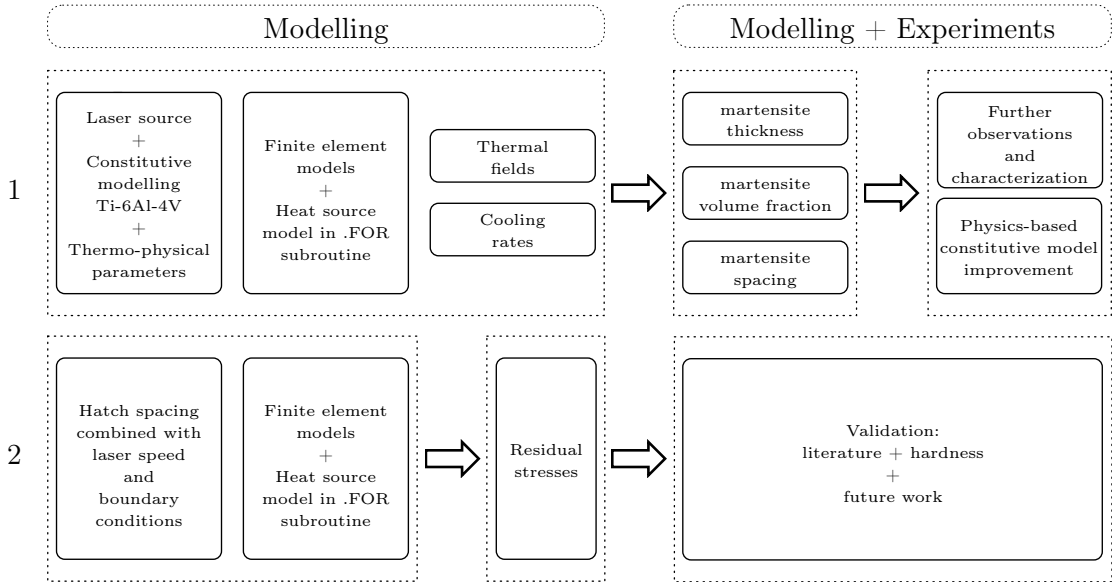

FIGURE 1.2: Overview of the research strategy and work structure.

1.3 Overview of the research principles and strategies, and thesis structure

The thesis structure mainly reflects the research paths followed during the research work and the progressive adjustment of objectives as knowledge of the problem increased and further questions arose. However, it is possible to recognise a certain unitary character, as this research was strongly inspired throughout by the fact that the additive manufacturing process can be thought of as a micro-welding process. The whole structure and methodology is briefly summarised in the schematic diagram presented in 1.2.

1.3.1 Research principles and strategies

Identifying a precise and unique research strategy is quite a complex task, because research often does not proceed along linear paths and this work is no exception. However, as already mentioned, the general principle which guided

the whole investigation was the concept of additive manufacturing as a micro-welding process. Since the welding process has been more extensively studied than the additive manufacturing process, using the increased knowledge developed in recent times on the former can help predict residual stresses for the new additive manufacturing process.

Another important principle which guided this research was the recognized necessity to combine theoretical modelling with laboratory experiments, because they cannot be seen as two completely separated and independent aspects, even if they sometimes start from different assumptions or if they rely on different methodologies.

1.3.2 Work structure

The present work opens with a background concerning literature review on additive manufacturing, titanium alloys, microstructure, followed by an introduction to heat source modelling, and residual stresses. In this first section some constitutive models for Ti-6Al-4V published in the literature have been investigated and implemented, and it is given a theoretical treatment of martensite generation within Ti-6Al-4V, followed by a description of residual stresses and an introduction to the Carllson-Larsson theory and its most recent advances. The whole structure is then broadly articulated into two parts, which can be considered complementary. In the first one the process model is presented and studied and the computational aspects defined in detail, including some models for predicting features of the martensitic structure. In the second part, the experimental set-up to study the martensitic structure is presented. Thanks to the results obtained by a consistent number of numerical simulations, some considerations about the magnitude and distribution of residual stresses induced by additive manufacturing can be outlined. Furthermore, the results from the experimental programme can help to understand the role of the cooling rate on the microstructure. Finally,

all the results obtained by the different strategies developed during the work are summed up and some useful guidance for an improvements of knowledge in the field, are summarised, discussed and applied, in preliminary fashion, to the fatigue behaviour of additively manufactured parts of Ti-6Al-4V. To this section is then added a general discussion regarding some future improvements and the work is completed with some appendices, the purpose of which is to provide more detailed results to the reader and to equip further researchers with some images and data elaborated during the experimental and numerical stages of the present work.

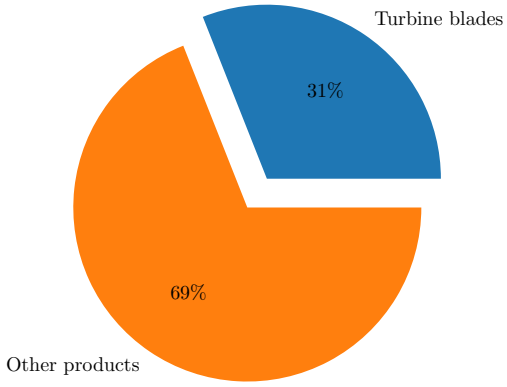

(a) Quota of additive remanufacturing of turbine blades. Data reproduced from [6, p. 225, fig. 7].

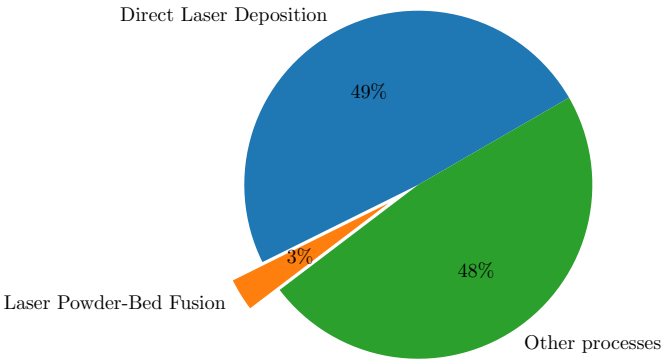

(b) Quota of remanufacturing with laser powder-bed fusion. Data reproduced from [6, p. 227, fig. 9].

FIGURE 1.3: Current status of additive manufacturing-based remanufacturing applications and techniques.

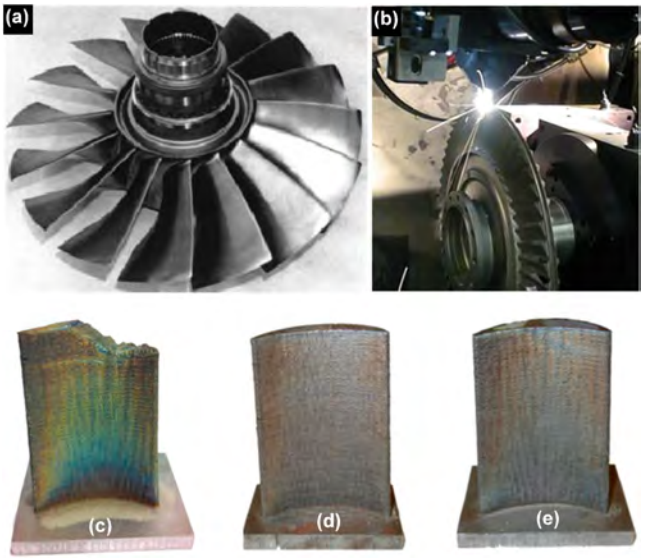

FIGURE 1.4: Repaired BLISK (a) and repairing in process (b), while below are the photographs of a damaged blade (d), an original undamaged blade, and a repaired blade (e). Image reproduced from [9, p. 5, fig. 4].

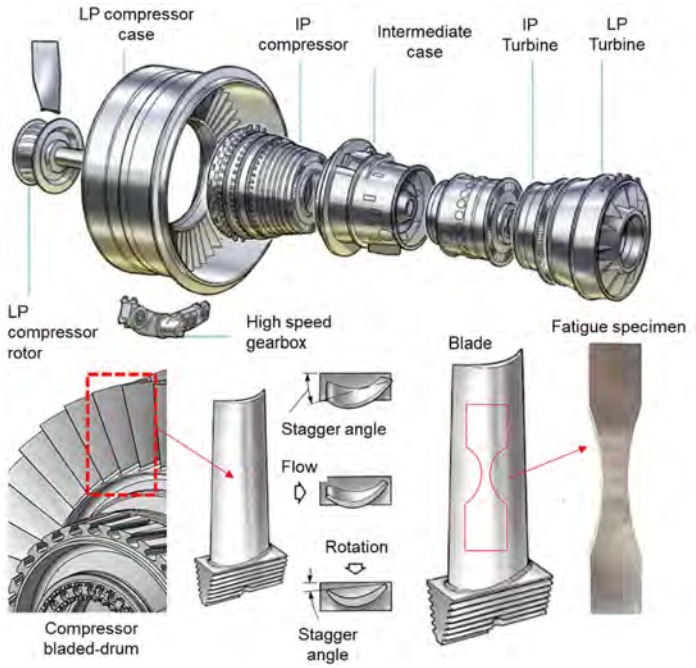

FIGURE 1.5: Fatigue specimen extracted from the compressor blade used for test procedures. Image reproduced from [10, p. 5, fig. 4].

Chapter 2

Literature review

2.1 Additive manufacturing

Additive manufacturing is a highly promising manufacturing process that permits to build three-dimensional objects in the physical world starting with a digital model. It can be useful for versatile applications, such as in those in the medicine, architecture, art, electronics, and aerospace industry. Its main benefit is the possibility to speed up the entire productive process and so shortening the time between the design and the usage of a product, but concomitant benefits include repairing components and using less material.

Despite having numerous interesting application possibilities, it is necessary to move forward and proceed with investigations in this field, because additive manufacturing can be considered in its early stages of development, and a better knowledge of the influence of various factors is required. This will certainly ensure that in a near future it will be a *de facto* standard in the manufacturing industry.

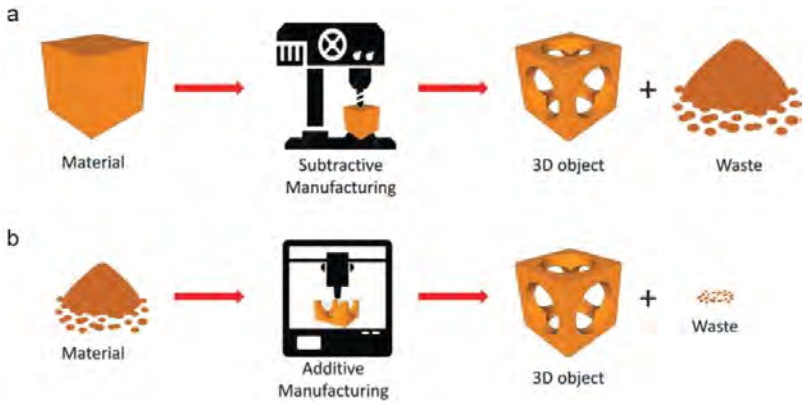

FIGURE 2.1: Scheme showing the differences between a subtractive (a) and an additive manufacturing process (b) in terms of initial material and final material waste. Image reproduced from [11, p. 2, fig. 1].

2.1.1 Overview of a new metallurgical process

Additive manufacturing process or *layered manufacturing*, better known as 3D printing in some contexts, permits to build arbitrarily shaped three-dimensional objects in the physical world starting with a digital model, which is usually a *computer-aided design* (CAD) model. The production of the physical object is based on an a layer-by-layer upwards sequential deposition of thickness of material, where each layer is a cross-section of the final part. It is called *additive* in contrast to the traditional manufacturing processes, where a part is built by subtraction of material, as represented in Figure 2.1.

As a result of development of the additive manufacturing techniques, extremely important and new exciting opportunities for different market sectors have been created. Indeed, it nowadays finds applications [12] in medicine, where it can be used to create patient-specific implants and biomedical devices, in art and architecture, where sometimes is required to study the model of a sculpture or of a building and to show it to different people, in the automotive and aerospace industry, where often the main requisite is to build lightweight components, with an improved weight-strength ratio. Indeed this requisite is achieved thanks to the

FIGURE 2.2: Necessary procedural steps for the additive manufacturing process, from the digital CAD model to the final 3D object. Image reproduced from [13, p. 3, fig. 1].

possibility offered by additive manufacturing to print parts with internal cavities.

The geometry of the digital model is firstly stored in a STL file, according to a file type introduced by 3D System Inc. in 1987 [12], which is currently the standard for every additive manufacturing process [12, p. 3]. This file contains a header and a triplet list of three-dimensional coordinates in the Cartesian coordinate system, which are the coordinates of the three vertex of each triangle into which the geometry is approximated, and the normal vector to the surface of each triangle. This procedure clearly induces an approximation, because continuous surfaces in the CAD model are replaced by a finite union of triangular surfaces and discrete stair steps in the STL file. This second approximated digital model is then elaborated by a slicing software and then by the printing system, following the steps shown in Figure 2.2. Although the STL file is generated by a geometrical minimising criterion that permits to approximate a surface fairly accurately, so the geometrical model created cannot be directly used for finite element calculations. A discretised mesh for finite element is indeed generated to ensure that a specific quality factor, related with the computation itself, is minimised. Nevertheless, an algorithm able to generate adaptive surface meshes suitable also for the finite element method calculations was proposed [14]. This algorithm can in theory open the possibility to use a single digital model both for prototypes and for mechanical interests in the same time, allowing a better

integration between the theoretical modelling and the laboratory experiments.

The materials used in 3D printing are in a certain way still limited, but nevertheless it is possible to use several polymers and also different metals, such as steel, titanium alloys, copper and aluminium, and finally some ceramics and composites, but even paper and fabrics [15, p. 3876]. Although the material used in this process can be solid, liquid or in powder form, the latter two seems to be more promising [12, p. 2]. Among the numerous number of materials, metal additive manufacturing is rapidly supplanting the traditional technologies, perhaps for greater benefits than other those obtainable with other materials.

2.1.2 Building technologies and process parameters

There are several different technologies to produce the manufactured metallic product and they are based on differing processes that use the required thermal energy from laser or electron beam to melt a metal powder and so build the part. A preliminary classification of two main building technologies is represented by melting and sintering. The electron-beam technology permits to electronically control electrons in vacuum and when they collide with matter, they are converted into heat or kinetic energy. On the other hand, sintering is a heat treatment in which some particles are are fused together. An essential difference between melting and sintering is that during the first procedure the material is turned from a solid into a liquid state, whilst in the second one the material is compacted without turning it into a liquid. The main differences between them are firstly based on the specific building apparatus and secondly on other variables, such as the material that can be used, the resolution and the complexity of the physical model. Here 'resolution' refers to layer thickness, which can vary from less than 10 µm to 0.25 mm, whilst 'complexity' refers to the possibility to build highly complex geometries, such as those with internal cavities.

Additive manufacturing techniques can be divided, in the first instance, into

powder bed fusion and direct deposition technologies. In powder bed fusion, a laser is used to melt a fine (20–100 µm) powder bed to create each layer, whilst in direct deposition the powder is deposited and simultaneously melted by the laser beam. This also makes possible to repair previously created parts, such as turbine blades [15, p. 3876], as in Figure 1.4, or to add material to them. Often the alloy is processed in an inert atmosphere, principally composed by nitrogen or argon (as in selective laser melting), whilst a high vacuum chamber can be used (as in electron beam melting), and this physical condition prevents the interaction of the heated material with the environment [16]. Direct deposition technologies include wire and arc additive manufacturing, which shares similarities with arc welding processes and is characterised by low tooling costs and the possibility of producing large parts [17].

The main numerical parameters controlled by an operator are the *laser beam radius*, *scanning speed*, and the *hatch spacing* and their values change according to the building process and to the material. For some of the more common building technologies for the titanium alloy Ti-6Al-4V, they are summarised in Table 2.1. However, they are not the only parameters involved in the process, because some additional process parameters are *laser type*, *laser power*, *layer thickness*, *ambient temperature*, *atmosphere*, *bed temperature* [18].

With regards to the powder, its *particle shape*, *particle size* and *particle distribution*, its *chemical composition*, *thermal conductivity*, *melting temperature*, and its *absorptivity* and *reflectivity* are some of the influential variables involved in additive manufacturing [18]. All these variabilities make it still difficult to completely understand the effect of each of them on the final mechanical performance.

An initial obstacle in researching about metal additive manufacturing is represented by the confusing nomenclature of the processes [19]. Surprisingly, same processes can have different names according to the different technology supplier and this can be attributed to the rapid growth of additive manufacturing during

the last years, although a systematic arrangement is recently emerging in the literature [19]. However, the problem is not only attributable to the industry, but also to research, because sometimes this confusion is exposed in the published works. For example, direct metal laser fabrication techniques are thought to include *selective laser sintering* (SLS), also known as *direct metal laser sintering* (DMLS), and *selective laser melting* (SLM) as subcategories [20]. Differently, in other works they are distinguished as different building techniques [19]. Again, for example, another publication lists laser powder-bed fusion (LPBF) as synonym of selective laser melting (SLM) and direct metal laser melting (DMLM) [21].

A first approach into classification is given by the *American society for testing and materials* (ASTM), which aim is to group additive manufacturing techniques into seven categories [22]. Subsequently, a further subdivision involves grouping techniques according to the heat source, then to the feedstock or feeding material, and then into the process name, as adopted in Table 2.1 [19]. A different classification approach can consider firstly the process and then a subdivision according to the heat source [23].

The work of categorisation perhaps needs to be consolidated in the future, and this will be facilitated as some of the processes will overcome the others thanks to the market development and more extensive research on the most promising methods, which will guide better the choice of the appropriate nomenclature. Indeed, in order to avoid confusion, it would be necessary that the scientific literature conforms to a specific standard of nomenclature.

Although there exist proven countless benefits in shifting towards additive manufacturing, there are some drawbacks that must be taken into account. First of all, additive manufacturing of large-sized object is not possible, due to lack of material strength and to the extended amount of time needed to complete the process. Furthermore, after the part is created, is sometimes necessary to

subject it to a finishing process, which include also the sterilisation in the medical context or a surface smoothing process, for mechanical purposes, or because it is required by some commercial market purposes. Indeed, from a purely mechanical standpoint the inconveniences are mainly related with the imperfections of the final product, which often has an unfinished look and a rough surface, which can reduce the fatigue strength [24]. Moreover, since additive manufacturing is only in theory capable of generating a fully dense structure, an important microstructural defect is the porosity. Finally, exactly like every manufacturing process, the main concern around the use of additive manufacturing is related with the presence of residual stresses, which is the main topic of the present study.

2.2 Titanium alloys and its processing

Titanium is a transition metal and it is the fourth most abundant of the structural metals on the Earth's crust, with a concentration of 0.6% [25, p. 3]. It was first independently discovered [25, p. 3] by William Gregor and Martin H. Klaproth in about 1790 in the rutile mineral, one of the crystalline variety [26, p. 695] of titanium dioxide (TiO_2), a bright white powder (more details about this discovery can be found in [27], but the good tribute to him, written by A. Russell in 1955 [28] can be also relevant for historical purposes). Despite its abundance, one might be tempted to think that its price would be low in an economy governed by a quantity-price relation. However, the energy required to produce a titanium sponge (the product in its purest form) is significantly more expensive than that required during the production process for other metals, such as steel, for example. One of the main methods of titanium production is named *Kroll process*, which employs magnesium to free Ti from $TiCl_4$ [25, p. 4], [29, 30]. Given the high amount of energy required for its production, additive manufacturing represents an alternative way to avoid waste and therefore to better employ energetic

resources.

Exactly like all transition metals, titanium has a closed-packed structure and a small atomic radius and both characteristics result in higher density and higher melting point than the other metals [31, p. 993]. Pure titanium has a hexagonal close-packed (HCP) crystal structure at room temperature, but at 882.5 °C (1155.65 K, also known as β-transus temperature) it shows an allotropic transformation and its structure becomes body-centred cubic (BCC). Whilst allotropy is the generally a term employed to indicate the property of an element to exist in two or more different forms within the same phase (solid, liquid, or gas states), it is here used to indicate that the titanium can exist in two or more crystal structures, which denote the different solid phases. Conventionally, the first phase, at room temperature, is referred as α-phase, whilst the second phase, above the β-transus temperature, is usually called β-phase. From a mechanical standpoint, a β titanium alloy has a higher yield strength (1150–1300 MPa, [32, p. 205]) than its α counterpart (800–1000, MPa [32, p. 205]), despite having approximately the same mass density. A simple schematic diagram summarising the crystal structure, the phase nomenclature, and yield stress for each phase is given in Figure 2.3. Furthermore, the β-phase is in general more ductile than the α-phase, because the β (BCC) has a greater number of possible slip systems if compared with the α (HCP) [33, p. 87].

Main physical properties of pure titanium at room temperature are [34]: melting temperature $T_m = 1665$ °C, mass density $\rho = 4.51\ \mathrm{g\,cm^{-3}}$, thermal conductivity $\lambda = 17.03\ \mathrm{W\,m^{-1}\,K^{-1}}$, coefficient of linear thermal expansion $\alpha = 8.9 \times 10^{-6}$ $\mathrm{K^{-1}}$, Young's modulus $E = 110$ GPa. Since the mechanical properties of pure titanium are affected by the oxygen and nitrogen content [35, 5:38] presence inside the solid solution, it is better to define a range for its mechanical properties. In particular, its Young's modulus can be in the range 105–125 GPa, whilst its tensile strength shows a great variability in the range of 270–740 GPa [35, 5:38]. One

$$\text{HCP if } T \in [T_r, T_\beta),\ \alpha\text{-phase}; \qquad \sigma_{y,\alpha} = 800\text{–}1000 \text{ MPa};$$
$$\text{BCC if } T \in [T_\beta, T_m),\ \beta\text{-phase}; \qquad \sigma_{y,\beta} = 1150\text{–}1300 \text{ MPa}.$$

FIGURE 2.3: Pure titanium crystal structure, phase nomenclature and typical values of the yield stress for each single phase.

last interesting property is that titanium is a very reactive metal and immediately after its surface is exposed to oxygen, a thin layer of oxide is formed and, for this reason, titanium has an excellent corrosion resistance at room temperature [35, 5:38].

2.2.1 Titanium alloys

After the first discovery of titanium in 1790, its alloys processing have become part of the modern industrial practice for more than 50 years now [36]. In the late 1940s, their initial applications were in the aircraft industry [37, p. 265], and, in particular, in the gas turbine engine, where is required a high ratio between strength and weight [36]. Titanium, indeed, has more or less half of the density of steel or nickel-base superalloys [36], while some titanium alloys show tensile strength comparable to steel and some of them can reach extraordinary tensile properties [37]. But these properties alone do not justify the enormous success of titanium alloys. Indeed, nowadays several titanium alloys have found a variety of applications also in the medical field (orthopaedics, dentistry, and vascular surgery), to build joint replacement prostheses, for dental implants and cardio-vascular stents, thanks to their high bio-compatibility (especially those with a reduced content of aluminium [38]), durability and corrosion resistance to bodily fluids [37, 39, 40, 41, 42]. In addition, they are successfully employed in oil, gas and petroleum processing, architecture and even for daily life products, thanks to its ability to be worked through different metallurgical processes [36], and among these, there is the most recent metal additive manufacturing.

The most remarkable mechanical characteristic of a titanium alloy is the high

strength-weight ratio and its good corrosion resistance [25] (better than high-strength aluminium alloys [32, p. 206]), until its temperature is below 600 °C [32, p. 206]. For these reasons and because they are able to retain their mechanical properties at high temperature [32, p. 9], titanium alloys have undergone an increase in demand predominantly in the aeronautical applications from about the early 1950s. In particular, titanium alloys are frequently used in aerospace to build parts that for which is required to occupy a minimum space, such as landing gears and wing–fuselage connections [32, p. 9], but also for jet engine parts, which need to operate at temperatures up to 500–600 °C [32, p. 202], as shown in Figure 1.1. However, is not yet possible to use titanium alloys in operating temperatures above 600 °C, such as those in the combustion chamber, mainly because the mechanical properties of the material fall away significantly and because there may occur oxidation [32, p. 202]. In the aerospace industry titanium alloys find applications mainly in the colder side of the aircraft engine, while for the hot turbine side are required BLISKs made of heat and corrosion resistant super alloys, such as nickel-based superalloys (Figure 1.1).

Additive manufacturing and microstructure of Ti-6Al-4V

Among the wide range of titanium alloys, Ti-6Al-4V has been selected as one the most versatile and promising and it is indeed the most widely used, the standard titanium alloy [37, p. 221], [36, p. 8]. More recently, its processing has been extended to new manufacturing technologies, including powder metallurgy processes, like the more recent metal additive manufacturing.

According to the additive manufacturing nomenclature previously established, the main process parameters for Ti-6Al-4V can be found in the literature published and they are summarised in Table 2.1. The literature found is certainly not exhaustive and some processes are better documented than others, because their use in the production of Ti-6Al-4V parts seem to be more prominent. More-

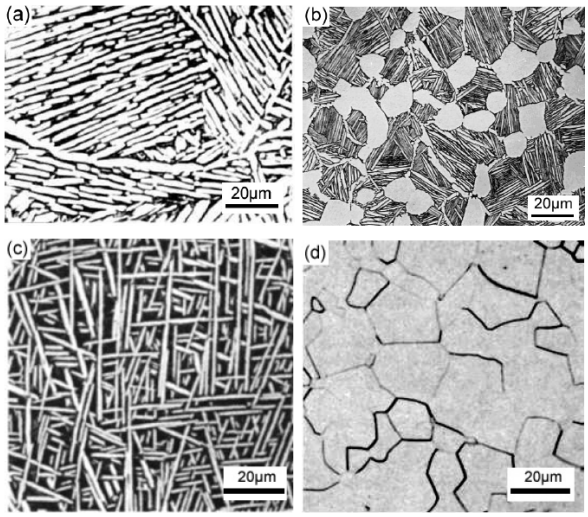

FIGURE 2.4: Typical microstructure of $\alpha + \beta$ titanium alloys: a) Widmanstätten; b) duplex microstructure; c) basket-weave microstructure; d) equiaxed structure. Image reproduced from [43, p. 5, fig. 1].

over, since there is still confusion in mentioning the process, the process name reported is the one in accordance with that chosen by the author, despite the fact that the same process can have different names. For this reason they should be taken as general study reference, but the specific parameters for each building scenario should be evaluated more specifically according to the design target and information by the machine supplier.

Typical microstructures for Ti-6Al-4V under different processing conditions are well represented in Figure 2.4. In Ti-6Al-4V parts fabricated by an additive manufacturing technology or altered by welding, due to the high temperature reached and the higher cooling rates, it can be observed the formation of a new phase, referred as *martensite*, or *martensitic* α. Therefore, it is not currently possible to understand the mechanical behaviour of such material in the final component without considering the importance of this new phase.

TABLE 2.1: Main building parameters associated with some of the most common additive manufacturing processes for Ti-6Al-4V (when the speed).

Heat source	Feedstock / feeding material	Process	Power	Speed	Hatch spacing
Laser	Powder bed	LPBF (Laser powder-bed fusion)	175 W [21] 120–170 W [44] 100–200 W [45] 200 W [46] 100–375 W [47]	200–1200 mm/s [44] 960–1500 mm/s [48] 200–1100 mm/s [45] 1000 mm/s [46] 375–1029 mm/s [47]	100 µm [21] 45–115 µm [44] 80–100 µm [45] 12000–13000 µm [47]
		LBM (Laser beam melting)	400 W [49] 175–250 W [50] 100 W [51]	200–1900 mm/s [52] 1000–1500 mm/s [53] 900 mm/s [50]	120 µm [50]
		SLM (Selective laser melting)	120–350 W [54] 100–370 W [55] 300–800 W [56] 50–400 W [57]	770–1200 mm/s [54] 200–2000 mm/s [55] 200–1000 mm/s [56] 600–1750 mm/s [56] 200–1600 mm/s [58]	0.10–0.18 µm [54] 30–100 µm [55] 40–120 µm [56]
		DMLS (Direct metal laser sintering)	100–200 W [59] 150–350 W [60]	50–100 mm/s [61] 400–1800 mm/s [59] 1000–1400 mm/s [60]	0.05–0.1 mm [61] 80 µm [59] 80–100 µm [60]
		Direct metal laser melting	—	—	—
		Direct metal laser forming	20–280 W [62]	80 mm/s [62]	—
	Nozzle	Direct energy deposition with laser (DED-L)	1000 W [63], 1600–2000 W [64] 800–2000 W [46]	≈ 17 mm/s [63] 6–10.6 mm/s [46]	—
		Laser metal deposition (LMD)	1000 W [65]	6 mm/s [65]	≈ 200 µm [65]

Continuation of Table 2.1

Heat source	Feedstock / feeding material	Process	Power	Speed	Hatch spacing
		Laser engineered net shaping (LENS)	330–780 W [66, 67] 350 W [68] 320 W [69] 710–940 W [70]	5 mm/s [67] 6 mm/s [66] 8.5–16.9 mm/s [68] 10 mm/s [69] 10 mm/s [70]	5000–10000 µm [67] 10000–20000 µm [66] 254–381 µm [69] 1.25 mm [69]
		Direct metal deposition (DMD)	1000 W [47]	≈ 17 mm/s [47]	—
		Laser cladding	90 W [71]	8–≈ 14 mm/s [71]	0.3–0.5 mm [69]
Electron beam	Powder bed	Electron beam melting (EBM)	—	—	—
		PBF-EB	50–7000 W [46]	1000–3000 mm/s [46]	—
		Electron Beam Selective Melting (EBSM)	—	—	—
		Selective electron beam melting (SEBM)	—	—	—
	Wire	DED-EB	170–3500 W [46]	7.5–1250 mm/s [46]	—
		Electron beam freeform fabrication (EBF3)	6 kW (maximum) [72] 2.1 W [73]	2 mm/s [72] ≈ 8.33 mm/s [74] 5 mm/s [73]	≈ 35/14 = 2.5 mm [72] 5.5 mm [73]
Arc	Wire	Wire and Arc Additive Manufacturing (WAAM)	160–180 A [75]	5 mm/s [76] 250 mm/s [77, 78] 5 mm/s [79] 180–200 mm/s [75] 1.67–6.67 mm/s [58]	—
Ultrasonic	Lamina	Ultrasonic Additive Manufacturing (UAM)	3–2 × 4.5 kW [80]	1–100 mm/s [81]	—

2.3 Martensitic transformation in Ti-6Al-4V

A metallographic phase resulting from rapid quenching in steel was called *martensite* in 1895 by Floris Osmond, as a tribute to the metallurgist Adolf Martens (1850-1914) [82]. In titanium alloys, formation of new additional phases, which appear formed by small elongated laths with a needle-like shape, under similar physical condition are observed and these are usually referred with the same generic term of *martensite*. This choice of nomenclature is possibly responsible for the belief that this phase is brittle even for titanium alloys, just as it is for ferrous martensite, while, in fact, it seems that it is neither stronger nor more brittle than the parent phase [83, 84]. Not only the idea that it is brittle has not been clearly demonstrated, but, on the contrary, this misconception has been recently dispelled in some studies [85], [86]. Nevertheless, the martensite formation is associated with a higher dislocation density in the material and its boundaries consist of walls of dislocations [37, 87, p. 235]. The increase in dislocation density associated with the quantity and morphology of martensite has been recently integrated in a physics-based constitutive model for Ti-6Al-4V developed by Galindo-Fernández *et al.* (2018) by using an equation previously found for steel, and showing a good agreement with a set of experiments [88]. In the presence of martensite the initial dislocation density has been estimated to be two orders of magnitude larger than that for Ti-6Al-4V wrought, leading to a higher yield strength and reduced ductility [88]. Furthermore, fracture toughness of an as-built Ti-6Al-4V component with martensitic structure is significantly lower than the same wrought alloy with a lamellar microstructure, although the fracture resistance can be improved with a post-process heat-treatment that breaks up the martensite laths [21, p. 15]. This reduced ductility clearly contrasts with the debunking of the idea that martensite is brittle, but its brittleness can perhaps be explained as an indirect effect due to an increased interaction between martensite

and dislocations, rather than attributing it only to the martensite. This aspect appears as a good area for a further investigations and can potentially lead to a better understanding of the martensite role in Ti-6Al-4V.

It is now possible to describe the necessary physical conditions for the formation of martensite, focusing on Ti-6Al-4V. In particular, this study considers only the thermodynamic formation process, ignoring the fact that the martensite formation can be also induced by plastic deformation [84]. The titanium alloy Ti-6Al-4V is an $\alpha + \beta$ alloy at room temperature, where the α-phase has a hexagonal close packed (HCP) crystal structure and the β is body-centred cubic (BCC). Whilst pure titanium is composed by only α-phase at room temperature, the necessity of the additional β-phase emerges as a possibility to overcome the limitation in strength as for a fully α alloy [37]. As the material is progressively heated, at the temperature T_β, called *β-transus temperature*, the titanium alloy Ti-6Al-4V undergoes an allotropic transformation $\alpha + \beta \rightarrow \beta$. However, the whole transformation is not instantaneous and it should be better regarded as a continuous process, under a continuous heating condition. In this case, T_β indicates the temperature at which this process is considered fully completed. It is usually assumed that this temperature, for Ti-6Al-4V, is $T_\beta = 980$ °C, but this value is also related to the varying chemistry of the alloy, so it can be in the range of temperature within 977–1032 °C and it can be calculated as a function of the amount of constituents [89]. By using the equation given in [89], considering only the nominal aluminium and vanadium content and ignoring the other constituents, the theoretical value obtained is $T_\beta = 887.50$ °C, which is a little lower than expected. Under further temperature increases, the material can reach the melting point, which is $T_m = 1668$ °C for pure titanium [36] and in the range $T_m = 1599.85$–1649.85 °C for Ti-6Al-4V [90]. As last condition under heating, the material can evaporate if the temperature is above the boiling point, which is $T_b = 2859$ °C for Ti-6Al-4V (for pure titanium is $T_b = 3260$ °C [36]) [91].

The microstructural transformation called *martensite transformation* can be summarised with the following oversimplified, for the purposes of explanation, scheme:

$$\alpha + \beta \xrightarrow{\text{heating}} \beta \xrightarrow{\text{cooling}} \alpha + \beta + \alpha' + \alpha'' + \cdots + \alpha^n, \tag{2.1}$$

where $n \in \mathbb{N}$, extending the convention given in [92]. The material, initially composed by two phases, becomes fully β after heating, as ultimate and extreme condition reaching T_β, and then it again becomes $\alpha + \beta$ after cooling. However, part of the β-phase transforms into martensite and, because of that, the former is generally referred as *parent phase*. Here the martensite is so distinguished, again in analogy with steel [87], into primary, secondary, tertiary and even quartic martensite, depending on its size [84, pp. 9–10], [37]. This hierarchy is reflected into the value assumed by the integer index n in the diagram (2.1). The smaller length of major axis, reached by quartic martensite, can be below 1 µm, while its minor axis can be less than 20 nm [87]. A summary of sizes for the martensite in Ti-6Al-4V is given in Table 2.2. The two principal martensites denoted as α' and α'' has, respectively, an HCP and an orthorhombic structure [92, p. 1] and the second one is also softer than the former [84]. The most important martensite is the α' type and it appears like parallel-sided plates or laths [37, p. 235] and this needle-like morphology inside the parent phase appears similar to an acicular alpha [36, p. 16]. The size of a single α' lath has been recently related to the cooling rate by Villa *et al.* (2020) [93, 94] and this was previously indicated by some scholars as one of the most important factors in its generation [37, p. 231], and this approach has been followed more recently to study the martensite size lath in electron beam welded Ti-6Al-4V plates [95].

In order to give a more accurate definition and avoid any confusion, a mathematical description of the two main thermodynamic conditions for the formation of α' martensite in titanium alloys is presented below.

The two conditions leading to the formation of martensite are the cooling of

Type of α'	Length of major axis	Length of minor axis
Primary α'	Tens of microns or larger (> 20 µm)	Several microns (1–3 µm)
Secondary α'	A dozen microns (10–20 µm)	Hundreds of nanometres (100–900 nm)
Ternary α'	Several microns (1–10 µm)	Tens of nanometres (20–90 nm)
Quartic α'	Hundreds of nanometres or smaller (< 1 µm)	Dozen nanometres or smaller (< 20 nm)

TABLE 2.2: Summary of sizes for the martensite in Ti-6Al-4V. Data reproduced from [87, p. 312, tab. 2].

the material starting from a temperature which is above the *martensite starting temperature* $T_{m,s}$ and the successive cooling stage with cooling rate above the *martensite critical cooling rate* $\dot{T}_c$ [21]. This means that if $T(x,t)$ denotes the temperature at the generic point $x \in \Omega$ and at the generic time $t \geq 0$, assuming that the cooling rate has a positive sign if there are heat losses, a point x belongs to the martensitic phase if:

$$T(x,t) \leq T_{m,s}, \quad t > t_c; \tag{2.2a}$$

$$\partial T/\partial t > \dot{T}_c, \qquad t > t_c; \tag{2.2b}$$

where t_c is the cooling starting time. In this case, the physical conditions lead to a Widmanstätten pattern [36] and the process by which the martensite is formed is called *diffusionless process* [84], because the cooling process is so rapid that the martensite does not have time to disgregate itself and so it remains trapped inside the parent β-phase. On the other hand, if the cooling rate is below $\dot{T}_c$ there is the so called *diffusion-controlled* nucleation of martensite [83]. This means that if (2.2a) is satisfied, but the second one (2.2b) is replaced by

$$\dot{T}_{c,2} < \partial T/\partial t < \dot{T}_c, \tag{2.3}$$

then there is a massive, but not complete, transformation into martensite, whereas

if (2.2a) is satisfied, but the second one (2.2b) is replaced by

$$\partial T/\partial t < \dot{T}_{c,2}, \tag{2.4}$$

a gradually diffusion-controlled Widmanstätten α formation has been observed and if the cooling rate is extremely slow the classical *basket-wave* Widmanstätten morphology is formed [96]. The critical cooling rate for Ti-6Al-4V is $\dot{T}_c = 410$ °C s^{-1}, while $\dot{T}_{c,2} = 20$ °C s^{-1} as reported in [96]. The martensite starting temperature, instead, is a function of the chemical composition of the alloy and it has been proposed the following equation for its determination [97]:

$$\begin{aligned} T_{m,s} = c_1 - c_2 w_{Fe} - c_3 w_{Cr} - c_4 w_{Mo} \\ - c_5 w_V - c_6 w_{Nb} - c_7 w_{Zr} + c_8 w_{Al}, \end{aligned} \tag{2.5}$$

where w_X is the amount of the generic alloying substance X, in wt%, and the constants are $c_1 = 1156$, $c_2 = 150$, $c_3 = 96$, $c_4 = 49$, $c_5 = 37$, $c_6 = 17$, $c_7 = 17$, $c_8 = 7$, $c_9 = 15$. In case of Ti-6Al-4V, in absence of other constituents, other than Al and V, this formula leads to 882.27 °C, but this value is quite high, because $T_{m,s}$ has been reported in the high range 575–800 °C for the same alloy, in a more recent study [21]. The whole transformation process is considered concluded when the material reaches the *martensite finishing temperature*, which is reported to be $T_{m,f} = 400$ °C for the titanium alloy under investigation [98]. Further temperature decrements below $T_{m,f}$ do not affect the martensite formation.

Now, if the material is heated above the β-transus temperature and it is partially melted, the $\alpha + \beta$ phases are transformed into $\beta + \ell$, where ℓ indicates the liquid phase and, again, if it is rapidly cooled, there is martensite formation. The Diagram (2.1) can now be redrawn, taking into account the considerations carried out until now:

$$\alpha + \beta \underset{|\partial T/\partial t| < \dot{T}_{c,2}}{\overset{T > T_\beta}{\rightleftarrows}} \beta + \ell \underset{T > T_\beta}{\overset{|\partial T/\partial t| > \dot{T}_c}{\rightleftarrows}} \alpha + \beta + \alpha' \ . \tag{2.6}$$

2.3.1 Volume fraction of martensite

As seen in the previous paragraph, if the cooling rate is above the critical value $\dot{T}_c$, then there is a diffusionless formation of martensite. The volume fraction of the martensite associated with this process was firstly described in carbon steel by the Koistinen-Marburger [99] equation and since then it was widely employed in several studies. It has more recently been introduced to describe also the volume fraction of the primary martensite in titanium alloys, under the form [100, 101, 102]:

$$V_{\alpha'}(t) = V_\beta \left[1 - \exp(-\chi(T_{m,s} - T(t)))\right], \tag{2.7}$$

where V_β is the volume fraction of the β-phase available for martensitic transformation and $\chi \in \mathbb{R}$ is a coefficient. It has to be noted that the parameter χ not only regulates the final amount of martensite at the end of the cooling process, but it also controls its amount during the temperature decrease. Furthermore, the time-dependency is being introduced in this Equation (2.7) for the first time in this study. Assuming that all the β-phase is available for the phase transformation, the former can be described by referring to the phase diagram as

$$V_\beta(T) = V_{\beta,i} + \Delta V_\beta(T), \tag{2.8}$$

where $V_{\beta,i}$ is the initial volume fraction of the beta phase at room temperature and its increment ΔV_β is a function of temperature [103, p. 312]:

$$\Delta V_\beta(T) = \begin{cases} 0, & T < T_{\beta,s}; \\ (T/T_\beta)^{10}, & T_{\beta,s} < T < T_\beta; \\ (T/T_\beta)^{10} - V_{\beta,i}, & T > T_\beta. \end{cases} \tag{2.9}$$

In this last formula we assume that the β transformation starts at $T_{\beta,s}$ and it is fully completed at T_β. This piecewise function describing the prediction of the β volume fraction evolution with temperature is shown in Figure 2.5.

With regard to the χ parameter, scholars have adopted different values depending on the production process. The value $\chi = 0.003$ was estimated for Ti-6Al-4V [100] (laser forming) and [101] (laser metal deposition), whereas others proposed $\chi = 0.005$ [102] (additive manufacturing).

2.3.2 Martensite dissolution through heat treatment

A martensitic structure, as previously mentioned, is sometimes associated with a negative impact in terms of mechanical performance of the components. This is represented in a summary of the mechanical properties, deformation localisation, and damage associated with the martensitic structure in Ti-6Al-4V, given in Figure 2.6. Since the martensite is generally considered detrimental with respect to some mechanical properties, some post-processing strategies have been designed in order to improve the tensile behaviour of Ti-6Al-4V [106]. Most of the post-heat treatments are in the solid solution temperature region, which is defined as the temperature region between the dissolution temperature $T_d \approx 700$ °C and the β-transus temperature [106]. The former is the temperature at which an exponential dissolution $\alpha' \rightarrow \beta$ starts, and it can be observed that it is almost equivalent to $T_{m,s}$. In Figure 2.8a is illustrated the hierarchical structure of the martensite and its dissolution after heat treatments. For Ti-6Al-4V parts built with laser powder-bed fusion, a partial decomposition has been observed for temperatures in the range 670–800 °C [21]. Sometimes a further dissolution of martensite is still desirable, so what is commonly suggested is a second heat treatment, in order to achieve the fragmentation of the bigger α'-martensite laths, which is a process that break them into smaller pieces, through cuts almost perpendicular to their larger length, as shown in Figure 2.8b. The disadvantage of these treatments is their energy consumption, as they usually require to heat the material at medium-high temperatures for hours. More specifically, martensite is partially decomposed for temperatures in the range 670-800 for two hours, and a

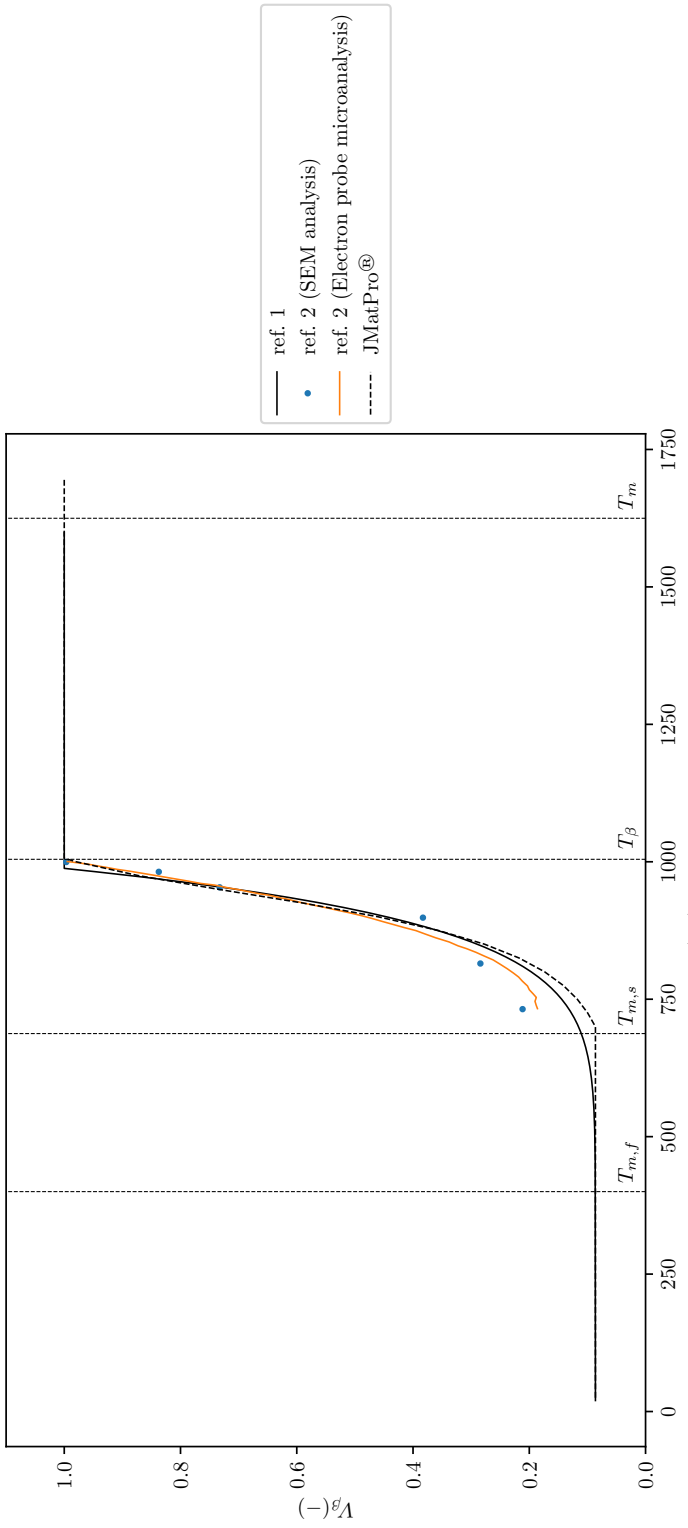

FIGURE 2.5: Phase diagram evolution for the β-phase of Ti-6Al-4V where are indicated the melting temperature T_m, the β-transus temperature T_β, the martensite starting temperature $T_{m,s}$ and the martensite finishing temperature $T_{m,f}$. The references are the following: ref. 1 = [103], ref. 2 = [104].

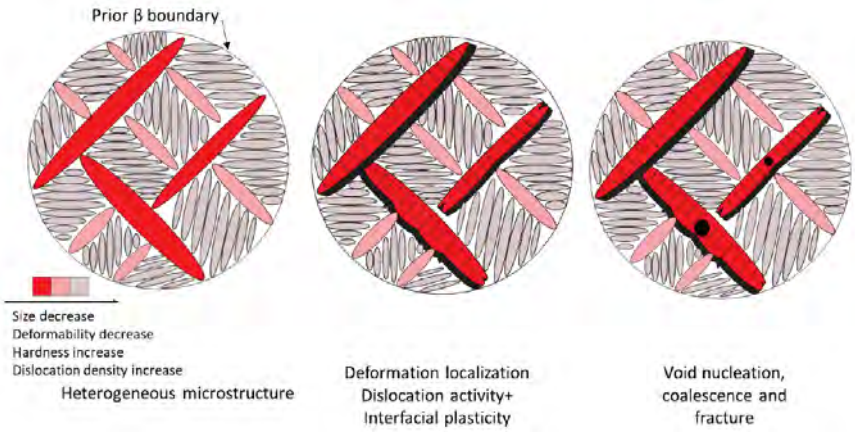

FIGURE 2.6: Mechanical properties, deformation localization, and damage associated with the martensitic structure in Ti-6Al-4V. Image reproduced from [105, p. 7, fig. 10].

full decomposition in the range 800–1050 °C for two hours [21].

An indirect effect of martensite dissolution obtained through a heat treatment is the reduction of dislocation density, as illustrated in Figure 2.7, because it is directly proportional to the thickness of the martensite laths, which usually increases during heat treatments [107].

2.4 Constitutive description of plasticity for Ti-6Al-4V

In the context of continuum mechanics, a constitutive model is a mathematical law that permits to relate the deformations to the stresses. As remarked in [109, p. 1161], constitutive laws can be distinguished into two categories: phenomenological constitutive models and physics-based models. Whilst the former tries to describe the behaviour of the material in an empirical way, the latter mainly relies on an understanding of the operating deformation mechanisms and their relation to the material microstructure. Although the implementation of phenomenological models is fairly simple and fast, physics-based models are preferable because

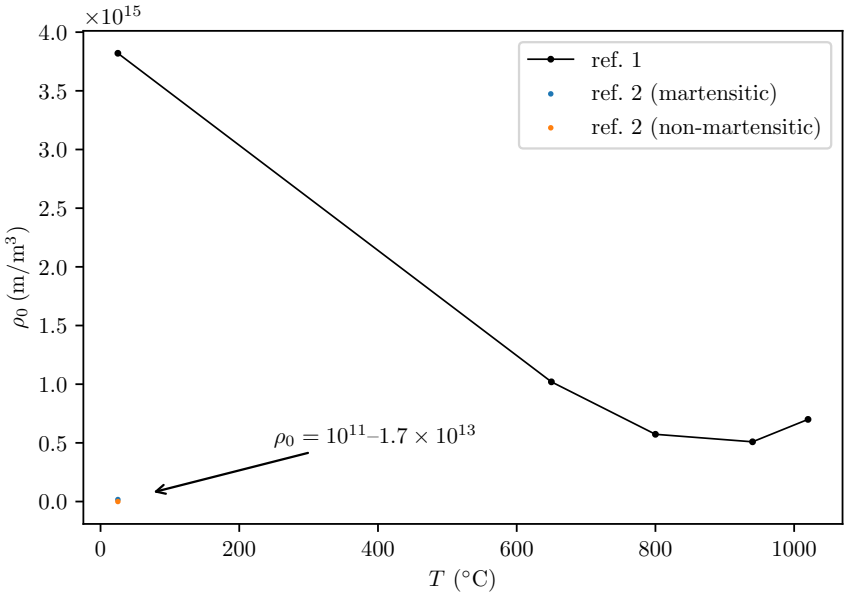

FIGURE 2.7: Values of initial dislocation density in Ti-6Al-4V. The references are the following: ref. 1 = [108], ref. 2 = [88].

they provide more accurate estimates.

Among all physical properties that can be included inside a physics-based model, the main ones are certainly the grain size and the dislocation density. However, one of the main phenomenological constitutive models widely used in mechanics of the materials is the Johnson-Cook model [110], thanks to its simplicity of implementation. Therefore, some constitutive models used the Johnson-Cook model as a starting point, trying to integrate it with some additional parameters, sometimes referring to physical variables. Finally, the most advanced constitutive models are able to take into account more complicated microstructure developments, such as texture evolution, recrystallisation, or grain growth [111].

Since deformation in metals during thermo-mechanical processing is not uniform, but occurs by forming slip bands, this led to the concept of *crystallinity* during the beginning of the 20th century, a theoretical development which was

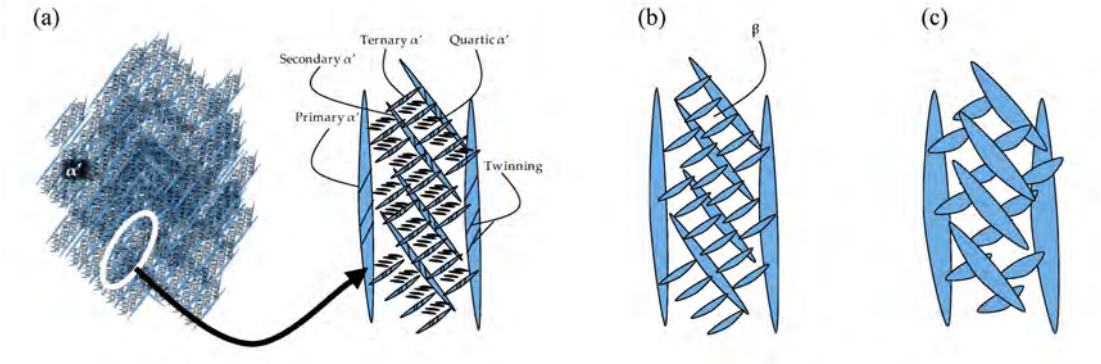

(a) Martensite hierarchical structure (a) and its progressive decomposition during low and medium heat treatment (b, c) in the solid solution temperature region. Image reproduced from [106, p. 11, fig. 6].

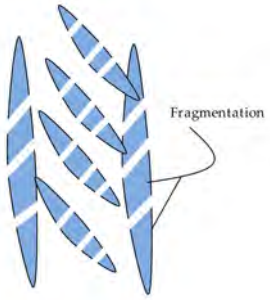

(b) Martensite decomposition obtained with a heat treatment, which breaks the α' lamellae into smaller pieces. Image reproduced from [106, p. 13, fig. 8].

FIGURE 2.8: Hierarchical structure of the martensite in Ti-6Al-4V and its dissolution obtained with a heat treatment.

also facilitated by the introduction of the X-ray diffraction technique [114]. However, while the atoms are arranged in specific and regular crystal structures, the earlier physical observations shown that there can exist defects of those arrangements and they were called *dislocations* [115]. The concept of dislocations had been doubted by numerous scholars until around 1950, but confirmation of their existence finally came with the introduction of transmission electron microscopy (TEM) [114]. Moreover, what was most surprising was that dislocations are not fixed in space and time, but as the material deforms, they can even move within the whole crystal structure. An example of the atoms arrangements in the space can be observed in Figure 2.9a, whilst the dislocation motion is shown in Figure

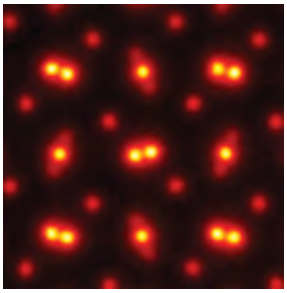

(a) The highest resolution atomic image ever captured, recently appeared in the scientific literature, is a good example of how matter is apparently perfectly ordered. Image reproduced from [112, p. 2, fig. 1D].

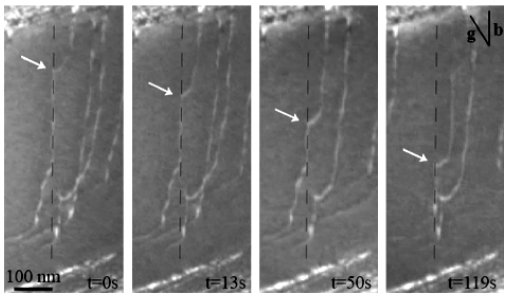

(b) Changes in the arrangement of atoms – usually called *dislocations* – and their movement, as shown in this picture of Ti-6Al-4V, captured at different instants of time. Image reproduced from [113, p. 6287, fig. 4].

FIGURE 2.9: Whilst the matter shows a nearly perfect arrangement of atoms, defects exist and they are not fixed, but can also move.

2.9b, where the dashed line represents a fixed position in the space. The magnitude and the direction of the lattice distortion is given by the definition of a dislocation-displacement vector, the *Burgers vector* [115]. If $C \subset \Omega$ denotes the closed curve forming a loop around the dislocation within the domain of interest $\Omega \subset \mathbb{R}^3$, also called as *Burgers circuit*, and $u : \Omega \to \mathbb{R}^3$ the elastic displacement vector field, then the Burgers vector $b \in \mathbb{R}^3$ is given by a line integral of the elastic displacement field $u : \Omega \to \mathbb{R}^3$ around the dislocation [115]:

$$b = \oint_C \frac{\partial u}{\partial l} \, \mathrm{d}l, \tag{2.10}$$

where with $\mathrm{d}l$ is indicated the length of an infinitesimal portion of the curve length l. Burgers vector is a measure of the lattice distortion due to the dislocation enclosed by the loop and usually this measure is also expressed by its magnitude $|b| \in \mathbb{R}$, which can appear in the mathematical expressions of some physics-based constitutive models. For the alloy Ti-6Al-4V, this magnitude was estimated to be around 2.9×10^{-10} m [88].

2.4.1 Fundamentals of the theory of plasticity

Every material response to applied loads can be ideally distinguished into an elastic response and a plastic response. The material is called *elastic* if it returns to its original shape after the stress that had caused the deformation is no longer applied. It is defined *plastic* if exhibits, after an initial elastic stage and for loads greater than those which generated an elastic response, a non-reversible and permanent deformation.

Mathematical description of a deformation process

Let be $\Omega \subset \mathbb{R}^3$ an open connected set, which describes the *reference* or *undeformed* configuration of a solid body and let be $\Omega^* \subset \mathbb{R}^3$ the configuration of the same solid body at the end of a deformation process. This last configuration is usually called *current* or *deformed* configuration [116]. For historical reasons, when a quantity describing the process from Ω to Ω^* is referred to the reference or undeformed configuration, then it is usually called *Lagrangian* (or *material*) description, while if it is referred to the current or deformed configuration it is called *Eulerian* (or *spatial*).

Let be $X \in \Omega$ two arbitrary points in the two distinct domains. The deformation process can be entirely described when it is known the relationship between all points belonging to both configurations, according to

$$x = x(X, t), \tag{2.11}$$

where the variable $t \in \mathbb{R}$ is the time. It is implicitly assumed here that the deformation process takes place in time and so it is known this relationship in every configuration and for any time.

Assuming that for any fixed instant of time $x \in C^n(\Omega^*, \mathbb{R}^3)$ and $X \in C^n(\Omega, \mathbb{R}^3)$, where $C^n(\Omega, \mathbb{R}^3)$ is the space of every continuously differentiable n-dimensional vector fields on Ω, the deformation gradient $F = \nabla x$ and its inverse F^{-1} are

defined by the equations

$$F(X,t) = \frac{\partial x}{\partial X}, \qquad F^{-1}(x,t) = \frac{\partial X}{\partial x}. \tag{2.12}$$

The latter tensor can be introduced only if the Jacobian of the transformation is different from zero [116]:

$$J(X,t) \neq 0, \qquad J(X,t) = \det(F(X,t)). \tag{2.13}$$

The deformation gradient tensor is called *two-point tensor*, because it related two points, one in the undeformed and one in the deformed configuration.

The deformation process can be also described by the displacement field $u : \Omega \times T \to \Omega^* \times T$, where $T = [t, t + \Delta t]$, with $t, \Delta t \in \mathbb{R}$. The displacement is therefore defined as $u(X) = x(X) - X$ in the reference configuration. Rewriting $x(X) = X + u(X)$, the displacement gradient is related to the deformation gradient by the equation

$$F = \nabla x = \frac{\partial}{\partial X}(X + u(X)) = I + \frac{\partial u}{\partial X}, \tag{2.14}$$

where I is the identity tensor. From Equation (2.14) is possible to introduce the *right Cauchy-Green deformation tensor*

$$C = F^T F, \tag{2.15}$$

from which follows the *Cauchy strain tensor* (or *Green-Lagrangian strain tensor*):

$$E = \frac{1}{2}(C - I). \tag{2.16}$$

If $x = (x_1, x_2, x_3)$ is the Cartesian coordinate system in the undeformed configuration and $u = (u_1, u_2, u_3)$ the displacement field in the same configuration for a fixed instant of time, the components of the Green-Lagrange strain tensor are:

$$E_{11} = \frac{\partial u_1}{\partial x_1} + \frac{1}{2}\left[\left(\frac{\partial u_1}{\partial x_1}\right)^2 + \left(\frac{\partial u_2}{\partial x_1}\right)^2 + \left(\frac{\partial u_3}{\partial x_1}\right)^2\right]; \tag{2.17a}$$

$$E_{22} = \frac{\partial u_2}{\partial x_2} + \frac{1}{2}\left[\left(\frac{\partial u_1}{\partial x_2}\right)^2 + \left(\frac{\partial u_2}{\partial x_2}\right)^2 + \left(\frac{\partial u_3}{\partial x_2}\right)^2\right]; \tag{2.17b}$$

$$E_{33} = \frac{\partial u_3}{\partial x_3} + \frac{1}{2}\left[\left(\frac{\partial u_1}{\partial x_3}\right)^2 + \left(\frac{\partial u_2}{\partial x_3}\right)^2 + \left(\frac{\partial u_3}{\partial x_3}\right)^2\right]; \tag{2.17c}$$

$$E_{12} = \frac{1}{2}\left(\frac{\partial u_2}{\partial x_1} + \frac{\partial u_1}{\partial x_2} + \frac{\partial u_1}{\partial x_1}\frac{\partial u_1}{\partial x_2} + \frac{\partial u_2}{\partial x_1}\frac{\partial u_2}{\partial x_2} + \frac{\partial u_3}{\partial x_1}\frac{\partial u_3}{\partial x_2}\right); \tag{2.17d}$$

$$E_{13} = \frac{1}{2}\left(\frac{\partial u_3}{\partial x_1} + \frac{\partial u_1}{\partial x_3} + \frac{\partial u_1}{\partial x_1}\frac{\partial u_1}{\partial x_3} + \frac{\partial u_2}{\partial x_1}\frac{\partial u_2}{\partial x_3} + \frac{\partial u_3}{\partial x_1}\frac{\partial u_3}{\partial x_3}\right); \tag{2.17e}$$

$$E_{23} = \frac{1}{2}\left(\frac{\partial u_3}{\partial x_2} + \frac{\partial u_2}{\partial x_3} + \frac{\partial u_1}{\partial x_2}\frac{\partial u_1}{\partial x_3} + \frac{\partial u_2}{\partial x_2}\frac{\partial u_2}{\partial x_3} + \frac{\partial u_3}{\partial x_2}\frac{\partial u_3}{\partial x_3}\right). \tag{2.17f}$$

The same tensor can be written in terms of displacement field, in compact notation, as

$$E(u) = \frac{1}{2}\left(\nabla u + (\nabla u)^T + \nabla u(\nabla u)^T\right). \tag{2.18}$$

If the displacement gradient is small, the deformation field can be simplified and the second order quantities can be ignored, so it will be linear respect with the gradient of the displacement field. The theory developed from this assumption goes under the name of *small displacement theory*, as opposed to the *large displacement theory*. The small deformation tensor is therefore

$$e(u) = \frac{1}{2}\left(\nabla u + (\nabla u)^T\right), \tag{2.19}$$

which in the same Cartesian coordinate system is expressed by:

$$e(u) = \frac{1}{2}\begin{pmatrix} 2\dfrac{\partial u_1}{\partial x_1} & \dfrac{\partial u_1}{\partial x_2} + \dfrac{\partial u_2}{\partial x_1} & \dfrac{\partial u_1}{\partial x_3} + \dfrac{\partial u_3}{\partial x_1} \\ \dfrac{\partial u_2}{\partial x_1} + \dfrac{\partial u_1}{\partial x_2} & 2\dfrac{\partial u_2}{\partial x_2} & \dfrac{\partial u_2}{\partial x_3} + \dfrac{\partial u_3}{\partial x_2} \\ \dfrac{\partial u_3}{\partial x_1} + \dfrac{\partial u_1}{\partial x_3} & \dfrac{\partial u_3}{\partial x_2} + \dfrac{\partial u_2}{\partial x_3} & 2\dfrac{\partial u_3}{\partial x_3} \end{pmatrix}. \tag{2.20}$$

Boundary value problem in mechanics

Once the quantities have been defined is now possible to introduce the standard boundary-value problem in mechanics. Given a solid body in the undeformed

configuration, find u and σ such that they equal the prescribed body forces $p \in \mathbb{R}^3$ and the prescribed tractions on the boundary $\partial\Omega$ [117, 116]. Solving a boundary-value problem in mechanics requires to find the displacement field u.

Plasticity according to von Mises

The stress tensor can be splitted into the hydrostatic and deviatoric tensor and the invariants of the deviatoric stress tensor are calculated as follows [116, pp. 11–12]:

$$J_1 = \mathrm{tr}(\sigma); \tag{2.21a}$$

$$J_2 = \frac{1}{2}\left[(\mathrm{tr}(\sigma))^2 - (\mathrm{tr}(\sigma^2))\right]; \tag{2.21b}$$

$$J_3 = \det(\sigma); \tag{2.21c}$$

where $\mathrm{tr}(\sigma)$ is the trace operator acting on the stress tensor. The von Mises yield criterion states that a stress tensor is elastic if

$$J_2 < k^2, \tag{2.22}$$

where $k > 0$ is a material constant. On the other hand, the condition

$$J_2 = k^2 \tag{2.23}$$

defines the *yield surface*. The representation of two different criteria for yielding are shown in Figure 2.10.

2.4.2 Crystal structure and deformation twinning in Ti-6Al-4V

Most of the deformation in metals is due to the shear and it occurs along shear planes, as it was found after the discovery of crystallinity of metals. Therefore, when describing the plasticity for metal-working processes, the most important

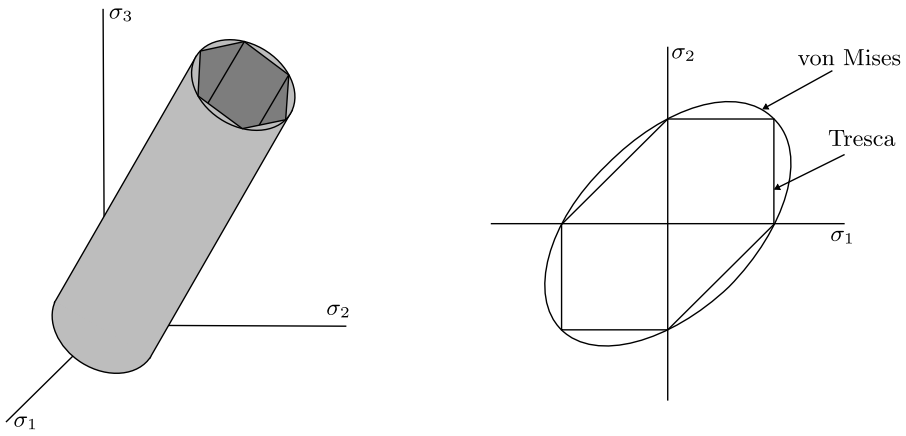

(a) (b)

FIGURE 2.10: Representation of the von Mises and Tresca yield volumes in (a) and yield surfaces in biaxial stress space (b). Images adapted respectively from [116, p. 63, fig. 3.9] and [116, p. 63, fig. 3.10].

variable is the shear strain-rate $\dot{\gamma}$, and so the constitutive models can be expressed as $\dot{\gamma} = f(\tau, T, S_i, P_j)$, where τ is the shear stress, T is the temperature, S_i is the i-th state variable describing the microstructure, and P_j is the j-th material property [118, pp. 2–3].

Deformation of metal crystals

One of the most important advancement in material science was the understanding that several properties of a metal depend on crystal orientation. Whilst tensile test is the most common mechanical test, this is not suitable to describe a deformation process as that of crystals, because this is mainly due to shear. Since the tensile test is still more convenient and practical to perform with respect to shear test, this was one of the main reasons that led to the concept of *resolved shear stress*, where the value of the tensile yield stress σ_y is corrected to determine its value along the crystallographic plane. This correction is usually performed with Schmid's law [119]:

$$\tau = \sigma_y \sin\chi \cos\lambda, \tag{2.24}$$

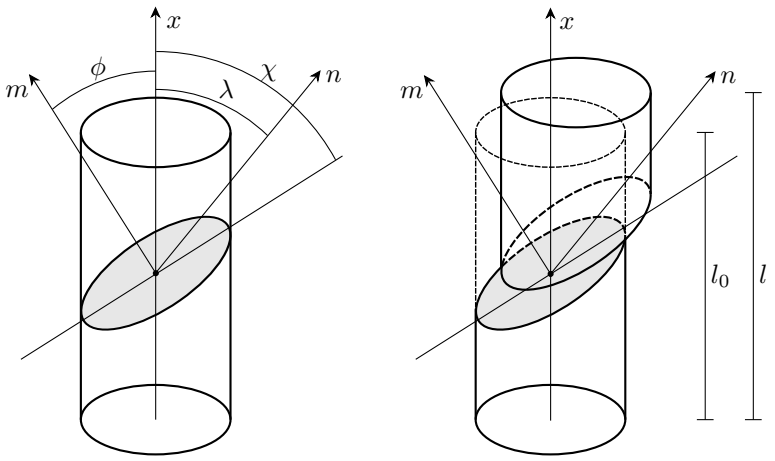

FIGURE 2.11: Illustration of Schmid's law and deformation mechanism of a crystal under uniaxial tensile test. It is shown in grey the slip plane, along which the deformation occurs. The crystal, constrained at the base, it loaded along the x axis and after and after the plastic deformation its original length l_0 becomes l. Concept image inspired by [119, p. 17, fig. 2.9].

where $\chi \in [-\pi, \pi)$ is the angle between the tensile axis and the slip plane and $\lambda \in [-\pi, \pi)$ is the angle between the tensile axis and the slip direction, as represented in Figure 2.11.

The great advantage in using the corrected value obtained with Equation (2.24) is that whilst the tensile stress varies with the orientation of the crystal, the shear value obtained along the slip plane is constant for a single metal. This value is usually indicated with τ_0 and is called *critical resolved shear stress* and it indicates the values above which the crystal starts deforming plastically [119].

Deformation twinning and martensite formation

A demonstration that five independent slip systems are required to plastically deform a crystal by slip has been provided in 1928 by von Mises [115, p. 293]. However, some crystals have only a few slip systems and therefore twinning is a deformation mechanism that can provide a further mechanism for reaching the five [115, p. 811]. In a HCP crystal structure (α phase in Ti-6Al-4V), plastic de-

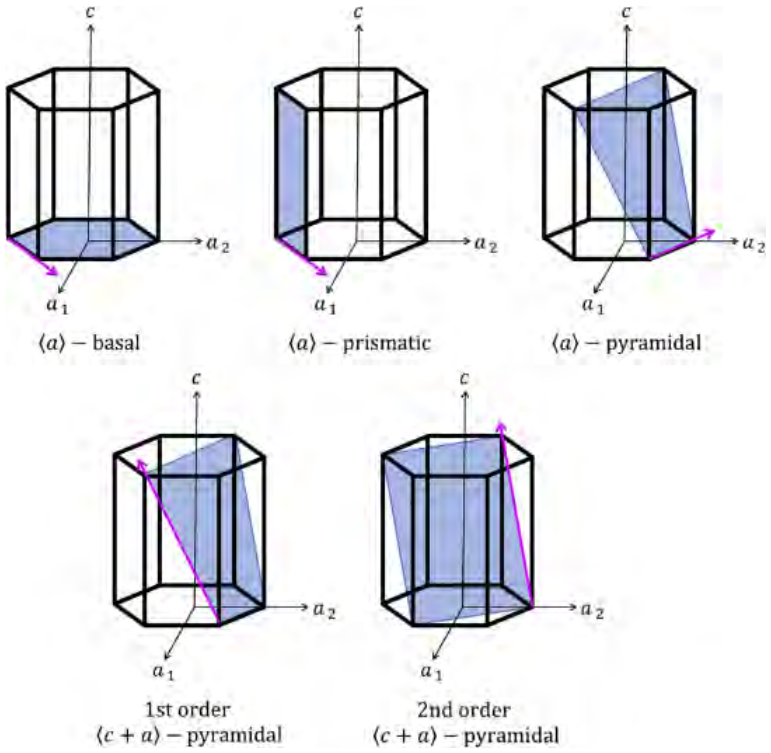

FIGURE 2.12: Diagram of HCP crystal slip systems, as those in α phase in Ti-6Al-4V. Image reproduced from [121, p. 19, fig. 1].

formation occurs along the prismatic plane and the basal plane, as represented in Figure 2.12. Therefore, alongside these mechanism, two pyramidal mechanisms are also well reported in the literature [120]. This $<c+a>$ second order pyramidal mechanism has been identified as responsible for the formation of martensite in Ti-6Al-4V, through some observations with transmission electron microscopy (TEM) [120]. Using the Miller-Bravais notation for an hexagonal crystal, it generally occurs along the $(10\bar{1}2)$ direction and it is attributed to a pole mechanism [115, 87], However, during high strain rate deformation both $(10\bar{1}2)$ and $(11\bar{2}1)$ directions have been observed [120].

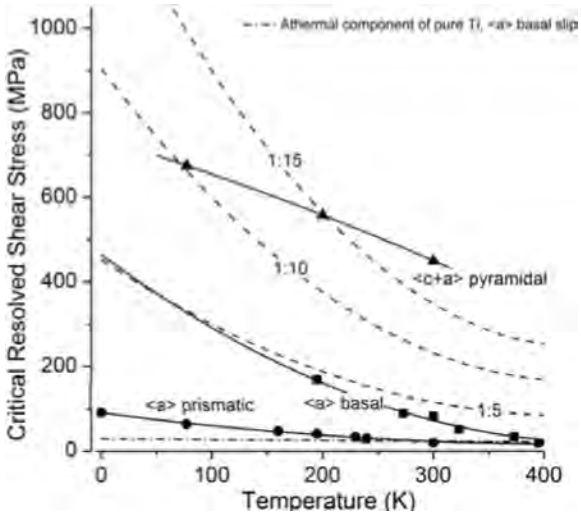

FIGURE 2.13: Critical resolved shear stress of α-Ti varying with temperature for <a> prismatic, <a> basal, and <c+a> pyramidal slips. Image reproduced from [122, p. 35, fig. 1].

2.4.3 Investigation and analysis of constitutive models

In this section some phenomenological and physics-based plasticity constitutive models for Ti-6Al-4V published in the literature are investigated. Table 2.3 provides a summary and a comparison between some of their main features, focusing also on their range of applicability. The list of constitutive models here presented is far from exhaustive, because new and more refined models are constantly published in the literature. Therefore, it should be read as a selection and introduction to possible candidate models capable of representing material plasticity for Ti-6Al-4V during the high-temperature numerical simulations developed later in this work.

Chen *et al.*, 2015

In the work done by Chen *et al.* [123] four different phenomenological models are described and validated with experiments: the Johnson-Cook (JC), the modified Johnson-Cook (JCM), the Khan-Huang-Liang (KHL) and the modified Khan-

Model	Temperature dependency	Strain rate dependency	Microstructure dependency	Building process applicability
Chen *et al.*, 2015	25– $\sim$ 900 °C	$10^{-4} - 10^{4}$ s^{-1}	No	-
Nemat-Nasser *et al.*, 2001	~ -200– $\sim$ 700 °C	$10^{-3} - 7 \times 10^{3}$ s^{-1}	No	Hot isostatic pressing
Picu-Majorell, 2001	~ -200– $\sim$ 1100 °C	$10^{-3} - 10$ s^{-1}	Yes	-
Mulyadi *et al.*, 2007	925 – 975 °C	$3 \times 10^{-3} - 3 \times 10^{-1}$	Yes	Forging
Wang-Li, 2018	No	No	No	SLM
Liović *et al.*, 2021	No	No	No	SLM
Galindo-Fernández *et al.*, 2018	$\sim$ 25– $\sim$ 1100 °C	$10^{-3} - 5 \times 10^{3}$ s^{-1}	Yes	Wrought, casting, ALM

TABLE 2.3: Summary of the constitutive model for Ti-6Al-4V investigated in the present work, here reported alongside some of their features, including their building process applicability.

Huang-Liang (KHLM). The original Johnson-Cook model has been introduced in 1983 [110], whilst the Khan-Huang-Liang model has been presented for the first time in 1999 [124]. The modified Johnson-Cook model is defined as the following:

$$\sigma(\epsilon, \dot{\epsilon}, T) = [A+B\epsilon^n h(T)] \left[1 + C \log\left(\frac{\dot{\epsilon}}{\dot{\epsilon_0}}\right)\right] \left[1 - \left(\frac{T - T_r}{T_m - T_r}\right)^m\right], \tag{2.25}$$

where

$$h(T) = \left(\frac{T_0 - T/2}{T_0}\right)^{n_2} \tag{2.26}$$

is an additional function, and the dimensional and adimensional positive, real constants A (MPa), B (MPa), n, C, m, T_0 (°C) have been found by the authors by using an optimisation algorithm. Instead, the modified Khan-Huang-Liang model is represented as:

$$\sigma(\epsilon, \dot{\epsilon}, T) = \left[A+B\left(1 - \frac{\log \dot{\epsilon}}{\log D_0}\right)^{n_1} \epsilon^{n_0} h(T)\right] \left(\frac{\dot{\epsilon}}{\dot{\epsilon_0}}\right)^C \left(\frac{T_m - T}{T_m - T_r}\right)^m. \tag{2.27}$$

In this case, the positive, real constants are A (MPa), B (MPa), n_1, n_0, C, m, n_2, T_0 (°C), so this second model introduces two additional constants and their values are given in Table 2.4. Other two constants used in the models are T_m and T_r, respectively the melting temperature and the reference ambient temperature. Additionally, there is the reference strain rate $\dot{\epsilon}_0$, which is set equal to the unity. In both models, it can be observed that the additional term $h(T)$ has been included in the equations (shown in Figure 2.14), in order to better describe the temperature work hardening, which decreases with temperature increasing. However, it should be noted that as the temperature T approaches to $2T_0$, this term vanishes and this makes the stress constant and independent from the strain ϵ, namely:

$$h(2T_0) = 0 \quad \Rightarrow \quad \forall \epsilon, \sigma(\epsilon) = K,\ K \in \mathbb{R}. \tag{2.28}$$

Therefore, the limitation

$$T < 2T_0 \tag{2.29}$$

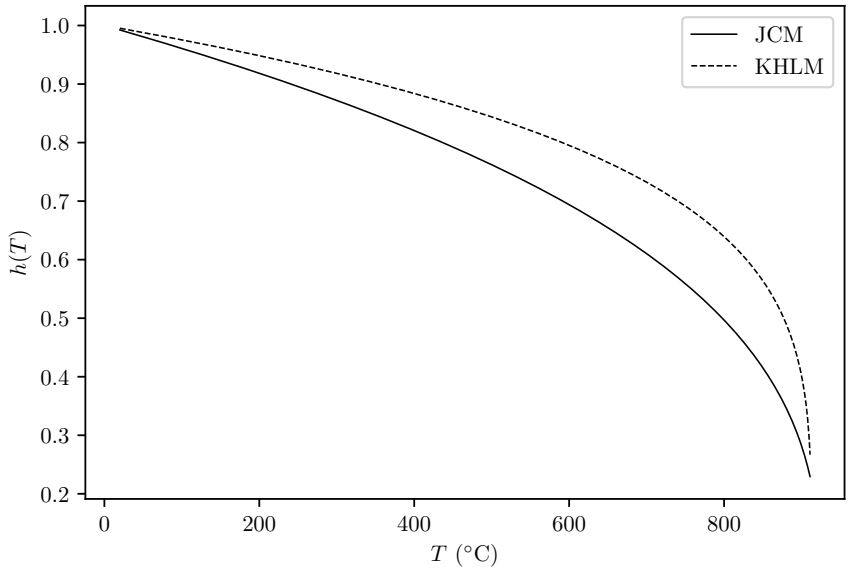

FIGURE 2.14: The additional functions varying with the temperature in the two modified models, calculated with the parameters T_0 and n_2 given in Table 2.4 and 2.5.

	A (MPa)	B (MPa)	n	C	m	n_2	T_0 (°C)
JC	831.355	857.932	0.302	0.015	0.724	–	–
JCM	789.566	911.446	0.306	0.012	0.952	0.349	462.314

TABLE 2.4: Optimised parameters for the Johnson-Cook (JC) and the modified Johnson-Cook model (JCM). Values reproduced from [123], tab. 2 and tab. 3, respectively on p. 605 and p. 606.

becomes intrinsic in both the modified models. This means that the temperature must be restricted to:

$$T \lesssim \begin{cases} 924.63\,^{\circ}\text{C}, & \text{JCM;} \\ 912.91\,^{\circ}\text{C}, & \text{KHLM.} \end{cases} \tag{2.30}$$

Some plots of the resulting flow stress according to Chen *et al.* (2015) are given in Figures 2.15 and 2.16.

This model is a clear example of how some phenomenological models can be easily adapted to take into account additional material properties, as the temper-

	A (MPa)	B (MPa)	n_1	n_0	C	m	n_2	T_0 (°C)
KHL	878.452	874.778	0	0.315	0.012	1.417	–	–
KHLM	872.791	906.428	0.012	0.327	0.011	1.211	0.214	456.453

TABLE 2.5: Optimised parameters for the Khan-Huang-Liang (KHL) and the modified Khan-Huang-Liang (KHLM) model. Values reproduced from [123], tab. 4 and tab. 5, respectively on p. 606 and p. 607.

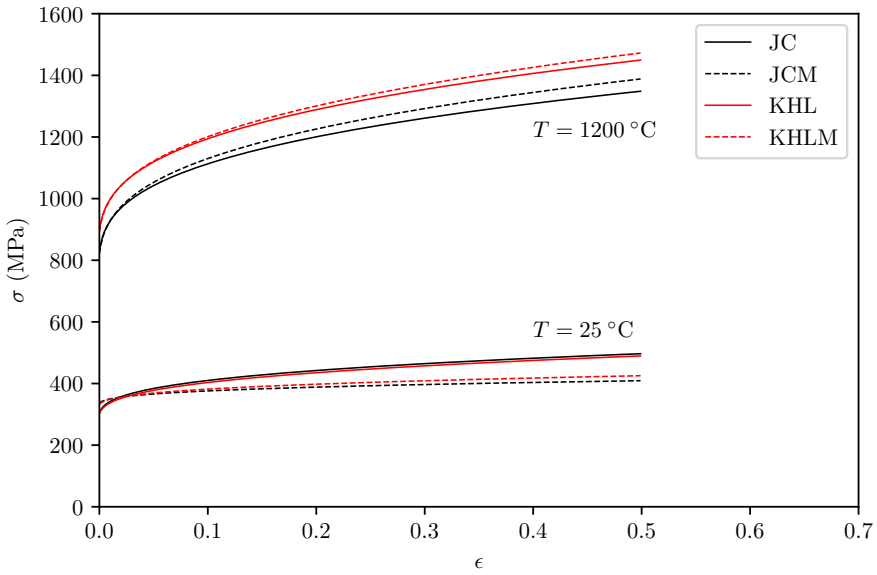

FIGURE 2.15: Comparison of the flow stress prediction between the four models at two different temperatures and at strain rate $\dot{\epsilon} = 0.001$ s^{-1} given in Chen *et al.* (2015).

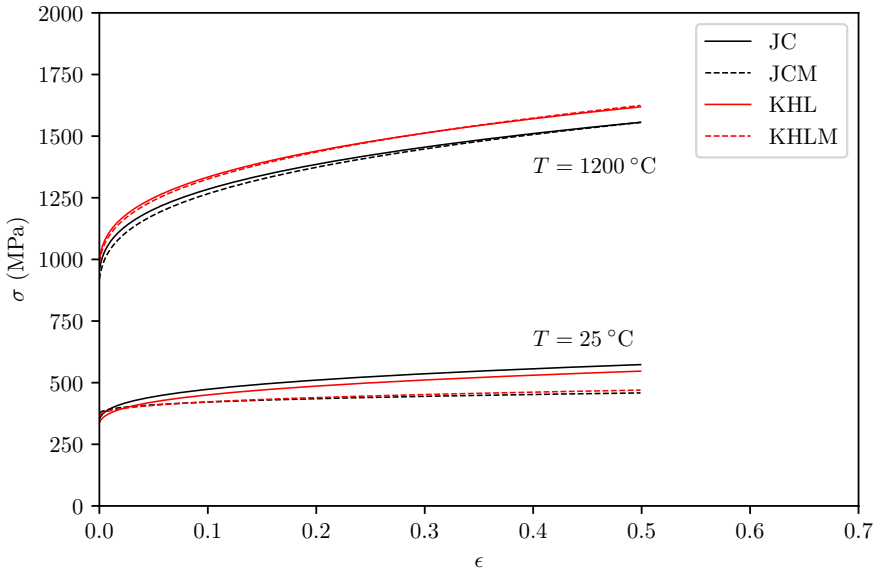

FIGURE 2.16: Comparison of the flow stress prediction between the four models at two different temperatures and at strain rate $\dot{\epsilon} = 10.0\ \mathrm{s}^{-1}$ given in Chen *et al.* (2015).

ature influence on the strain, in this case, represented through the introduction of $h(T)$ in Equation (2.26). However, it is also an example of how the possibility to overcome a limitation can sometimes lead to other limitations, as the conditions expressed by Equation (2.30).

Nemat-Nasser *et al.*, 2001

Nemat-Nasser *et al.* performed some experiments on the Ti-6Al-4V alloy with different microstructures, finding that the initial microstructure affects only the athermal activated part of the stress [125], independently of the type of microstructure. The new constitutive model so formulated is governed by the equation:

$$\sigma(\epsilon, \dot{\epsilon}, T) = \sigma_a^0 \epsilon^n + \sigma^0 f(\epsilon, T) \left\{ 1 - \left[\frac{kT}{G_0} \left(\log \frac{\dot{\epsilon} f(\epsilon, T)}{\dot{\epsilon}_0} \right) \right] \right\}, \tag{2.31}$$

where $\sigma_a^0 \in \mathbb{R}$, n and $\sigma^0 \in \mathbb{R}$ are constants and depend on the different processing techniques of the alloy. In this last Equation (2.31) both the strain rate and the

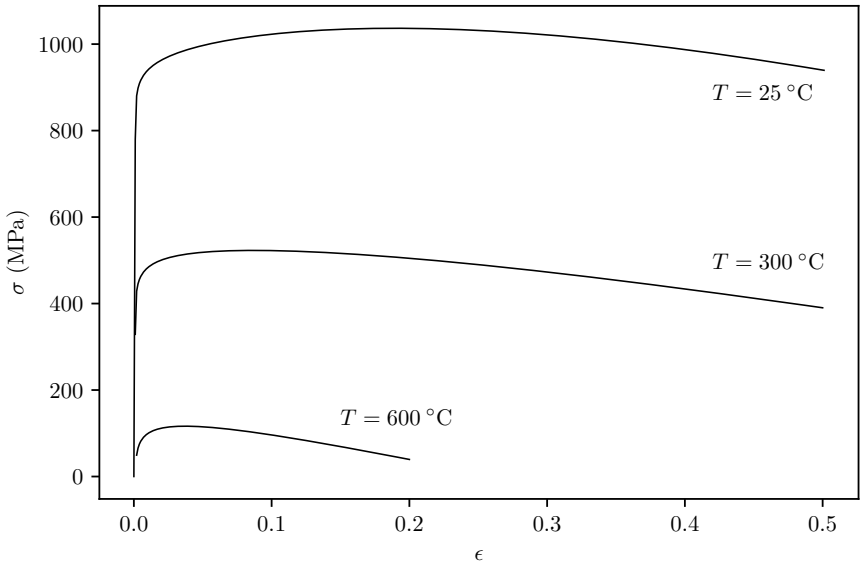

FIGURE 2.17: Flow stress prediction according to Nemat-Nasser *et al.* (2001) for Ti-6Al-4V, at different temperatures and at strain rate $\dot{\epsilon} = 0.001$ s^{-1}.

stress σ^0 are multiplied by the formula

$$f(\epsilon, T) = 1 + a_0 \epsilon \left[1 - \left(\frac{T}{T_m} \right)^2 \right], \tag{2.32}$$

where the temperature is history-dependent, namely it depends on the stress-state developed before the current strain value:

$$T = T_0 + \Delta T; \tag{2.33a}$$

$$\Delta T = \int_0^\epsilon \frac{\sigma(\epsilon)}{c C_v(T)} \, \mathrm{d}\epsilon; \tag{2.33b}$$

$$C_v(T) = c_1 \exp(T/c_2). \tag{2.33c}$$

In Table 2.6 the model parameters are reported and some flow stress predictions are plotted in Figure 2.17. Even if this model recognises the importance of the microstructure, this model also introduces a corrective factor, using a conceptually similar approach to that used by Chen *et al.* (2015), described in the

σ_a^0 (MPa)	n	σ^0 (MPa)	k/G_0 (K^{-1})	$\dot{\epsilon}_0$ (s^{-1})	a_0	T_m (K)	c_1	c_2 (K)
685	0.05	1560	6.2×10^{-5}	1.32×10^{10}	2.4	1933	0.56	2000

TABLE 2.6: Nemat-Nasser *et al.* (2001) parameters model for commercial Ti-6Al-4V. Parameters for other process conditions can be found in [125, p. 437, tab. 2].

previous paragraph. Its main peculiarity is the strain history dependency that affects the thermal-activated component of the flow stress, introduced through Equations (2.32) and (2.33).

Picu-Majorell, 2001

The idea behind this physics-based model is that the flow stress term can be decomposed into a thermal and an athermal component, as in Nemat-Nasser *et al.* (2001) [125]. Moreover, at the same time the idea was also to preserve the different behaviours between the α and β-phase [126, 103]. The flow stress is then expressed with a modified rule of mixtures, accounting for α and β-phase content at different temperatures:

$$\sigma(\epsilon, \dot{\epsilon}, T) = [1 - C_\beta(T)]^w \left(\sigma_\alpha^* + \sigma_{\mu\alpha}\right) + [C_\beta(T)]^w \, \sigma_{\mu\beta}. \tag{2.34}$$

The thermally activated stress for the α phase is given by:

$$\sigma_\alpha^*(\dot{\epsilon}, T) = \sigma_{Oeq}^*(\dot{\epsilon}, T) + \sigma_{Al}^*(\dot{\epsilon}, T), \tag{2.35}$$

where

$$\sigma_{Oeq}^*(\dot{\epsilon}, T) = C_{\alpha,Oeq} \left[1 - \left(\frac{kT}{\Delta G_{Oeq}(T)} \log_{10} \frac{10^7}{\dot{\epsilon}}\right)^{1/2.7}\right]^{1/0.7}, \tag{2.36a}$$

$$\sigma_{Al}^*(\dot{\epsilon}, T) = C_{\alpha,Al} \left[1 - \left(\frac{kT}{\Delta G_{Al}(T)} \log_{10} \frac{10^7}{\dot{\epsilon}}\right)^{1/2.7}\right]^{1/0.7}. \tag{2.36b}$$

On the other hand, the athermal component of the stress, for the α phase is given by

$$\sigma_{\mu\alpha} = \zeta \mu(T) |b| \sqrt{\rho} + \kappa D^{-1/2}, \tag{2.37}$$

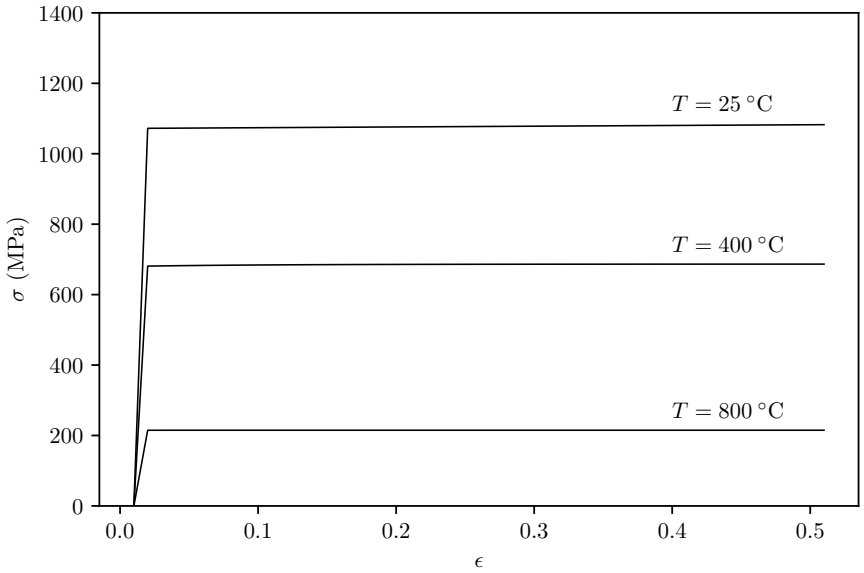

FIGURE 2.18: Flow stress prediction according to Picu-Majorell (2001) for Ti-6Al-4V, at different temperatures and at strain rate $\dot{\epsilon} = 0.01\ \mathrm{s}^{-1}$.

where $\zeta, \kappa \in \mathbb{R}$ are parameters, $|b| \in \mathbb{R}$ is the magnitude of the Burgers vector, $D \in \mathbb{R}$ is the grain size and $\rho \in \mathbb{R}$ is the dislocation density, which is the only deformation-dependent parameter and it follows the Mecking-Kocks (1981) formulation [127]. Some flow stress prediction according to Picu-Majorell (2001) are represented in Figure 2.18.

The main contribution of this model is the recognised necessity to evaluate the mechanical behaviour of the material independently of the additional chemistry of the alloys, through the notion of equivalent concentrations of oxygen and aluminium effect on the stresses σ^*_{Oeq} and σ^*_{Al}.

Mulyadi *et al.*, 2007

As seen in the previous paragraphs, the titanium alloy Ti-6Al-4V is a dual phase $\alpha+\beta$ alloy at room temperature, but during some manufacturing processes, it can reach temperatures where the phase transformation $\alpha+\beta \rightarrow \beta$ starts. Therefore,

Q_α (J mol^{-1})	m (-)	K_α (-)	$\lambda_{0,\alpha}$ (-)	q_α (-)	a_α (-)	b_α (-)
394000	0.218	0.0705	1.49	−0.0180	1.31	53.5
Q_β (J mol^{-1})	m (-)	K_β (-)	$\lambda_{0,\beta}$ (-)	q_β (-)	a_β (-)	b_β (-)
115000	0.259	5.30	0.840	0.001	3.79	110

TABLE 2.7: Mulyadi *et al.* (2007) model parameters for each phase of Ti-6Al-4V.

Mulyadi *et al.* proposed the idea to study independently the flow stress of each phase and then build a final model in which the flow stress is determined by the amount of each phase at a given temperature [128, 129]. The general concept behind this model framework was also used in other works, as, for example, the flow stress description in a nickel superalloy, where it is expressed as deriving from a balance between hardening and softening mechanisms [130].

In this model, the flow stress evolves with strain, for each phase, according to the following differential equation:

$$\frac{\partial \sigma}{\partial \epsilon} = \beta(\sigma_t - \sigma), \tag{2.38}$$

so the flow stress obtained by solving this last equation is

$$\sigma(\epsilon, \dot{\epsilon}, T) = \sigma_t \left[1 - \exp(-\beta\epsilon)\right]. \tag{2.39}$$

In this last Equation (2.39), $\sigma_t = K\lambda^n Z^m$, where the scaling constant $K \in \mathbb{R}$ and the coefficients $n \in \mathbb{R}$ and $m \in \mathbb{R}$ are given in Table 2.7. The parameter λ also evolves during the deformation according to the following set of equations:

$$\frac{\partial \lambda}{\partial \epsilon} = a(\lambda_{ss} - \lambda); \tag{2.40a}$$

$$\lambda_{ss} = \lambda_0 Z^q; \tag{2.40b}$$

$$Z(\dot{\epsilon}, T) = \dot{\epsilon} \exp(Q/RT). \tag{2.40c}$$

The two-phases material flow stress is then given by

$$\sigma(\epsilon, \dot{\epsilon}, T) = V_\alpha \sigma_\alpha + V_\beta \sigma_\beta, \tag{2.41}$$

C (-)	Q (J mol^{-1})	λ_0 (-)	q (-)	a (-)
1.08	142000	1.19	−0.06	3.39

TABLE 2.8: Mulyadi *et al.* (2007) model parameters for the combined phases alloy.

where $V_\beta \in [0, 1]$ is calculated as:

$$V_\beta(T) = c_1 T^2 - c_2 T + c_3, \tag{2.42}$$

with the constants $c_1 = 1.26 \times 10^{-5}$, $c_2 = 2.598 \times 10^{-2}$, $c_3 = 13.583$ and $V_\alpha = 1 - V_\beta$. However, since there is an interaction between the two phases, the authors decided to model the final behaviour by rewriting Equation (2.41) as:

$$\sigma(\epsilon, \dot{\epsilon}, T) = C\lambda(V_\alpha \sigma_\alpha + V_\beta \sigma_\beta), \tag{2.43}$$

where the scaling constant $C \in \mathbb{R}$ is given in Table 2.8 along with the values to calculate $\lambda \in \mathbb{R}$, which is determined, again, by using Equations (2.40).

It should be noted that the article was written to summarise the work in a doctoral thesis, and the constants given in Table 2.8 are slightly different from the previous work. In the thesis work [128], indeed, they are defined more accurately as ranges of numbers, obtained by some numerical calibration procedures.

The main contribution of this study is the description of the deformation process of Ti-6Al-4V at high temperature as a series of evolution laws in the form of first order differential equations, but the most relevant microstructural informations are lacking.

Wang-Li, 2018

Additive manufacturing permits the operator to build lightweight structures, including complex lattice structures. However, in order to evaluate the mechanical performance for micro-lattice structures made by Ti-6Al-4V and built with selective laser melting, some authors [131] proposed and tested with experiments a new constitutive model, based on the Johnson-Cook model:

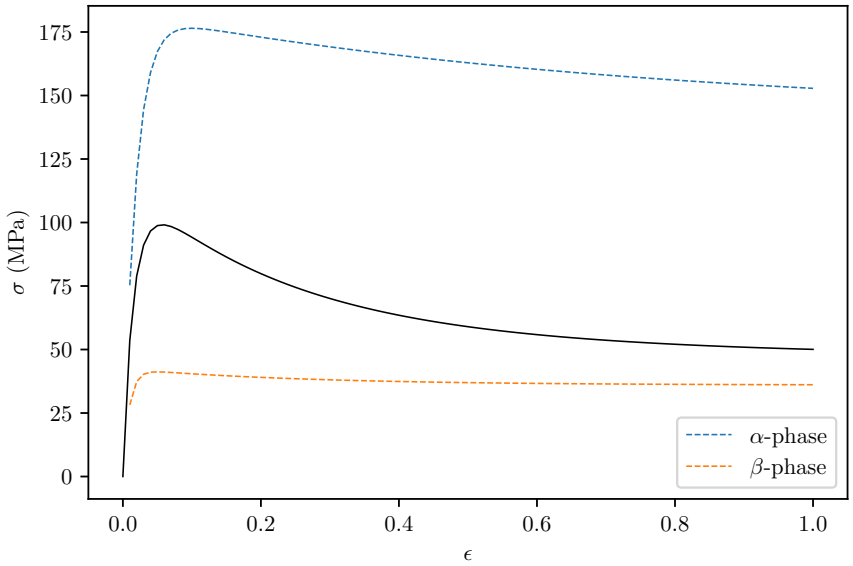

FIGURE 2.19: Mulyadi *et al.* (2007) flow stress prediction of single phases and combined model (black solid line) for $T = 925$ °C and $\dot{\epsilon} = 0.03$ s^{-1}.

$$\sigma(\epsilon, \dot{\epsilon}, T) = (A + B\epsilon^n)(1 + C \log \dot{\epsilon}^*)(1 - (T^*)^m), \tag{2.44}$$

where:

$$\dot{\epsilon}^* = \frac{\dot{\epsilon}}{\dot{\epsilon}_r}, \qquad T^* = \frac{T - T_r}{T_m - T_r}. \tag{2.45}$$

This model has been coupled with the equivalent plastic strain at fracture:

$$\epsilon_f(\dot{\epsilon}, T) = D_1 + D_2 \exp(D_3 \sigma^*)(1 - D_4 \log \dot{\epsilon})(1 - D_5 T). \tag{2.46}$$

This last formula introduces a stress triaxiality factor dependent on the size of the struts cross-section:

$$\sigma^* = \frac{1}{3} + \log\left(1 + \frac{a_0}{2R}\right), \tag{2.47}$$

where $a_0 = D_e/2$ and $R = (D_F - D_e)/4$ are, respectively, the original specimen radius at the notch centre and the notch radius, defined as functions of the Feret diameter $D_F \in \mathbb{R}$ and the equivalent diameter $D_e \in \mathbb{R}$. These two parameters

A (MPa)	B (MPa)	n	D_1	D_2	D_3
997	746	0.325	0.005	0.43	−0.48

TABLE 2.9: Wang-Li (2018) model parameters (table adapted from [131, p. 22]).

are related by the following formula:

$$D_e = D_F\sqrt{1-\exp(-kD_F)}, \tag{2.48}$$

where $k = 0.0023\ \mu m^{-1}$. Since the uniaxial tension tests have been performed at constant strain rate ($\dot{\epsilon} = 0.001\ s^{-1}$, which is quasi-static) and constant temperature, the Equations (2.44) and (2.46) simplify as:

$$\sigma = A + B\epsilon^n, \qquad \epsilon_f = D_1 + D_2\exp(D_3\sigma^*); \tag{2.49}$$

where the constant parameters are given in Table 2.9.

This constitutive model was successfully applied for evaluating micro-lattice structures, which was the scope for which it was designed. However, having a constitutive model only applicable in a small range of conditions does not permit its applicability outside of them.

Liović *et al.*, 2021

The constitutive model recently developed by Liović *et al.* [132] is based on the earlier Ramberg-Osgood model [133], but it is adapted for the material processed under selective laser melting and its aim is modelling the monotonic and cyclic elasto-plastic behaviour. However, the model presented does not take into account the strain-rate and temperature effect. The constitutive equation developed by Ramberg and Osgood describes the deformation in terms of true stress and it is splitted into two parts: an elastic term and a plastic term. The constitutive model is therefore given in the following form, expressing the deformations as function of the strains:

$$\epsilon(\sigma) = \epsilon_e(\sigma) + \epsilon_p(\sigma) = \frac{\sigma}{E} + \left(\frac{\sigma}{K}\right)^{1/n}, \tag{2.50}$$

where E is the Young's modulus (MPa) and $K \in \mathbb{R}$ (MPa) and $n \in \mathbb{R}$ are constants to be calibrated for the specific material, such that they completely describe the hardening behaviour of the material. The author found that the behaviour depends on the orientation of the specimen fabricated with SLM, as it can be viewed in Figure 2.20. If it is loaded vertically it is indeed more resistant, because the elongated β grains formed after the cooling process in additive manufacturing are loaded along their longer axis [132] (this grain structure is visible in Figure 2.38). Therefore, calling $K_v, n_v \in \mathbb{R}$, and $K_h, n_h \in \mathbb{R}$, respectively, the parameters for the vertical and horizontal loading condition, the authors found that they are: $K_v = 1400$ MPa, $n_v = 0.036$, and $K_h = 1480$ MPa, $n_h = 0.034$. A plot of the flow stress prediction, according to the direction of the load, is given in Figure 2.20.

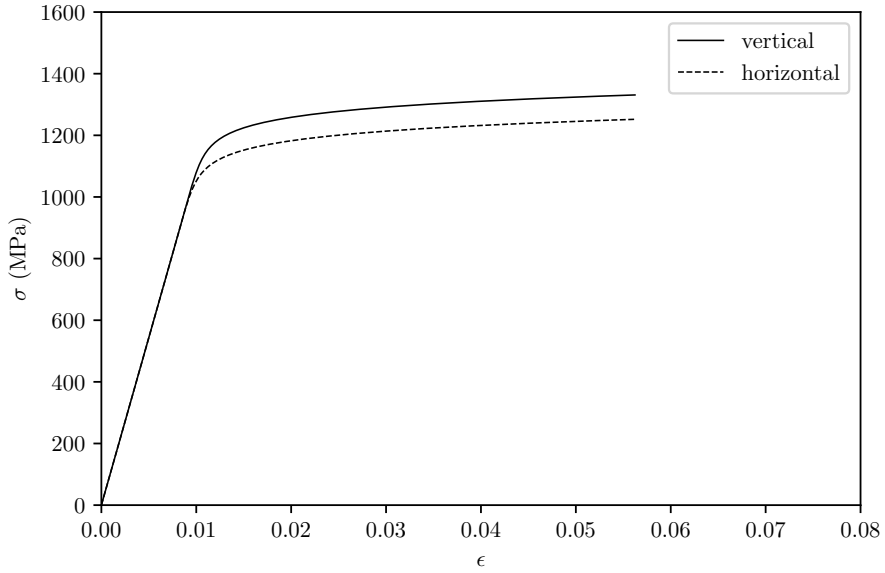

FIGURE 2.20: Liović *et al.* (2021) flow stress prediction for Ti-6Al-4V fabricated by selective laser melting, according to different loading directions (here *vertical* indicates a specimen loaded along the building direction, while *horizontal* means perpendicular to it).

Galindo-Fernández *et al.*, 2018

Although most constitutive models for Ti-6Al-4V do not take explicitly into account the microstructure of the starting material, a more recent physics-based model for this alloy developed by Galindo-Fernández *et al.* [88] is able to relate the flow stress with different microstructural features, including the martensite. Additionally, this model is able to describe the stress state of the material, according to different manufacturing methods and it is also able to predict with sufficient accuracy the stress state for a component of the alloy produced by additively manufacturing, for a wide strain-rate and temperature range. In this model, as in the one developed by Picu-Majorell (2001), the dislocation density evolution during the deformation process follows the classical Mecking-Kocks (1981) formulation [127]. According to this theory, the plastic behaviour can be represented as $\sigma = \sigma(\rho, \dot{\epsilon}, T)$, whereby an infinitesimal variation of the dislocation density ρ during the deformation process is equal to an evolution law E

$$\frac{\mathrm{d}\rho}{\mathrm{d}\epsilon} = E(\rho), \tag{2.51}$$

assuming that the dislocations structure evolves with strain and depends only on the dislocation density ρ. The dislocation evolution is usually described as a process that takes place over time, given by a competition between the generation and annihilation of dislocations, usually described by a rate equation, calculated respect to the deformation, such that there is a balance between created and annihilated dislocations at every time t:

$$\dot{\rho}(t) = \dot{\rho}^{+}(t) + \dot{\rho}^{-}(t). \tag{2.52}$$

The dislocation density evolution is then described as dependent on the deformation stage according to the differential equation

$$\frac{\mathrm{d}\rho}{\mathrm{d}\epsilon} = \frac{k_1}{|b|}\sqrt{\rho} - f\rho, \tag{2.53}$$

which has the solution:

$$\rho(\epsilon) = \left[\left(\frac{k_1}{|b|f} - \left(\frac{k_1}{|b|f} - \sqrt{\rho_0}\right)\right)\exp\left(-\frac{1}{2}f\epsilon\right)\right]^2, \tag{2.54}$$

where $k_1 \in \mathbb{R}$ is the dislocation generation coefficient, $f \in \mathbb{R}$ is the recovery coefficient, $|b| \in \mathbb{R}$ is the magnitude of the Burgers vector. The dislocation density evolution so obtained is then incorporated into the flow stress rule through Taylor's equation:

$$\sigma = \sigma_y + 0.3M\mu|b|\sqrt{\rho}, \tag{2.55}$$

where $M \in \mathbb{R}$ is the Taylor's factor ($M \approx 3$), $\mu \in \mathbb{R}$ is the shear modulus, and σ_y is the yield stress, calculated taking into account the Hall-Petch formula and the different phase strengths. Ignoring some intermediate steps, the final formula for the flow stress is as follows:

$$\begin{aligned}\sigma(\epsilon, \dot{\epsilon}, T) = &\left(\sigma_\alpha V_\alpha + \sigma_\beta(1 - V_\alpha) + \frac{k_{HP}}{\sqrt{D_\alpha}}\right)\left(\frac{\kappa\mu(T)|b|^3}{k_B T \log(10^7/\dot{\epsilon})}\right)^n \\ &+ 0.3M\mu|b|\left\{\left[\frac{k_1}{|b|f} - \left(\frac{k_1}{|b|f} - \sqrt{\rho_0}\right)\right]e^{-1/2f\epsilon}\right\},\end{aligned} \tag{2.56}$$

where $k_{HP} = 300$ MPa, D_α is the average α grain size (ranging from 1.5 to 13 µm), $\kappa = 0.23$, $\mu(T) = 54 - 0.03T$ is the temperature-dependent shear modulus (GPa), $k_B \approx 1.381 \times 10^{23}$ is the Boltzmann constant ($\mathrm{J\,K^{-1}}$), $n = 0.4$. The martensite enters into this last Equation (2.56) through the expression for the initial dislocation density, because it has been found that the initial dislocation density is affected by the presence of martensite lamellae. Therefore, in presence of α' martensite the initial dislocation density is expressed as:

$$\rho_0 = \frac{12 w_{\alpha'}}{(1 + 2\nu^2)\mu|b|}\frac{{\epsilon_0}^2}{{d_{\alpha'}}^2}, \tag{2.57}$$

where $w_{\alpha'}$ is the α martensite lath thickness, $d_{\alpha'}$ is the α martensite lath spacing. Both these values can be found in Table 2.10, even if those measurements are currently scarcely reported in the literature, as it can be observed in the same Table 2.10, column 7. The average size for the martensite α' lamellae spacing

was reported to be as 0.75 µm, while its thickness was indicated as 1 µm by Galindo-Fernández *et al.* (2018) [88], which is a value that is in agreement with those reported in Table 2.2.

To understand the origin of Equation (2.57), it is necessary to consider that Galindo-Fernández *et al.* (2018) adapted it from a previous work made by Galindo-Nava *et al.* (2015) [134] on low and medium carbon steel, again using the conceptual analogy between the martensitic structures in the two different alloys. Indeed, Galindo-Nava *et al.* referring to the concept of *Cottrell atmosphere*, found that the initial dislocation density in steel can be given by [134, p. 86, equation 5]:

$$\rho_0 = \frac{3E}{(1+2\nu^2)\mu|b|}\frac{4\epsilon^2 d_C}{{d_{\ell,0}}^2|b|}, \tag{2.58}$$

where $d_C \in \mathbb{R}$ is the thickness of a Cottrell atmosphere, $d_{\ell,0} \in \mathbb{R}$ is the lath thickness after quenching and $\epsilon \in \mathbb{R}$ is the lattice strain produced by carbon redistribution [134]. This formula was not new, but it was adapted from a previous equation found while estimating the dislocation density in lath martensite obtained by neutron diffraction measurements [134]. Therefore, this formula has a strong physical connection with the inner structure of the matter.

The Cottrell atmosphere was introduced in 1949 by Alan H. Cottrell, portrayed in Figure 2.21, and it is an equilibrium atmosphere which forms when dislocations are surrounded by solute atoms, in general impurities, present in the alloy [135]. It occurs in body-centred cubic (BCC) materials with small impurity atoms, as is the case for carbon inside iron at low temperatures. It can be used to explain a deformation mechanism, because if a small force is applied to the material, a dislocation cannot escape from the atmosphere where it is trapped, while if a large force is applied, a dislocation becomes highly mobile, resulting in rapid flow stress under small deformations. A scheme of the martensite laths and the respective Cottrell atmosphere in carbon steel is represented in Figure 2.22. Therefore, this mechanism can explain the so-called *yield point phenomenon*,

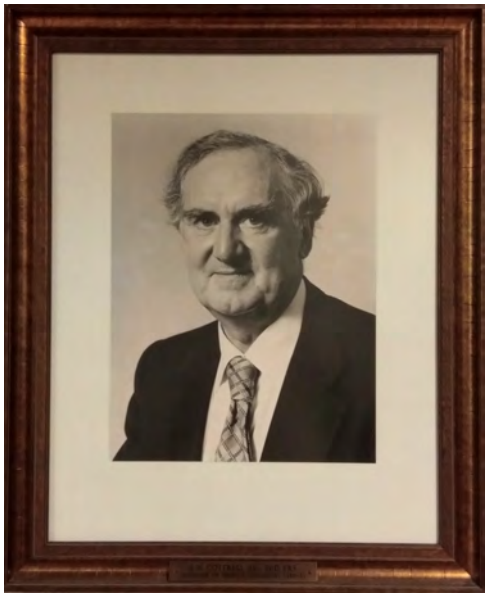

FIGURE 2.21: Portrait of Alan H. Cottrell. University of Birmingham (UK), School of Metallurgy and Materials.

which occurs after reaching the yield point, the material suddenly relieves a large amount of accumulated stress, resulting in an elongation with a small increase in the applied stress. This also gives rise to the difference between the *upper yield point* and the *lower yield point* in the flow stress curve, during which the strain increase is also called *Lüders strain* (illustrated in Figure 2.23).

Some flow stress predictions are plotted in Figure 2.24 and 2.25, respectively for different temperatures and for different strain rates, using the constitutive model developed by Galindo-Fernández *et al.* (2018). Due to the range of applicability and the possibility of describing the microstructure of Ti-6Al-4V in detail, including martensite, this model can be assumed as an almost perfect candidate for the numerical simulations developed within the present work.

2.4.4 Brief comparative analysis of constitutive models

The constitutive models investigated in the previous paragraph show that multiple approaches and multiple process conditions can lead to different equations.

Author	Alpha average grain size D_α (μm)	Alpha lamella width W_α (μm)	Total volume fraction alpha V_α	Volume fraction lamellar alpha V_α	Volume fraction of equiaxed alpha (bimodal) V_α	Martensite average lath width $W_{\alpha'}$ (μm)	Volume fraction of martensite $V_{\alpha'}$	Microstructure type	Temperature (K)	Strain rate (s^{-1})
Park et al. [32]	9	0.6	0.72	0.28	0.85	–	–	Bimodal	298	10^{-3}–10
Park et al. [32]	13	–	0.85	–	–	–	–	Equiaxed	298	10^{-3}–10
Park et al. [32]	–	2.6	–	0.9	–	–	–	Lamellar	298	10^{-3}–10
Zheng et al. [34]	6	0.8	0.8	0.2	0.9	–	–	Bimodal	298	2600
Zheng et al. [34]	8	–	0.85	–	–	–	–	Equiaxed	298	2600
Zheng et al. [34]	9	2	–	0.9	–	–	–	Lamellar	298	2600
Khan et al. [16]	8	–	0.83	–	–	–	–	Equiaxed	298–755	10^{-6}–3378
Lee & Li [60]	8	–	0.9	–	–	–	–	Equiaxed	298–1373	2000
Li et al. [61]	–	–	–	–	–	0.75	1	PLD (α′)	298–1273	0.1–5000
Kasperovich et al. [4]	5	–	0.83	–	–	–	–	Equiaxed	298	10^{-3}
Kasperovich et al. [4]	–	–	–	–	–	0.75	1	SLM (α′)	298	10^{-3}
Kasperovich et al. [4]	1.5	–	0.98	–	–	–	–	SLM (α + β)	298	10^{-3}
Kasperovich et al. [4]	2	–	0.97	–	–	–	–	SLM (α + β)	298	10^{-3}
Kasperovich et al. [4]	3	–	0.95	–	–	–	–	SLM (α + β)	298	10^{-3}

TABLE 2.10: Summary table with the microstructural features of Ti-6Al-4V, as reported in other works. It can be observed that while the average grain size is well documented in the literature, in contrast, martensite characteristics are only reported by a few scholars. Table reproduced from [88, p. 355, fig. 3].

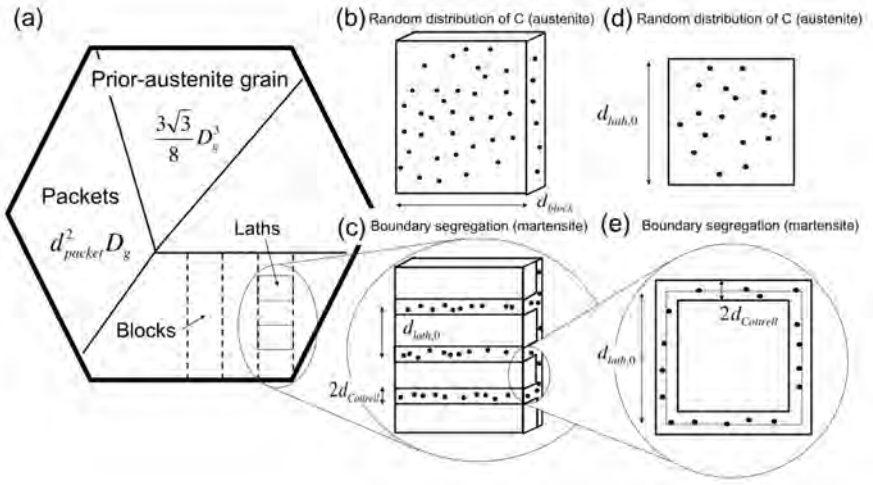

FIGURE 2.22: Martensite hierarchical structure and Cottrell atmosphere in low and medium carbon steel, with a random arrangement of carbon impurities within an austenite grain. Image reproduced from [134, p. 84, fig. 1].

Accordingly, the flow stress behaviour can then vary sensibly, showing a great scatter in the material plastic response, as shown in Figure 2.26. Therefore, one may ask which one represents the real material behaviour: this question does not has a unique answer, because it depends on the weight that each variable has on the particular physical application. In other words, the behaviour is influenced by the initial hypothesis that led to the constitutive theory. In conclusion, in selecting a plastic constitutive model for a specific study, the choice can fall on the one that incorporates the most relevant microstructural features.

2.5 Heat source modelling and residual stress

Analogously to the efforts done in the theory of the constitutive models, during the past decades there were numerous efforts to correctly describe, in mathematical terms, a model that could represent the moving heat source used in welding applications. The main contributors to these models are Daniel Rosenthal and John A. Goldak [137], and this strand of research started from the evidence of the

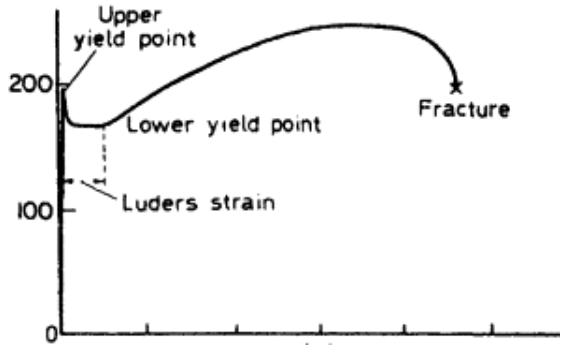

FIGURE 2.23: The upper and lower yield points and the Lüders strain in metals, occurring in impure iron and low-medium carbon steels. Image reproduced from [136, p. 198, fig. 7.1a].

surface temperature distributions, as can be deduced from the early appearance of physical models (Figure 2.28), which for several years were a common tool to understand the temperature distribution in proximity of a weld line.

2.5.1 Heat source modelling

The interaction between the heat source and the material is a rather complex phenomenon, because part of the material is liquefied and it is in contact with the solid material and with the surrounding environment [137]. This is particularly true when modelling the interaction between the laser source and the powder in laser powder-bed fusion, which can be view as a sequence of micro-explosions, as represented in Figure 2.27. The difficulties increase also because the heat source is not fixed in space, but it is moves along one or more coordinates in the tridimensional space. Whilst these purely mathematical abstractions appear unimportant, it must be remembered that the mathematical model of a moving heat source finds its natural application in the description of some metallurgical processes such as welding [138, 137], and, by using the analogy of the micro-welding process, also in additive manufacturing.

Basic moving heat sources are the moving punctiform source, the line or the

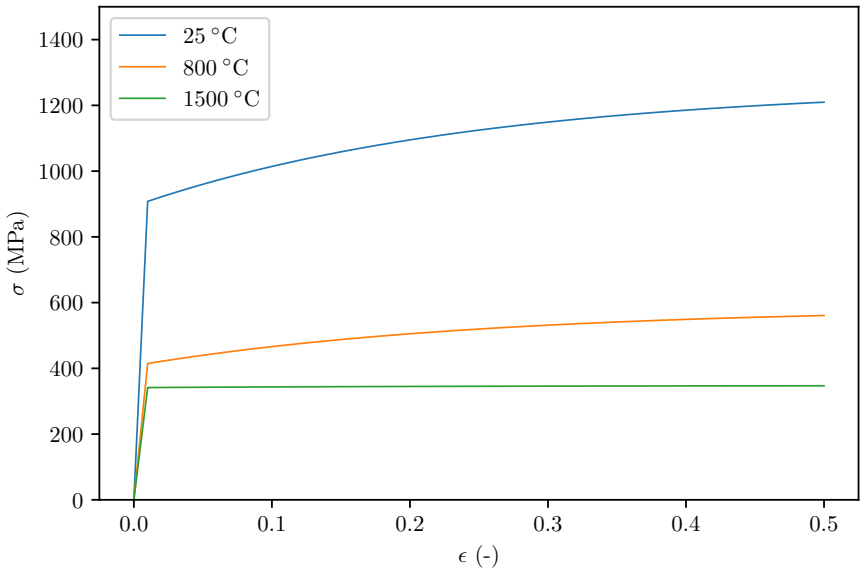

FIGURE 2.24: Flow stress prediction according to Galindo-Fernández *et al.* (2018) at different temperatures ($\dot{\epsilon} = 0.01$ s^{-1}).

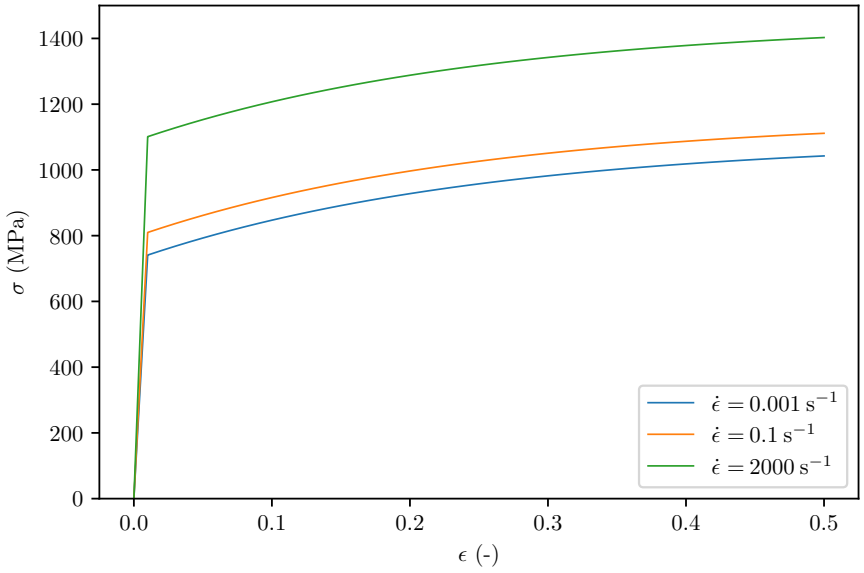

FIGURE 2.25: Flow stress prediction according to Galindo-Fernández *et al.* (2018) at different strain rates ($T = 25$ °C).

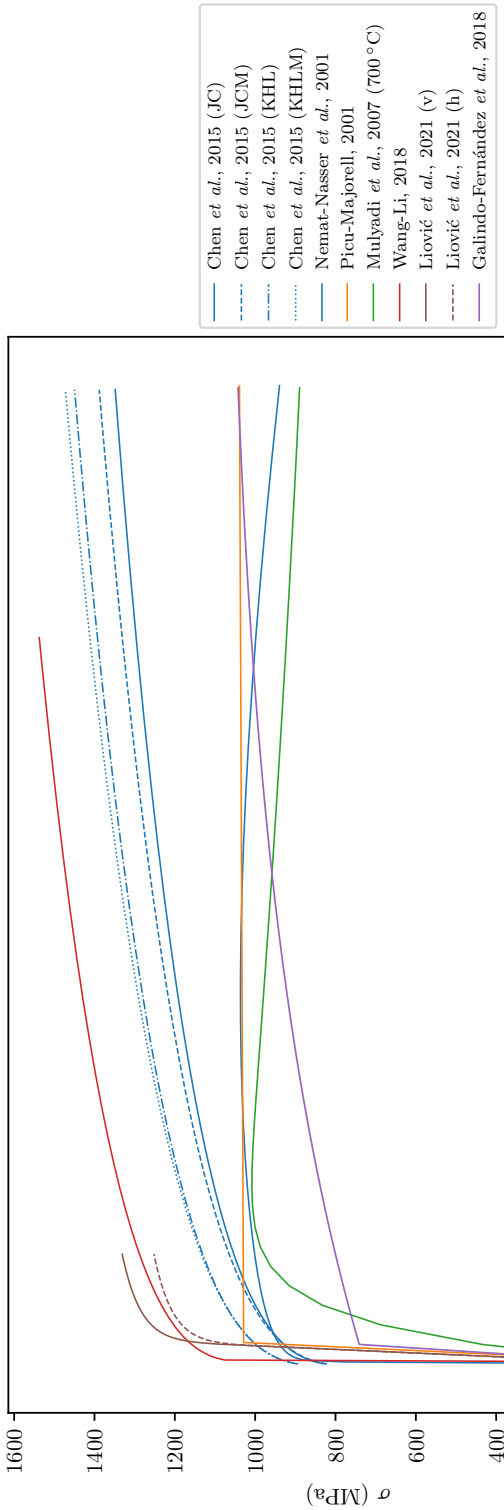

FIGURE 2.26: Comparison of some flow stress prediction for Ti-6Al-4V, according to the constitutive models investigated in this study ($T = 25$ °C, $\dot{\epsilon} = 0.001$ s^{-1}).

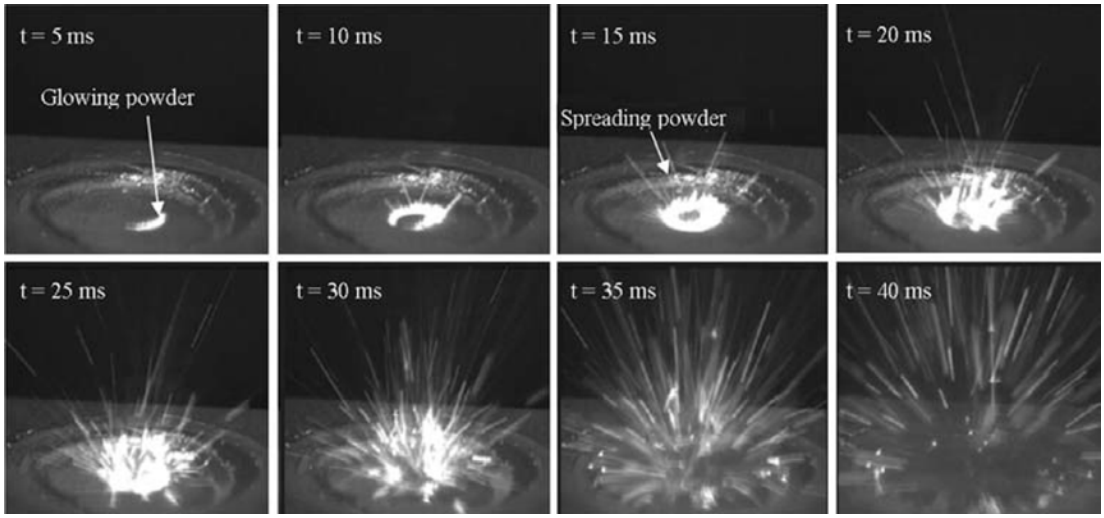

FIGURE 2.27: Interaction between heat source and powder layer showing micro-explosions. Image reproduced from [139, p. 119, fig. 4].

planar heat source. Alongside these, some more refined models have been developed mainly with the objective to describe better the temperature profile and thermal gradient during the welding process and, more recently, to model additive manufacturing.

Rosenthal, 1946

In the early 1930s, the first investigation into the theory of moving heat sources was marked by Rosenthal's pioneering analysis of a point, line and planar moving heat source for a *quasi-stationary* condition by using analytical methods [138]. The latter assumption is mathematically defined as $\partial T/\partial t = 0$ and so the temperature distribution around the heat source is constant. The distribution of the heat rate of surface described by a moving point heat source as in Rosenthal's study leads to complex expressions using a combination of exponential and trigonometric functions and they have some limitations, because a heat source represented as a point source is far from the realistic-distributed temperature field. Therefore, Rosenthal's expressions for the weld pool shape were approx-

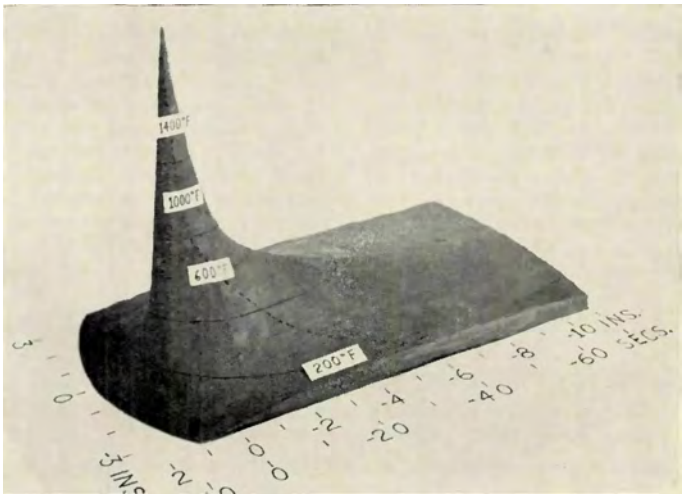

FIGURE 2.28: A three dimensional physical heat model representing the surface temperature distribution in arc welding built in the 1970s, with the aim to illustrate some concepts like the centreline cooling rates, the peak temperatures, and the duration of heating. Before the advent of high-performance computers this was an interesting tool to predict the temperature field around the heat source. Image reproduced from [140, p. 410s, fig. 1].

imated by the so-called *Gaussian heat source*, which simplifies the model and introduces a more-distributed and realistic heat source field [141].

Goldak *et al.*, 1984

In 1984 a new mathematical model proposed by Goldak *et al.* has been introduced, in order to allow a better description of the temperature field obtained by the heat-source penetration inside the material during arc welding, laser and electron beam welding and to improve the agreement with experimental results. This model was intended to replace the Rosenthal model, which was subject to some errors in the temperature profile, such as, in particular, the infinite temperature at the heat source location. The model proposed introduced an ellipsoidal and a double ellipsoidal power density function, expressed as a product of Gaussian heat sources. The power density expression for the Goldak ellipsoid in a fixed

coordinate system assumes the following form:

$$q(x,y,z,t) = \frac{6\sqrt{3}Q}{abc\pi\sqrt{\pi}} e^{-3x^2/a^2} e^{-3y^2/b^2} e^{-3[z+\nu(\tau-t)^2]/c^2}. \tag{2.59}$$

This power density expression can be split into two contributions, leading to a more general formulation. Indeed, if $f_f + f_r = 2$ the so-called *Goldak double ellipsoid* in a fixed coordinate system, for the front quadrant, is

$$q(x,y,z,t) = \frac{6\sqrt{3}f_f Q}{a_f b_f c_f \pi\sqrt{\pi}} e^{-3x^2/a^2} e^{-3y^2/b^2} e^{-3[z+\nu(\tau-t)^2]/c^2}, \tag{2.60}$$

while for the rear quadrant is

$$q(x,y,z,t) = \frac{6\sqrt{3}f_r Q}{a_r b_r c_r \pi\sqrt{\pi}} e^{-3x^2/a^2} e^{-3y^2/b^2} e^{-3[z+\nu(\tau-t)^2]/c^2}. \tag{2.61}$$

In general, it is assumed that $a_f \neq a_r$, $b_f \neq b_r$, $c_f \neq c_r$, so the two expressions can be regarded as different and the heat source becomes then asymmetrical.

The results obtained by implementing a numerical simulation with Goldak's model can be very detailed, but it has been found that the calculation time required for a model implementing Goldak's model can be more than twice as long as that using a concentrated heat source model [142]. Therefore, a good compromise is the use of a Gaussian heat source model, which describes better the field than the point source and avoids longer calculation times. Moreover, a Gaussian source is usually employed in welding simulations with good results [143].

2.5.2 Residual stresses development in additive manufacturing

Residual stresses occur when localised heating causes an expansion of the material, which, upon cooling, is limited by the surrounding material. This is further emphasised by the different expansion rates in the melted and unmelted regions.

One of the aims that have guided research in the field of heat sources has undoubtedly been the possibility to predict residual stresses [138, 137]. Residual

stresses can be defined as internal stresses inside a body, which remain after the production process in the absence of external forces or thermal gradients [144]. They can be framed as secondary stress (primary stress is a load-controlled stress, whilst secondary stress is a displacement controlled stress [145]), caused by the impossibility of the constrained material to support thermal expansion, thermal gradients or plastic strains. Indeed, the major sources for residual stresses are different cooling rates (the surface always cool faster) after a heat treatment, a non-uniform material (different thermal expansion coefficients), stresses due to the interactions of different materials in welding (at the interface between the parent metal and the filler material), stresses from mechanical working (plastic deformation only on the surface) [146, pp. 312-316]. Therefore, it is clear that since any manufacturing process involves plastic deformations, which in turn induce residual stresses, they cannot be completely eliminated. Although they are usually an unwanted production consequence, such that can lead to premature cracking of a mechanical part, it seems more appropriate distinguishing between those which are beneficial to the general mechanical behaviour of the desired part. Indeed, just to cite one, tempered safety glass is manufactured by a technique that allows the development of residual stresses which the product takes advantage of. Glass sheets, for example, are cooled with forced air, in order to leave the surface under residual compression. Not only does the glass become much more resistant to the fracture under bending, but also if a crack starts, the glass rapidly breaks into small pieces for safety [146, p. 321]. This example proves that the study of residual stresses is important not only to avoid or reduce them, but, under certain specific circumstances, to use them for the benefit of the manufactured product.

The residual stresses contained within a component can influence a large range of mechanical behaviours, such as like fatigue life, distortion, dimensional stability, corrosion resistance, and brittle fracture [144]. As a general criterion, it can be stated that tensile residual stress at surface can exacerbate brittle fracture of

the material, whilst compressive residual stress at the surface are in general beneficial for the manufactured part [145, p. 6167]. Therefore, the study of residual stresses has gained importance in all applications in which they can potentially affect the final product performance in service conditions.

Residual stresses are usually classified into three types, accordingly to the scale on which they act or they are measured. Type I, a macroscopic residual stress, is a stress that is inside a body or inside a portion of a body larger than the single grain; type II or type III are microscopic residual stresses, respectively the microscale and nanoscale (or atomic-scale) residual stresses [145]. The difference between them is that type II act at grain level while type III is generated by dislocations and other crystalline defects and so they are present within a single grain [144].

Several different methods to measure residual stress were developed and they can be classified into three categories: non-destructive, semi-destructive, and destructive. The latter two are also called *mechanical methods* and it should be noted that also the semi-destructive methods are actually destructive, but they are called in this way because the part of the component to be inspected requires some previous machining operation that can be used in the same time for the measurement. Some of the destructive methods are the hole-drilling, the deep hole, the sectioning and the contour methods, while non-destructive relies on diffraction techniques (X-ray diffraction method, neutron diffraction method) or on other physical phenomena, such as the magnetic Barkhausen noise, revealing small and rapid changes in magnetic flux, and the ultrasonic method, making use of mechanical, or vibrational, waves of short wavelength and high-frequency [144]. Techniques for the determination of residual stresses always measure a quantity related to the stress level, rather than directly measure stress, which is obviously impossible. In particular, destructive and semi-destructive methods measure displacement or strain by using electrical or mechanical gauges

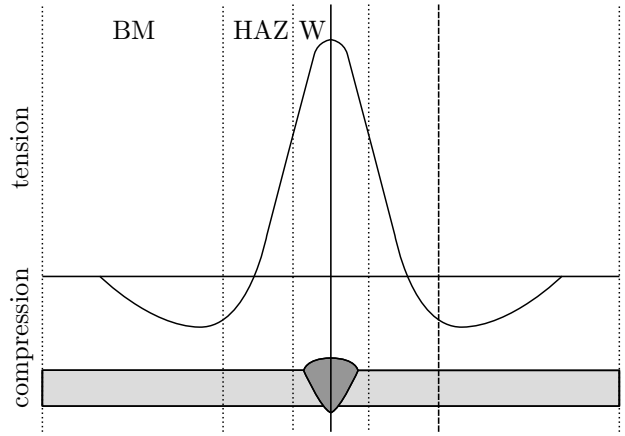

FIGURE 2.29: Illustration of the residual stresses induced by a welding process of two plates in the cross section (perpendicular to the welding line). The influence of this process can be subdivided into three zones: a welding zone (W), a heat affected zone (HAZ), and a base material zone (BM). Image concept adapted from [145], p. 6168.

and they both rely on the analysis of the stress relaxation, that is the elastic strain slowly conversion to plastic strain, occurring when removing some material. Non destructive techniques were mainly developed from the physical fact that the deformation is related to the interplanar spacing between planes of atoms, to the relationship between magnetic properties of a material or to the propagation of waves inside it. Among all non destructive methods, it is noteworthy that the possibility to measure internal residual stress of a material (up to 100 mm in aluminium or 25 mm in steel [144, p. 581]) by neutron diffraction, which has an excellent accuracy, with an error of about 40×10^{-6} in terms of strain in additively manufactured parts [147, p. 349].

Some of the consequences of residual stresses in additive manufacturing is the formation of cracks in the part or a premature disconnection of the part from the substrate, as represented in Figure 2.31. The additive manufacturing process leads to a similar residual stress formation mechanism that occurs in a welding process [147, p. 349], despite the fact that in additive manufacturing there is a

FIGURE 2.30: Residual deformations produced by a metal deposition process, usually called *angular distortion* in welding. Image reproduced from [150].

partial re-melting process when the subsequent layers are deposited [148, p. 169]. A good example of the similar so-called *angular* or *butterfly distortion*, usually obtained after welding two metal pieces, but obtained also during metal deposition, can be grasped by looking at Figure 2.30. Since the additive manufacturing process can be viewed as a rapid sequence of micro-welding processes [149], and because both additive manufacturing and welding are processes that involve a moving heat source, it is convenient to briefly remark some known aspects related to the residual stresses and the fracture behaviour of welded parts and successively focus on the residual stresses in additively manufactured part.

Operations like welding introduce both tensile and compressive residual stress. They are due to the highly localized heating and rapid cooling and the associated thermal gradient [145, p. 6167]. The main factors that affect the residual stress distribution, but which are also directly related with the additive manufacturing problem, are the material thermo-physical properties, the process parameters and the operations after the process [145]. After two parts of metal are joined by welding it can be observed that a region of tensile residual stress is present in the weld metal zone and in an adjacent area, called *heat affected zone* (often abbreviated as HAZ), while distant regions are under compressive residual stress [145] . Whilst this statement is generally accepted, according to some scholars this is not always true and may depend on some particular processing parameters or technologies [145, p. 6169]. Indeed, some scholars agree that heat input affects

the magnitude and distribution of residual stresses and that it is better to use lower heat inputs to reduce residual stresses [145, p. 6169]. However, there are others who state that heat input has a little influence on them [145, p. 6169]. In general, it is important to mention that in welding processes a commonly used method for reducing or eliminating residual stresses is a heat treatment, a preheat or a post-heat process of the parts to be joined. The scope of such treatments is the reduction of the thermal gradient and sometimes an improved fracture toughness was found after post-heat of welded parts [145, p. 6171].

Macroscopic mechanism of formation

Development of residual stresses in additive manufacturing is associated with two basic macroscopic mechanisms related to the heating and cooling stage as in welding, with the peculiarity that they act in rapid and alternate repetitive sequence. The first mechanism is due to the high thermal gradient, causing an expansion force outside the melt pool, whilst the second one is due to the cooling stage, creating a shrinkage of the material [19, p. 2955], [22]. The first mechanism is often associated with the generation of compressive residual stresses, while the second one is responsible for the tensile residual stresses, as can be immediately elucidated by looking at the diagram in Figure 2.32. The initial irradiation on the surface of the material generates an expansion, which results in plastic stresses, above the yield stress. Therefore, the material plastically deforms according to a bending shape in direction opposite to the laser beam, if the part is looked from its cross-section side, but the subsequent cooling generate the shrinkage, which results into an opposite bending towards the laser beam [151].

Since the heat source moves in the space, the heating-cooling process can be imagined as cyclic, and those two mechanisms act sequentially and very rapidly on a small portion of the material. Therefore, this theoretical subdivision is conceptual, but the residual stresses generation is a more complex phenomenon.

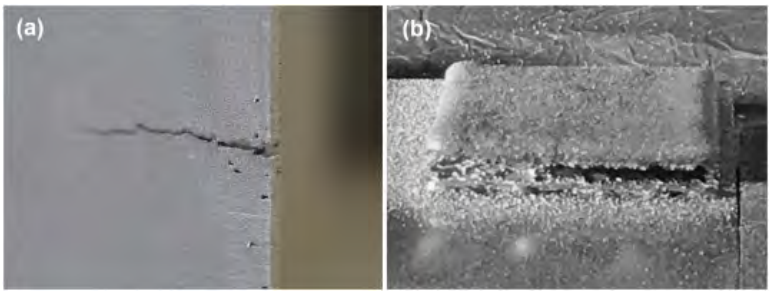

FIGURE 2.31: Consequences of residual stress in parts of Ti-6Al-4V during additive manufacturing: (a) crack formation; (b) disconnection of the piece from the substrate. Image reproduced from [9], p. 8, fig. 9.

Indeed, it should be also observed that during material deposition, the thermal expansion is vertically constrained and this can result in mixed mechanisms of residual stresses formation [22]. This means that the mechanism is always driven by the non-uniform contraction and expansion [152, p. 5]. The *bending mechanism*, which is a temperature-gradient mechanism, has been often used to explain the macroscopic generation of residual stresses [151]. Additionally, rise of residual stresses is also related to residual deformations and they are inversely proportional, as it is illustrated in Figure 2.33. When removing a part from the substrate, a stress relaxation occurs and this often leads to distortions according to the material rigidity [153].

Microscopic mechanism of formation

As it has emerged so far, the thermal expansion is one of the main macroscopic physical properties contributing more to residual stresses development in additive manufacturing [154]. However, some material as Ti-6Al-4V, are composed by two or more phases, and therefore the thermal expansion varies according to them. Indeed, in duplex stainless steel a microstructural difference in distribution of residual stresses has been observed and related to the austenite or ferrite phases [155]. The tensile microscopic residual stresses were localised in the austenite

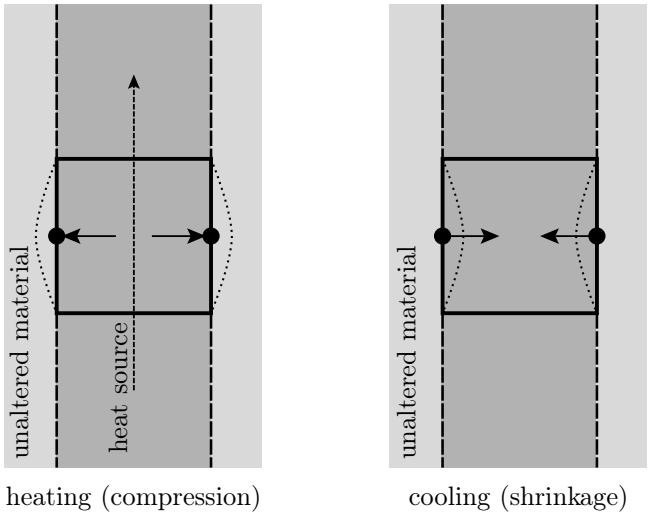

FIGURE 2.32: Illustration of the residual stresses formation mechanism during a single laser scan, when looked from above.

phase and the compressive in the ferrite. This difference in grain shrinkage was explained on the evidence of a different coefficient of thermal expansion for each phase [155]. An analogous microscopic mechanism can perhaps be used when studying the dual $\alpha + \beta$-phase Ti-6Al-4V. In this regard, it emerged that the unit cell volume for the α and β phases increases differently during a temperature increase, especially for the BCC β-phase and after the β-transus temperature [156]. The lattice parameter a_0 as function of the temperature is represented in Figure 2.34.

The microscopic mechanism also depends on the porosity of the fabricated parts, because more pores tend to decrease the residual stresses, for the reason that the stress normal to a pore is zero [157]. One of the main factor affecting porosity is the presence of the type of gas used during fabrication [158]. In Ti-6Al-4V has been found that parts realised in a helium environment have higher residual stresses and this was attributed to the higher thermal conductivity if compared with argon [158].

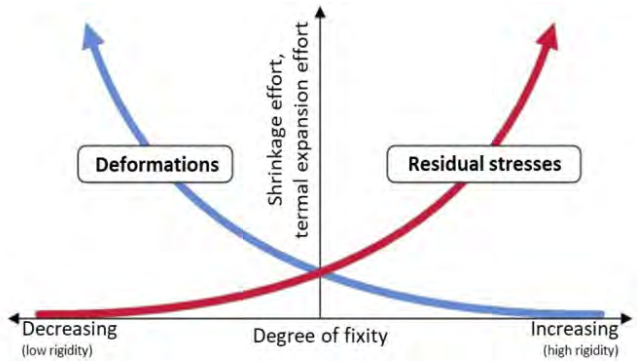

FIGURE 2.33: Ratio between residual stresses and deformations for a varying degree of fixity. Image reproduced from [153, p. 1556, fig. 13].

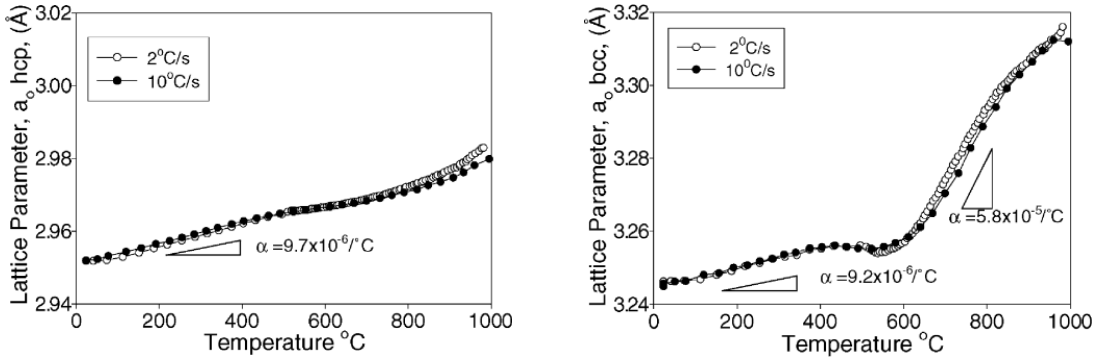

(a) HCP (α-phase).

(b) BCC (β-phase).

FIGURE 2.34: Lattice parameters of the BCC and HCP phases in Ti-6Al-4V as a function of temperature, during heating at two different rates. Images reproduced from [156, p. 111, fig. 10].

Residual stresses distribution and magnitude

According to the experimental evidence, the residual stress distribution and magnitude can vary significantly [152]. It has been found that along the longitudinal direction (parallel to the scanning direction) the residual stresses are higher than in the transversal and normal direction [152]. Moreover, the magnitude of residual stresses was found to be affected by the layer thickness in Ti-6Al-4V, so reducing it can be beneficial [159]. The magnitudes of von Mises stresses found in the literature shows that the minimum and maximum values obtained ranges in the

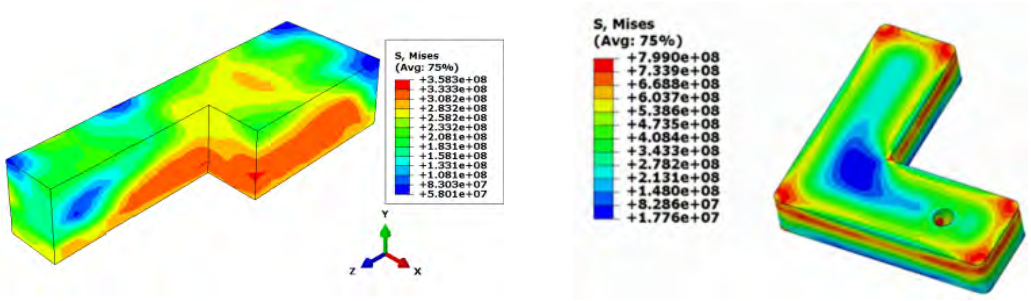

(a) Image reproduced from [150, p. 245-7, fig. 4d].

(b) Image reproduced from [160, p. 9, fig. 5d].

FIGURE 2.35: Magnitude of von Mises residual stress in Ti-6Al-4V for different geometries in additive manufacturing simulations [150, 160].

intervals 58–358 MPa and 17-799 MPa and they are attained always at the base and at the corners [150, 160].

Residual stress measurement

As anticipated, residual stresses measurement techniques can be distinguished into destructive or non-destructive and a summary of typical residual stresses measurement methods used in the additive manufacturing context for Ti-6Al-4V can be found in Table 2.11, where it is evident that most of them are classified as non-destructive and applicable for a microscale analysis. A classification of these methods, specifically for additively manufactured parts, is also illustrated in Figure 2.37.

For the evaluation of residual stresses it is generally possible to use both neutron diffraction, a non-destructive method, and the contour method, a destructive method, but, even better, both methods can also be used in conjunction to cross validate the results [162]. Another technique recently employed to estimate residual stress distribution on the surface in additively manufactured parts is the X-ray diffraction method. By looking at the XRD patterns, using the method elaborated by G. K. Williamson and W. H. Hall, it is possible to [163]. Indeed, it was found that residual stresses can affect the X-ray pattern distribution. However, it

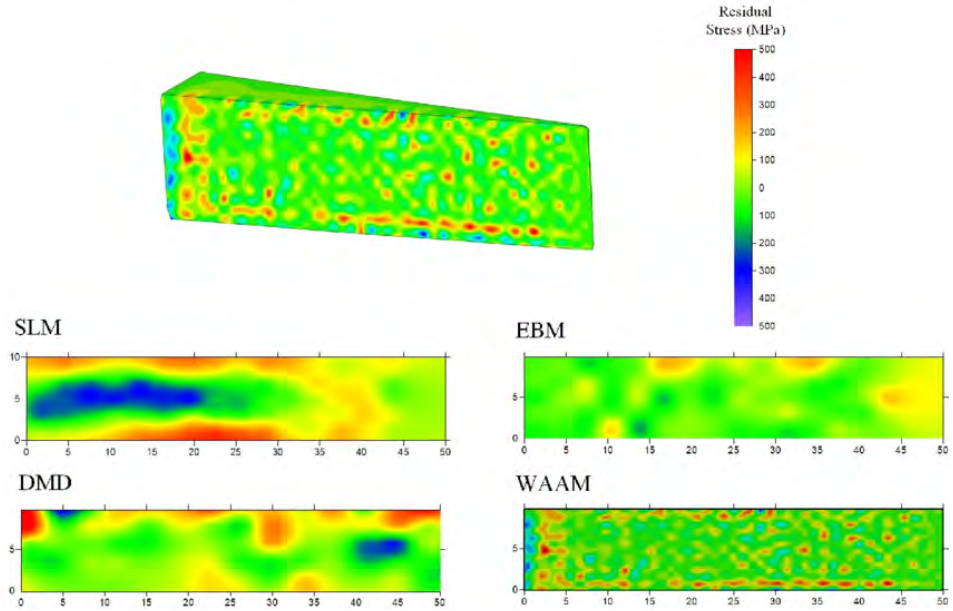

FIGURE 2.36: Magnitude of residual stress along the central cross-section of a wedge-shaped sample of Ti-6Al-4V for four different additive manufacturing processes [161, p. 9, fig. 5].

is not possible to quantitatively determine the stress values, although it is possible to see if they are compressive or tensile and the Williamson-Hall method is based on the evidence that the imperfections can cause diffraction-line broadening [163]. On the other hand, the most commonly used methods for measuring macroscopic residual stresses in additively manufactured parts are the *bridge curvature method* and the *cantilever method* [153].

Microstructure of additive manufactured components

Additive manufacturing of metals show a columnar grain microstructure, namely highly oriented and elongated grains, and a strong texture, which is the *preferred orientations* [25, p. 51], in the build direction, because their growth is driven by the solidification front [147, p. 350]. An example of the columnar microstructure obtained by additive manufacturing is represented in Figure 2.38.

Residual stresses in the scanning direction are more tensile than in the perpen-

Method	Destructive	Scale
Cutting / hole drilling / bridge curvature method / contour method	Yes	Macroscale
X-ray diffraction	No	Microscale
Neutron diffraction	No	Microscale
High speed X-ray diffraction	No	Microscale
Ultra-high speed X-ray synchrotron radiation	No	Microscale
Ion beam milling	Yes	Microscale
TEM/SEM/OM (optical laser confocal scanning microscope)	Yes	Microscale
Digital image correlation (DIC)	No	Mesoscale
High speed imaging technology	No	Mesoscale
Micro-CT imaging	No	Microscale
X-CT analysis	No	Mesoscale
Laser line scanning profiler	No	Microscale
X-ray micro-diffraction	No	Microscale
Synchrotron energy dispersive	No	Microscale
Thermal sensor (infrared/imaging/pyrometer/thermocouples)	No	Mesoscale
Optical method (photodiode/spectrometer/CMOS camera/CCD camera/plume camera)	No	Mesoscale
Acoustic sensor (ultrasonic)	No	Macroscale

TABLE 2.11: Summary of the measuring methods used to evaluate the magnitude of residual stresses of parts build with selective laser melting. Table adapted from [164, p. 7, tab. 2].

Variable	Maximum value (MPa)	Simulation / Experiment	Process	Parameters	Ref.
$\sigma_1, \sigma_2, \sigma_3$	818	Simulation	Direct laser energy deposition	$p = 300$ W, $s = 2$ mm s^{-1}	ref. 1
σ_x, σ_y	607, 693	Simulation	Direct lase energy deposition	$p = 300$ W, $s = 2$ mm s^{-1}	ref. 1
σ_M	772–1226	Simulation	Laser powder-bed fusion	$p = 375$ W, $s = 1100$ mm s^{-1}, $h = 120$ µm	ref. 2
σ_1, σ_2, σ_3, σ_M	203, 211, 439, 772	Simulation	—	—	ref. 3
σ_M	358	Simulation	—	—	ref. 3
σ_1, σ_2, σ_3 (BD)	1259, 1274, 1128	Simulation + Neutron diffraction	Laser powder-bed fusion	—	ref. 4
σ_M	799	Simulation + Neutron diffraction	Laser powder-bed fusion	—	ref. 4
σ_{xx}	$\approx$ 300–325	Contour method	Wire and Arc Additive Manufacturing	$s \approx 60$ mm s^{-1}	ref. 5
σ_{xx}	$\approx$ 200–250	Neutron diffraction	Wire and Arc Additive Manufacturing	$s \approx 60$ mm s^{-1}	ref. 5
σ (BD)	$\approx$ 500	Contour method	Selective laser melting	$p = 280$ W, $s = 1200$ mm s^{-1}, $h = 140$ µm	ref. 6
σ (BD)	$\approx$ 200	Contour method	Electron beam melting	—	ref. 6
σ (BD)	$\approx$ 500	Contour method	Direct metal deposition	$p = 1600$ W, $s = 1$ mm s^{-1}	ref. 6
σ (BD)	$\approx$ 450–500	Contour method	Wire and Arc Additive Manufacturing	$I = 140$ A, $s \approx 2.5$ mm s^{-1}	ref. 6
σ_z (BD)	325	Simulation	Selective laser melting	$p = 200$ W, $s = 200$ mm s^{-1}	ref. 7
σ (BD)	325	Simulation + Neutron diffraction	Deposition through a nozzle	$p = 197$ W, $s = 1000$ mm s^{-1}	ref. 8
σ_x, σ_y, σ_z (BD)	700, 600, 500	Simulation	—	$p = 200$–2000 W, $s = 4$–15 mm s^{-1}	ref. 9
σ_M	600	Simulation	—	$p = 2000$ W, $s = 15$ mm	ref. 10
σ	$\approx$ 450	Hole drilling	Selective laser melting	$p = 280$ W, $s = 400$ mm s^{-1}, $h = 60$ µm	ref. 11
σ	$\approx$ 475	X-ray diffraction	Selective laser melting	$p = 280$ W, $s = 400$ mm s^{-1}, $h = 60$ µm	ref. 11
σ	$\approx$ 450	Contour method	Selective laser melting	$p = 280$ W, $s = 400$ mm s^{-1}, $h = 60$ µm	ref. 11
σ_x, σ_y, σ_z (BD)	700, 600, 1200	Simulation	Laser beam melting	$p = 400$ W, 0.1 mm	ref. 12
σ_x, σ_y, σ_z (BD)	1040, 1085, 1799	Simulation + X-ray diffraction	Selective laser melting	$p = 250$ W, $s = 600$ mm s^{-1}, $h = 0.12$ mm	ref. 13

TABLE 2.12: Maximum values of the macroscopic residual stresses for additive manufacturing of Ti-6Al-4V published in the literature. The residual stress components are cited keeping as much as possible the same nomenclature used in the reference, and the building direction is identified as 'BD'. The references are the followings: ref. 1 = [165], ref. 2 = [166], ref. 3 = [150], ref. 4 = [160], ref. 5 = [167], ref. 6 = [161], ref. 7 = [168], ref. 8 = [169], ref. 9 = [170], ref. 10 = [171], ref. 11 = [172], ref. 12 = [173], ref. 13 = [174].

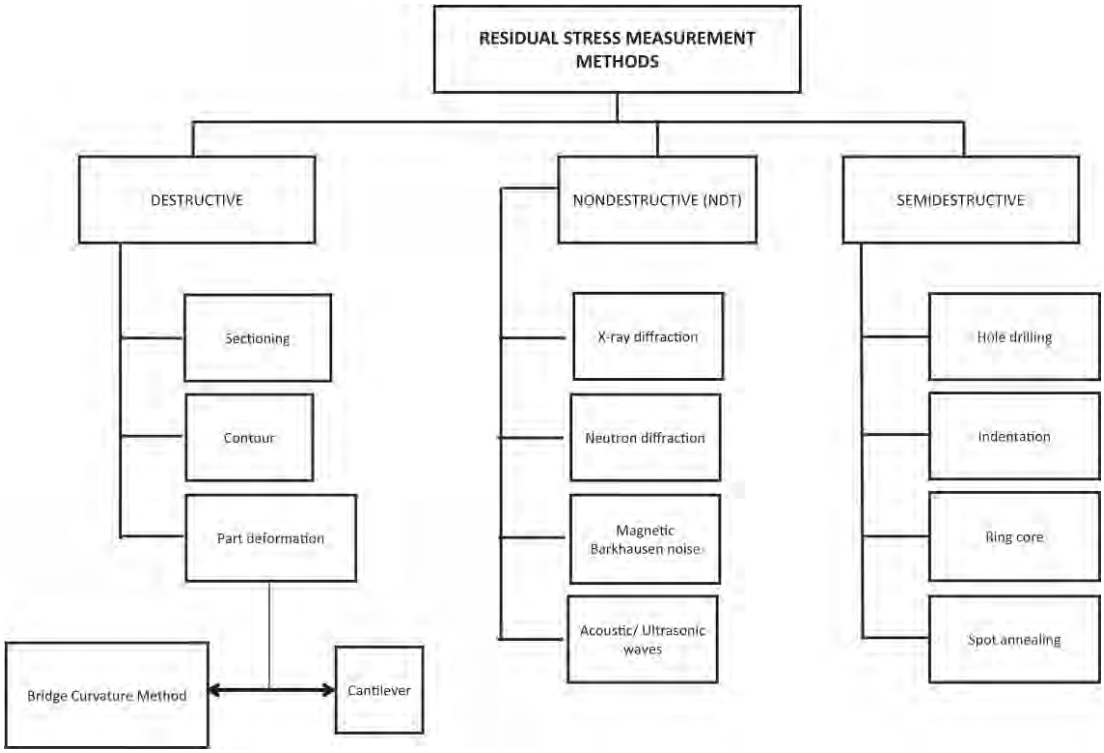

FIGURE 2.37: Classification of residual stress measurement methods. Image reproduced from [153, p. 1552, fig. 6].

dicular direction. In general, residual stresses near the centre of the manufactured part tend to be compressive, while they are tensile on the external surface [147, p. 350]. If the material is deposited by following a chessboard strategy for the laser scanning (called *island scanning strategy*), smaller residual stresses were observed [147]. An opportunity for the foreseeable future in additive manufacturing could be the development of algorithms specifically designed to minimise residual stresses during the scanning process. Early stage works in this area are already available, such as the innovative LaserCUSING® approach [147].

One of the challenging physical aspect of an additive build, influencing the microstructural changes occurring in a material, is the cooling stage. Many metallurgical studies have observed that as a result of different cooling rates the alloy

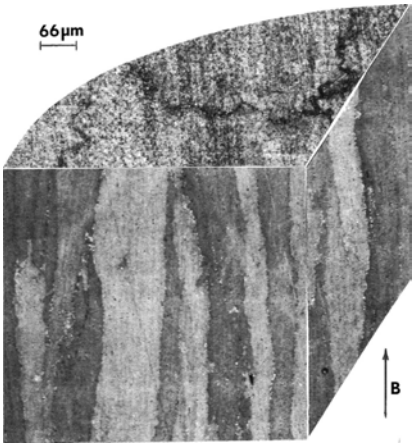

FIGURE 2.38: A tridimensional optical micrograph of columnar microstructure obtained by electron beam melting, along the building direction, indicated with B. Image reproduced from [175].

of interest can see substantially different microstructure, influencing the mechanical response of the material. When compared to this, titanium alloys are not an exception [36, p. 23]. Whilst in some manufacturing processes the cooling rate can be directly controlled, during a welding or additive manufacturing process the cooling rate is largely dictated by the process parameters, material, and geometry of the component itself. The rapid solidification in welding and additive manufacturing, reaching values around 10^4 K s^{-1}, is primarily responsible for the formation of the martensite in steel or titanium alloys. This is a new phase solution which is, as seen in the previous paragraphs, considered both unintentional and potentially harmful for the manufactured component [84]. Nevertheless, at the same time the role of the martensite in metal additive manufacturing is not fully understood, since it seems also beneficial to the mechanical properties of the material [84].

It is true that the final phase composition, and so the mechanical properties, can be tuned, as anticipated, by a post-heat treatment [84], but one of the ultimate long-term goals in metal component fabrication could be to no longer process the material after a component has been built, as these add in manufac-

turing costs and slow down the manufacturing time. The challenge is so to obtain, in an imminent future, a nearly perfect as-built mechanical part, fabricated by new processes as additive manufacturing.

Failure modes due to surface conditions in additively manufactured parts

The surface conditions have been widely accepted as one of the most prominent influential factors on fracture and fatigue behaviour in every metal part. Many defects originate within the material volume, but the influence of surface defects plays a key-role in fatigue. Indeed, it has been shown that failure strain for Ti-6Al-4V is highly sensitive to both the roughness magnitude and orientation [176].

The fatigue limit of a material is represented through its σ-n curve (sometimes indicated as S-N and called *stress-life fatigue curve*), which is a plot of the stress applied during a cyclic loading condition and the number of cycles. It has been found that the failure mechanism can potentially change from surface to volume if the number of cycles increases, or it can switch from volume to surface, according to the material, as represented in Figure 2.39. The surface geometric factors, like the roughness, have an important role on the final behaviour of the component, because they alter the local stress state, the same must then hold for the surface residual stresses.

In additively manufactured parts, the surface conditions plays a key-role and, in particular, for Ti-6Al-4V the surface defects can lead to fracture for any number of cycles during fatigue [24]. Usually, the most important factor is considered to be the surface roughness, because the peaks and valleys can alter locally the stress state as a consequence of a notch effect [24]. This has a detrimental effect on the fatigue response of the manufactured part and recently it has been found a method to take into account the surface roughness of the as-built additively

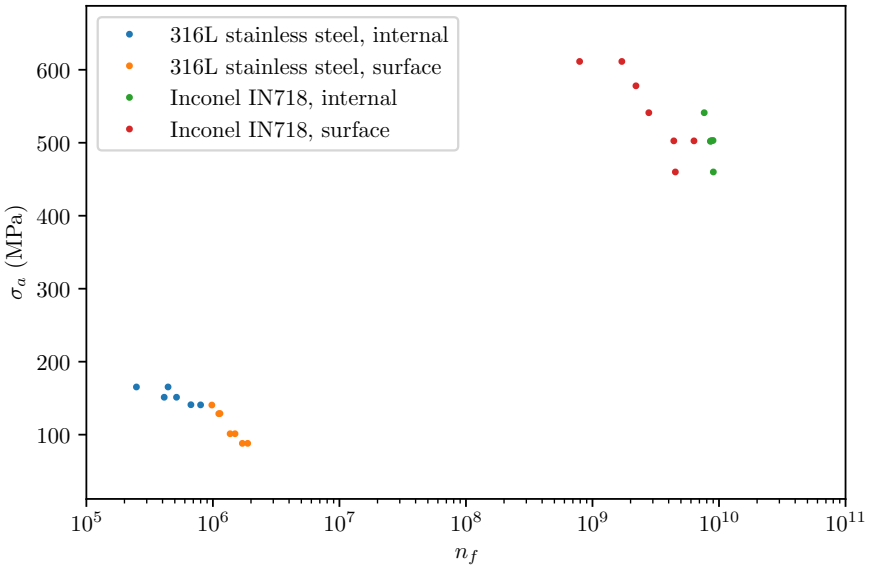

FIGURE 2.39: Experimental σ-n curves, showing two failure modes for two different materials during fatigue experimental testing. Data reproduced from [177, p. 1955, fig. 10A] and [177, p. 1956, fig. 11A].

manufactured parts of Ti-6Al-4V into the usual stress concentration factor [178]. This permits to calculate immediately the fatigue response in presence of surface defects. A method to take into account both surface conditions, as well as the α' martensite geometry, is therefore outlined below.

The stress concentration factor is defined as the following ratio:

$$K_t = \frac{\sigma_m}{\sigma}, \tag{2.62}$$

where σ_m is the maximum stress around the defect and σ is the stress given by the applied load (also called *reference stress* or *far-field stress*). In order to incorporate surface roughness within the stress concentration factor for Ti-6Al-4V additively manufactured parts, it is possible to introduce an *effective stress concentration factor* [179, 178]:

$$\overline{K}_t = 1 + n\left(\frac{R_a}{\overline{\rho}_{10}}\right)\left(\frac{R_t}{\overline{R}_Z}\right) \approx 1 + n\left(\frac{R_a}{\overline{\rho}_{10}}\right), \tag{2.63}$$

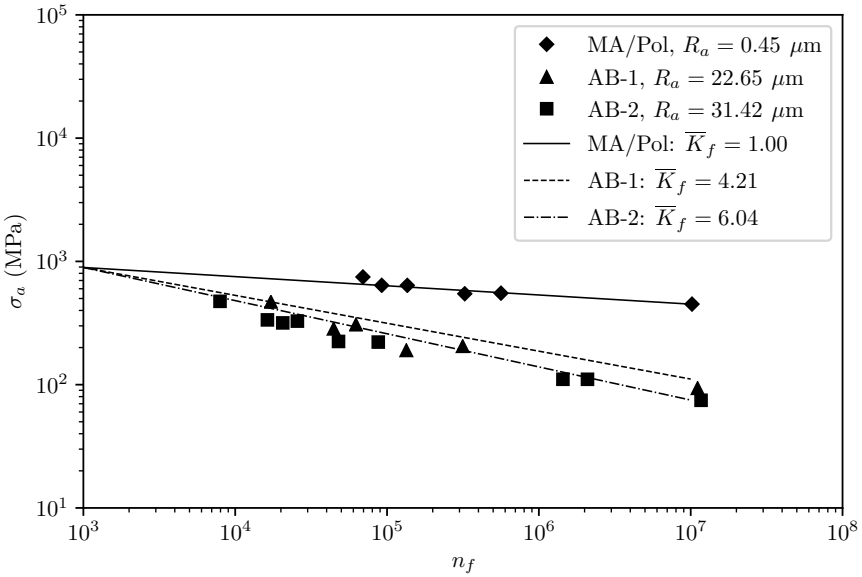

FIGURE 2.40: Stress-life fatigue curves estimated for a polished sample (MA/Pol) and for two additively manufactured as-built samples of Ti-6Al-4V (AB-1 and AB-2) for different roughness conditions. Data reproduced from [178, p. 6, fig. 5].

which does not depend directly on the stress state. In this last Equation (2.63), R_a, $\overline{\rho}_{10}$, R_t, R_Z are micro-notches geometrical parameters, all expressed in µm, and the approximation on the right-hand side holds because the ratio R_t/R_Z is equal to the unit under the assumption of a ideal sinusoidal surface [178]. The actual values of the parameters for different surface conditions are reported in Table 2.13. Moreover, $n \in \mathbb{N}$ is a parameter depending on the loading conditions and it is $n = 1$ for shear, $n = 2$ for tension. This term $\overline{K}_t$ is then related to the *effective fatigue notch factor*, defined as [179, 178]:

$$\overline{K}_f = 1 + q(\overline{K}_t - 1), \tag{2.64}$$

where the *notch sensitivity factor* has been defined for Ti-6Al-4V, including surface roughness, as [179, 178]:

$$q = 1/(1 + \gamma/\overline{\rho}_{10}), \tag{2.65}$$

with $\gamma \in \mathbb{R}$ assumed as the average acicular α' grain width ($\gamma \approx 1.5$ µm; in the present work the α' martensite width is indicated with the symbol $w_{\alpha'}$, but in the following formulation it is possible to keep the original notation) [178]. Therefore, this method permits to take into account a geometric length of the primary martensite. Nevertheless, the effect of residual stresses is not considered in this formulation [178, p. 3], especially those present at the surface of the specimens. However, they can be incorporated into this formulation, defining a *modified effective stress concentration factor* in the following way [180]:

$$\overline{K}_t{}' = \left[1 + n\left(\frac{R_a}{\overline{\rho}_{10}}\right)\right] \pm \frac{\sigma_{ij,r}}{\sigma}, \tag{2.66}$$

where $\sigma_{ij,r}$ is the ij-component of the residual stress tensor, along the same direction of the stress σ generated by the applied load, and its sign is chosen according if the stress is compressive or tensile. Additionally, an interpolation of the data found in [178] permits to calculate the *endurance stress*, which is the limit stress for $n_f \geq 10^7$ as a function of the effective fatigue notch factor, where n_f is the number of cycles to fracture:

$$\sigma_e(\overline{K}_f) = k_1 \exp(-k_2 \overline{K}_f), \tag{2.67}$$

where $k_1 = 599.36$ and $k_2 = -0.35$. It can be assumed that the same Equation (2.67) holds if one replaces $\overline{K}_f$ with $\overline{K}_f{}'$, where $\overline{K}_f{}'$ is obtained through $\overline{K}_t{}'$ in Equation (2.64). From Equation (2.67) is evident that an increase (tensile residual stresses) in $\overline{K}_f$ will lead to a decrease of the σ_e limit and, conversely, a decrease in $\overline{K}_f$ (compressive residual stresses) will lead to an increase of σ_e limit. The interpolated endurance function and the experimental points for some dog-bone specimens of Ti-6Al-4V, under different surface conditions, are plotted in Figure 2.41. It is evident how the polishing of the samples increases significantly the endurance stress. As represented in Figure 1.5, this type of specimen is usually extracted from a single blade to evaluate fatigue in aerospace components.

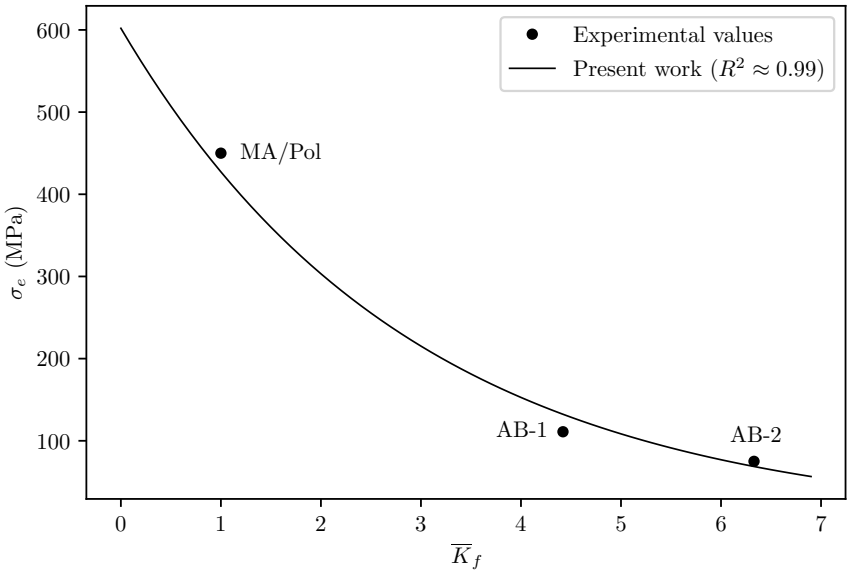

FIGURE 2.41: Interpolated endurance limit σ_e (determined as the stress for $n_f \geq 10^7$) for Ti-6Al-4V as a function of the effective stress concentration factor (as found for different surface roughness values). Experimental values reproduced from [178, p. 6].

Finally, residual stresses, surface condition and microstructure are well known as having a serious impact when considering the the growth of cracks due to stress corrosion cracking. Further details about this failure are given in Appendix A.

2.6 Current state of the studies

As seen, the nomenclature for additive manufacturing processes still presents some issues. On the other hand, the current studies show a tendency of preferring some technologies with respect to others and a wide range of processing parameters have been experimentally and numerically investigated for Ti-6Al-4V. The martensite formation in Ti-6Al-4V is well understood, thanks to the analogy with martensite carbon steel, and its geometrical features have been recently incorporated into a constitutive model, which, among the others, permits to di-

Specimen type	R_a (µm)	R_t (µm)	$R_{y,10}$ (µm)	$\overline{\rho}_{10}$ (µm)
MA/Pol	$\mu = 0.45$	$\mu = 4.63$	$\mu = 3.58$	NA
AB-1	$\mu = 22.65$	$\mu = 126.92$	$\mu = 75.23$	$\mu = 23.77$
AB-2	$\mu = 31.41$	$\mu = 172.08$	$\mu = 97.19$	$\mu = 20.58$

TABLE 2.13: Summary of different fatigue conditions on the Ti-6Al-4V specimens according to the nomenclature used. Data reproduced from [178, p. 3, tab. 1], where the standard deviations are also reported.

rectly incorporate them within the dislocation density evolution formula and so have a direct impact on the flow stress. An overview of the growing interest in this type of topics is depicted in Figure 2.42.

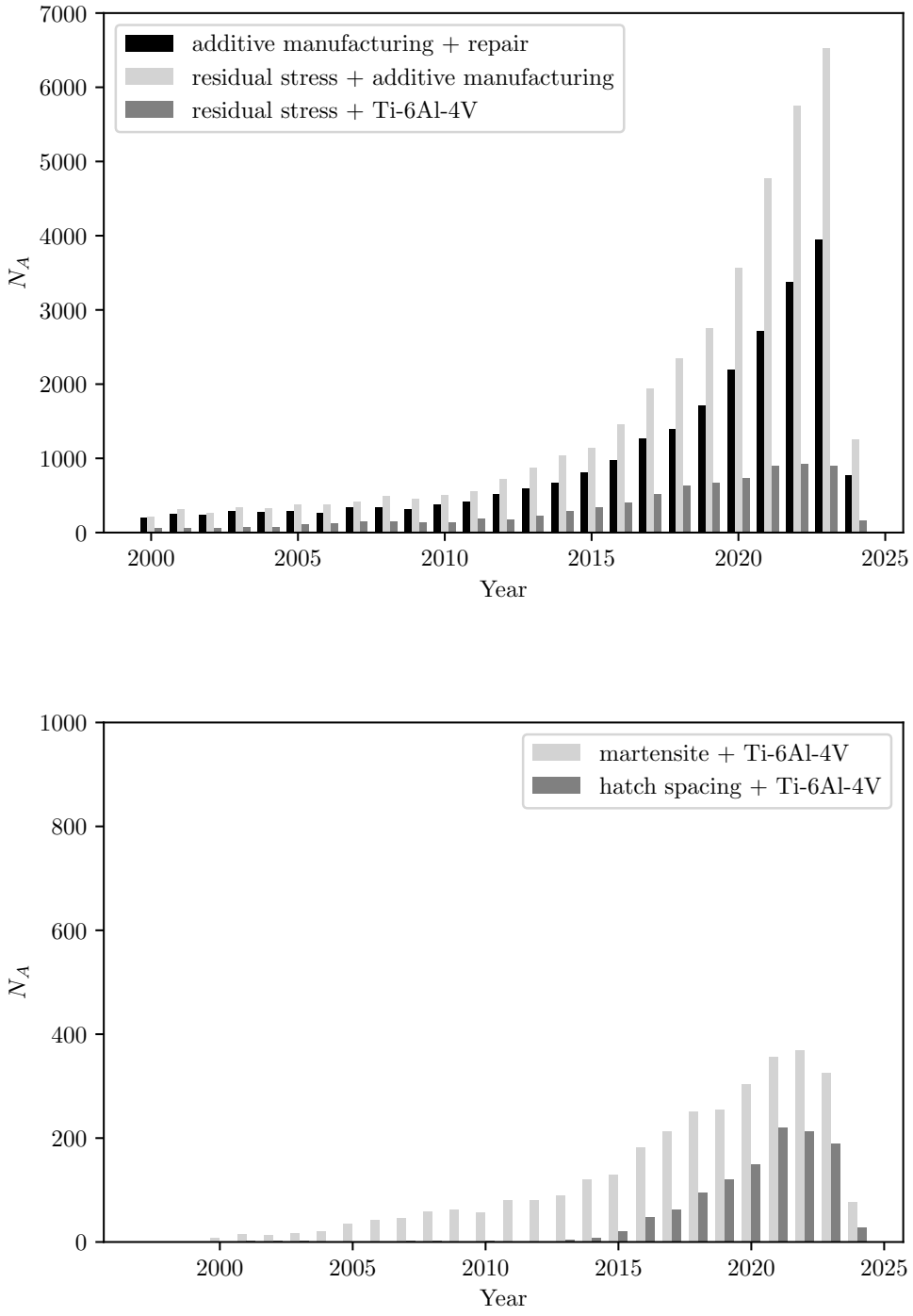

FIGURE 2.42: Frequency number of articles appeared on Sciencedirect in the period 2000–2024.

Chapter 3

Computational framework

One of the main advantages of performing numerical simulations lies in the possibility to have a 'virtual laboratory', in the form of a computer machine, in which to conduct some numerical experiments. This kind of 'experiments' make it possible, under appropriate assumptions, to obtain prediction of material behaviour that would otherwise be very difficult to achieve using traditional physical experimental techniques. In the field of metallurgy these difficult to achieve measurements are, for example, the temperature or the microstructure evolution, at every point of the solid and for any temporal increment. Moreover, since physical experiments can be time-consuming and expensive, as it is particularly true for a new manufacturing process as additive manufacturing, then a numerical simulation can help, at least, to predict how to conduct or refine them better.

Starting from the concept of additive manufacturing as a micro-welding process [149], the numerical modelling technique here presented is therefore closely related to the more well-established welding simulations. Since they both involve a moving heat source, the knowledge gained in both sectors can be shared to provide concomitant benefit. Again, the intention is to focus on the general aspects common, or not common, between the two processes, in order to the derive a

knowledge base that will be usable for different processes in which there is a need to describe the impact of a high density laser source on the material.

Since numerical simulations in thermo-mechanical processes, especially those involving material plasticity, are computationally expensive, it is often necessary to use a high-performance computing system, in order to process data and perform complex calculations at high speeds. This permits to test faster the model and so to get an appropriate solution in a reasonable time. Numerical simulations presented in this chapter were performed on Broadwell microarchitecture, available on BlueBEAR, the University of Birmingham supercomputer for high-performance computing (HPC) and high-throughput computing (HTC), equipped with Sandy Bridge and Cascade Lake, the Intel® processor microarchitectures for servers and workstations. Management of simulations and access to the system was performed via Slurm Workload Manager, installed on Red Hat Enterprise GNU/Linux operating system v. 8.3. Therefore, the finite element calculations with the commercial finite element software SIMULIA/Abaqus [181] have been running on a GNU/Linux environment by using the job scheduler Slurm Workload Manager. The jobs simulations were submitted through a GNU/Linux Bash script (.sh) and the results were stored in the Research Data Store (RDS) available on BEAR (Birmingham Environment for Academic Research).

3.1 Process model and thermo-mechanical finite element model

In order to calculate the thermal field induced by a laser scan or by a sequence of laser scans, it is possible to introduce a general mathematical model of a thermal system, using the concept of energy balance. The energy dissipation predicted by this model will be approximated by the finite element method. In order to calculate the residual distortions and stresses, the elastic and plasticity constitutive

description of the material need to be provided. During the laser scan, both the thermal field and the deformation state of the material are affected, resulting in a mutual influence on heat transfer. This can be seen in the Taylor-Quinney hypothesis, which suggests that a portion of plastic work is transformed into heat, although different interpretations of this concept can also be considered valid [182]. Therefore, the most accurate finite element analysis is the so-called *fully-coupled thermal-stress analysis* and this approach was preferred for all analyses for residual stresses in the present work, as opposed to an initial thermal field calculation followed by mechanical analysis (called *sequentially coupled thermal-stress analysis*), even if the fully coupled thermal-mechanical analysis has generally much higher computational cost and negligible difference observed if compared to a sequentially coupled thermal-mechanical model [165]. This decision, along with the choice not to conduct a comparative analysis, were a consequence from the restrictions imposed by the current timeline for the investigation. Indeed, a comparative analysis always seems necessary, in order to avoid wrong generalisations, especially when considering different boundary conditions, as in the present case.

3.1.1 A process model for laser powder-bed fusion

With the capabilities offered by some commercial finite element software like SIMULIA/Abaqus [181], multiple laser pass and layer-by-layer deposition can be simulated taking into account laser path and speed, hatch spacing, substrate temperature, and layer thickness. This opens the possibility to include different variables within a finite element scheme and therefore define a process model.

A process model for laser powder-bed fusion was originally developed by CASIM2 (Centre for Advanced Simulation and Modelling for Manufacturing) research group, a collaborative project partly funded by the European Regional Development and composed by the partnership between University of Birming-

ham, the Manufacturing Technology Centre, and Rolls-Royce [183]. However, initially designed for calculating residual stresses in CM 247 LC superalloy, it was never fully developed and its implementation presented a substantial number of difficulties. Most of those difficulties were related to its mathematical foundation, never rigorously defined, and its adherence to the physics. From the accuracy point of view, its main limitation, only overcome in the present work, was the technical difficulty to reach the convergence and at the same time model a higher and realistic temperature heat source within a limited computational time frame.

The process model presented in Figure 3.1 is, in a certain sense, completely generic, because it takes into account only those parameters that can be considered independent of technological devices, which are moreover very often momentary and subject to market logic leading to continuous improvement and replacement. Therefore, it should be noted that in this numerical exploration there is no reference to any particular building machine. Although at first glance this may appear to be a limitation, focusing the present analysis to the parameters which can be used by a single machine would not have allowed this research to explore precisely the role of the physical variables in the construction of the parts.

Large-scale simulations in the field of thermo-mechanics require always a certain degree of approximation. Approximations like those presented in this study are necessary because stress analysis simulations in additive manufacturing are very time-consuming and an acceptable balance between accuracy and efficiency is usually needed [184]. In particular, transient models for additive manufacturing like those presented in this study, are more accurate, especially when temperature-dependent properties are implemented, but only a few examples are available in the literature due to the extremely large computational cost [184].

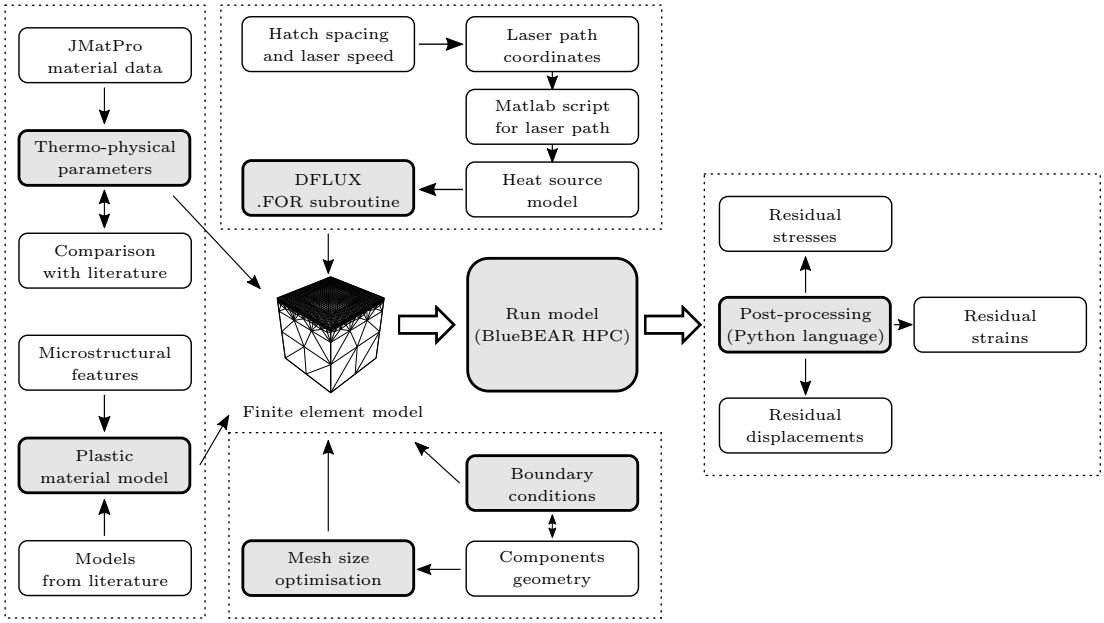

FIGURE 3.1: Flowchart illustrating the multi-pass and multi-layer process model for laser powder-bed fusion and its input/output data.

3.1.2 Mathematical statement of thermal problem with a moving heat source

Let be $\Omega \subset \mathbb{R}^3$ an open and bounded set, representing the configuration of a solid body under thermal analysis (Figure 3.2). The body under analysis is considered rigid, so no deformation phenomena occur during its entire analysis. The principle of the conservation of energy can be mathematically stated as an equality between the time rate of change of thermal energy in Ω and total heat energy flowing across the boundary $\partial\Omega$, plus the heat energy generated in solid in a certain amount of time T [185, 186, 187]:

$$\begin{aligned}\int_{\Omega} \left[c_p(x,t,u(x,t))\rho(x,t,u(x,t))u(x,t)\right] \, \mathrm{d}V \\ = -\int_0^T \int_{\partial\Omega} q(x,t)\cdot n \, \mathrm{d}S\mathrm{d}t + \int_0^T \int_{\Omega} Q(x,t) \, \mathrm{d}V\mathrm{d}t,\end{aligned} \tag{3.1}$$

where $u(x,t)$ is the scalar temperature field defined for each point in the spatial domain $x \in \Omega$ and for any instant of time $t \in (0,T]$, $c_p(x,t,u)$ is the specific heat

capacity at constant pressure ($\mathrm{J\,kg^{-1}\,K^{-1}}$), $\rho(x,t,u)$ is the mass density of the material ($\mathrm{kg\,m^{-3}}$), $q(x,t)$ is the vector field representing the heat flow ($\mathrm{J\,s^{-1}\,m^{-3}}$), $Q(x,t)$ is the rate of heat generated inside the volume (*i.e.* the amount of heat absorbed or liberated in a unit of volume, per unit time), n is the outward unit normal at the boundary $\partial\Omega$. Differentiating the Equation (3.1) respect to time leads to:

$$\begin{aligned}\frac{\partial}{\partial t}\int_{\Omega}\left[c_p(x,t,u(x,t))\rho(x,t,u(x,t))u(x,t)\right]\,\mathrm{d}V\mathrm{d}t \\ = -\int_{\partial\Omega}\left[q(x,t)\cdot n\right]\mathrm{d}S + \int_{\Omega}Q(x,t)\,\mathrm{d}V.\end{aligned} \tag{3.2}$$

Ignoring the spatial and time-dependence of both c_p and ρ and applying the divergence theorem to the surface integral on Equation (3.2), it is possible to obtain:

$$\frac{\partial}{\partial t}\left[c_p(u)\rho(u)u(x,t)\right] = \nabla\cdot q(x,t) + Q(x,t). \tag{3.3}$$

The vector field defining the heat flow $q = q(x,t)$, measured in $\mathrm{J\,s^{-1}\,m^{-3}}$, can be related with the gradient of the scalar temperature field by Fourier's law:

$$q(x,t) = -K(x,t)\nabla u, \tag{3.4}$$

where $K(x,t)$ is the thermal conductivity matrix of the material defined as follows:

$$K(x,t) = \begin{pmatrix} k_1(x,t) & 0 & 0 \\ 0 & k_2(x,t) & 0 \\ 0 & 0 & k_2(x,t) \end{pmatrix}, \tag{3.5}$$

whose elements are measured in $\mathrm{W\,m^{-1}\,K^{-1}}$. However, if the material is isotropic, then $k_1 = k_2 = k_3 = k$, with $k \in \mathbb{R}$, and both the matrix and the heat flow reduce to scalar fields, so Fourier's law becomes:

$$q(x,t) = -k(x,u(x,t))\nabla u. \tag{3.6}$$

Finally, if the material is homogeneous, the conductivity does not depend directly on the spatial coordinate. Combining the Equations (3.3) and (3.6), leads to a

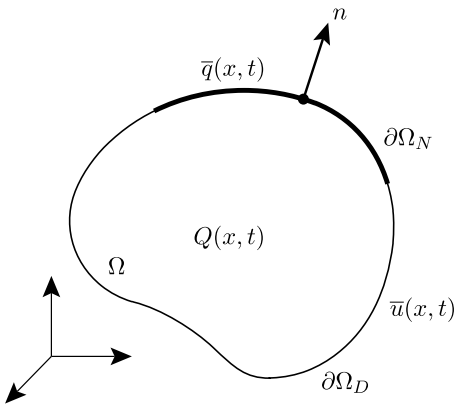

FIGURE 3.2: Tridimensional domain Ω with its boundary $\partial\Omega$ subdivided into two portions.

second-order, non-linear, parabolic partial differential equation:

$$\frac{\partial}{\partial t}\left[c_p(u)\rho(u)u(x,t)\right] = k(u)\nabla^2 u(x,t) + Q(x,t). \tag{3.7}$$

Solving this last partial differential Equation (3.7), together with the conditions specified in the following paragraphs, will allow to determine the temperature field in every point of a domain and for any instant of time. However, since a closed form solution is often difficult to obtain, especially for complex geometries, the solution will be found in an approximate or discrete form by the finite element method. Therefore, the solution will be known only in a finite set of points and in a finite set of temporal instants.

Initial condition and boundary conditions

In order to solve the Equation (3.7), this has to be accompanied by some further conditions, called *initial condition* and *boundary conditions* [185, 186, 187]. This is achieved specifying the value assumed by the temperature function and/or its derivative respectively at the beginning of the time of analysis and at the boundary surface of the domain. The solution of the heat transfer problem then found will be a solution to the differential equation, but it will also satisfy the prescribed boundary conditions. The initial condition associated with the problem can be

defined as:

$$u(x,0) = u_0, \quad \forall x \in \Omega. \tag{3.8}$$

Now let the boundary be subdivided into two portions $\partial\Omega_D$ and $\partial\Omega_N$, such that they satisfy the following conditions:

$$\partial\Omega_D \cup \partial\Omega_N = \partial\Omega, \tag{3.9a}$$

$$\partial\Omega_D \cap \partial\Omega_N = \emptyset. \tag{3.9b}$$

It can be defined the inhomogeneous Dirichlet conditions by assigning a given temperature on a first portion of the boundary:

$$u = \overline{u}(x,t), \quad \forall x \in \partial\Omega_D, \tag{3.10}$$

while the inhomogeneous Neumann condition can be defined by assigning the heat transfer rate $\overline{q}(x,t)$ on its complementary portion as

$$\nabla u \cdot n = \overline{q}(x,t), \quad \forall x \in \partial\Omega_N. \tag{3.11}$$

3.1.3 Heat transfer in a plate of Ti-6Al-4V

Calculating the cooling rates in a plate of Ti-6Al-4V titanium alloy subjected to a laser scan requires the solution to the initial-boundary value problem presented in the previous section. However, in order to reduce the computational time needed to complete the simulations, the computational domain can be a sub-region of the whole physical space under consideration. For a large plate, for example, it is possible to consider only a small three-dimensional rectangular cuboid. Let the simulation domain be

$$\Omega = \{x, y, z : x \in (-l_w/2, l_w/2),\ y \in (-l_h, 0),\ z = (0, l_w)\}, \tag{3.12}$$

where l_w and l_h are the domain length and thickness, respectively. This definition reflects the choice of the origin of the Cartesian coordinate system at the midpoint

of an edge, because this point, without loss of generality, will coincide with the starting point of the moving heat source. Now, let be its boundary subdivided as:

$$\partial\Omega = \bigcup_{i=1}^{n} \partial\Omega_i, \tag{3.13}$$

with $n = 6$ denoting the number of faces of the three-dimensional solid. The initial condition can be expressed as a constant temperature u_0, which can represent room temperature, for every point of the solid at time $t = 0$:

$$u(x,t) = u_0, \qquad \forall x \in \Omega,\ t = 0. \tag{3.14}$$

In order to define the boundary conditions, it is possible to denote with $n = 1, 2$ respectively the top and the bottom faces in the following way:

$$\partial\Omega_1 = \{x, y, z : x \in (-l_w/2, l_w/2), y = 0, z \in (0, l_w)\} \tag{3.15}$$

and

$$\partial\Omega_2 = \{x, y, z : x \in (-l_w/2, l_w/2), y = -l_h, z \in (0, l_w)\}. \tag{3.16}$$

The boundary conditions applied to the top and bottom faces are Neumann (or second-type), while the Dirichlet conditions (or first-type) can be applied at the other faces of the solid:

$$\nabla u \cdot n = \overline{q}(u), \qquad \forall x \in \partial\Omega_i, \quad i = 1, 2; \tag{3.17}$$

$$u(x,t) = u_0, \qquad \forall x \in \partial\Omega_i, \quad i = 3, \ldots, 6. \tag{3.18}$$

The applied rate of heat loss $\overline{q}$ is usually described by Newton's law of cooling, which states that the rate of heat transfer is directly proportional to the difference between the body temperature and the environment:

$$\overline{q} = h(u)A(u - T_r), \tag{3.19}$$

where $h(u)$ is the heat transfer coefficient ($\mathrm{W\,m^{-2}\,K^{-1}}$), $A \in \mathbb{R}$ is the area of the surface, $T_r \in \mathbb{R}$ is the room temperature, or, more generally, it is also called

sink temperature, the prescribed temperature of the environment surrounding the body [188]. When the Neumann boundary conditions are coupled with the Newton's law of cooling, these conditions are usually referred as *Robin condition*.

For the simulation of a single-pass laser scan on a plate the domain side length can be choosen as $l_w = 2 \times 10^{-2}$ m, and its thickness $t_w = 3 \times 10^{-3}$ m. The geometrical domain Ω can be approximated with a mesh composed by 150000 3D 8-node linear isoparametric element (DC3D8), with a side dimension of 2×10^{-4} m, for a total of 163216 nodes.

3.1.4 Heat transfer in a cube of Ti-6Al-4V

For a cube, representing a small subset of a component, the simulation domain can be called Ω. One part of this domain can represent the powder bed and another part the substrate, and thus the whole domain can be divided into two portions:

$$\Omega_p = \{x, y, z : x \in (0, l_x),\ y \in (0, -h_p),\ z = (0, l_z)\}, \tag{3.20}$$

$$\Omega_s = \{x, y, z : x \in (0, l_x),\ y \in (-h_p, -h_p - l_y),\ z = (0, l_z)\}, \tag{3.21}$$

where l_x, l_y, l_z are the sizes of its sides, and h_p is the thickness of the deposition layer. Both domains are such that $\Omega_p \cup \Omega_s = \Omega$ and $\Omega_p \cap \Omega_s = \emptyset$. In addition, the deposition layer can be further subdivided, taking into account the removal of the fabricated layer from the entire powder bed. This can be mathematically expressed by defining a final deposition subset $\Omega_{p,f} \subset \Omega_p$, which is:

$$\Omega_{p,f} = \{x, y, z : x \in (l_r, l_x - l_r),\ y \in (0, -h_p),\ z = (l_r, l_z - l_r)\}, \tag{3.22}$$

where l_r is the side length of the portion removed. Therefore, at the end of the simulation, only $\Omega_{p,f} \subset \Omega_p \subset \Omega$ can be taken into account for the residual stress estimation. The result of this discussion is better elucidated in Figure 3.3, where the geometry of the domain and its size is represented. The geometrical

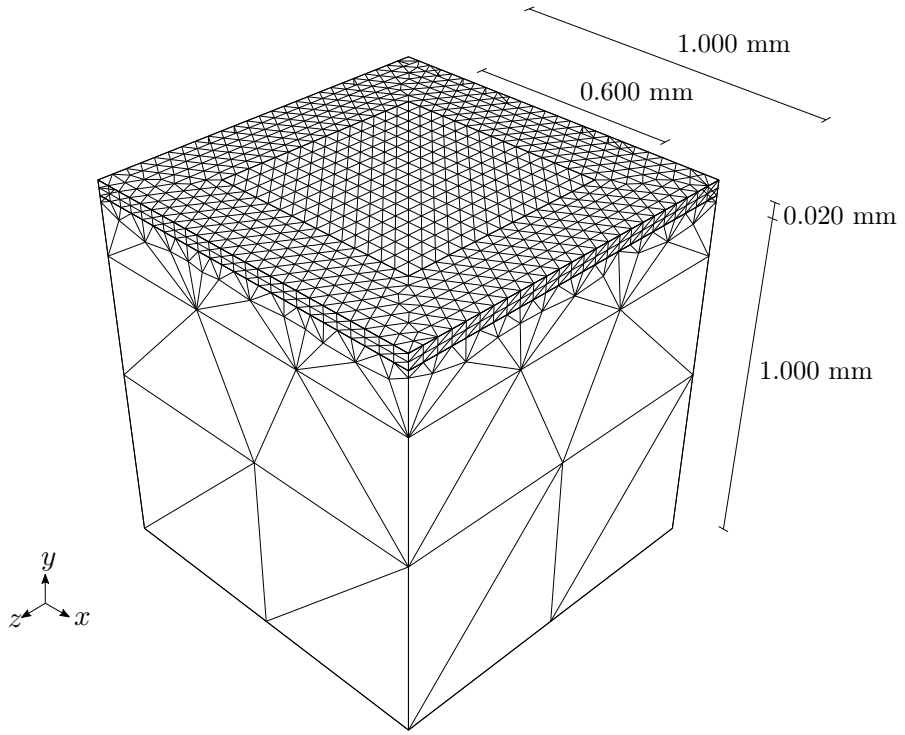

FIGURE 3.3: Tridimensional finite element model mesh and sizes of the reference volume element used for the multi-pass and multi-layer additive manufacturing process model.

parameters assume the following values: $l_x = l_y = l_z = 1$ mm, $l_r = 0.20$ mm, $h_p = 20$ µm. It can be distinguished the substrate in the lower zone where there is a higher mesh size.

3.1.5 Finite element model set-up, domain and time discretization

The exact solution of the Equation (3.7), together with the initial condition (Equation (3.8)) and boundary conditions (Equations (3.10) and/or (3.11)), poses several different mathematical complications. The finite element method permits to solve a partial differential equation in an approximate way, by redefining the problem in the so-called *weak* or *variational form*. For many differential problems

in physics, a variational principle exists and it is so possible to define a functional, but for most cases, as for non-linear heat transfer problems in complex domains, this solution does not exist. Nevertheless, it is still possible to define a variational principle even in absence of a functional, through the form of least-squares principle of the method of weighted residuals, and so use the finite element method [189]. Given the new variational formulation so defined, indeed, the way of identifying an approximate solution is also known as the *Galerkin method* [190]. This high flexibility of the finite elements formulation, along with the increased computational capacity over the years, allowed the birth and proliferation of several commercial codes.

The heat model described so far has been so implemented within the commercial finite element software SIMULIA/Abaqus [181], with the non-uniform distributed flux, variable with position and time, defined in the external DFLUX subroutine [181, vol. III, pp. 24.2.3-1–3]. The martensite evolution can be calculated using the Koistinen-Marburger model [99], implemented in a HETVAL subroutine [181, vol. III, pp. 24.2.12-1–3], storing the results in additional state variables. Both subroutines were written in Fortran 90 (fixed format) language.

Material model integration and solution scheme

In order to integrate a non-linear material response and so obtain the solution in terms of displacements, the commercial finite element software SIMULIA/Abaqus permits to choose between two solving schemes: Abaqus/Standard, and Abaqus/Explicit [191, 192]. The default solution procedure is the general-purpose Abaqus/Standard, which is also called 'Implicit' [191]. The solution procedure is always decided at the beginning of the analysis, but a more advanced approach, using the two explicit-implicit algorithms sequentially for the same analysis, can also be possible [193].

In an implicit procedure the state at time $t + \Delta t$ is determined on the in-

formation at time $t + \Delta t$, while for the explicit procedure is determined on the information at the previous time t [192]. The implicit scheme of Abaqus/Standard implements the Newton-Raphson integration method to iteratively determine the material state. For the explicit procedure, the forward Euler integration is used [192]. An informative summary of the solution schemes is reported in Table 3.1.

When selecting the algorithm, it is necessary to evaluate in advance its accuracy, efficiency, and stability. Some comparative studies between the two methods have been published in the literature with the aim to investigate the best approach for different computational problems and looking into the literature can be a good approach in selecting the best one for each application [194]. The explicit scheme is more suitable to solve dynamic problems in deformable bodies with high non-linearity, such as impact and blast problems, for which it was originally designed, or for solving contact problems [191, 192]. Therefore it is more efficient for these applications, even though it can be used for different problems [192]. Additionally, in terms of efficiency, in most of the computational studies in welding or additive manufacturing, the Abaqus/Standard, or Implicit, scheme has often been selected. In particular, this was also the choice used for uncoupled thermal analysis of Ti-6Al-4V [195]. This choice seems to be dictated by the long computational time specifically involved in residual stresses calculations using the Explicit mode [184]. In terms of stability, the main advantage is obtained using the Explicit mode for particular sets of problems as those already mentioned [192, 196]. Abaqus/Standard and therefore the Implicit scheme with the Newton-Raphson algorithm, has been selected for the numerical simulations carried out.

Element types and shape functions

As summarised in Figure 3.4, it is possible to use solid elements to approximate the tridimensional geometry of the domain in a finite element analysis. Moreover,

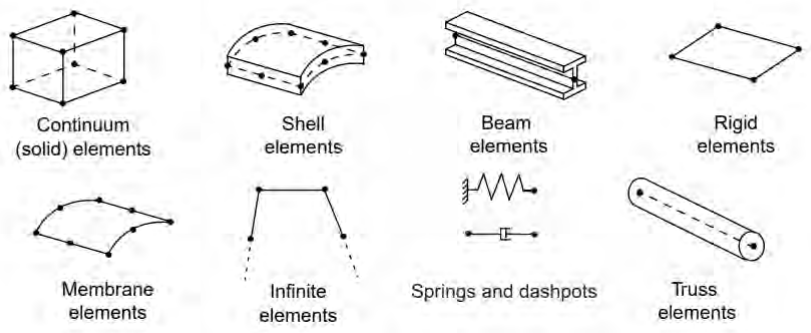

FIGURE 3.4: Families of finite elements. Image reproduced from [191, p. 3-2, fig. 3-1].

Solution scheme	Time information used	Solution algorithm	Iterations
Abaqus/Standard = Implicit	$t + \Delta t \rightarrow t + \Delta t$	Newton-Raphson	Yes
Abaqus/Explicit	$t \rightarrow t + \Delta t$	Forward Euler	No

TABLE 3.1: Summary of the solution schemes used by the commercial finite element software SIMULIA/Abaqus.

once selected the appropriate solution scheme, implicit or explicit, it is possible to have access to the element library, which is wider in case of Abaqus/Standard [191, p. 3-4]. This library of element is summarised in Figure 3.5, where the faces and nodes are numbered, and they are indicated following a naming convention as shown in Figure 3.6.

Since the domain of interest is a portion of a square cuboidal plate, as defined in Equation (3.12) and represented in Figure 5.4, the solution of the heat transfer problem can be obtained discretising the domain with continuous brick solid elements, or hexahedrons, named DC3D8 in SIMULIA/Abaqus, because they exhibits faster solution convergence with respect to the tetrahedral elements [198]. However, for more complex domains as the one represented in Figure 3.3 a tetrahedral element, named C3D4T in SIMULIA/Abaqus, is more suitable than the hexahedron, because it has excellent geometric adaptability [198]. A summary of the element types used in the simulations presented is reported in Table 3.2. To each element type is associated a set of interpolation functions, which

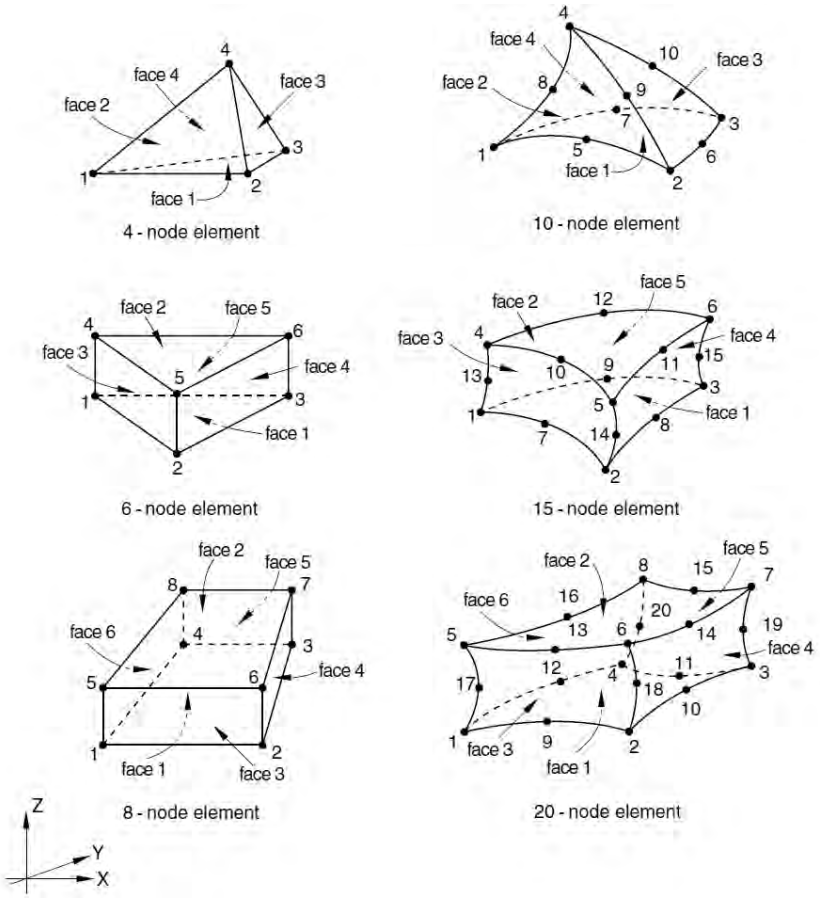

FIGURE 3.5: Elements available in Abaqus/Standard. Image reproduced from [197, p. 25.1.4–17].

are continuous polynomial functions having continuous derivatives [199]. For the hexahedron the shape functions are the following:

$$\begin{aligned} N_1 &= \frac{1}{8}(1-\xi)(1-\eta)(1-\zeta); \qquad N_2 = \frac{1}{8}(1+\xi)(1-\eta)(1-\zeta); \\ N_3 &= \frac{1}{8}(1+\xi)(1+\eta)(1-\zeta); \qquad N_4 = \frac{1}{8}(1-\xi)(1+\eta)(1-\zeta); \\ N_5 &= \frac{1}{8}(1-\xi)(1-\eta)(1+\zeta); \qquad N_6 = \frac{1}{8}(1+\xi)(1-\eta)(1+\zeta); \\ N_7 &= \frac{1}{8}(1+\xi)(1+\eta)(1+\zeta); \qquad N_8 = \frac{1}{8}(1-\xi)(1+\eta)(1+\zeta); \end{aligned} \tag{3.23}$$

where $-1 \leq \xi \leq 1$, $-1 \leq \eta \leq 1$, $-1 \leq \zeta \leq 1$ are the so-called *parent coordinates* [199]. The shape function for the tetrahedron, in natural coordinates, are given

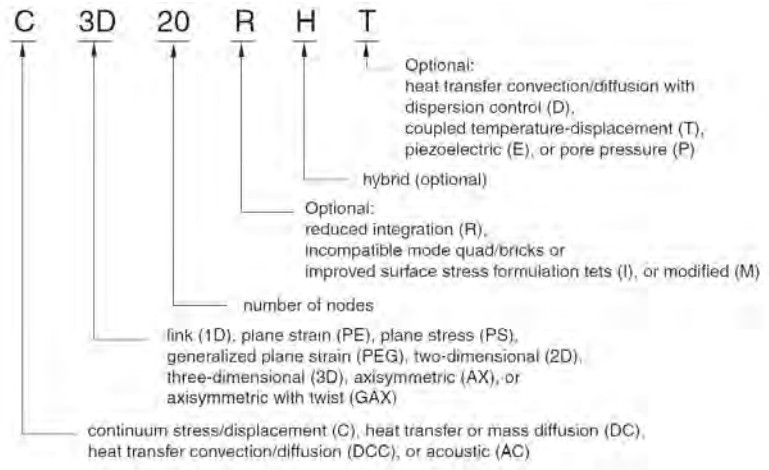

FIGURE 3.6: SIMULIA/Abaqus naming convention for the elements. Diagram reproduced from [197, p. 25.1.1–12].

Simulation	Element name	Element description
Single-pass (thermal analysis only)	DC3D8	3D 8-node linear brick hexahedron
Single-pass (fully coupled thermal-stress analysis)	C3D8T	3D 8-node linear brick hexahedron
Double-pass (thermal analysis only)	DC3D8	3D 8-node linear brick hexahedron
Multi-pass (fully coupled thermal-stress analysis)	C3D4T	3D 4-node linear tetrahedron

TABLE 3.2: Summary of the element types selected for the simulations in the present work.

by:

$$N_i(x, y, z) = \frac{1}{6V}(a_i + b_i x + c_i y + d_i z), \tag{3.24}$$

with $i = 1, 2, 3, 4$ and where V is its volume [199, p. 162].

Time discretisation

For a time-dependent analysis, other than spatial discretisation, it is necessary to discretise the equation in time, as it happens for Equation (3.7). SIMULIA/Abaqus permits to define four time values: the initial increment, the time period, the minimum increment, and the maximum increment. The time period

is the total simulation time, while the other values are the input for the algorithm, which automatically adjust the time incrementation, unless a constant increment is specifically selected.

The simulations carried out in the present work use an automatic time incrementation. Having fixed the laser speed in the Fortran 90 (fixed format) DFLUX subroutine, the total time was calculated starting from this information and the laser track length, according to the definition of speed as distance covered in time.

The single-pass model simulation time was subdivided into two steps: *Heating* and *Cooling*. The total simulation time in the multi-pass model has been subdivided into three steps, named *Heating1*, *Heating2* and *Cooling*. The first one describes the first linear track of the laser, the second one the second linear track and the last one the cooling process, during which the heat source is switched off by defining $Q = 0$ in Equation (3.7).

3.1.6 Thermal and mechanical temperature-dependent material behaviour: bulk material

Numerical solution of the thermo-mechanical problem for additive manufacturing requires knowledge of material specific parameters and behaviour. Since the accuracy of the results will depend on their numerical value, a preliminary review of material data in the literature can be carried out. However, it was found that reported values of thermo-physical parameters for titanium alloys showed a considerable scatter and was limited in the temperature range and there is very little thermo-mechanical data near and after the melting point. Additionally, they can be also calculated with JMatPro®, an acronym for *Java-based Materials Properties* software, a simulation software that enables the user to predict general material properties for multi-component alloys, taking into account also the mass percentage of constituents [200, 201].

In some cases, the behaviour predicted by JMatPro® differed from the mea-

surements or models reported in the literature. While the results of JMatPro® may be more realistic, as for the rapid decay of the Young's modulus near the melting point – justified by the fact that the material is no more solid and therefore has no elasticity at all – the choice adopted by several scholars is more conservative in terms of numerical stability, because a rapid increase or decrease in a portion of the finite element model, as happens in the melt pool area, can lead to discontinuity zones where the material has significantly different behaviour.

After the collection of data is completed, it is possible to use a best-fit approximation procedure in order to find a suitable approximation of the given set of data. JMatPro® data can be excluded in this calculation and they can only be used as a visual verification of the assumed behaviour. It is possible to calculate the goodness of fit starting from the 2×2 correlation coefficient matrix, calculated as

$$R = \begin{pmatrix} r_{11} & r_{12} \\ r_{21} & r_{22} \end{pmatrix}, \tag{3.25}$$

where each element is called product-moment correlation coefficient (or Pearson correlation coefficient), and the generic off-diagonal element is given by

$$r_{ij} = \frac{\sum_{k=1}^{n}(x_k - \bar{x})(y_k - \bar{y})}{\sqrt{\sum_{k=1}^{n}(x_k - \bar{x})^2 \sum_{k=1}^{n}(y_k - \bar{y})^2}}, \tag{3.26}$$

where $\bar{x}$, $\bar{y}$ are respectively the average values of x_k and y_k, and n is the number of available points. This coefficient is such that $-1 < r_{ij} < 1$, where 1 indicates a full relationship between variables, 0 a neutral, and -1 a not strong relationship [202]. The coefficient of determination, also known as *R-squared*, is a statistical measure of how well the fit equation approximates the data points from the literature. This parameter is a measure of uncertainty, being defined as proportionate reduction in uncertainty [202]. It is determined as $R^2 = {r_{ij}}^2$, with $i \neq j$, and it ranges from 0 to 1. Whilst this measure is valid in the case of standard linear regression, its application to non-linear regression models can generally lead to values outside the $[0, 1]$ interval [203]. The only exception is the use of a non-linear least squares

procedure, which has been chosen in the present work when a linear relation was not suitable to represent the data.

For each parameter is below reported the result of the analysis, together with the bibliographic references and a graph representing both the data found in the literature and the temperature-dependent behaviour assumed in the present work, calculated by a best-fit procedure in Python language with the coefficient of determination indicated.

Mass density (ρ)

Mass density has been measured for the solid and the liquid alloy up to 1880 °C with an accuracy of 3% ([204] = ref. 1) and up to the smaller value of 1997 K with an accuracy of 1% ([205] = ref. 2). In other contexts, the given behaviour has been used to model with finite elements a deposition process ([206] = ref. 3), a selective laser melting process ([207] = ref. 4), and a laser assisted machining ([208] = ref. 5). The fit equation found is

$$c_p(T) = c_1 + c_2 T, \tag{3.27}$$

where $c_1 = 1.97 \times 10^{-1}$ and $c_2 = 4.47 \times 10^3$ for $T \leq T_m$, and $c_1 = -1.64$ and $c_2 = 6.82 \times 10^3$ for $T > T_m$. The data and the behaviour assumed in the present work are represented in Figure 3.7, whilst the bibliographic references are the following:

- ref. 1 = Mills [204, p. 212], plot, fig. 1 (the data are also tabulated at p. 217, tab. 1);
- ref. 2 = Li, Johnson, and Rhim [205, p. 111913-2], plot, fig. 2;
- ref. 3 = Nikam and Jain [206, p. 3], plot, fig. 1c;
- ref. 4 = Park and Ansari [207, p. 6], tabulated data, tab. 2;
- ref. 5 = Sim and Lee [208, p. 1720], tabulated data, tab. 2.

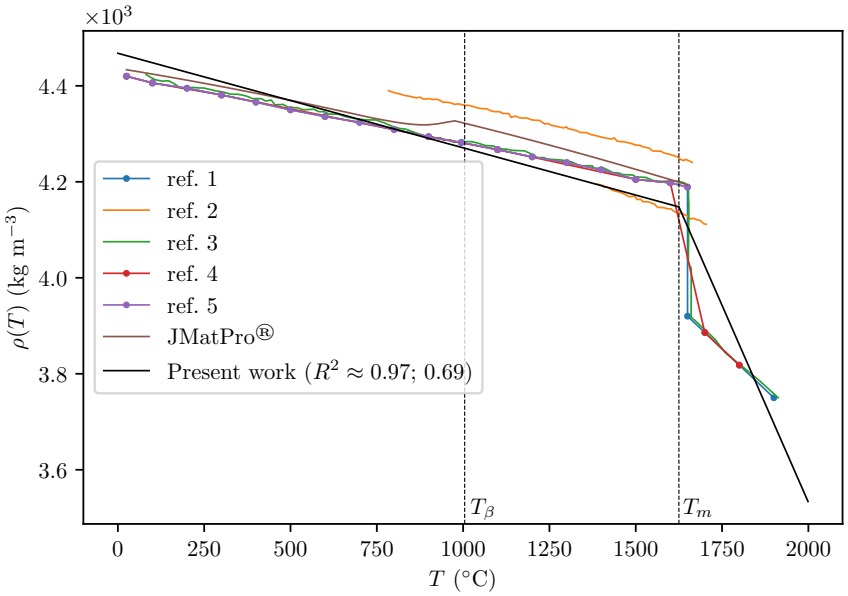

FIGURE 3.7: Comparison of the temperature-dependent mass density ρ of Ti-6Al-4V with the data reported in the literature. The references are the following: ref. 1 = [204, p. 212], ref. 2 = [205, p. 111913-2], ref. 3 = [206, p. 3], ref. 4 = [207, p. 6], ref. 5 = [208, p. 1720].

Specific heat capacity (c_p)

This parameter has been successfully implemented in an arc deposition process finite element simulation ([206] = ref. 1), in a selective laser melting simulation ([207] = ref. 2), and in a laser assisted machining simulation ([208] = ref. 3). Only in the first reference NIKAM and JAIN [206] the behaviour was sensibly different from the others, especially below 1000 °C, where the values assumed were about 1/3 of the others. Moreover, in the same study, there is a sudden and vertical increase of the value around the melting point. No explanation has been given by the scholars for the adoption of such material description in this report. A difference is found also in the data calculated by JMatPro®, where a rapid increase of the specific heat capacity near the β-transus temperature is predicted, and the value becomes double after an increment in the temperature

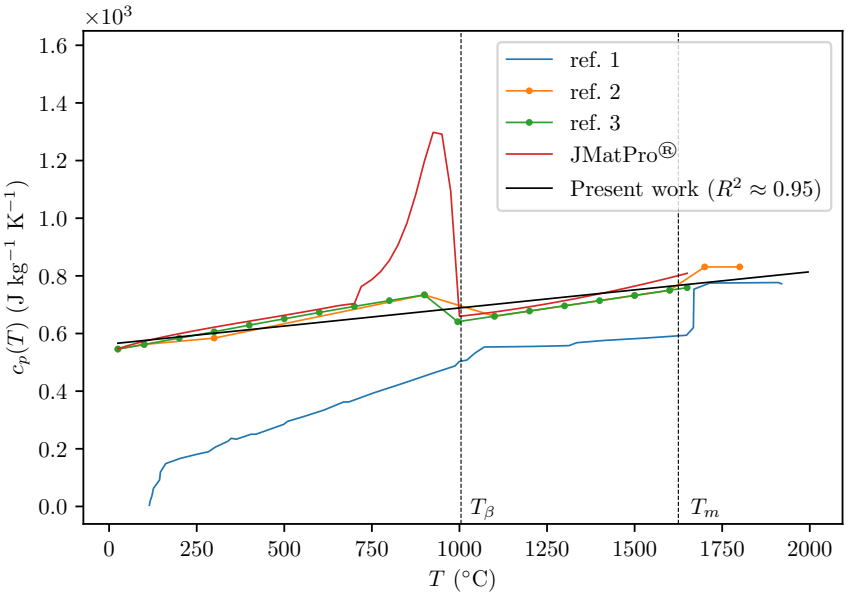

FIGURE 3.8: Comparison of the temperature-dependent specific heat capacity at constant pressure c_p of Ti-6Al-4V with the data reported in the literature. The references are the following: ref. 1 = [206, p. 3], ref. 2 = [207, p. 6], ref. 3 = [208, p. 1720].

of about 200 °C. The fit equation found is

$$c_p(T) = c_1 + c_2 T, \tag{3.28}$$

where $c_1 = 1.25 \times 10^{-1}$ and $c_2 = 5.63 \times 10^2$. The data and the behaviour assumed in the present work are represented in Figure 3.8, whilst the bibliographic references are the following:

- ref. 1 = NIKAM and JAIN [206, p. 3], plot, fig. 1a;
- ref. 2 = PARK and ANSARI [207, p. 6], tabulated data, tab. 2;
- ref. 3 = SIM and LEE [208, p. 1720], tabulated data, tab. 2.

Thermal conductivity (k)

The thermal conductivity property has been derived in a fundamental study of thermal and electrical properties related to the process of electrical discharge

machining ([209] = ref. 1) as well as it has been adopted to the machining process-investigation ([210] = ref. 2), in laser welding of dissimilar materials ([211] = ref. 4), and in selective laser melting ([212] = ref. 3 and [207] = ref. 6). Only in one numerical study of selective laser melting it has been assumed a extremely huge and sudden increase after the melting point, reaching four times the value before it ([207] = ref. 6), whereas a smaller increase it has been given in another study ([204] = ref. 5). On the other hand, it has been observed by direct measurements that the thermal conductivity of an additive manufactured part is slightly higher than its wrought counterpart, especially when it is approaching the β-transus temperature. Ignoring the data after the melting point in the fitting procedure, in order to obtain a better fit for the whole domain of data, represented by a higher R^2, the linear thermal expansion can be represented by the best-fit equation

$$k(T) = c_1 T + c_2, \tag{3.29}$$

where $c_1 = 1.42 \times 10^{-2}$, and $c_2 = 6.41$. The data and the behaviour assumed in the present work are represented in Figure 3.9, whilst the bibliographic references are the following:

- ref. 1 = Fonda, Wang, Yamazaki, and Akutsu [209, p. 585], plot, fig. 3;
- ref. 2 = Nouari and Makich [210, p. 342], plot, fig. 4;
- ref. 3 = Mertens, Reginster, Paydas, Contrepois, Dormal, Lemaire, and Lecomte-Beckers [212, p. 188], (W1, W2 and AM), plot, fig. 6;
- ref. 4 = D'Ostuni, Leo, and Casalino [211, p. 3], tabulated data, tab. 4;
- ref. 5 = Mills [204, p. 217], tabulated data, tab. 1 (the data are also plotted at p. 214, fig. 4);
- ref. 6 = Park and Ansari [207, p. 6], tabulated data, tab. 2.

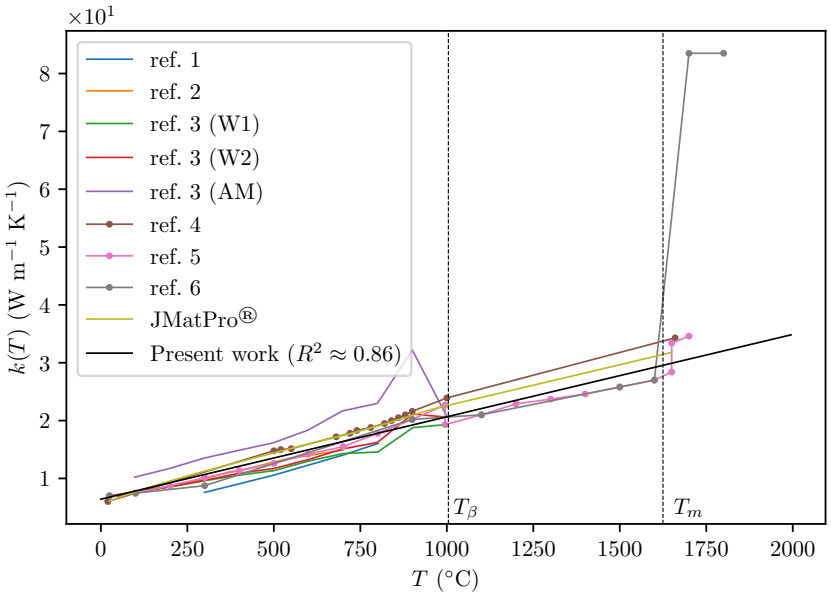

FIGURE 3.9: Comparison of the temperature-dependent thermal conductivity $k(T)$ of Ti-6Al-4V with the data reported in the literature. The references are the following: ref. 1 = [209, p. 585], ref. 2 = [210, p. 342], ref. 3 = [212, p. 188], ref. 4 = [211, p. 3], ref. 5 = [204, p. 217], ref. 6 = [207, p. 6].

Linear thermal expansion (α)

Linear thermal expansion data were used to successfully calculate residual distortions in laser metal deposition ([213] = ref. 1), electron beam welding ([214] = ref. 2), residual stresses at the interface between Ti-6Al-4V and another material when using chemical vapour deposition technique ([215] = ref. 3), residual stresses and strains during selective laser melting ([207] = ref. 4). The fit equation found is

$$\alpha(T) = c_1 + c_2 T, \tag{3.30}$$

where $c_1 = 6.72 \times 10^{-9}$, and $c_2 = 4.10 \times 10^{-6}$. The data from the literature and the behaviour assumed in the present work are represented in Figure 3.10, whilst the bibliographic references are the following:

- ref. 1 = GOLOVIN, VILDANOV, BABKIN, IVANOV, and TOPALOV [213, p. 5],

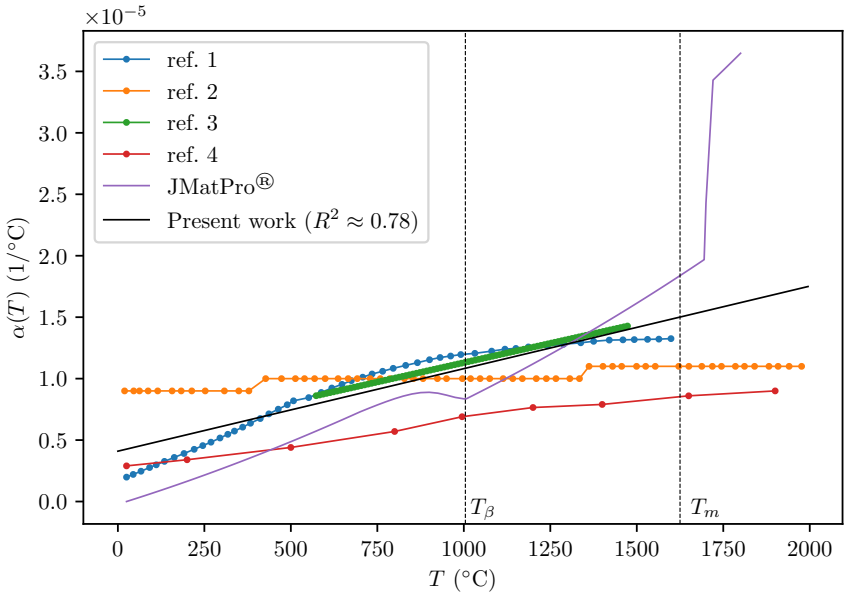

FIGURE 3.10: Comparison of the temperature-dependent linear thermal expansion $\alpha(T)$ of Ti-6Al-4V with the data reported in the literature. The references are the following: ref. 1 = [213, p. 5], ref. 2 = [214, p. 926], ref. 3 = [215, p. 3261], ref. 4 = [207, p. 7].

plot, fig. 6b;

- ref. 2 = XIE, ZHAO, WU, and GONG [214, p. 926], plot, fig. 7b;
- ref. 3 = NIBENNAOUNE, GEORGE, AHZI, RUCH, REMOND, and GRACIO [215, p. 3261], analytical linear interpolation formula ($\alpha(T) = a + bT$, with $a = 6.72 \times 10^{-6}$, $b = 0.63 \times 10^{-8}$), tab. 2 (the function is also plotted in the cited paper, p. 3262, fig. 1);
- ref. 4 = PARK and ANSARI [207, p. 7], tabulated data, tab. 3.

Young's modulus (E)

Whilst in most of the recent studies the Young's modulus is assumed decreasing by approximately 50% between the β-transus and the melting temperature ([216] =

ref. 3) or immediately after the melting temperature in an additive manufacturing simulation ([207] = ref. 4), in one previous experimental study, a drastic decrease between 1173 and 1273 K is reported, just before the β-transus temperature ([217] = ref. 1). However, this has been attributed to the beginning of superplasticity, a phenomenon indicating the deformation of the material beyond its breaking point. The dataset provided by JMatPro® shows too abrupt a change after the melting point in just an interval of few degrees of temperature. This behaviour, in addition to being unrealistic as confirmed by the experimental study just cited ([217] = ref. 1), is not beneficial for a numerical analysis, because it can potentially lead to numerical instabilities. Nevertheless, in all cases the slope of the curve is almost the same. In particular, it can be observed that some scholars made measurements with a new technique to determine the modulus at cryogenic temperatures ([218] = ref. 2). Even if this was clearly out of the range of interest for the purpose of the present study, it is interesting to note that the slope in this temperature range matches those reported in the studies for higher temperatures, to the point that they seem to complete and extend the data of another independent study ([218] = ref. 2). The fit equation found is

$$E(T) = c_1 T + c_2, \tag{3.31}$$

where $c_1 = -5.33 \times 10^{-2}$, $c_2 = 1.11 \times 10^2$. The data and the behaviour assumed in the present work are represented in Figure 3.11, whilst the bibliographic references are the following:

- ref. 1 = Fukuhara and Sanpei [217, p. 1122], plot, fig. 1;
- ref. 2 = Zhang, Nyilas, and Obst [218, p. 887], plot, fig. 5;
- ref. 3 = Pengfei, Shen, Li, and Zhou [216, p. 6], plot, fig. 6a;
- ref. 4 = Park and Ansari [207, p. 7], tabulated data, tab. 3.

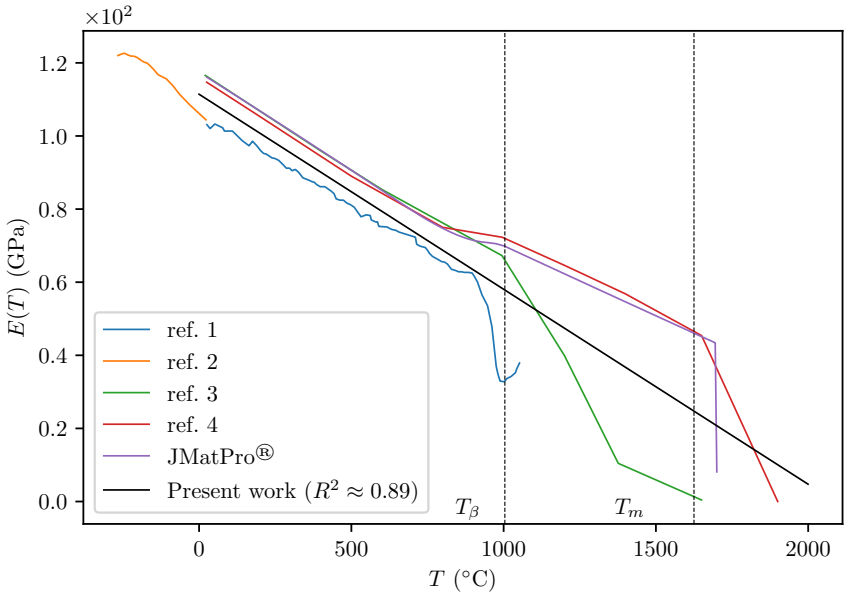

FIGURE 3.11: Comparison of the temperature-dependent Young's modulus $E(T)$ of Ti-6Al-4V with the data reported in the literature. The references are the following: ref. 1 = [217, p. 1122], ref. 2 = [218, p. 887], ref. 3 = [216, p. 6], ref. 4 = [207, p. 7].

Poisson's ratio (ν)

A peak in the Poisson's ratio has been found experimentally, followed by a rapid increase, and it has been related by some scholars to the relief of the shear stress at higher temperatures ([217] = ref. 1), possibly associated with the superplasticity, as already discussed for the Young's modulus. Other thermo-dependent values have been successfully adopted during modelling selective laser melting, in order to calculate residual deformation, stresses, and strains ([216] = ref. 2 and [207] = ref. 3). In one case the behaviour is quite similar to the one predicted by JMatPro® ([207] = ref. 3). The fit equation found is

$$\nu(T) = c_1 T + c_2, \tag{3.32}$$

where $c_1 = -1.97\times10^{-1}$ and $c_2 = 4.47\times10^{3}$ for $T_r < T < T_m$, and $c_1 = -1.64$, and $c_2 = 6.82\times10^{3}$ for $T_m < T < 2000$ °C. The data and the behaviour assumed in the present work are represented in Figure 3.12, whilst the bibliographic references

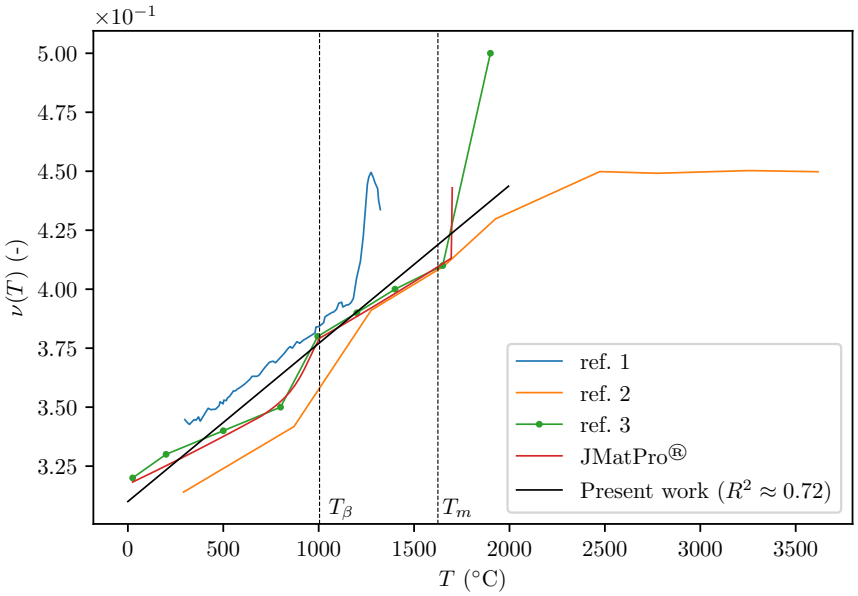

FIGURE 3.12: Comparison of the temperature-dependent Poisson's ratio $\nu(T)$ of Ti-6Al-4V with the data reported in the literature. The references are the following: ref. 1 = [217, p. 1123], ref. 2 = [216, p. 6], ref. 3 = [207, p. 7].

are the following:

- ref. 1 = FUKUHARA and SANPEI [217, p. 1123], plot, fig. 3;
- ref. 2 = PENGFEI, SHEN, LI, and ZHOU [216, p. 6], plot, fig. 6c;
- ref. 3 = PARK and ANSARI [207, p. 7], tabulated data, tab. 3.

3.1.7 Thermal and mechanical temperature-dependent material behaviour: powder

The physical properties of the aggregate, or bulk, form differ from those of the metal powder. More specifically, the unmelted powder just deposited can be assimilated to a porous medium composed by the particles and gas [219, 220]. Since the correct description of powder properties is crucial when estimating the heat diffusion in a thermal process, a number of studies have recently emerged

trying to define the thermophysical behaviour of metal powder. Among those studies, the thermal conductivity variation with temperature of Ti-6Al-4V powder is the best studied property, whilst less data are available in the literature for specific heat capacity, mass density, and thermal expansion. It is also important to remember that when using a finite element at macroscopic level the powder bed is modelled as a continuum [221].

Thermal conductivity (k)

In general, it is difficult to estimate the thermal conductivity of a metal powder, especially when trying to determine the temperature-dependent behaviour. Given the presence of space between particles, the heat flows through a small contact area between powder particles and therefore the thermal conductivity of the powder is significantly lower than that of the bulk material [220]. This evidence led to the notion of *effective thermal conductivity* [219, 220]. A further confirmation of the difficulty in these studies is given by the evidence that thermal conductivity of some laser powder-bed fusion manufactured samples varies with the laser power [222]. In particular, the thermal conductivity of the solid part after processing varies about in the range 2–8 at 100 $\mathrm{W\,m^{-1}\,K^{-1}}$ at room temperature. This behaviour can be attributed to the different densities of the part, because the thermal conductivity can be expressed by recurring to the thermal diffusivity $D = k/(\rho c_p)$ ($\mathrm{mm^2/s}$):

$$k(T) = D(T)c_p(T)\rho(T), \tag{3.33}$$

where c_p is the specific heat, and ρ is the density [222, 223].

Another possible approach would be studying the thermal conductivity of the powder as an approximation of the porous bulk material. In this case, the effective thermal conductivity $\overline{k}$ is related to the cross-sectional pore fraction ϕ_c [226]:

$$\overline{k} = (1 - \phi_c)k, \tag{3.34}$$

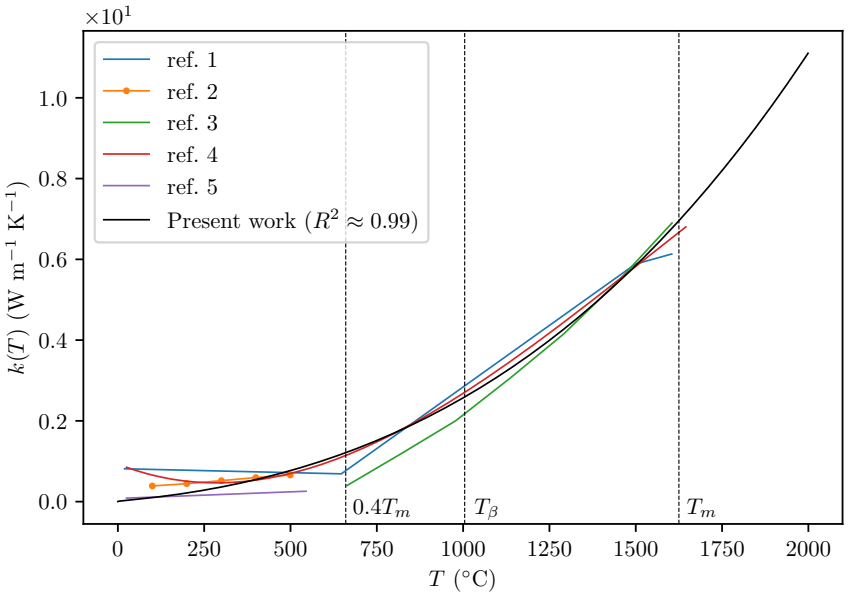

FIGURE 3.13: Thermal conductivity of Ti-6Al-4V powder compared with that of bulk material. The references are the following: ref. 1 = [224, p. 819], ref. 2 = [219, p. 1805], ref. 3 = CHUA, LEE, and AHN [220, p. 262], ref. 4 = RAHMAN, SCHILLING, HERRINGTON, and CHAKRAVARTY [225, pp. 021003–3], ref. 5 = BARTSCH, HERZOG, BOSSEN, and EMMELMANN [223, p. 12].

but then a description of how porosity changes with temperature is necessary. Moreover, after the cooling stage, when grains are formed, the grain size also affects thermal conductivity [226].

According to several studies, thermal conductivity of Ti-6Al-4V powder is almost constant up to 0.4–0.6 T_m, which is a preheating temperature necessary to obtain sintering between particles [220]. After the particles are bonded together, the thermal conductivity is linear with temperature increase [220]. This behaviour founds confirmation in the vast majority of the studies [224, 219, 220, 225, 223]. An exception is also possible, because a higher thermal conductivity increasing linearly from about 2.5 to 10.5 W m^{-1} K^{-1} was also reported [227]. However, this has been excluded from the present analysis, because these values are exceptionally high and too close to those reported for the bulk material. The

shift in behaviour in the range 0.4–0.6 T_m may be explained as due to the agglomeration of fine particles that start gradually sintering to adjacent particles at lower temperature [228, p. 478].

The data and the behaviour assumed in the present work are represented in Figure 3.13, whilst the bibliographic references are the following:

- ref. 1 = Vastola, Pei, and Zhang [224], plot, p. 819, fig. 3;
- ref. 2 = Zhang, Lane, Whiting, and Chou [219], plot, p. 1805, fig. 10a;
- ref. 3 = Chua, Lee, and Ahn [220], tabulated data, p. 262, tab. 4;
- ref. 4 = Rahman, Schilling, Herrington, and Chakravarty [225], equation, p. 021003-3, tab. 1;
- ref. 5 = Bartsch, Herzog, Bossen, and Emmelmann [223], equation, p. 12, eq. 25.

The fitting curve is given by the following equation:

$$k(T) = c_1 \exp(T^{c_2}) \tag{3.35}$$

where $c_1 = 2.68 \times 10^{-3}$, $c_2 = 2.79 \times 10^{-1}$.

Specific heat capacity (c_p)

Little data are available in the literature regarding the specific heat capacity of Ti-6Al-4V powder. A study presents also the volumetric heat capacity, which is given by the product of specific heat capacity and the density [227], but starting from this parameter to calculate the specific heat capacity necessarily requires the density variation of powder with temperature. The data and the behaviour assumed in the present work are represented in Figure 3.14, whilst the bibliographic references are the following:

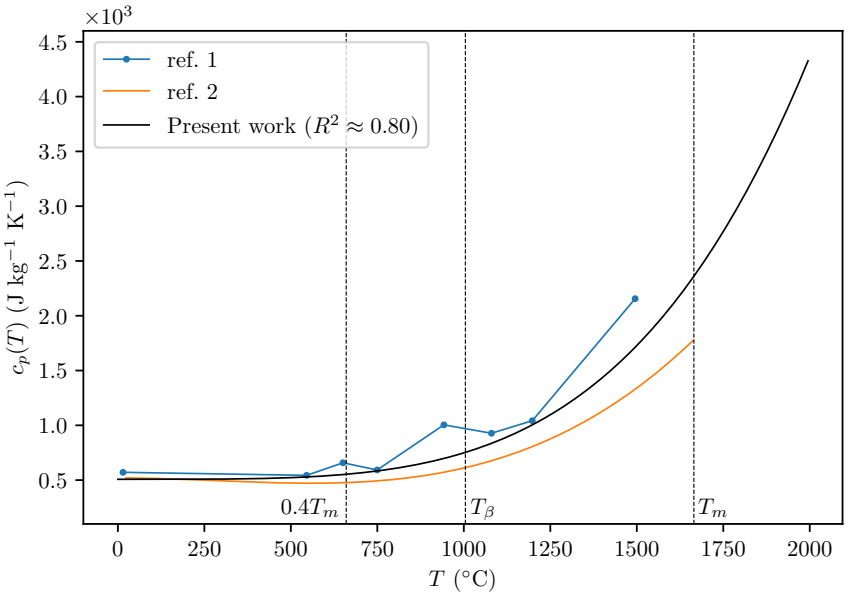

FIGURE 3.14: Specific heat capacity of Ti-6Al-4V powder compared with that of bulk material. The references are the following: ref. 1 = [224, p. 819], ref. 2 = [225, p. 1805].

- ref. 1 = VASTOLA, PEI, and ZHANG [224, p. 819], plot, fig. 3;
- ref. 2 = RAHMAN, SCHILLING, HERRINGTON, and CHAKRAVARTY [225, p. 1805], plot, tab. 1;

The computed fitting curve is given by the following piecewise Equation:

$$k(T) = c_1 T^4 + c_2 \tag{3.36}$$

where $c_1 = 2.41 \times 10^{-10}$, $c_2 = 5.07 \times 10^2$, and it plot is given in Figure 3.14.

Thermal expansion (α)

Thermal expansion of powder is affected by thermal expansion of single particles, but also from the change of porosity deriving from the particles. The volumetric thermal expansion of powder has been expressed as [221]:

$$\alpha_{V,p} = (1 - \phi(T))\alpha_V, \tag{3.37}$$

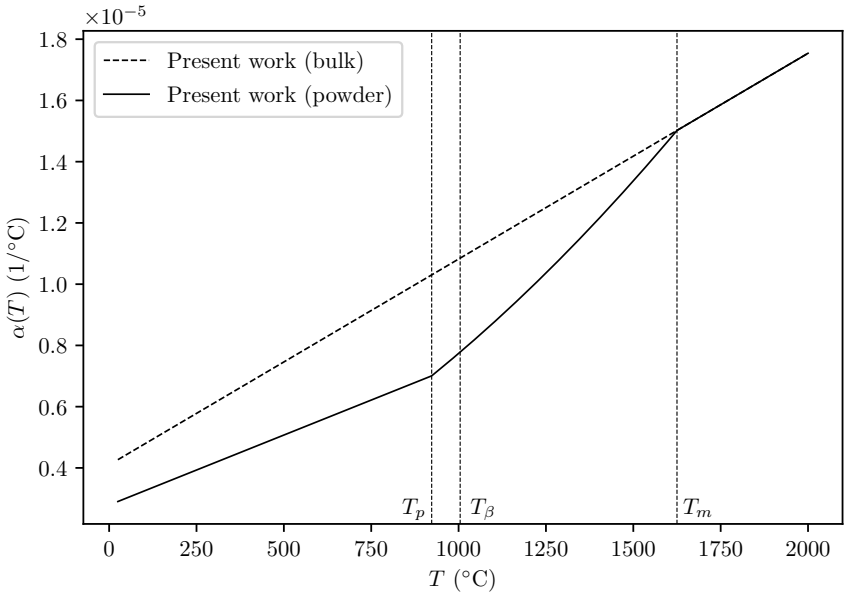

FIGURE 3.15: Linear thermal expansion of Ti-6Al-4V powder compared with that of bulk material.

where α_V is the volumetric thermal expansion of the bulk material and $\phi(T)$ is the temperature-dependent porosity. Assuming that a similar relation is valid for linear thermal expansion, it is possible to rewrite

$$\alpha_p = (1 - \phi(T))\alpha, \tag{3.38}$$

where the porosity term has the following form, supposing that it starts from 0.32 and it reaches almost zero at the melting point [221]:

$$\phi(T) = \begin{cases} 0.32, & T \leq T_p; \\ -4.558 \times 10^{-4} T + 7.407 \times 10^{-1}, & T_p < T < T_m, \end{cases} \tag{3.39}$$

assuming for simplicity that $T_m = 1625$ °C. In Equation (3.39) T_p is the preheating temperature and it has been assumed $T_p = 923$ °C [221]. The linear thermal expansion so obtained is represented in Figure 3.15.

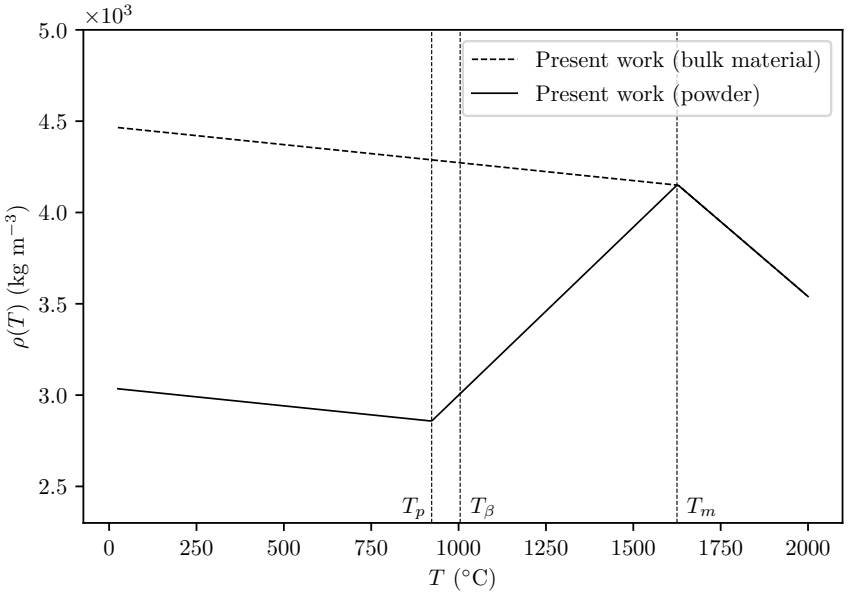

FIGURE 3.16: Mass density of Ti-6Al-4V powder compared with that of bulk material.

Mass density (ρ)

Powder bed density strongly depends on the particles arrangement and voids between them, and, together with thermal conductivity, it influences powder solidification [228]. On the other hand, powder flowability, which is the ability of a bulk of powder particles to move, does not have a significant impact on mass density for Ti-6Al-4V [228]. Similarly to Equations (3.34) and (3.38), the powder mass density ρ_p taking into account the porosity ϕ is given by [225]:

$$\rho_p = (1 - \phi)\rho. \tag{3.40}$$

Therefore, assuming that the porosity term depends on the temperature [221], Equation (3.40) can be rewritten taking into account Equation (3.38). A comparison between the mass density of the bulk material and that of powder is represented in Figure 3.16.

3.1.8 Rate and temperature-dependent constitutive model

Given the numerous constitutive models present in the literature for Ti-6Al-4V, the constitutive model employed in the present study was chosen with the physical characteristics of the mechanical process in mind. Indeed, during the passage of a laser source, the material is subjected to sudden changes in temperature, which will impose a sudden material expansion causing high strain rates. Therefore, an ideal constitutive bond to model this type of phenomena should necessarily take into account these variabilities. In this sense, the most appropriate of those in the literature and examined in this study was that developed by Galindo-Fernández *et al.* (2018), because it takes into account both the strain rate and the temperature variation. Furthermore, in addition to being calibrated on experimental data, it is one of the few models to have a direct dependence on physical microstructure variables, such as the grain size, the initial dislocation density, and, importantly, the martensite size.

The data were provided into the SIMULIA/Abaqus input file (INP) in the form of tables, in which the actual value of the flow stress is function of the strain, the temperature, and strain rate. Tabulated data serve as a discrete approximation of the continuous flow stress curve and the finite element code is able to interpolate between the data points when needed. The data are firstly arranged by the strain rate, then by the temperature and then by the strain value. The discrete values chosen for the approximation of the flow stress are the following:

$$\dot{\epsilon} = \{0.000, 0.001, 0.010, 0.100, 1.000, 10.000, 50.000\}; \tag{3.41a}$$

$$T = \{25, 200, 400, 600, 800, 1000, 1200, 1400, 1500\}; \tag{3.41b}$$

$$\epsilon = \{0.00, 0.01, 0.02, 0.03, \ldots, 0.50\}; \tag{3.41c}$$

where $\dot{\epsilon}$ is expressed in s^{-1} and T in °C.

Since there is no plasticity when the material is completely melted and there-

fore the model is not able to make predictions near that point, for the purposes of a numerical study it is reasonable to assume $\sigma(\epsilon, \dot{\epsilon}, T) = \sigma(\epsilon, \dot{\epsilon}, T_l)$ when $T \geq T_l$, with $T_l \approx 1526$ °C, which leads to $\sigma(T_l) \approx 10.80$ MPa when $\dot{\epsilon} = 10^{-3}$ s^{-1} as can be found numerically.

The input parameters for the Galindo-Fernández *et al.* (2018) model were chosen again by referring to the process and making some assumptions and approximations, starting from the values suggested by the same scholars in their paper. For example, it is well-known that the average grain size of a material varies with the deformation temperature and Ti-6Al-4V is not an exception. It has therefore been chosen to characterise the material α grain size by referring to the similar average grain size value of those calculated by different scholars for different microstructure types at room temperature and reported in [88, p. 355, tab. 3], obtaining $D_\alpha = 6.59$ µm, postponing a more in-depth study of the influence of this parameter on residual stresses. Although the average grain size value seems somewhat higher than that usually assumed for pure titanium and Ti-6Al-4V, it is nevertheless representative of the average behaviour of α grain size evolution, implemented in the constitutive model, during temperature variations, as represented in Figure 3.17. At the same time, an average value for the grain size corresponds to a low flow stress value in both pure titanium and Ti-6Al-4V, as represented in Figure 3.18, potentially leading to values too different from the real ones for the residual stresses. As already mentioned, this analysis is outside the scope of this work and the average value can be considered valid for the time being.

3.1.9 Thermal boundary conditions and heat transfer parameters

The thermal boundary conditions include the prescribed temperature at the substrate and the interaction of the heated surfaces with the surrounding environ-

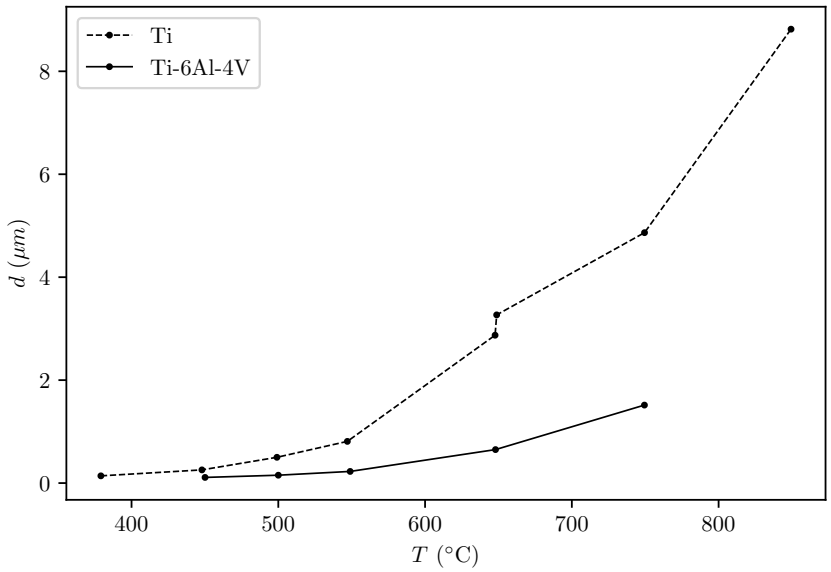

FIGURE 3.17: Temperature-dependent grain size d of pure titanium and Ti-6Al-4V. Data reproduced from [229, p. 964, fig. 3a].

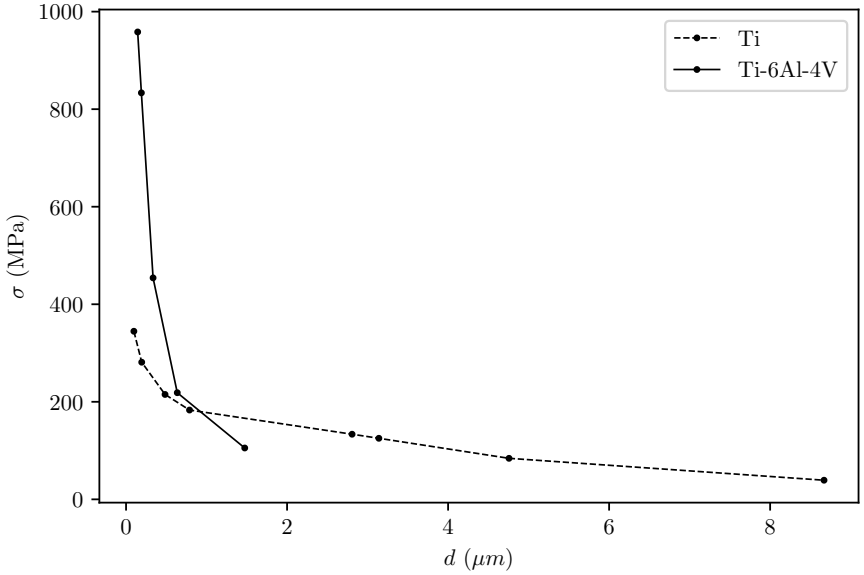

FIGURE 3.18: Grain boundary strengthening, relating the stress value σ with the grain size in pure titanium and Ti-6Al-4V. Data reproduced from [229, p. 964, fig. 3b].

ment.

Heat transfer coefficient

During any thermal process such as additive manufacturing or welding there is a certain amount of heat loss, which occurs through conduction, convection, radiation, and evaporation. Starting from a theoretical calculation, it is possible to prove that in powder-bed-fusion the influence of the heat loss due to the surface radiation and convection is negligible, because it is smaller than the input power by four orders of magnitude [230]. However, they can be mathematically described by a temperature-dependent combined heat transfer coefficient, also called *film coefficient*, as usually done for welding [231, 143]:

$$h(T) = h_r(T) + h_c, \tag{3.42}$$

where h is expressed in $\mathrm{J\,s^{-1}\,m^{-2}\,K^{-1}}$. The radiation term h_r is a monotonically increasing function of the temperature:

$$h_r(T) = \frac{\epsilon\sigma\left(T^4 - {T_r}^4\right)}{T - T_r}. \tag{3.43}$$

In this Equation (3.43), $\epsilon \in [0, 1]$ is the emissivity coefficient, $\sigma \approx 5.670 \times 10^{-8}$ $\mathrm{W\,m^{-2}\,K^{-1}}$ is the Stefan-Boltzmann constant, and T_r is the room temperature. The term h_c is the convective heat transfer coefficient.

Another model recently reported in the literature [232, 188] describes the heat losses due to radiation in selective laser melting of Ti-6Al-4V, using the function

$$h_r(T) = \epsilon\sigma(T^2 + {T_r}^2)(T + T_r). \tag{3.44}$$

Both heat transfer coefficient models for the bulk material produce similar values for temperatures below the β-transus, whilst they differ for higher temperatures, as shown in the Figure 3.20. However, from the equations indicated, it is clear that the knowledge of emissivity is crucial when determining the heat losses.

Emissivity in additive manufacturing of Ti-6Al-4V

Emissivity is a measure representing the ability of the material to emit thermal radiation [233]. The extreme values of the emissivity coefficient are 0 (perfect reflector, also called *white body*) and 1 (perfect emitter, *black body*). However, in the case of real material, it is usually common to talk about *gray body* to indicate that it has an intermediate value.

Determining emissivity is a complex task, mainly because it depends on the surface temperature, wavelength, surface material geometry, oxidation, and even surface pollution [234, 235]. It is generally calculated by the relation

$$T_r{}^4 = \epsilon T_s{}^4, \tag{3.45}$$

where T_r is the radiance temperature, measured indirectly with a pyrometer, and T_s is the surface temperature, usually measured with thermocouples [234].

In the second model expressed by Equation (3.44), the emissivity varies with respect to the temperature, as in the Equation (3.43), but it is defined as a temperature-dependent recursive function:

$$\epsilon(T) = \begin{cases} e(T), & e(T) \leq 1; \\ 1, & e(T) > 1; \end{cases} \tag{3.46}$$

with

$$e(T) = c_1 + c_2 \exp(c_3 T), \tag{3.47}$$

where the fitting constants assume the values of $c_1 = 0.231$, $c_2 = 3.06 \times 10^{-4}$, $c_3 = 7.55 \times 10^{-3}$ and T expressed in degrees Celsius [232].

Since no relation for the emissivity of Ti-6Al-4V metal powder has been found in the literature, and since the temperature-dependent emissivity for both 316L and IN718 powder follows approximately the same behaviour, the discrete data available in the literature have been interpolated starting from Equation (3.46) and using a non-linear fit procedure to recalculate and readapt the coefficients.

Therefore, for the emissivity of metal powder Equation (3.47) is still valid, but with coefficients $c_1 = 2.027 \times 10^{-5}$, $c_2 = 1.312 \times 10^{-2}$, $c_3 = 3.770 \times 10^{-1}$, and the temperature in degrees Celsius. According to this new formula, the maximum emissivity of powder is achieved when $T \geq 787.60$ °C.

The temperature-dependent emissivity function is plotted in Figure 3.19 together with some experimental measurements carried out on both Ti-6Al-4V and other materials. It can be observed that the bulk material, initially having a low emissivity, after around the β-transus temperature behaves approximately like a blackbody, reflecting all the thermal energy.

Convective heat transfer coefficient

As anticipated, the heat losses due to convection and radiation in laser-powder-bed-fusion are negligible. Furthermore, it has been estimated that the heat loss through surface radiation is about five times higher than the loss through convection [230]. In several numerical studies about additive manufacturing of Ti-6Al-4V, the convective term h_c in Equation (3.42) was chosen equal to 10 [236], 18 [237], 20 [232], 80 [238], or 100 $\mathrm{W\,m^{-2}\,K^{-1}}$ [230]. Differently, other authors estimated the coefficient $h_c = 1$ for laser powder-bed fusion of Ti-6Al-4V in surrounding argon [239] or for laser directed energy deposition [240]. However, non-accurate justifications has been given for these values, which seem to be more of an assumption. Additionally, if $h_r \approx 5h_c$ is a valid assumption, the exact temperature at which this relation holds has not been specified. Moreover, a more in-depth study shown that is an increasing function of thermal conductivity of the deposited material and it depends also on the geometry of the final part, and, for Ti-6Al-4V, values around 4–12 were also recommended [241].

Assuming that $h_r \approx 5h_c$ holds at the melting point, since in the first model (Equation (3.43)) $h_r(T_m) \approx 91.50$ and in the second model (Equation (3.44)) $h_r(T_m) \approx 245.88$, then h_c must be bounded in the range 18.30–49.18. On the

other hand, the assumption that the same relation holds at room temperature leads to values that are too small, which, therefore, would roughly correspond to the assumption that $h_c \approx 0$, Indeed, if $h_r(T_r) \approx 1.16$ and $h_r(T_r) \approx 4.52 \times 10^{-4}$, then $h_c = 0.23$ and 9.04×10^{-5}, respectively in the first and second model. An alternative could be considering $h_c = 5h_r$ for any temperature in the interval $[T_r, T_m]$, with the results represented in Figure 3.21, but in this way an indirect dependency of h_c on temperature is introduced and this is not supported by any study at present. Finally, given these considerations, a rounder conventional value $h_c = 20$ can be fixed in the present study both for bulk material and powder.

Ambient or sink temperature during laser powder-bed fusion

As anticipated, in the Equation (3.19) the sink temperature can be considered equivalent to the room temperature. However, during laser powder-bed fusion, this value can be fixed equal to the temperature inside the building chamber, which is equivalent to the temperature of the gas flowing into it. Nevertheless, the temperature of argon, for example, is not fixed, but due to convection in the above region in proximity of the melt pool it can reach up to 800 °C [242]. One of the consequence, is that the powder bed is heated before the laser pass, because the mass of heated gas flows ahead of the laser. However, for the present study, this micro-description of gas heating can be ignored. Additionally, there is no possibility, at present, to implement this feature in Abaqus/Standard, where the only option would be setting a varying discrete *Sink definition* valid for nodes or elements, but fixed during time evolution. Therefore, the assumption $T_r = 25$ °C both for the powder bed and for the substrate can be considered valid, as in recent studies [243].

In the commercial finite element software SIMULIA/Abaqus [181], the heat loss can be described accordingly by using the **Sfilm* option, which refers to the surface-based temperature-dependent heat transfer coefficient defined within

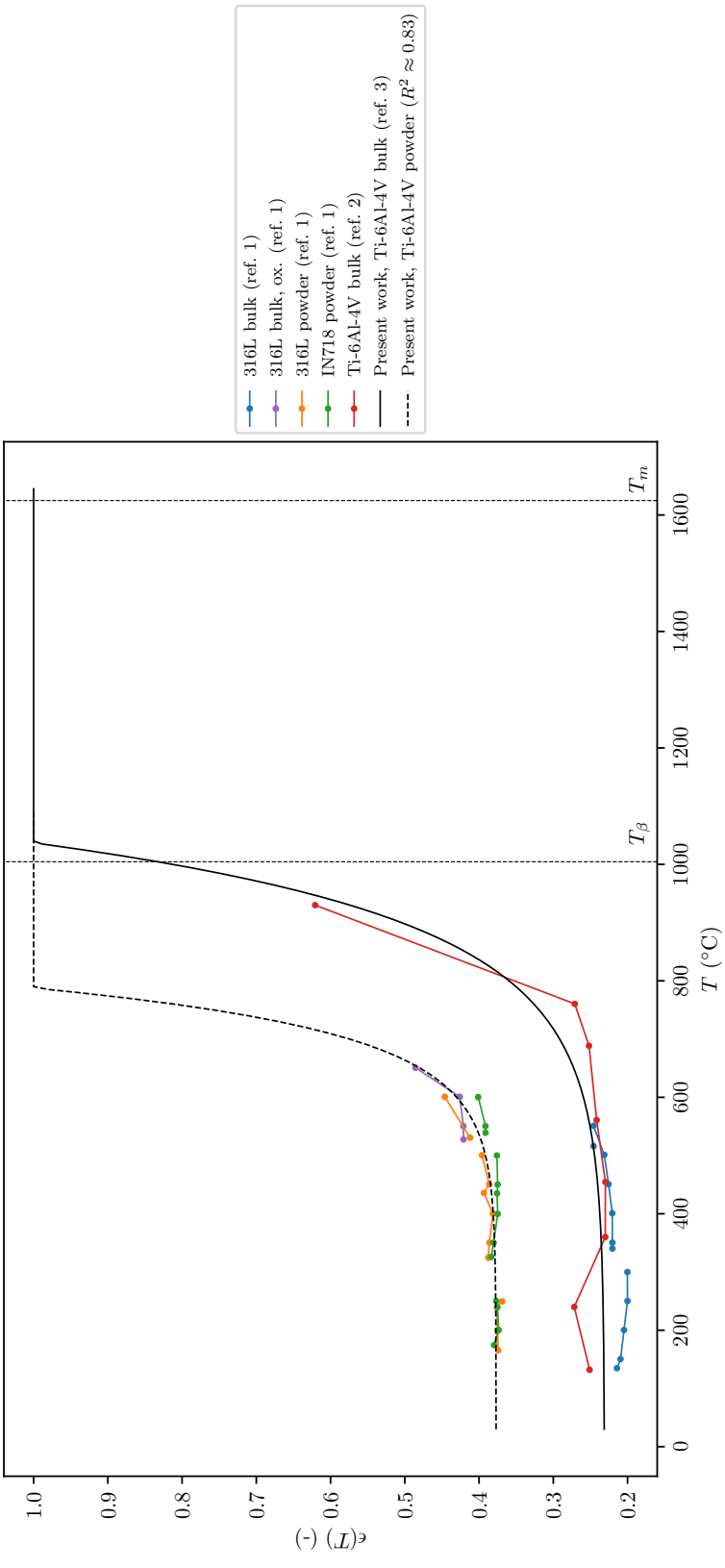

FIGURE 3.19: Emissivity as a function of temperature for Ti-6Al-4V. The references are the following: ref. 1 = [235, p. 21, fig. 15], ref. 2 = [233, p. 2217, fig. 2], ref. 3 = [232, p. 4, fig. 3].

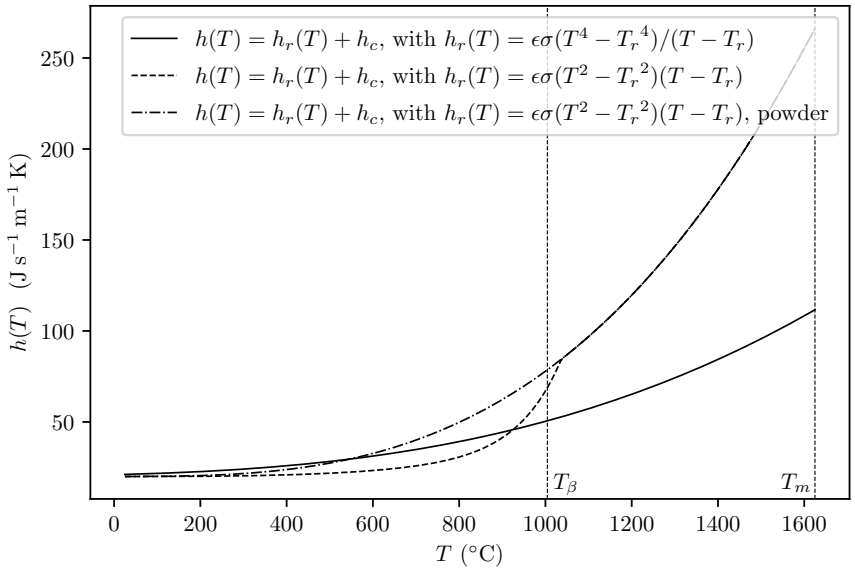

FIGURE 3.20: Comparison between two temperature-dependent combined heat transfer coefficients for Ti-6Al-4V, with different radiation terms. Up to the β-transus temperature both models show a similar trend.

the **Film Property*, which essentially contains a table of discrete values for the coefficients alongside with the temperatures [181, vol. II, p. 18.4.3-4]. In the **Sfilm* option is also possible to specify the sink temperature, which can be made equal to the room temperature [181, vol. II, p. 18.4.3-4].

3.1.10 Definition of a Gaussian moving heat source

The moving heat source can be implemented by defining a Gaussian heat flux per unit volume, with the following equation, valid for any point $x \in \Omega$ and for any time $t \in (0, t_m]$, with t_m maximum simulation time:

$$Q(x, y, z) = \frac{2\eta k_p p}{\pi r^2} \exp\left(-\frac{2d}{r^2}\right), \tag{3.48}$$

where $\eta \in \mathbb{R}$ is the efficiency (adimensional), $k_p \in \mathbb{R}$ is an adimensional calibration parameter, $p \in \mathbb{R}$ is the heat input or laser power density (J s^{-1} m^{-3}), $r \in \mathbb{R}$ is

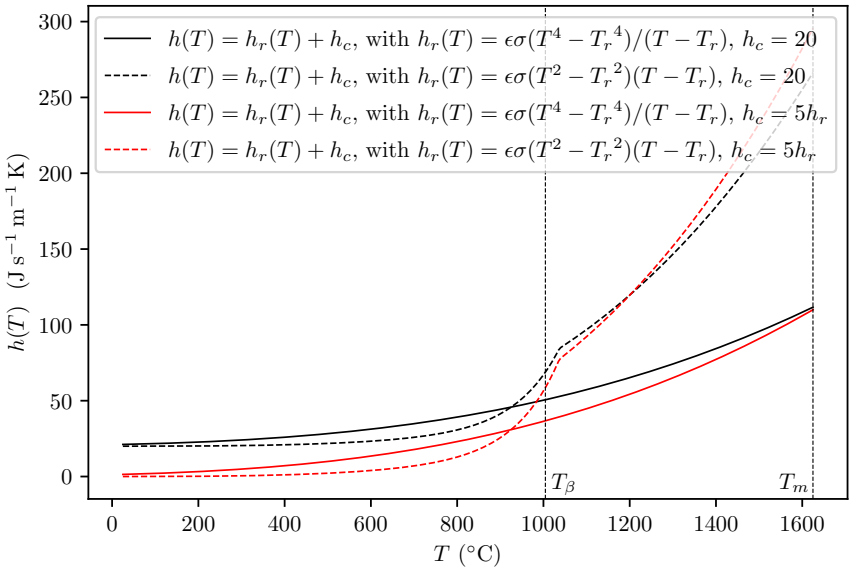

FIGURE 3.21: Comparison between two temperature-dependent combined heat transfer coefficients for Ti-6Al-4V, with different radiation terms for two different assumption about the convective term h_c.

the laser beam radius (m), and d is a function defined as following:

$$d(x, y, z) = (x - x_0)^2 + (y - y_0)^2 + (z - z_0)^2, \tag{3.49}$$

where the initial point of the laser source is described by the coordinates $x_0, y_0, z_0 \in \mathbb{R}$. If the heat source moves only along the z axis, its trajectory is then described by the following equations:

$$x_0 = 0, \tag{3.50a}$$

$$y_0 = 0, \tag{3.50b}$$

$$z_0(t) = z_0 + st, \tag{3.50c}$$

where $s \in \mathbb{R}$ is the laser speed (m s^{-1}). In this way it is introduced a dependence of time and the Equation (3.49) becomes:

$$d(x, y, z, t) = x^2 + y^2 + (z - z_0)^2. \tag{3.51}$$

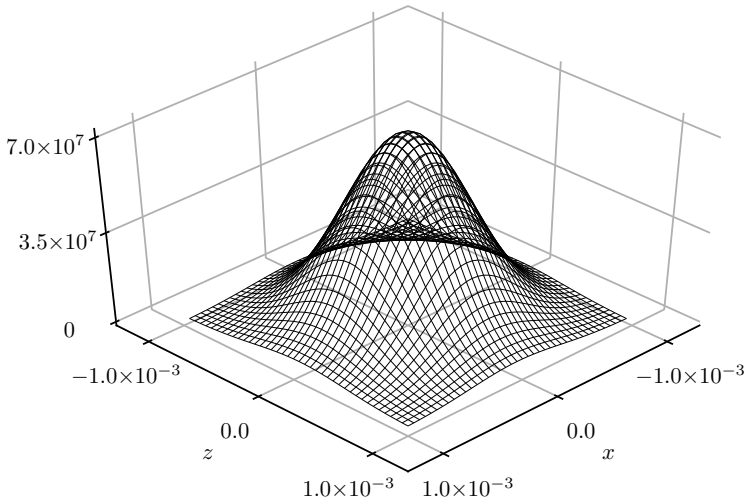

FIGURE 3.22: Tridimensional Gaussian heat source plot at a specific time t as a model for the laser heat source in the additive manufacturing process, with the fixed parameters: $p = 100$ J s^{-1} m^{-3}, $\eta = 0.75$, $r = 0.001$ m, $k_p = 1.00$.

In other words, the distance between the coordinate z at time t and the one coordinate varies with time, so the final expression for the Gaussian heat source, in case of a linear trajectory, is:

$$Q(x, y, z, t) = \frac{2\eta k_p p}{\pi r^2} \exp\left[-\frac{2}{r^2}\left(x^2 + y^2 + (z - z_0)^2\right)\right]. \tag{3.52}$$

For a fixed generic time t, the tridimensional Gaussian heat source model is plotted in Figure 3.22, whilst in Figure 3.23 are shown some cross-sections of this heat source model for different laser power values.

The heat source model can be implemented within SIMULIA/Abaqus by programming a DFLUX Fortran 90 (fixed format) subroutine [181, vol. III, pp. 24.2.3-1–3], which can be able to read the scanning strategy stored in an external text file as a set of points, which runs from the starting to the ending point. This task of accessing this information is performed using a UEXTERNALDB subroutine.

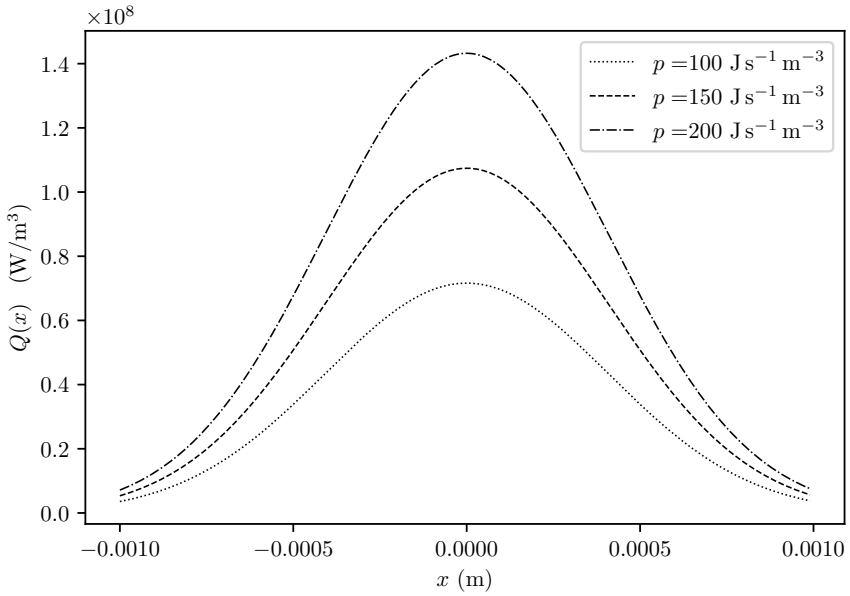

FIGURE 3.23: Cross-section of a tridimensional Gaussian heat source at different laser power values p for a fixed instant of time t. Varying the parameter p permits to control the amount of the heat flux and therefore the laser penetration within the material.

Scanning strategy

The scanning strategy can be illustrated as a definition of the laser's spatial path. The different tracks are spaced by a certain distance and, as is usually the norm, the laser goes from one point to another along a rectilinear path, then back again and so on, following the so-called *zigzag pattern* [244]. Therefore, having decided upon this scanning strategy, according to the hatch spacing value input, the scanning path has been designed to fill the top surface of the finite element model. A similar approach can be used for the subsequent layer, but the paths can be rotated by 90°, as is often the case in SLM to reduce residual stresses [244]. Other scanning strategies exist, but were not considered in this study, going beyond the scope and investigative possibilities of this work. The approach used here for the first and second layer is represented in Figure 3.24.

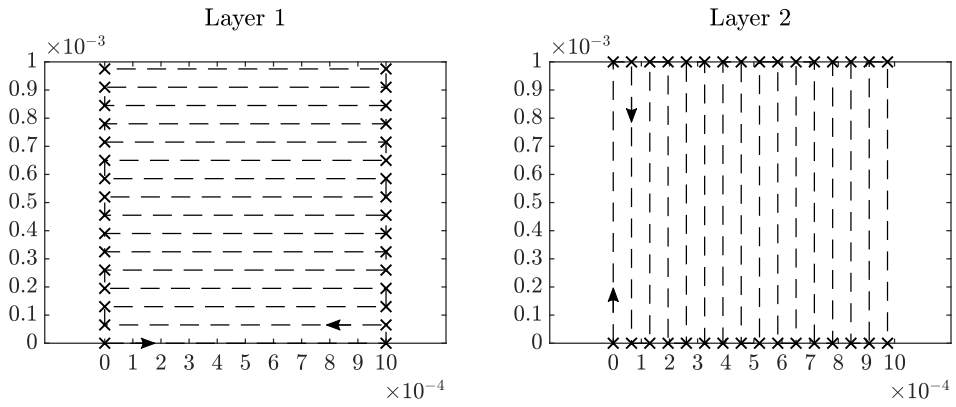

FIGURE 3.24: Typical laser scanning paths for the first and the second layer, in the multi-pass simulation. The arrows indicate the direction of the laser along the path and the crosses indicate the linear path where the laser is turned on or off.

Using a MATLAB® script, the coordinates of the laser were written in a text file, which was subsequently read by the SIMULIA/Abaqus DFLUX Fortran 90 (fixed format) subroutine [181, vol. III, pp. 24.2.3-1–3].

Pre-heating and substrate temperature

In laser powder-bed fusion of Ti-6Al-4V, the substrate temperature usually varies between 70 and 500 °C, and the microstructure so obtained, without any post-heating treatment, gives raise mainly to an α' structure [21]. In order to obtain superior material properties for an as-built part, it is convenient to bound the substrate temperature in the interval $T_s \in [370, 570]$ (°C), where still there is martensite formation. Indeed, it has been recently found this as the best range to obtain higher elongation, and so better ductility, and maximum ultimate tensile stress (above 1200 MPa) in laser powder-bed fusion of Ti-6Al-4V, as represented in Figure 3.25 [245]. Similar values were previously found in a study that combined results from several research studies [21]. Whilst the substrate temperature oscillates during the heat source pass, fixing the temperature at the bottom of the substrate can represent a numerical method to control its minimum. Therefore, the temperature $T_s = 500$ °C can be chosen for the whole duration of the

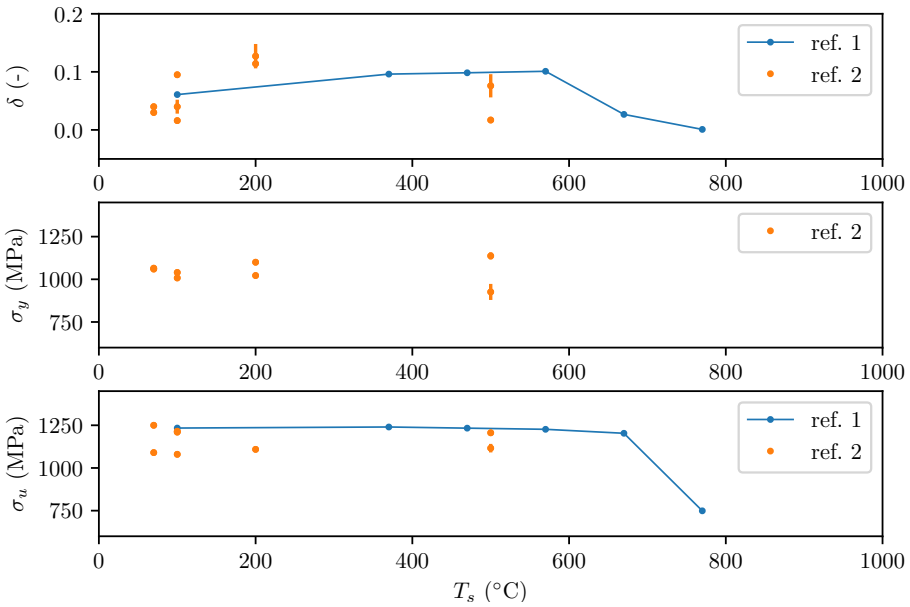

FIGURE 3.25: Elongation, yield stress, and ultimate tensile stress of as-built Ti-6Al-4V specimens for different substrate temperatures T_s. The references from which the data are reproduced are: ref. 1 = [245], ref. 2 = [21].

simulation, which will lead approximately to the following values, grasped from Figure 3.25: $\delta \approx 0.09$, $\sigma_y \approx 1000$ MPa, $\sigma_u \approx 1200$ MPa.

The process of pre-heating consists of bringing the material up to a specified temperature before processing, to control the temperature gradient in the welding area, to reduce the cooling rate and so also to avoid the risk of cracking the material during its processing [246]. It is employed both in welding and in additive manufacturing, and it can be confined to a portion of the material or can be extended to the entire part [246]. The pre-heating temperature can reach up to 300 °C [247]. Small variations are recorded up to 570 °C, as represented in Figure 3.26. However, in terms of residual stresses, a sensible reduction has been found even when the sample has been pre-heated, as reported in [248].

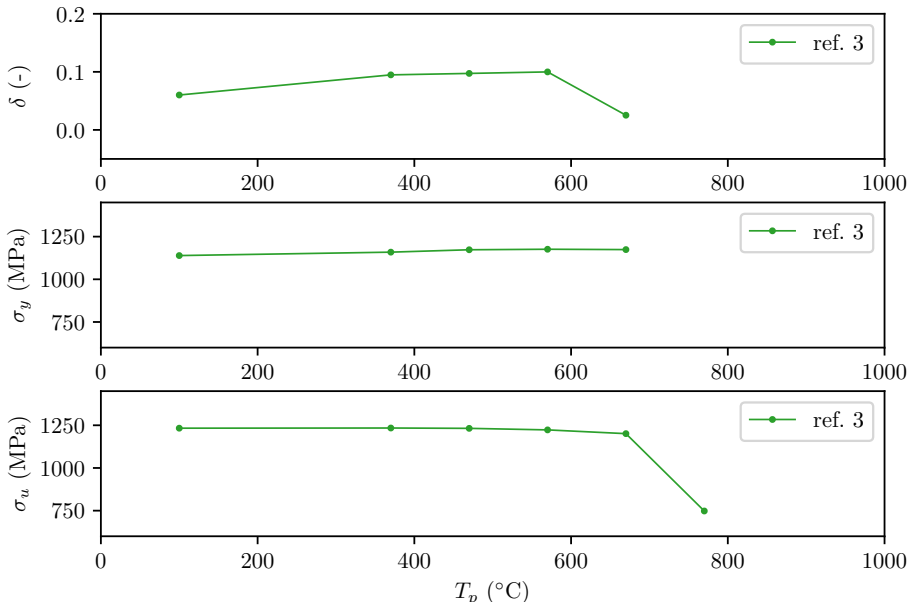

FIGURE 3.26: Elongation, yield stress, and ultimate tensile stress of as-built Ti-6Al-4V specimens for different pre-heating temperatures T_p. The reference from which the data are reproduced is: ref. 3 = [248].

3.1.11 Mechanical boundary conditions, simulation time discretisation, and process model parameters

As seen, a thermo-mechanical model, representing the reference volume element was modelled using finite element technique implemented in the commercial software SIMULIA/Abaqus [181]. The finite element model was constrained at the base, preventing displacements and rotations, in order to represent a fixed substrate, as in reality, which is represented by the coarser mesh in Figure 3.3 and that can be removed at the end of the simulation and other boundary conditions can be implemented as necessary, such as those represented in Figure 3.28.

The mechanical boundary conditions need to be coupled with the proposed scanning strategies, both for the single-layer and for the double-layer model, as in Figure 3.27. Since as seen in Table 2.1 the process parameters for additive manufacturing are in wide ranges, the decision to use realistic parameters similar

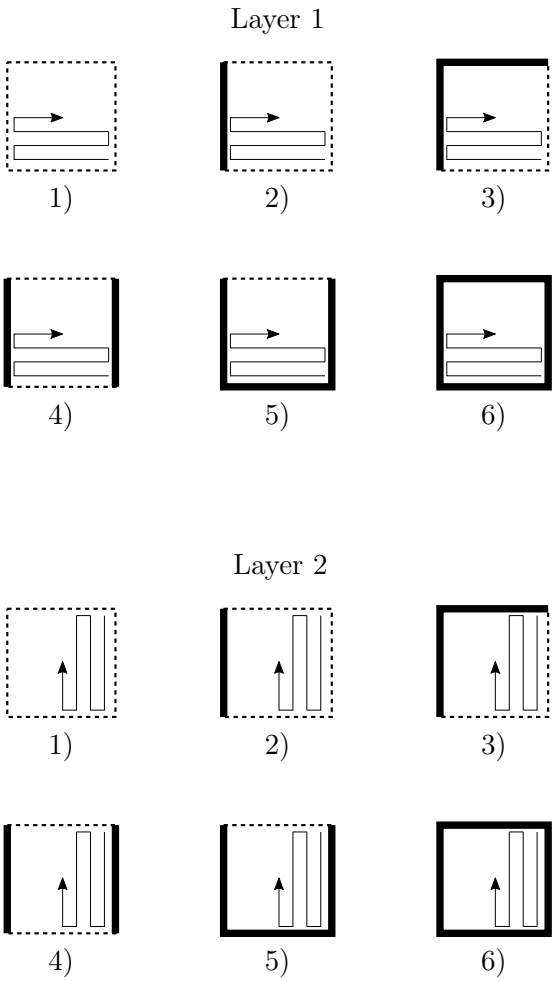

FIGURE 3.27: Diagram illustrating the different boundary conditions coupled with the scanning strategies for the first and second layer. The solid line represents the fixed support (*i.e.* no displacements and no rotations admitted), whereas the dashed line represents the free edge. In all the cases the base of the multi-pass model is considered fixed (*i.e.* no displacements and no rotations admitted).

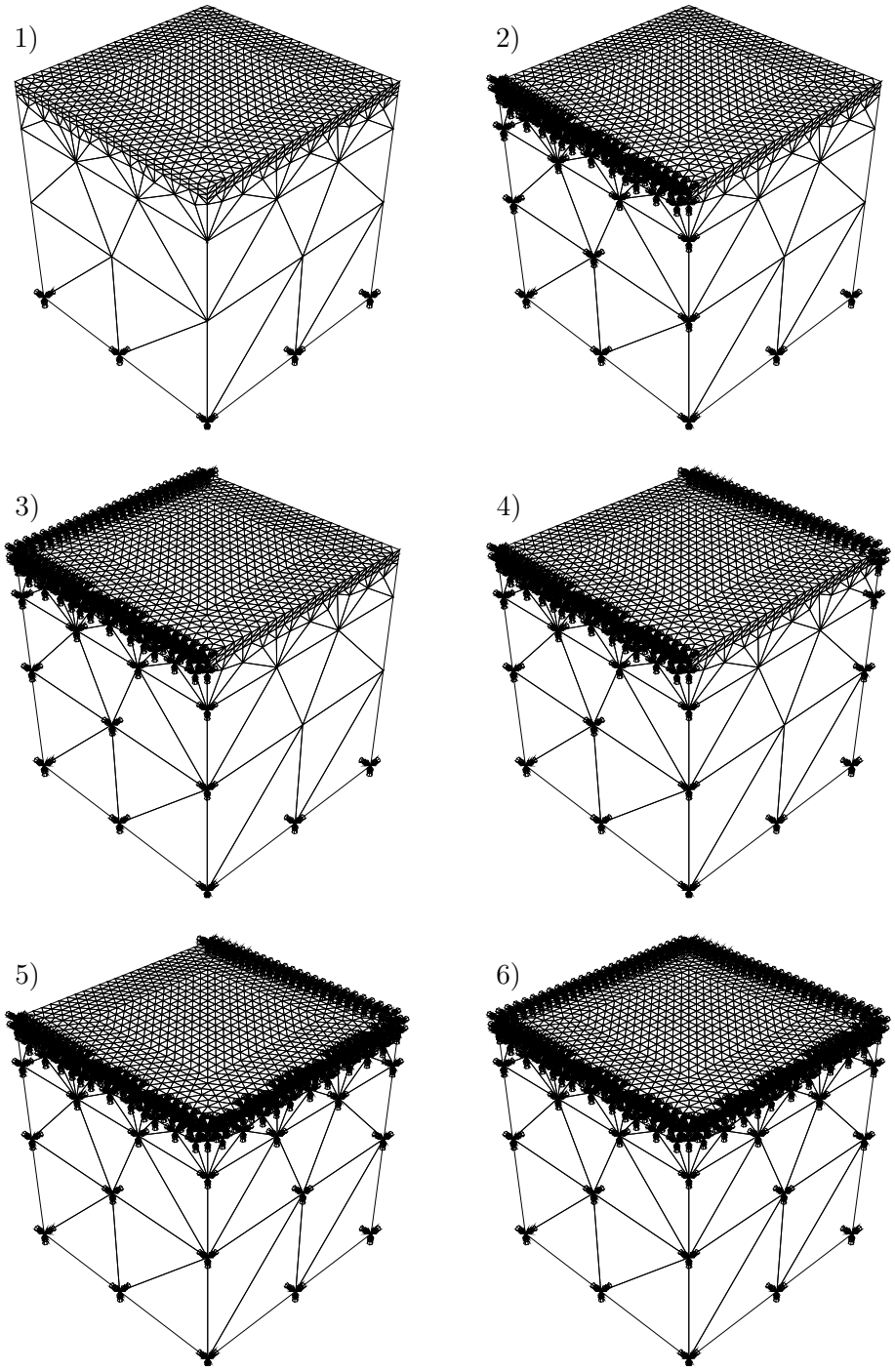

FIGURE 3.28: Illustration of the displacement constraints applied to the sides of the six models, according to the definition of the boundary conditions and the convention adopted in this work.

to those used in SLM of Ti-6Al-4V has been made [244]. Therefore they were the following:

$$s = \{800, 900, 1000, 1100, 1200\} \text{ mm s}^{-1}; \tag{3.53a}$$

$$h = \{60, 70, 80\} \text{ µm}. \tag{3.53b}$$

The simulations were performed by testing all different parameter combinations, with all six boundary conditions described with the layer properties equal to the bulk material. Furthermore, only for the unconstrained single and double layer models using the powder properties, a larger process window were considered and therefore the following processing parameters were used:

$$s = \{200, 400, 600, 800, 1000, 1200, 1400, 1600\} \text{ mm s}^{-1}; \tag{3.54a}$$

$$h = \{40, 60, 70, 80, 100, 120\} \text{ µm}. \tag{3.54b}$$

3.1.12 Simulations steps, time step and time increments definition

The total simulation time has been subdivided into one heating step and one cooling step when the model was composed by one layer, otherwise into two heating steps and two cooling steps interspersed, with each heating-cooling couple associated with one of the two layers. A summary of the typical values for the total time and the time steps used for the multi-pass double-layer model is reported in Table 3.3.

3.1.13 Mesh convergence study

A mesh convergence study is useful to assess the validity of the results, with respect to different boundary conditions, as in Figure 3.29, because these can influence the convergence of the models and the numerical results. In model A (Figure 3.29) all nodes at the base are constrained for both displacements

Step name	Initial (s)	Time period (s)	Minimum (s)	Maximum (s)
heating1	5.00×10^{-5}	8.13×10^{-2}	1.00×10^{-11}	5.00×10^{-5}
cooling1	5.00×10^{-5}	1.00×10^{1}	1.00×10^{-11}	5.00×10^{-1}
heating2	5.00×10^{-3}	8.13×10^{-2}	1.00×10^{-11}	5.00×10^{-3}
cooling2	5.00×10^{-5}	1.00×10^{1}	1.00×10^{-11}	5.00×10^{-1}
Remove_Substrate	1.00×10^{-1}	1.00×10^{-1}	1.00×10^{-6}	1.00×10^{-1}

TABLE 3.3: Typical step times and time increments definition used in SIMULIA/Abaqus for a multi-pass double-layer model.

and rotations; in model B only vertical displacements are constrained for all nodes at the base; in model C only nodes at the four corners are constrained for both displacements and rotations; in model D only nodes at the four corners are constrained for displacements.

Gaussian heat source calibration study

A calibration of the Gaussian heat source is necessary, in order to guarantee that the right temperature is achieved during the laser pass. This can be achieved by running some simulations with varying k_p, obtain a best-fit and then calculate the parameter such that the maximum temperature in the melt-pool is around 2700 °C, as observed experimentally at the centre of the scanning track during selective laser melting in [249], or 2760 ± 31.71 °C, as indicated more recently [250]. Having fixed $p = 150.0$ W and $\eta = 0.20$, the result is $k_p = 7372.36$ and the numerical procedure is graphically represented in Figure 3.30.

3.1.14 Post-processing of the finite element results

Once the set of simulations is completed, the numerical results can be processed by calculating the maximum of the residual stress on each Gaussian point of the finite element model. In SIMULIA/Abaqus, this process can be automatised, whereby the extraction of the values can be performed using a Python script, which can

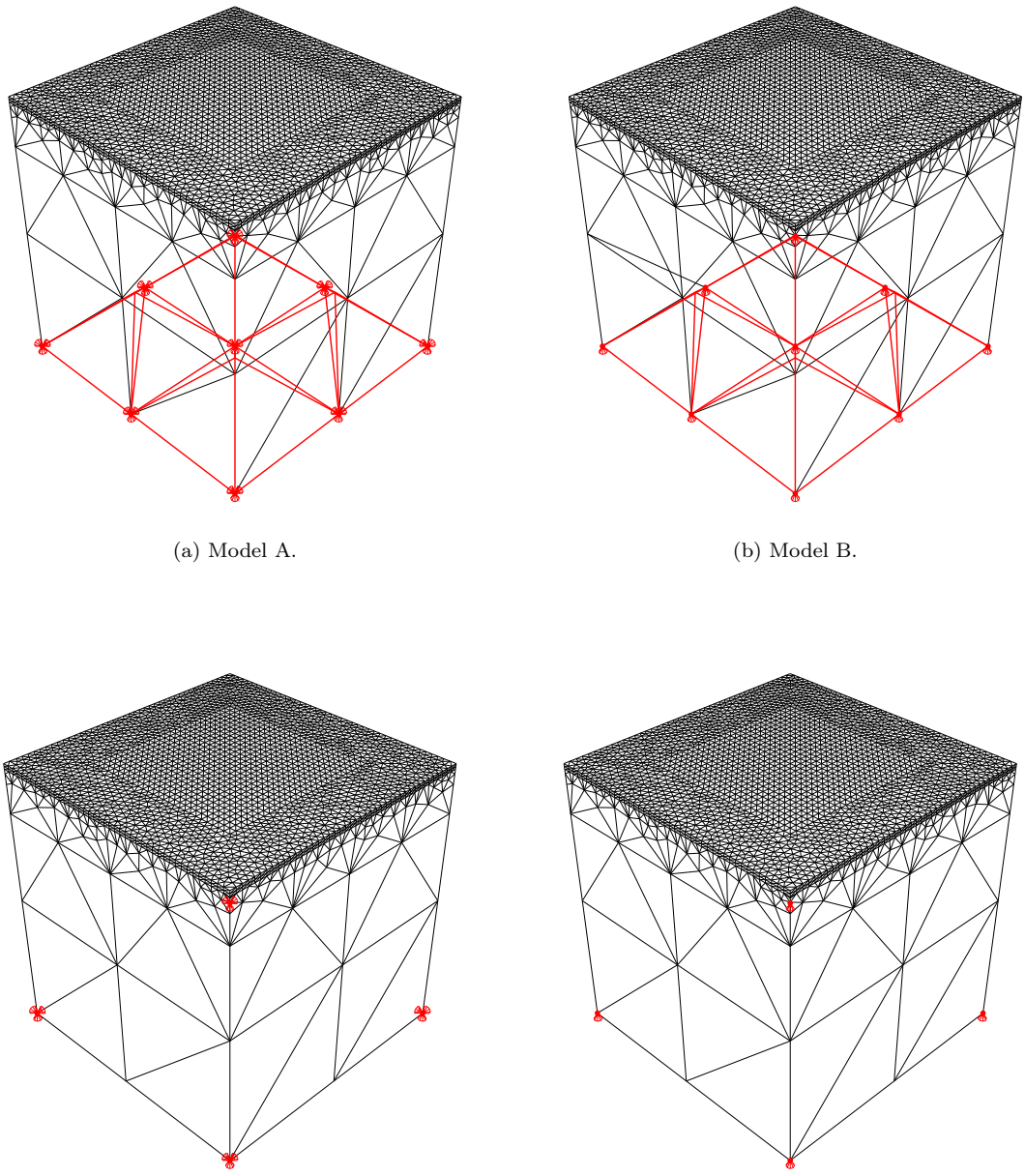

(a) Model A.

(b) Model B.

(c) Model C.

(d) Model D.

FIGURE 3.29: Boundary conditions applied to the models used for the mesh convergence study.

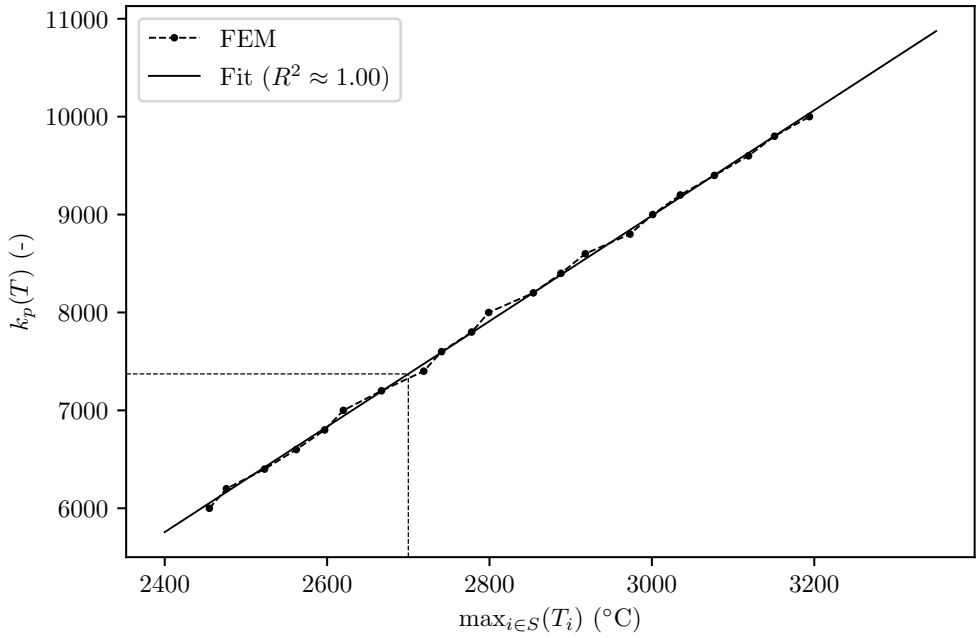

(a) Relationship between the maximum temperature and the calibration parameter k_p, as obtained in the numerical study.

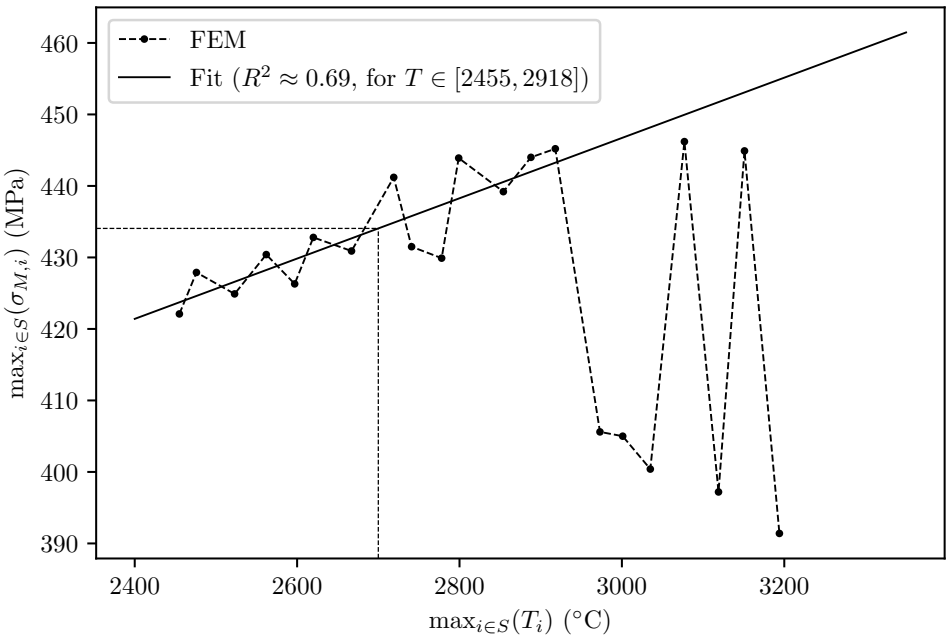

(b) Relationship between the maximum von Mises stress and the calibration parameter k_p, as obtained in the numerical study.

FIGURE 3.30: Numerical study to determine the correct calibration parameter k_p.

read the output database (ODB file) of the calculations. The same script can then write the numerical results to some text files, which can be subsequently further processed by other Python script files to plot the results.

3.1.15 Brief discussion about uncertainty of the model

As seen in the previous sections, the computational model presented in this work has different inputs and variables and their knowledge can affect the final result. In the case under examination, each residual stress component is a function of several variables:

$$\sigma_i = f\left(G_j, x, k(T), c_p(T), \alpha(T), \rho(T), C_j, Q, B_j, n_e\right), \tag{3.55}$$

where G_j is the j-th geometrical parameter, $x \in \mathbb{R}^3$ is the point where the residual stress is calculated, $k(T)$, $c_p(T)$, $\alpha(T)$, $\rho(T)$ are the thermo-physical parameters, which can be further differentiated into bulk and powder properties, C_j is the j-th parameter defined into the constitutive model, B_j is the j-th boundary condition, n_e is the number of the elements in the finite element model approximating the geometry under analysis. Therefore, the uncertainty associated with each quantity requires further study and cannot be determined in the present study.

3.2 Microstructure modelling and prediction for different hatch spacing values

3.2.1 Martensite needles thickness

For welding and for some laboratory-controlled heat treatments an empirically derived formula to calculate martensite needle thickness in Ti-6Al-4V has been extensively validated and used during very recent times by Villa *et al.* (2020) [93, 94]. It has been shown that the needle thickness (expressed in µm) is proportional

to the natural logarithm of the cooling rate:

$$w_{\alpha'} = a \log \left(\frac{\partial T}{\partial t} \right) - b, \tag{3.56}$$

where $a = 0.0895$, $b = 0.138$ and the cooling rate is in °C/s. This Equation (3.56) shows a good agreement with experimental data, mainly revealing that the cooling rate seems to be the primary factor affecting the martensitic needle thickness. On the contrary, its thickness seems not much affected by the parent β grain size [93, 94]. The reason for this can be found in the fact that often martensite extends across the β-grain boundary [87].

3.2.2 Martensite volume fraction

Assuming that upon cooling the material from temperatures above the β-transus temperature, the martensite volume fraction at room temperature has been described in the same cited studies on welding and laboratory-controlled heat treatments by the following equation [93, 94]:

$$V_{\alpha'} = a \left[b \arctan \left(\frac{\partial T}{\partial t} \right) - c \right], \tag{3.57}$$

where the best fit with experimental data has been found for $a = 20.4$, $b = 2.62$, $c = 65.0$. This last Equation (3.57) shows again a strong dependency on the cooling rate. However, several studies, both in stainless steel and in Ti-6Al-4V, pointed out that the martensite volume fraction is entirely independent from the cooling rate. On the contrary, some authors showed that for Ti-6Al-4V there is a good agreement with the results provided by the Koistinen-Marburger model [99], initially developed for carbon steel and currently extensively used for this material [100, 101, 102].

3.2.3 Martensite needles spacing

Since no model can be found in the literature describing the spacing value between two parallel martensite needles, in the following subsection a new geometrical

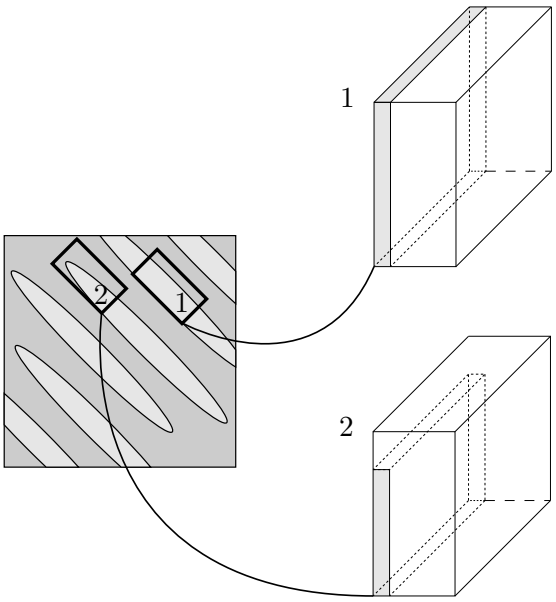

FIGURE 3.31: Illustration of two models for the martensite spacing description and their derivation from the lath martensite structure within the material.

approach will be followed [251].

Martensite spacing model 1

According to Figure 3.32a, the total cell volume V can be written as a sum of the α' martensite volume fraction $V_{\alpha'}$ and β-phase volume fraction V_β:

$$\begin{aligned} V &= V_{\alpha'} + V_\beta \\ &= w_{\alpha'} h_{\alpha'} l_{\alpha'} + d_{\alpha'} h_{\beta\beta}, \end{aligned} \tag{3.58}$$

where $w_{\alpha'}$ is the martensite thickness, $d_{\alpha'}$ is the martensite spacing, $h_{\alpha'}$ and h_β are respectively the major axis length of the martensite lath and that of the β-face included into the cell volume element, and $l_{\alpha'}$ and l_β are respectively the out-of-plane depth of the martensite lath and that of the β-face included into the cell volume element.

From Equation (3.58) it follows that the β-phase volume fraction can be writ-

ten as

$$V_\beta = \frac{d_{\alpha'} h_{\alpha'} l_{\alpha'}}{V}, \tag{3.59}$$

but, combining Equation (3.58) and this last Equation (3.59):

$$V_\beta = \frac{d_{\alpha'} h_{\alpha'} l_{\alpha'}}{w_{\alpha'} h_{\alpha'} l_{\alpha'} + d_{\alpha'} h_{\beta\beta}}. \tag{3.60}$$

Now, rearranging the terms as follows

$$V_\beta \left(w_{\alpha'} h_{\alpha'} l_{\alpha'} + d_{\alpha'} h_{\beta\beta} \right) = d_{\alpha'} h_{\alpha'} l_{\alpha'} \tag{3.61}$$

and expanding the product as

$$\begin{aligned} V_\beta w_{\alpha'} h_\beta l_\beta &= d_{\alpha'} h_{\alpha'\alpha'} - V_\beta d_{\alpha'} h_{\alpha'\alpha'} \\ &= d_{\alpha'} \left(h_{\alpha'} l_{\alpha'} - V_\beta h_{\alpha'} l_{\alpha'} \right), \end{aligned} \tag{3.62}$$

it follows that:

$$d_{\alpha'} \frac{V_\beta w_{\alpha'} h_\beta l_\beta}{h_{\alpha'} l_{\alpha'} - V_\beta h_{\alpha'} l_{\alpha'}}. \tag{3.63}$$

Since $h_{\alpha'} = h_\beta$ and $l_{\alpha'} = l_\beta$, then

$$d_{\alpha'} = \frac{V_\beta w_{\alpha'}}{1 - V_\beta}. \tag{3.64}$$

Finally, remembering that $V_{\alpha'} = 1 - V_\beta$, the martensite spacing can be expressed as:

$$d_{\alpha'} = \frac{(1 - V_{\alpha'}) w_{\alpha'}}{V_{\alpha'}}. \tag{3.65}$$

This means that the α' martensite lath spacing is now completely defined once the martensite volume fraction and its thickness is known.

Martensite spacing model 2

According to Figure 3.32b, in this second case the total cell volume is

$$\begin{aligned} V &= V_{\alpha'} + V_\beta \\ &= w_{\alpha'} h_{\alpha'} l_\beta + d_{\alpha'} h_{\alpha'} l_{\alpha'} + (w_{\alpha'} + d_{\alpha'})(h_\beta - h_{\alpha'}) l_{\alpha'} \end{aligned} \tag{3.66}$$

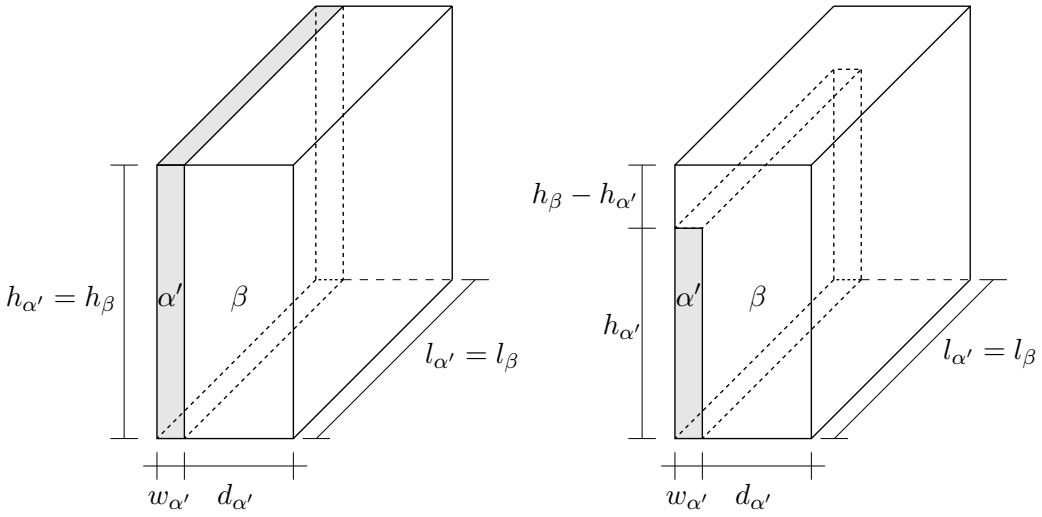

FIGURE 3.32: Representation of the assumed geometry of the cell in the first (a) and in the second model (b).

and, accordingly, the β-phase volume fraction is

$$V_\beta = \frac{1}{V}\left[d_{\alpha'} h_{\alpha'} l_{\alpha'} + (w_{\alpha'} + d_{\alpha'})(h_\beta - h_{\alpha'}) l_{\alpha'}\right]. \tag{3.67}$$

Combining the last two Equations (3.66) and (3.67), using a mathematical procedure similar to the previous one and simplifying, it is possible to write:

$$w_{\alpha'}(h_\beta - h_{\alpha'})V_{\alpha'} + w_{\alpha'} h_{\alpha'} V_{\alpha'} - w_{\alpha'}(h_\beta - h_{\alpha'}) = d_{\alpha'} h_\beta (1 - V_{\alpha'}) \tag{3.68}$$

and from this last Equation (3.68), it follows that:

$$d_{\alpha'} = 2\frac{h_{\alpha'}}{h_\beta}\frac{V_\beta}{V_{\alpha'}} w_{\alpha'}. \tag{3.69}$$

Therefore, according to this second formulation, the α' martensite spacing is proportional to the ratio between the laths length and the cell size.

3.2.4 Model parameters optimisation

Let $\delta_{h,P}$ be the difference between the martensite property value calculated with the model and the value obtained by experimental measurement at hatch spacing

value h and point P within the laser track at the end of the cooling stage:

$$\delta_{h,P} = t_{h,P} - \bar{t}_{h,P}. \tag{3.70}$$

For each hatch spacing value h_i and point P_i, it is possible to define the sum of those differences, which can be called *residual* R:

$$R = \sum_{i=1}^{N} \delta_{h_i,P_i}. \tag{3.71}$$

A new model calibrated on the experimental data can be therefore obtained by minimising the residual. This procedure can be easily integrated into any programming language or, as an alternative, the function *Goal Seek* in Microsoft® Excel® can be used. This function perform a so-called *What-if-Analysis* and it provides a method of equation a function to a desired value by iteratively modifying the source or input data.

Chapter 4

Experimental set-up

The generation of appropriate experimental data is key in supporting the development and validation of the computational models. In additive manufacturing, a number of process variables can be studied at any given time and include: characteristics of the powder, influence of geometry on build distortions, scanning strategies, power and speed of the heat source and so on. In this study, the main focus is on understanding the microstructure evolution according to the thermal fields induced by different hatch spacing values. In particular, the intent of the experiments carried out and reported in the present work was to characterise the shape, the volume fraction, and the dispersion of martensite in Ti-6Al-4V for different hatch spacing values. The aim of this research was that once this theoretical gap was filled, the data generated can be used to improve the description of the initial dislocation density adopted by some physics-based constitutive models and, possibly, provide new insights. This can result in a more accurate prediction of the flow stress behaviour during a deformation process. At the same time, the characterisation can clarify or uncover some relations between the hatch spacing and the new phase formation.

4.1 Experimental procedure, equipment, and processing conditions

The objective of the experimental programme is to generate data from a laser track on a Ti-6Al-4V plate, by varying the hatch spacing values and then metallurgically characterise the martensite distribution and its size. Indeed, as seen in Table 2.10, the martensite thickness and spacing are scarcely reported in the available literature. To be more accurate, martensite characterisation can be performed in three different locations of the melt pool, denoted as A, B, C in Figure 4.1, because they represent, respectively, a location at the centre of the first-track melt pool, a location at the intersection between two melt pools, and a location at the heat affected zone of the first melt pool.

The laser scan induces some alterations in the microstructure which are clearly visible with the optical microscope. However, in order to achieve good data collection for the purpose, there are some intermediate passages to be performed before starting the investigations with microscopes. First of all, a sample must be extracted from the workpiece and to facilitate inspection of its external characteristics it must be enhanced by some surface polishing techniques. There is no universal method to process the sample, but usually there is a general sequence to follow in studies like the present one. Nevertheless, the passages carried out during this study, and for the specific purposes related to it, are usually reflected into the list of equipment. Therefore, the equipment used throughout the whole experimental process is briefly listed below, according to the temporal sequence of their use:

1. hole making machine, Kennametal® (Figure 4.4);
2. laser metal deposition machine, Trumpf® TLC1005 (Figure 4.5);
3. electrical discharge machine, AgieCharmilles® CUT20 (Figure 4.6);

4. hot mounting hydraulic press machine, Aptex® Presidon® (Figure 4.7);
5. polishing machine, Struers® Tegramin-25® (Figure 4.8a);
6. optical microscopes
   - ZEISS® Axioskope® 2, equipped with ZEISS® AxioCam® HRc digital camera (Figure 4.8b);
   - Brunel® Microscopes Ltd., equipped with Canon® EOS 1100D digital camera (Figure 4.9);
7. scanning electron microscope, Hitachi® TM3000 Tabletop Microscope (Figure 4.10);
8. micro-hardness tester machine, Buehler® Wilson VH1202.

Some rectangular titanium alloy Ti-6Al-4V Grade 5 ASTM B265-15 sheets supplied by Titanium Metals UK Ltd., West Bromwich (United Kingdom), have been employed in this experimental study. Their dimensions were 125×150 mm with a thickness of 3 mm (tolerance of +1 mm/-0 mm). The sheets were processed by VAR/rolling method in the direction parallel to the shorter edge and annealed. The full chemical composition of the alloy sheets as-received is given in Table 4.1, where it is also compared with the standard composition.

	Al	V	Fe	C	N	H	O	Ti
as-received	5.78	3.92	0.11	0.018	0.009	0.001	0.123	balance
standard	5.50-6.75	3.50-4.50	< 0.40	< 0.08	< 0.05	< 0.015	< 0.2	balance

TABLE 4.1: Chemical composition of the as-received Ti-6Al-4V plates used in this study and of that according to the standard composition (quantities in wt%).

Processing conditions

The laser scans have been performed using a Trumpf® laser metal deposition machine, usually used to produce near net-shape components (meaning as near as

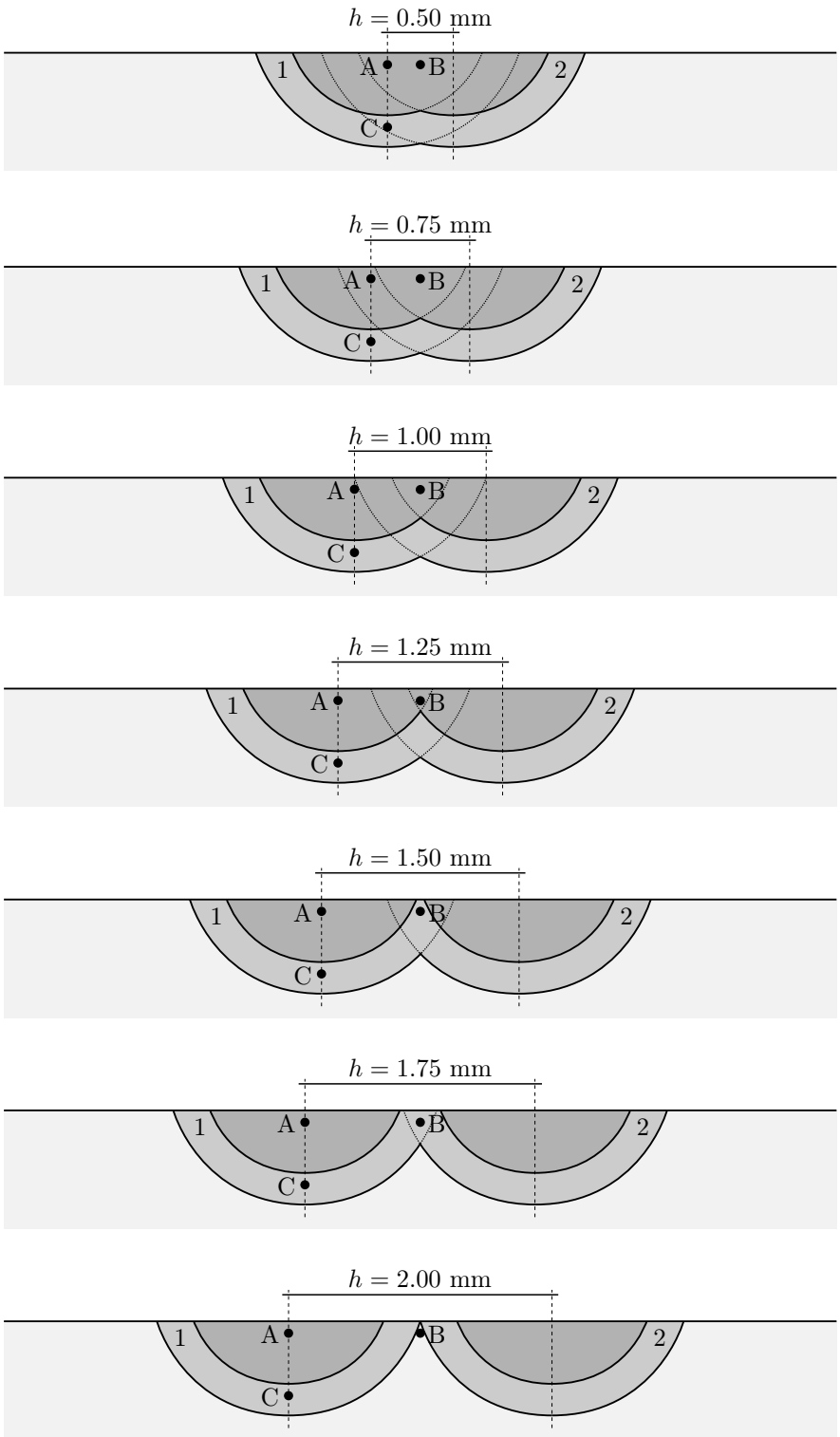

FIGURE 4.1: Diagram illustrating the hatch spacing variation in the experiments and the position of the three points of interest (A, B, C). The numbers 1 and 2 refer to the laser track scanning order.

Laser power	Beam diameter	Laser speed	Hatch spacing	O_2
1000 W	2.00 mm	2000 mm/min	variable (0.5-2.0 mm)	$< 0.4\%$

TABLE 4.2: Processing parameters employed as inputs in the Trumpf® machine for the present set of experiments. The hatch spacing is variable in the interval 0.50-2.00 mm with steps of 0.25 mm.

possible, in size and shape, to the finished product) and also to repair damaged parts. The Trumpf® machine was initially introduced in the commercial market back in 2016 [252], so it can be considered both recent but also sufficiently widespread to justify its use in an experimental study. This machine is utilised to melt the material, create a weld pool on the component surface and simultaneously deposit metal powder via a nozzle. However, as already mentioned, in these experiments no powder has been employed, because the aim was to investigate solely the effect of the laser power on the base material microstructure. The oxygen content has been lowered inside the chamber where the plate was processed, before starting the trial, in order to prevent the natural oxidation of the plate in the region of the laser scan. The process parameters used as inputs in the machine are summarised in Table 4.2.

4.1.1 Temperature recording: hole drill and thermocouple

To measure the temperature inside the material is necessary to drill a hole, into which can be inserted the small cable end of a thermocouple. This choice was necessary after a first trial during which only the surface temperature were recorded, obviously producing a limited representation of the temperature profile, which was not sufficient to perform a correct temperature calibration of the finite element model. Moreover, in order to be more accurate and minimise the errors, the temperature was recorded at two aligned points parallel to the laser track, where two thermocouples were placed, as represented in Figure 5.4.

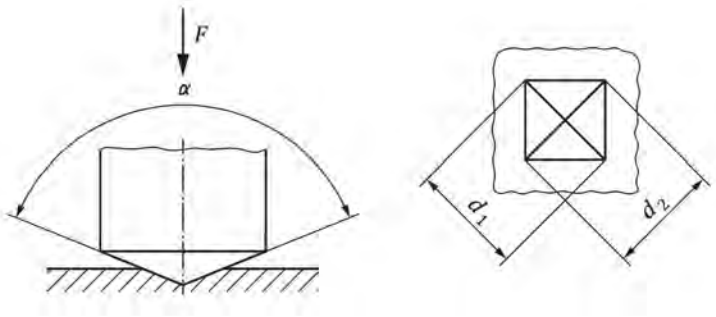

FIGURE 4.2: Representation of the diamond-shape indenter of a right pyramid with a square base used in the Vickers hardness test (on the left), and its shape impression on the metal surface (on the right), according to EN ISO 6507-1. A force F is applied and the mean angle between the opposite faces at the vertex of the pyramidal indenter is indicated as α and its value is usually 136°. The shape of the metal impression on its surface is characterised by the two diagonal lengths d_1 and d_2. Image adapted from [253, p. 2, fig. 1].

4.1.2 Hardness measurement

Hardness is a measure of the resistance to permanent change or the capacity of the material to resist plastic deformation, when an indentation force is applied. Therefore, different hardness measurements methods exist, but perhaps the test most used in engineering is the Vickers hardness test. It is performed by applying a force which will impress a mark on a metal surface through a diamond pyramidal indenter, as represented in Figure 4.2. The Vickers hardness number $H_V \in \mathbb{R}$ is then expressed as the ratio between the test force F and the surface area of indentation A:

$$H_V = \frac{1}{g_n}\frac{F}{A} = \frac{1}{g_n}\frac{F}{d^2/(2\sin(\alpha/2))}, \tag{4.1}$$

where $g_n = 9.80665$ is the conversion factor from kgf to N (the force must be expressed in N and d in mm). If the nominal angle is $\alpha = 136°$, as in most cases, then $H = 0.1891F/A$. Finally, particular care must be taken when using the Vickers hardness test, because the distance between two indentations should be not less than 3 times the average diagonal of the indentation d for hard metals,

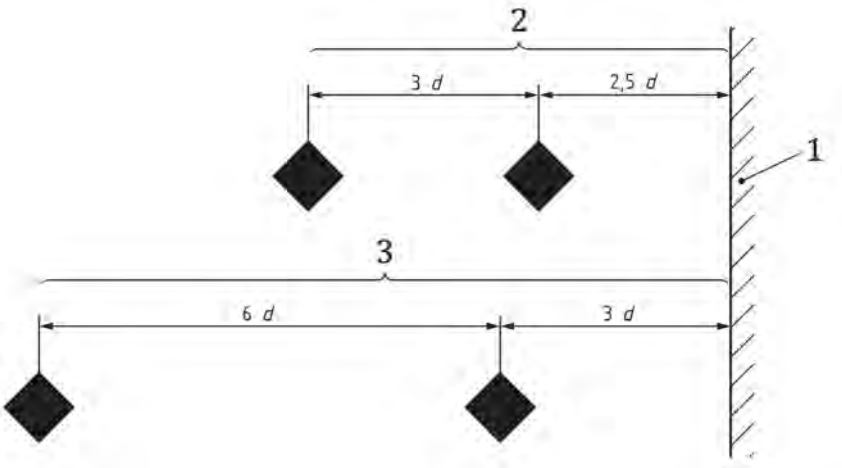

FIGURE 4.3: Minimum distances between Vickers indentations, according to EN ISO 6507-1. (1) edge of test piece, (2) steel, copper and copper alloys, (3) = light metals, lead and tin and their alloys). Image reproduced from [253, p. 7, fig. 2].

although some manufacturers suggest 2.5 times, as represented in Figure 4.3.

4.1.3 Specimen preparation

The intermediate step between an actual experiment and sample analysis is the creation of metallographic samples that must undergo a preparation process in order to be analysed. The purpose of this type of activity is to make the microstructure of a particular type of material examinable by metallographic methods. This section provides a brief introduction to the techniques and operational details of each procedure used during the course of the laboratory activity.

Sectioning

Sample sectioning is the first step in specimen preparation, and it can be performed with several techniques. In selecting a suitable method, it is necessary to consider the possible alterations that this operation may cause to the microstructure, or the generation of some small cracks and even mechanical residual stresses they can induce. One of the best processing methods makes use of Electrical Dis-

charge Machine (EDM), creating electrical discharges in a metallic wire in contact with the workpiece to be cut, with both immersed in a dielectric fluid. Therefore, sectioning of the workpiece has been carried on with the wire-cut electrical discharge machining technique and the pieces extracted from the plate measured $7 \times 10 \times 3$ mm (where 3 mm corresponds with the thickness of the plate).

Embedding and grinding

When the sample is small, soft, or fragile or when it is needed to combine multiple samples into a single specimen, the small pieces extracted from the main workpiece can be embedded in a plastic material. The process is distinguished into cold mounting or hot mounting, depending on whether heat is used to process the plastic surrounding the sample and this technique is called also *compression moulding*. The material used to mount the samples has to be sufficient resistant to mechanical and chemical actions that will be performed in the subsequent steps. At the same time, the material can be opaque or transparent, but it should adhere to the specimen and, finally, it should also be not too expensive. One of the materials commonly used in the hot process is the Bakelite, a thermosetting phenol formaldehyde resin usually available as powder, which is heated and compressed at the same time to form a whole with the metal sample. The samples so extracted from the workpiece have been embedded with a hot mounting machine using a Bakelite powder. Sample grinding has been performed manually in water with some Silicon Carbide (SiC) papers, characterised by a particle size ranging from 180 to 4000 mesh, whilst the polishing wheel was rotating at a speed of 250 rpm.

Polishing, ultrasonic washing, and etching

After embedding the material, its surface can be gradually polished using finer abrasive particles, which flatten the surface and make it mirror-like. Since this

process clearly induces abrasion, the sample can be cleaned with an ultrasonic bath to remove any residual material left over from the polishing process. Finally, the process of using a chemical acid solution to reveal the microstructure or phases present on a metal surface is called *etching* [30]. The prepared surface is chemically attacked with dilute acid for a short time and this process preferentially erodes the grain boundaries, making them clearer under a microscope. This can be explained by the increased susceptibility of the metal to the acid along the grain boundaries, which leads to a higher corrosion rate and this occurs essentially because the atomic bond between the grains is weaker than that within them. The most common etchant used to treat titanium samples is the Kroll's reagent, which consists of 100 mm of water, 1-3 mm of hydrofluoric acid and 2-6 mm of nitric acid [254, 30]. As a method to increase the efficiency of the chemical reaction, sometimes the sample is submerged in the etching solution inside an ultrasonic cleaner machine [254]. During the process heat is generated and depending on the small variations in etching procedure, included time, the sample can lose a certain quantity of mass and the surface roughness appears different (in this regard, a good comparative study can be found in [254]).

The first step of sample polishing has been performed with a Struers® Inc. MD-Dac® cloth, with a water based diamond suspension of 2 µm. During this operation, the plate was rotating at the speed of 250 rpm with a perpendicular applied force of 20 N. A second and last step of polishing has been done with a Struers® Inc. MD-Chem® cloth with an oxide polishing suspension. During this last step, the plate was rotating at a speed of 150 rpm with a perpendicular applied force of 20 N. After that, all the samples have been washed in an ultrasonic cleaning machine, submerging them in ethanol, to completely remove the smaller residual particles.

Finally, an electrochemical etching, which is a controlled corrosion process, has been performed by submerging the samples in a Kroll's reagent for 25-30 s.

After this procedure, since the β-phase is attacked by the reagent, it appears dark, whereas the α-phase regions look bright. This different colouration is due to the difference in the chemical potential between the two phases, which alters the rate of attack [255].

4.2 Data collection, processing and analysis

The steps adopted after the samples preparation are the collection of data, its processing and analysis. The collection usually employs additional instruments, such as the optical (OM) and the scanning electron microscope (SEM), whilst their processing and analysis is done by image processing tools, such as ImageJ, which can help to collect data that are afterwards analysed using statistical techniques.

4.2.1 Data collection: optical and scanning electron microscopy

The main techniques for investigating the surface microstructure of a metallic sample are by means of the optical microscope (OM) and the scanning electric microscope (SEM). Whilst the former uses visible light to generate an image of the sample, the latter uses an electron beam and is therefore more precise, generating high-resolution images. Main scanning electron microscope detector techniques are the following: *backscattered electrons* (BSE), *secondary electrons* (SE), and *electron backscatter diffraction* (EBSD).

In the present work, two optical microscopes were used and one backscattered electron microscope and detector. The former was used to reveal some details about the laser track and melt pool, while the second one was used to conduct a more in-depth study of the microstructure and, in particular, an in-depth characterisation of the martensite. As anticipated, the martensite shape and distribution has been investigated in three locations of the cross-section of

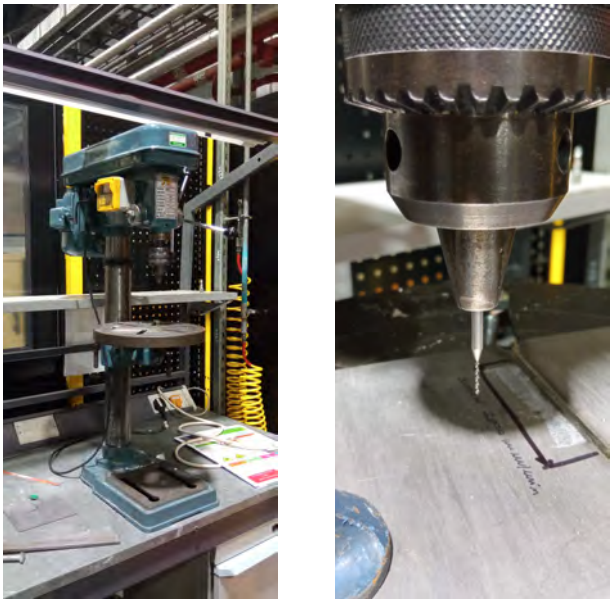

(a) (b)

FIGURE 4.4: Pillar drilling machine on the left (a) and a detail with the Ti-6Al-4V plate on the right (b).

(a) (b)

FIGURE 4.5: Control panel of the Trumpf® machine on the left (a) and entrance of the chamber on the right (b).

(a)

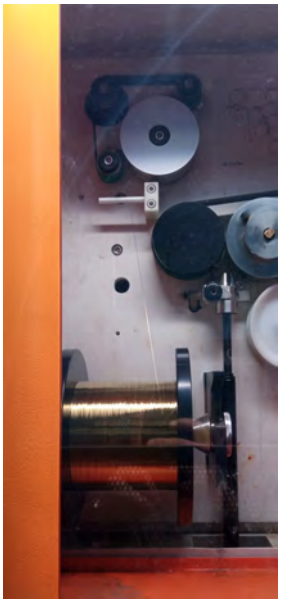

(b)

FIGURE 4.6: Electric Discharge Machine on the left (a) and a detail of the metallic wire spool on the right (b).

(a)

(b)

FIGURE 4.7: Hot mounting machine on the left (a) and the Bakelite powder on the right (b) used to embed the specimens.

(a) (b)

FIGURE 4.8: Polishing machine on the left (a) and the Brunel Microscopes Ltd optical microscope on the right (b).

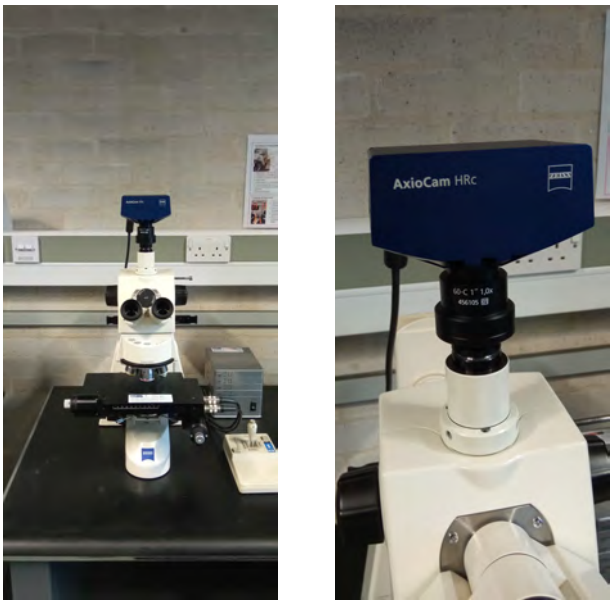

(a) (b)

FIGURE 4.9: ZEISS® optical microscope on the left (a) and detail of the camera on the right (b).

(a) (b)

FIGURE 4.10: Scanning electron microscope connected to a computer for image capturing and specimen positioning on the sample holder (a) and a detail of the opened specimen chamber door with the specimen inside it (b).

the laser track and in the present work they are named A, B, C (Figure 4.1).

4.2.2 Data analysis

Images acquired with SEM were digitally analysed with ImageJ software, a public domain tool developed at the National Institutes of Health and the Laboratory for Optical and Computational Instrumentation (LOCI, University of Wisconsin). It is specifically designed for image processing and analysis and it uses some fully automatic numerical algorithms as well as it permits some manual intervention, in order to determine the edges of the objects and quantify the morphology and the distribution of particles within a picture acquired with the microscope. In particular, this software is designed to calculate some statistical analysis of the microstructure according to the image pixel values, such as areas, distances, and angles, after proper definition of the image scale. Automating the process of

analysis not only speeds up the measurements, but also yields consistent and repeatable results.

The image acquired with the scanning electron microscope is a greyscale .tif image, so the values of the pixels are in the range $[0, 1]$, where the value 0 represents the colour black and the value 1 represents white. However, the automatic particle analysis module of ImageJ can be used only after the acquired image has been converted to a binary image. An image is binary if all the pixels assume the value 0 or 1 and this can be achieved by using an appropriate built-in threshold function, which uses an image segmentation process. The process of thresholding an image of the material under investigation captured with the microscope is represented in Figure 4.11.

After the image content is processed, all the data appears on a separate results window and can be saved in a CSV (comma-separated values) file, in which all the data are arranged in columns and rows. The content of this file can be further processed by some Python or MATLAB® programming scripts. Those scripts can help to rapidly obtain statistical information about some microstructural properties, across a considerable number of samples.

Since microscopes are only capable of processing bidimensional images, which can be obtained from cross-sections of samples, certain volumetric quantities can only be approximated, assuming that the measure sought in three-dimensional space is almost equal to that in two-dimensional space. This is the case, for example, of the volume fraction, which is usually replaced by the area fraction, which is easier to quantify.

Distribution analysis of the data

Once all the images had been acquired, the data need to be processed in order to obtain some statistical information about the microstructure. In the analysis necessary for the present scope, the procedure is illustrated in Figure 4.12.

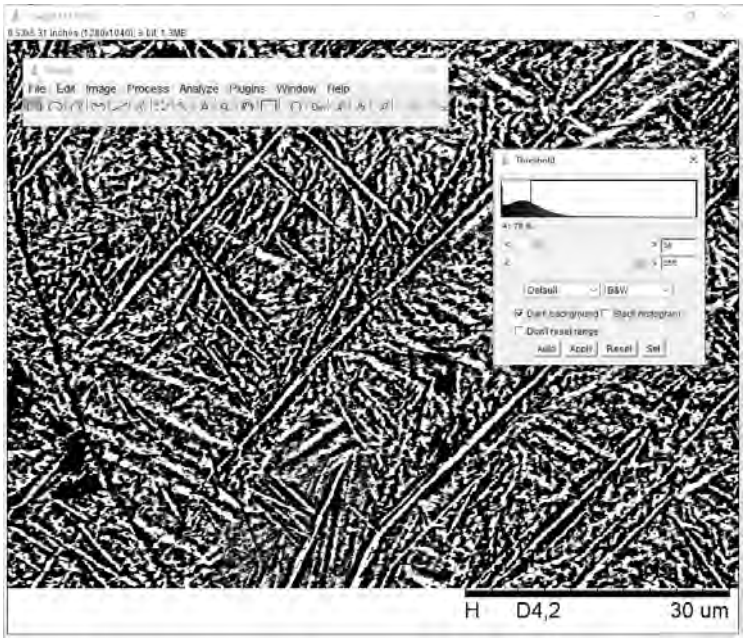

FIGURE 4.11: Thresholding process of an image captured with the scanning electron microscope within the ImageJ software environment. It is visible the image histogram in the small window on the right.

The distribution of the data are usually inspected by looking at their normal or *Gaussian distribution*, defined as:

$$f(x) = \frac{1}{\sigma\sqrt{2\pi}} \exp\left[-\frac{1}{2}\left(\frac{x-\mu}{\sigma}\right)^2\right]. \tag{4.2}$$

However, sometimes the data are not naturally distributed according to the normal distribution, often because the values are non-negative, and therefore the so-called *log-normal distribution* or *skew Gaussian distribution* can be introduced:

$$f_X(x) = \frac{2}{\omega}\phi\left(\frac{x-\xi}{\omega}\right)\Phi\left(\alpha\left(\frac{x-\xi}{\omega}\right)\right), \tag{4.3}$$

where $\phi(x)$ is the standard normal distribution function and $\Phi(x)$ the standard normal cumulative distribution function, ξ is the *location parameter*, ω is the *scale parameter*, and α is the *skew parameter*. The standard normal distribution function is defined as

$$\phi(x) = \frac{1}{\sqrt{2\pi}} \exp\left(-x^2/2\right), \tag{4.4}$$

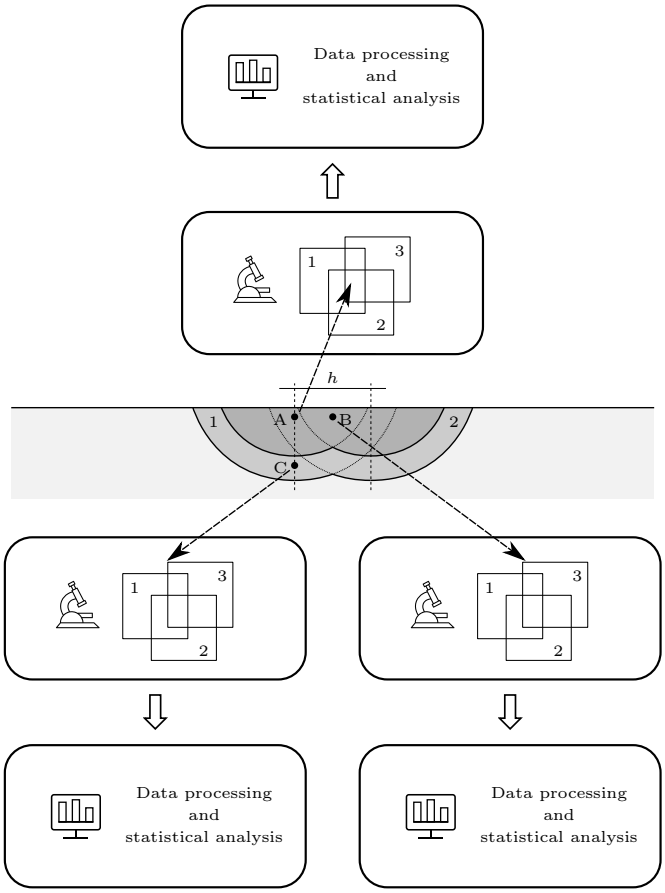

FIGURE 4.12: Scheme representing the data acquisition and elaboration process for the three different points within the laser track. For each hatch spacing value, a set of three SEM micrographies were chosen to represent with sufficient accuracy the microstructure statistical informations.

and the standard normal cumulative distribution function as

$$\Phi(x) = \int_{-\infty}^{x} \phi(t)\,\mathrm{d}t = \frac{1}{2}\left[1 + \mathrm{erf}(x/\sqrt{2})\right], \tag{4.5}$$

and where the error function is:

$$\mathrm{erf}(z) = \frac{2}{\sqrt{\pi}} \int_{0}^{z} \exp(-t^2)\,\mathrm{d}t, \tag{4.6}$$

with, in general, $z \in \mathbb{C}$. In a log-normal distribution the mode, median and mean values differ, as opposed to the Gaussian distribution. Given the diversity of values between mode, median, and mean, it is generally preferable to use the

median as an indicator of central tendency, because it lies between the other two. Starting from the median value, it is therefore possible to define two percentiles as the value below which a given percentage of values in its frequency distribution falls (in particular, the 50th percentile is exactly the median value).

Chapter 5

Results

The main results obtained during this study were the implementation and use of a process model based on the finite element method to study and predict residual stresses during laser-powder bed fusion of Ti-6Al-4V, in its common process window (laser speed 200-1600 mm, hatch spacing 40-120 µm). This model incorporates temperature-dependant material thermo-physical parameters (mass density, specific heat capacity, thermal conductivity, linear thermal expansion, Young's modulus, Poisson's ration), differentiated both for the substrate and the powder layer. It also incorporates a physics-based thermo-viscoplastic constitutive model, which takes into account the microstructure and the evolution of dislocation density during deformation, which is also differentiated with respect to the substrate and the actual deposition layer.

Other interesting results were achieved in this study by combining experimental techniques with modelling to calculate and validate the residual stresses and to determine the influence of the hatch spacing on the microstructure – in particular the primary martensite – of Ti-6Al-4V.

5.1 Experimental observations and heat source model calibration

5.1.1 Laser track and melt pool

Before looking into details of the microstructure, some preliminary observation can be done optically, such as the morphology and the general appearance of the track left by the laser on the plate.

Firstly, it was observed that the actual shape of the track left by the laser of the Trumpf® laser machine is well approximated by a Gaussian if viewed from above. This is particularly clear by superimposing some isothermal curves generated by a Gaussian heat source implemented within a finite element scheme on a photograph of the track left on the plate, as in the Figure 5.2. This empirical evidence justifies the assumption of a Gaussian model for the heat source, carried out in the computational framework.

A second observation regards the depth and the shape of the track on the plate. An immediate comparison can be made between the track at the starting point and the one at the end point. As visible in Figure 5.3, the starting point, obtained when the laser is switched on, is concave with respect to the plane of the plate, whereas the end point, when the laser is switched off, is convex, resulting in an excess of material even in the absence of powder deposition. However, this is a secondary aspect that is difficult to adequately implement within a modelling scheme, but it can be regarded as a possible starting point for further investigations. Indeed, the inhomogeneity of the surface potentially can create some issues on the final component, with regards to a non-uniform heating profiles and associated stress.

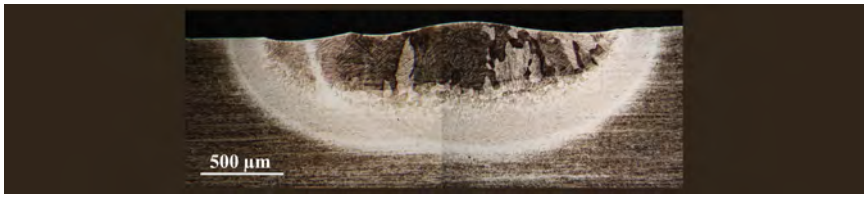

(a) $h = 0.50$.

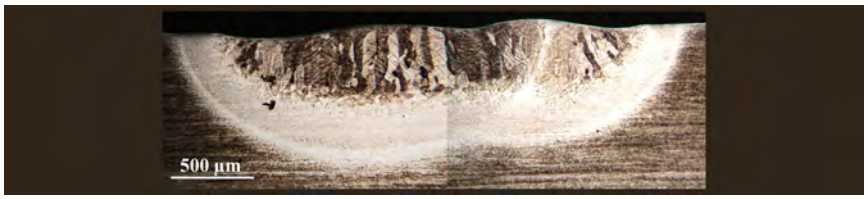

(b) $h = 0.75$.

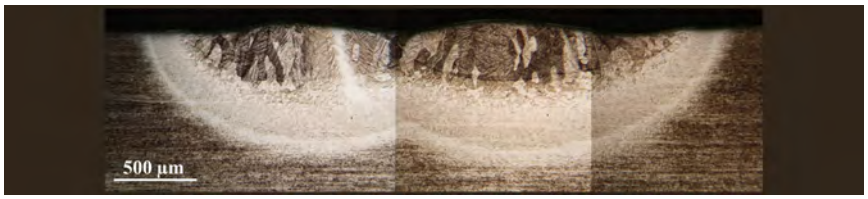

(c) $h = 1.00$.

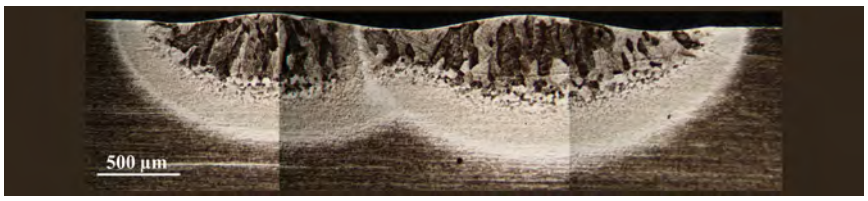

(d) $h = 1.25$.

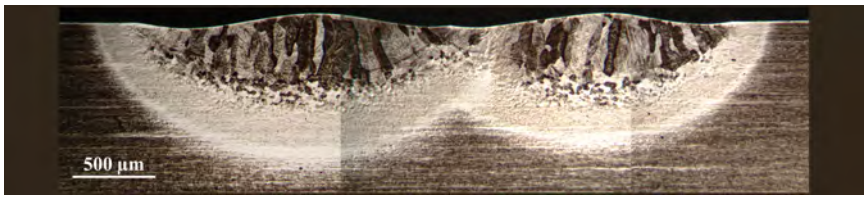

(e) $h = 1.50$.

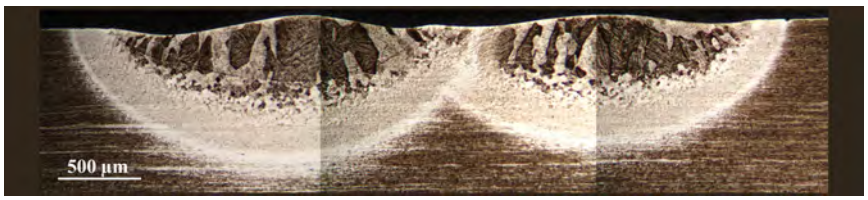

(f) $h = 1.75$.

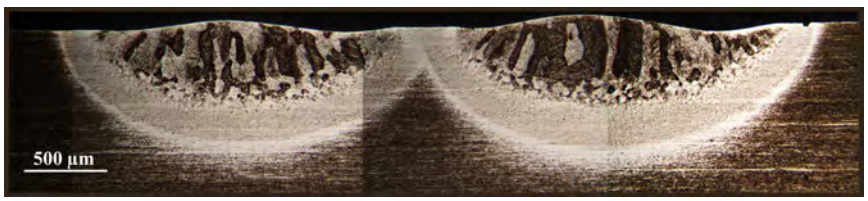

(g) $h = 2.00$.

FIGURE 5.1: Melt pool cross-section area images for different values of hatch spacing.

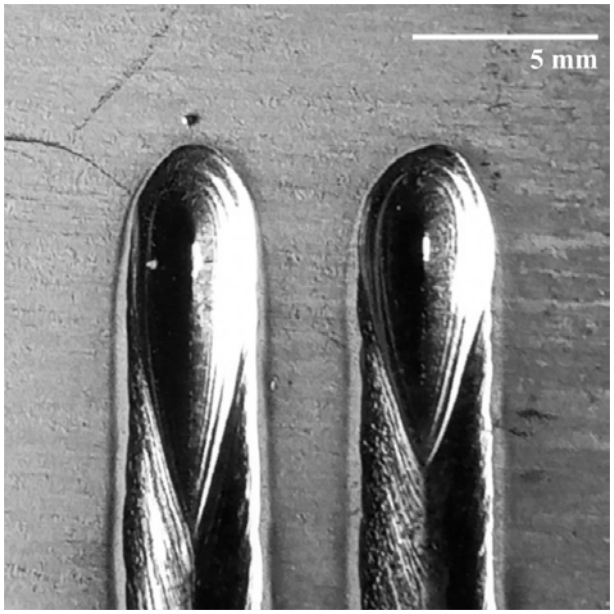

(a) Detail of two end points of laser tracks from above.

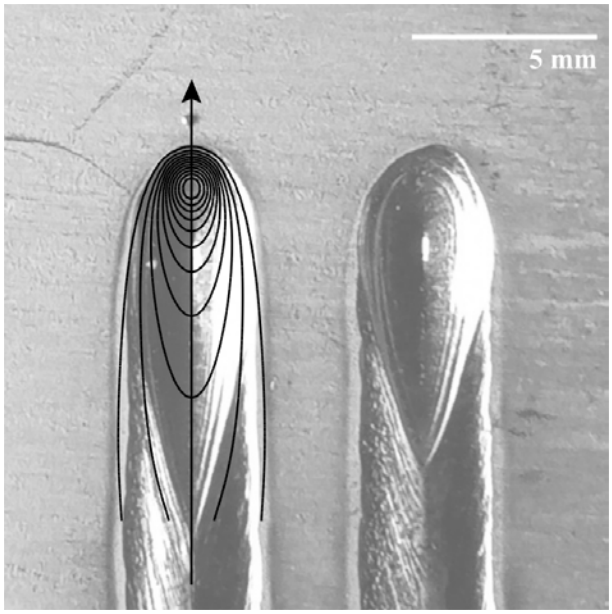

(b) Detail of two end points of laser tracks from above, with superimposed isothermal curves of the travelling Gaussian heat source, obtained by the finite element model.

FIGURE 5.2: Perpendicular images of some melt pools and superimposed isothermal curves of the travelling Gaussian heat source. The laser tracks have been obtained during some preliminary tests with the laser source of the Trumpf® machine.

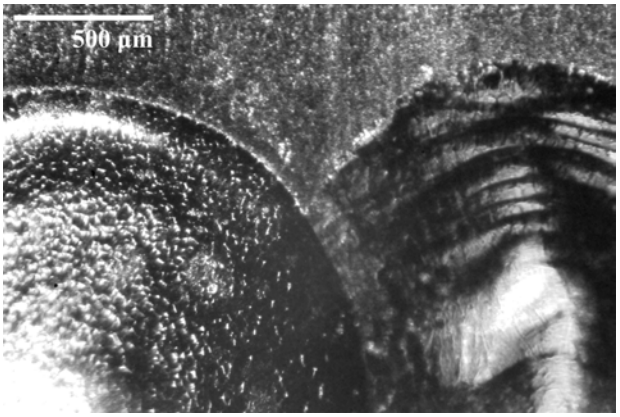

(a) Two overlapped laser tracks from above (optical microscope image).

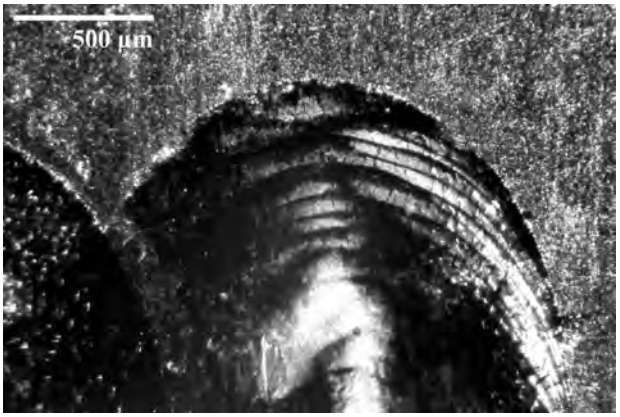

(b) Convex starting point of the laser track from above (optical microscope image).

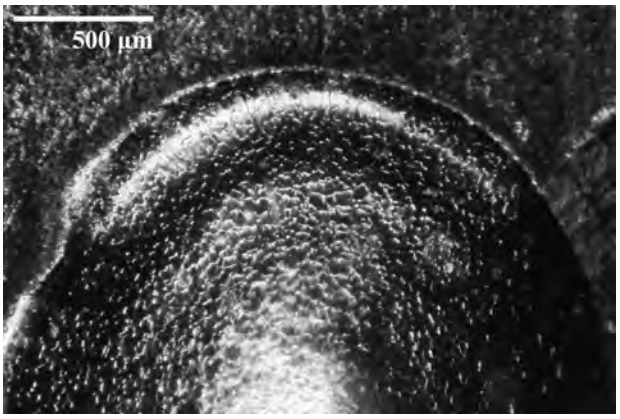

(c) Concave end point of the laser track from above (optical microscope image).

FIGURE 5.3: Optical microscope images from above (plane parallel to the laser track) of the two overlapped melt pools ($h = 1.00$ mm). (A): overlapping of the melt pools at the starting point, on the right, and at the end point, on the left. (B): convex starting point. (C): concave end point.

5.1.2 Parameter calibration, temperature profiles and cooling rates

Having a finite element model calibrated not only permits the model to match some experimental data, as the temperature, at the specific locations, but also to predict with sufficient precision the temperature field in every point of the domain and for every instant of time. The calibration of a thermal finite element model has been performed by an iterative semi-empirical procedure in a point P of the finite element model, as shown in Figure 5.5. However, it must be specified that the calibration results shown here are only valid for a specific set of physical conditions (*i.e.* laser speed s, laser power p, laser radius r, whose values are reported in Table 5.1).

The numerical parameters found by the iterative procedure are listed in Table 5.1 and only the parameter k_p in the Gaussian function has been progressively adjusted to match the experimental data as much as possible. However, a discrepancy between the model and the thermocouple-measured values still persists, as can be observed in the thermal profiles represented in Figure 5.7. Nevertheless, this difference is more pronounced during the last stage of the cooling process, while the peak temperature falls between the two experimental ones by choosing $k_p = 650$. This difference hardly exceed 5 °C, and the experimental data can also be affected by the accuracy of a K-type thermocouple, which is ±1.5 °C or $0.004T$ for $T > 375$ °C (Class 1) [256, p. 2962].

As anticipated before, a calibrated model permits to predict the temperature profile evolution in any point of the domain, so Figures 5.8, 5.9, 5.10 respectively represent the thermal profile and the corresponding cooling rate in the locations A, B and C of the laser track, for different hatch spacing values. The peak temperature predicted by the model after the calibration is consistent with the results obtained by Du *et al.* [249] at the centre of the scanning tracks during

powder deposition.

To analyse results, starting from the cooling rate evolution found, it can be defined a single cooling rate value for each condition. A summary of the cooling rates values, for each point within the track and for each hatch spacing, is therefore given in Table 5.2. Once calibrated the peak temperature for the laser source, the finite element model can be modified and a second laser pass with a varying hatch spacing value, according to the experimental programme, can now be introduced. Therefore, a temperature evolution profile can be determined for points A, B, and C for different hatch spacing values, as shown in Figures 5.8a, 5.9a, and 5.10a. Accordingly, once the thermal profiles have been determined for each location A, B, and C, for different hatch spacing values it is possible to determine the cooling rates, as shown in Subfigures 5.8b, 5.9b, and 5.10b.

From Figure 5.8, it can be seen as in the location A, at the centre of the melt pool, the material received the same amount of heat energy during the first and during the second laser scan. Progressively the temperature diminishes during the second scan, as the hatch spacing increased. Therefore, the second passage of the laser determined different cooling rates only during the second laser scan.

The condition is different in point B, at the intersection of the two laser tracks, where the thermal profiles and cooling rates are represented in Figure 5.9. The amount of heat absorbed during the two laser scans is almost the same and therefore the temperature profiles appear similar for each hatch spacing value. However, it can be observed that the temperature tends to increase slightly as a result of a superposition of heat energy.

The condition in point C, the inner point of the first laser track, is interesting, because the material is not melted by passage of the laser source. Indeed, this point lies within the so-called *heat affected zone*. The temperature shows a sensible increase in this point only as a consequence of the second laser passage and only the cooling rates obtained during this second scan are comparable to

η (-)	k_p (-)	p ($\mathrm{J\,s^{-1}\,m^{-3}}$)	r ($\mathrm{m^{-3}}$)	s ($\mathrm{m\,s^{-1}}$)	h_c ($\mathrm{J\,s^{-1}\,m^{-2}\,K^{-1}}$)
0.85	650	1000	0.001	1/30	20

TABLE 5.1: Numerical parameters adopted in the Gaussian heat source function to validate the finite element model, according to the thermal profiles obtained experimentally.

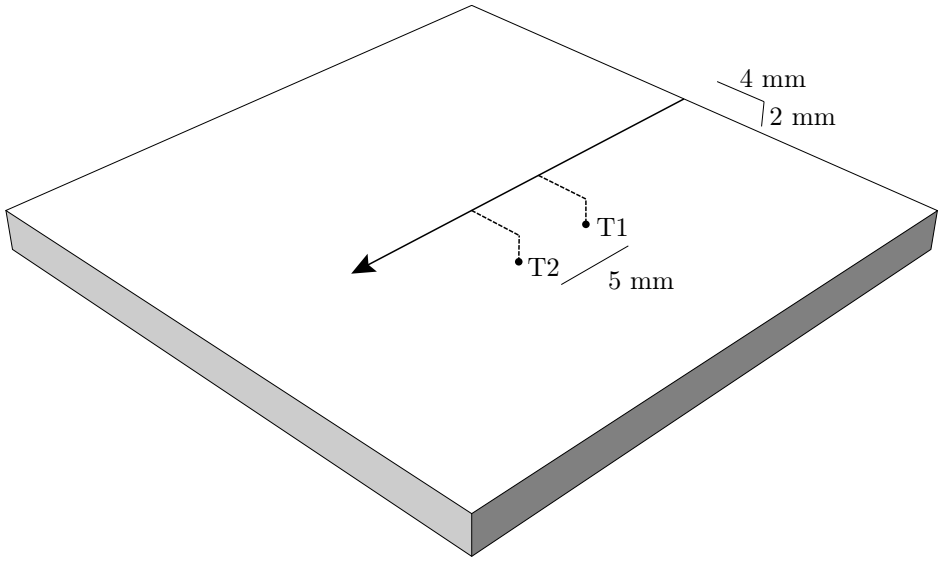

FIGURE 5.4: Spatial location of the two thermocouples T1 and T2 used for the calibration of the heat source (the arrow represents the direction of the laser).

those calculated in the other locations A and B.

As mentioned in the previous chapters, in order to have martensite generation within the laser track, two mathematical thermodynamical conditions have to be satisfied at the same time and they are expressed by the Equations (2.2). The first one states that the temperature must be above the martensite starting temperature $T_{m,s}$. As can be grasped by Figures 5.8, 5.9, this condition is verified immediately for both locations A and B. However, for location C, as in shown in Figure 5.10, this condition is verified only as a consequence of a second laser passage. The second condition for its generation is a cooling rate above the critical cooling rate, which is $\dot{T}_c = 410\ ^\circ\mathrm{C\,s^{-1}}$ for Ti-6Al-4V, and this condition is amply verified at all locations A, B, and C, since the first laser scan.

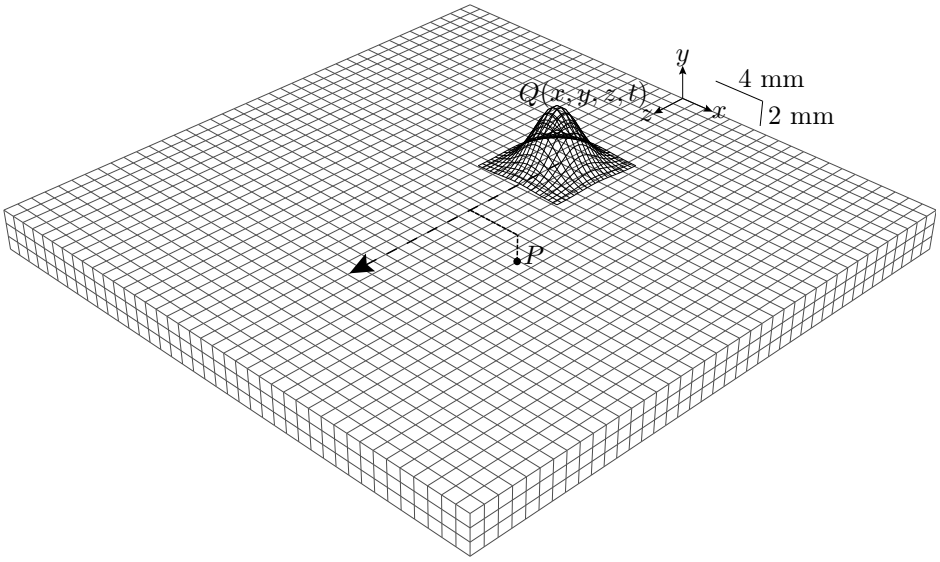

FIGURE 5.5: Spatial location of the point P in the finite element model used for the calibration of the heat source. The domain has the size of $40.0 \times 40.0 \times 3.0$ mm, the mesh consist of 6724 nodes and 4800 elements, and therefore each element is represented as a cube with a side of 1 mm.

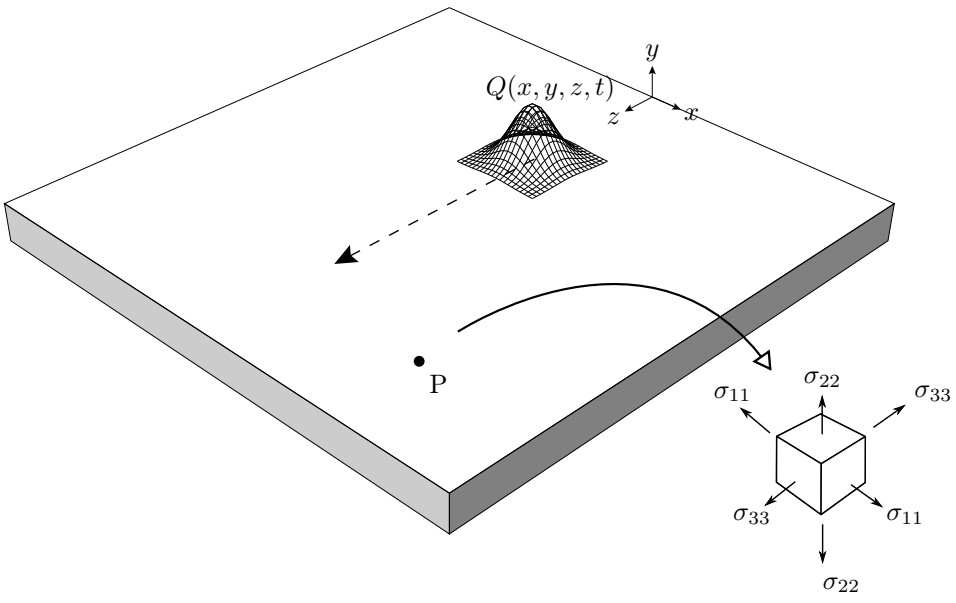

FIGURE 5.6: Stress convention adopted in this study, where the principal stresses $\sigma_{11}, \sigma_{22}, \sigma_{22}$ in the generic point P are represented for a reference cube. It is assumed that a positive stress value corresponds to a tensile stress.

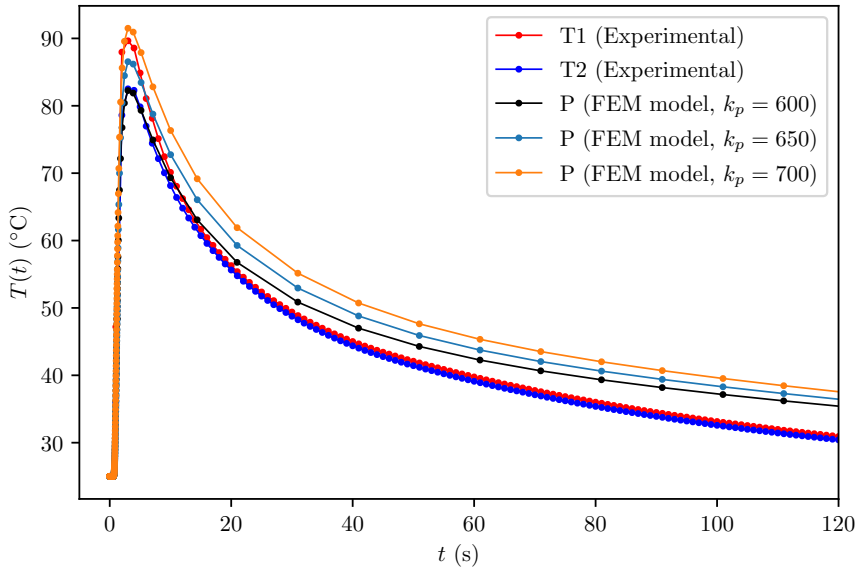

FIGURE 5.7: Temperature profile showing the result of the model calibration against two temperature profiles obtained by monitoring two different thermocouples T1 and T2. The maximum difference between the temperature predicted by the model and that measured by the two thermocouples occurs in the final stages of the cooling process.

5.2 Martensite dispersion and its impact on the residual stresses

According to the nomenclature provided schematically in Figure 5.11, it is possible to quantify the distribution and the shape of the martensite in the alloy, at different locations and for different hatch spacing values.

5.2.1 Martensite needle thickness

Since the different locations within the laser track correspond with different cooling rates, it is possible to describe the α' martensite needle thickness according to the formula given in Villa *et al.* (2020) [93, 94]. However, to better fit the

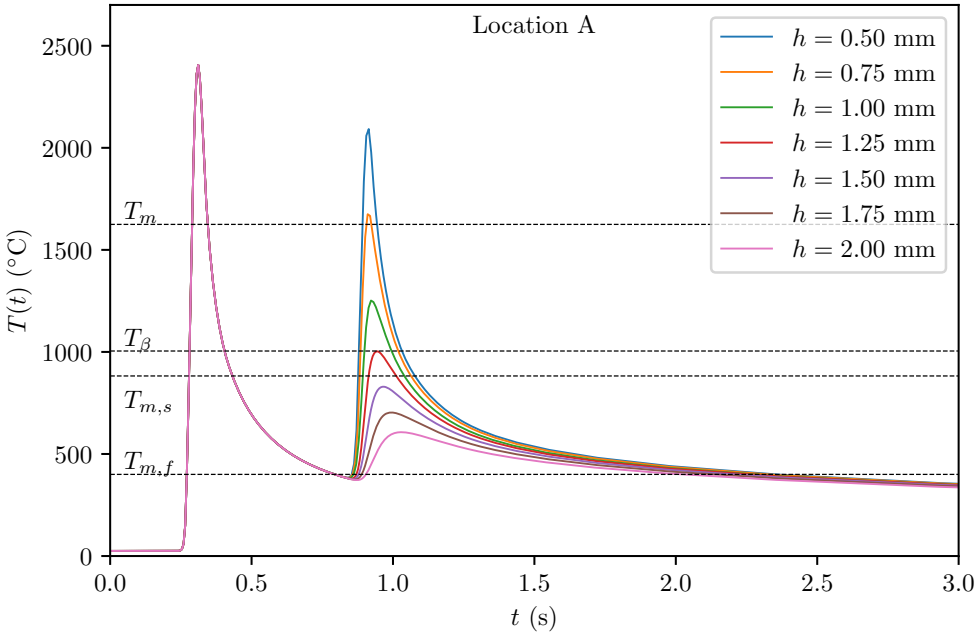

(a) Thermal profiles obtained by finite element analyses at the location A within the laser track.

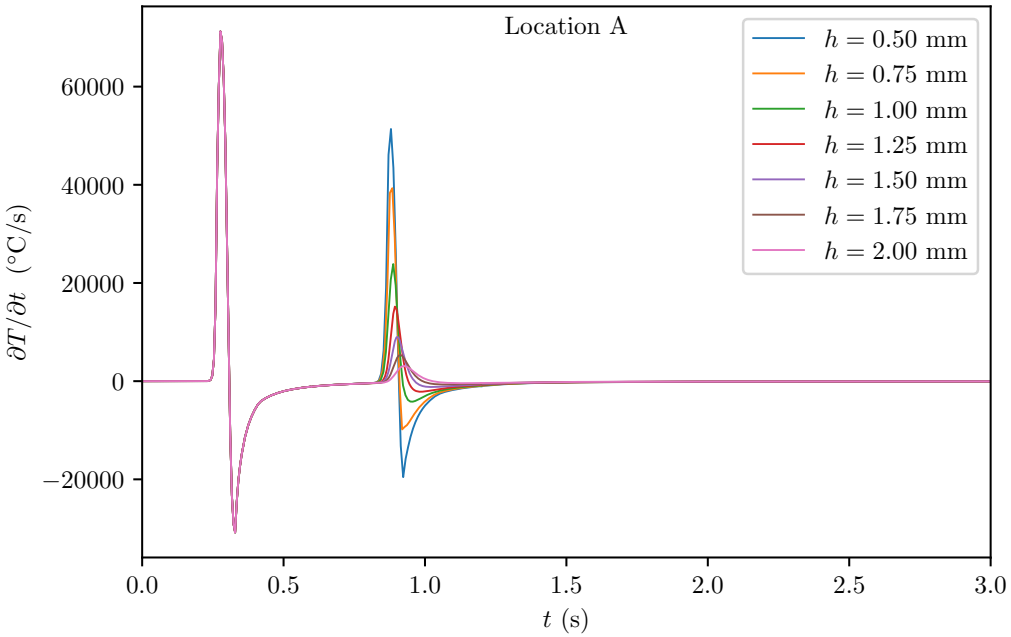

(b) Cooling rates obtained by finite element analyses at the location A within the laser track.

FIGURE 5.8: Thermal profiles and cooling rates obtained by finite element analyses at the location A within the laser track, for different hatch spacing values.

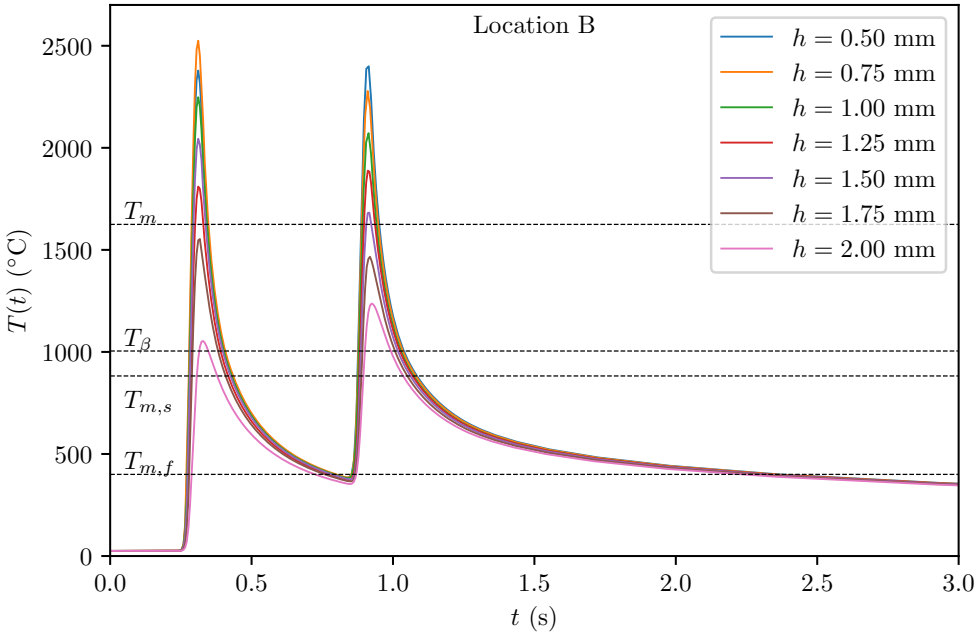

(a) Thermal profiles obtained by finite element analyses at the point B within the laser track.

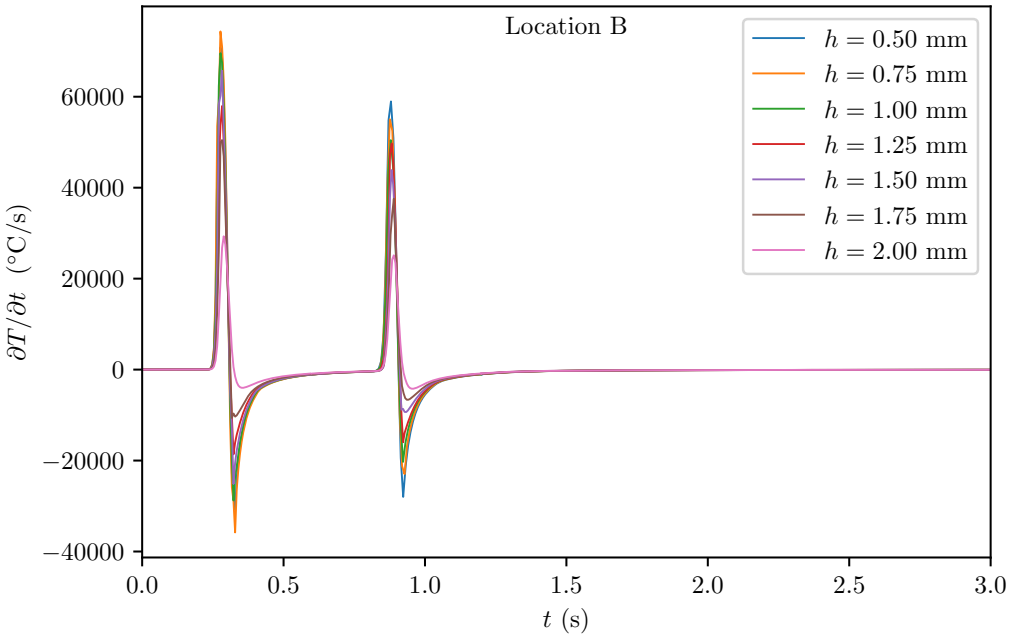

(b) Cooling rates obtained by finite element analyses at the point B within the laser track.

FIGURE 5.9: Thermal profiles and cooling rates obtained by finite element analyses at the point B within the laser track, for different hatch spacing values.

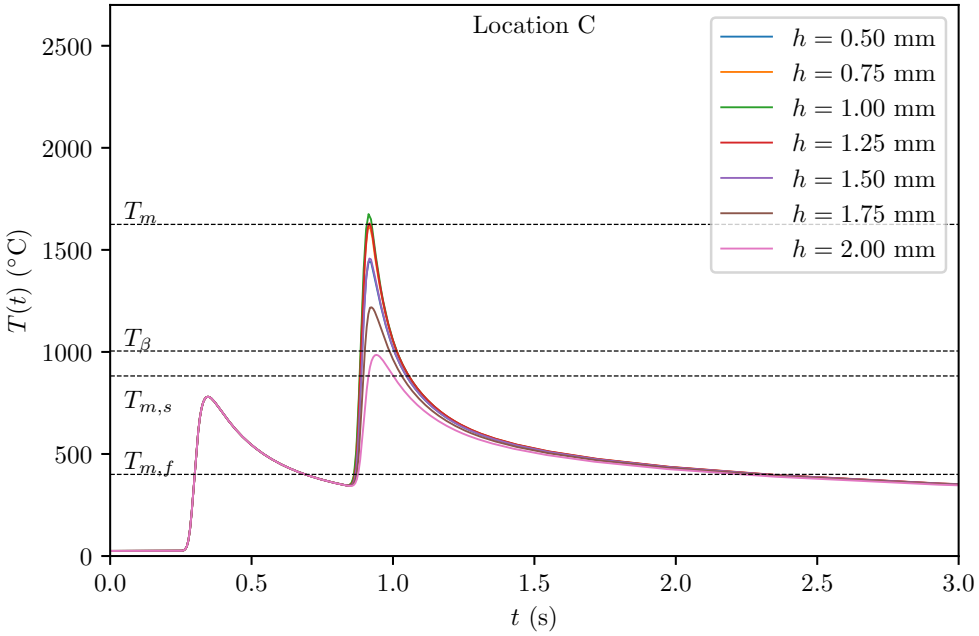

(a) Thermal profiles obtained by finite element analyses at the point C within the laser track.

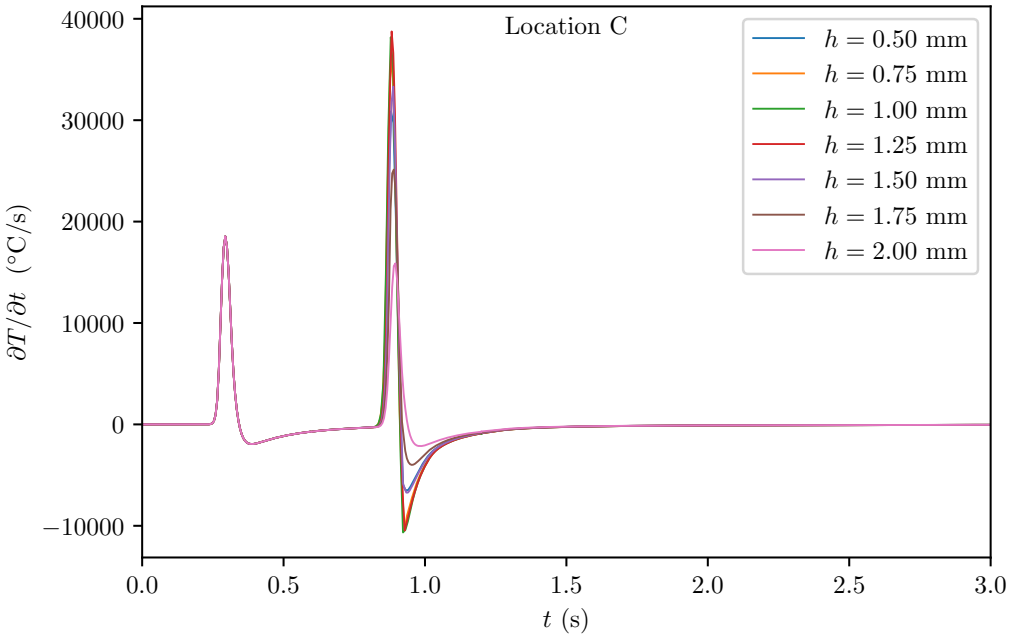

(b) Cooling rates obtained by finite element analyses at the point C within the laser track.

FIGURE 5.10: Thermal profiles and cooling rates obtained by finite element analyses at the point C within the laser track, for different hatch spacing values.

A		B		C	
h (mm)	$\partial T/\partial t$ (°C/s)	h (mm)	$\partial T/\partial t$ (°C/s)	h (mm)	$\partial T/\partial t$ (°C/s)
0.50	19753.75	0.50	19358.09	0.50	1222.58
0.75	1479.23	0.75	14434.88	0.75	9908.96
1.00	1285.01	1.00	17388.36	1.00	4472.38
1.25	639.78	1.25	968.83	1.25	3220.05
1.50	10905.15	1.50	8825.01	1.50	804.72
1.75	10905.15	1.75	3607.14	1.75	1255.42
2.00	10905.15	2.00	717.88	2.00	469.48

TABLE 5.2: Cooling rates obtained by the finite element analysis for the three locations (A, B, C) within the cross-section of the laser track, at different values of hatch spacing h, as calculated according to the scheme illustrating the experimental programme shown in Figure 4.1.

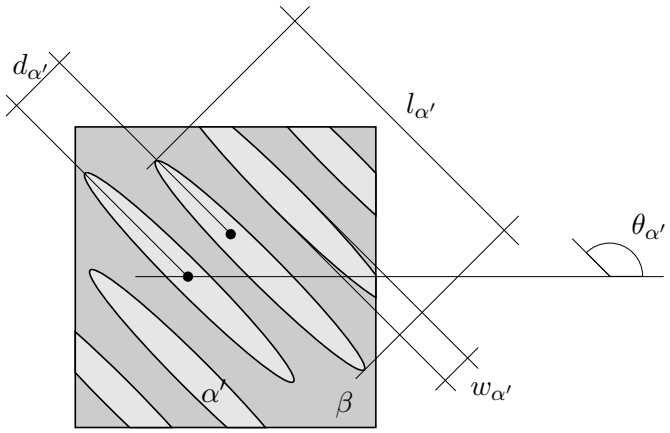

FIGURE 5.11: Schematic representation of the α' martensitic phase within the parent β-phase and nomenclature used for its quantitative analysis.

measurements obtained experimentally for each point within the laser track, for different values of hatch spacing, and shown in Table 5.3, such formula can be slightly re-adapted and restated in the form of the following:

$$w_{\alpha'} = a \log(\partial T / \partial t), \tag{5.1}$$

with the only constant $a = 0.056$ found by an iterative procedure, finally setting the residual $R = 0.000$ ($R = -2.434$ for the model elaborated in Villa *et al.* (2020) [93, 94]).

In Figures 5.12a, 5.13a, 5.14a a plot of the new expression can be found, alongside with experimental points and the equation given in Villa *et al.*, (2020) [93, 94] work, respectively for each point of interest within the laser track. For each point in the graphs is plotted the interquartile range (*i.e.* the spread of the middle half of data distribution).

Matching between the adapted formula proposed in this study, and the experimental measurements for each point of the laser track and for each hatch spacing value can be immediately appreciated by referring to the Figures 5.12, 5.13, 5.14, where the difference between the models and the experimental values (expressed in µm) and indicated as $|w_{\alpha',i} - \tilde{w}_{\alpha',i}|_{i=1}^{N}$ is plotted, where i is an integer index corresponding the current value of hatch spacing.

In general, it can be stated that the equation developed by Villa *et al.* (2020) [93, 94] is able to capture the thickness with a tolerable error for the different conditions, within the standard deviation values, however in some cases the difference becomes marked, as in location A and point B within the laser track, where the difference can be bigger than 0.35 µm. On the other hand, the equation developed by Villa *et al.* (2020) [93, 94] shows a better agreement, when compared to the present model, for higher values of hatch spacing for the inner location C.

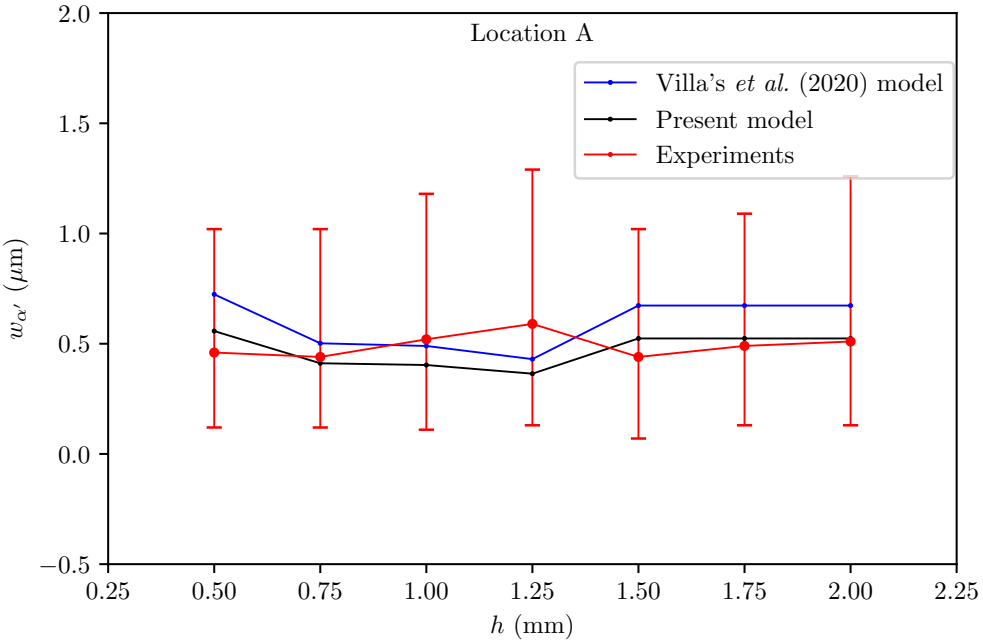

(a) Comparison between Villa *et al.* model (2020) [93, 94], experimental values and the model here proposed for α' martensite thickness in location A. The error bars indicates the lower and the upper quartile.

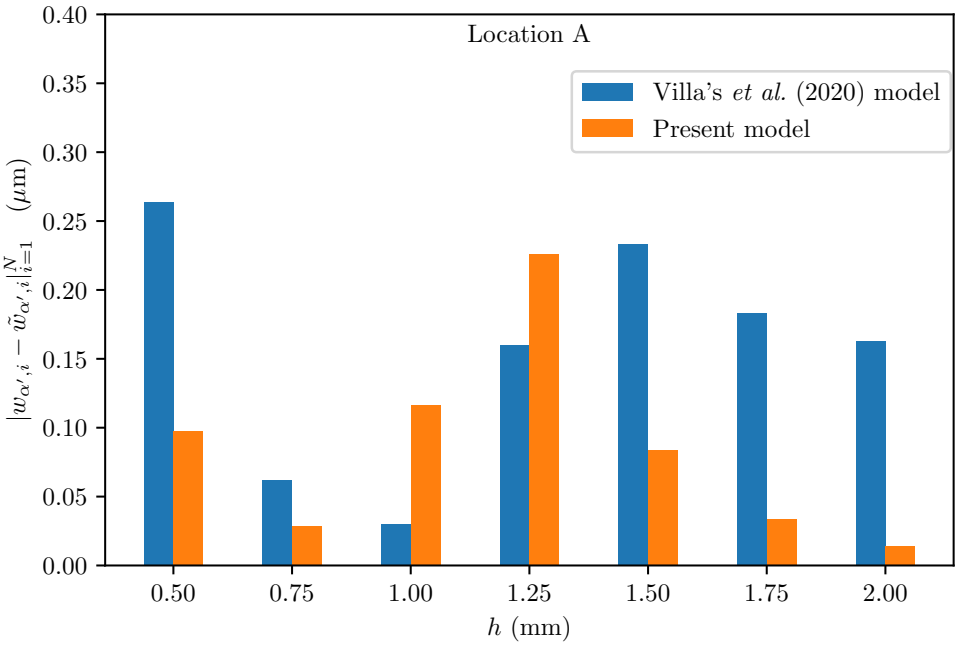

(b) Difference between experimental data and the two models, expressed in µm.

FIGURE 5.12: Comparison between Villa *et al.* model (2020) [93, 94], experimental values and the model here proposed for α' martensite thickness in location A.

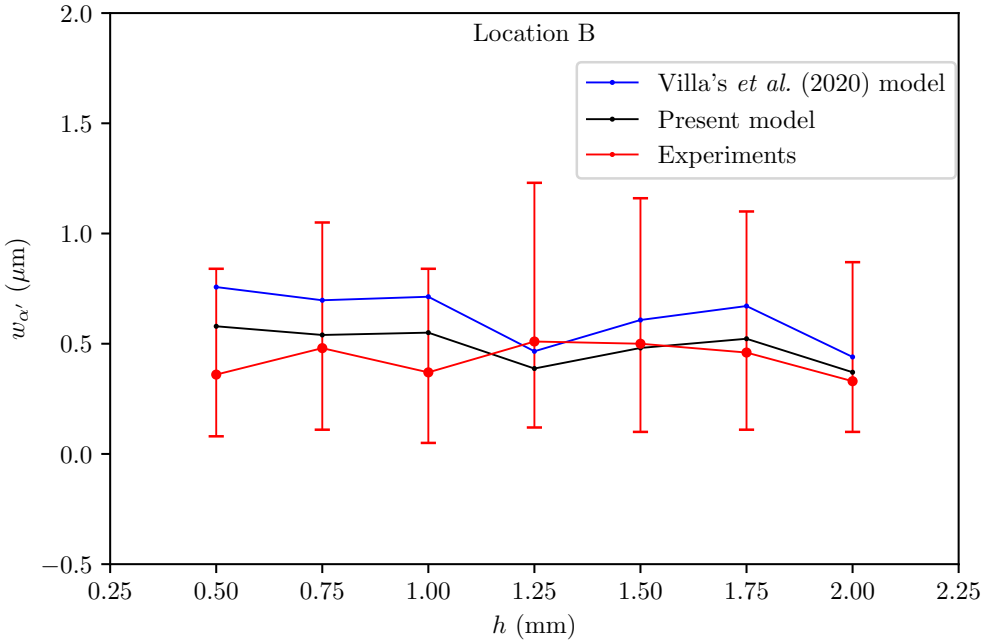

(a) Comparison between Villa *et al.* model (2020) [93, 94], experimental values and the model here proposed for α' martensite thickness in location B. The error bars indicates the lower and the upper quartile.

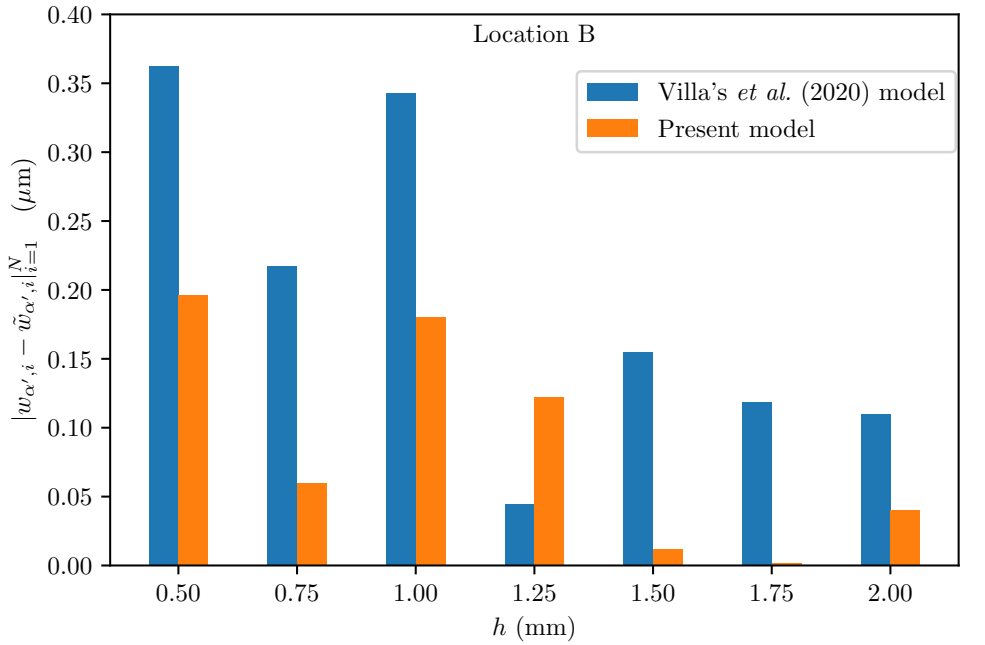

(b) Difference between experimental data and the two models, expressed in μm.

FIGURE 5.13: Comparison between Villa *et al.* model (2020) [93, 94], experimental values and the model here proposed for α' martensite thickness in location B.

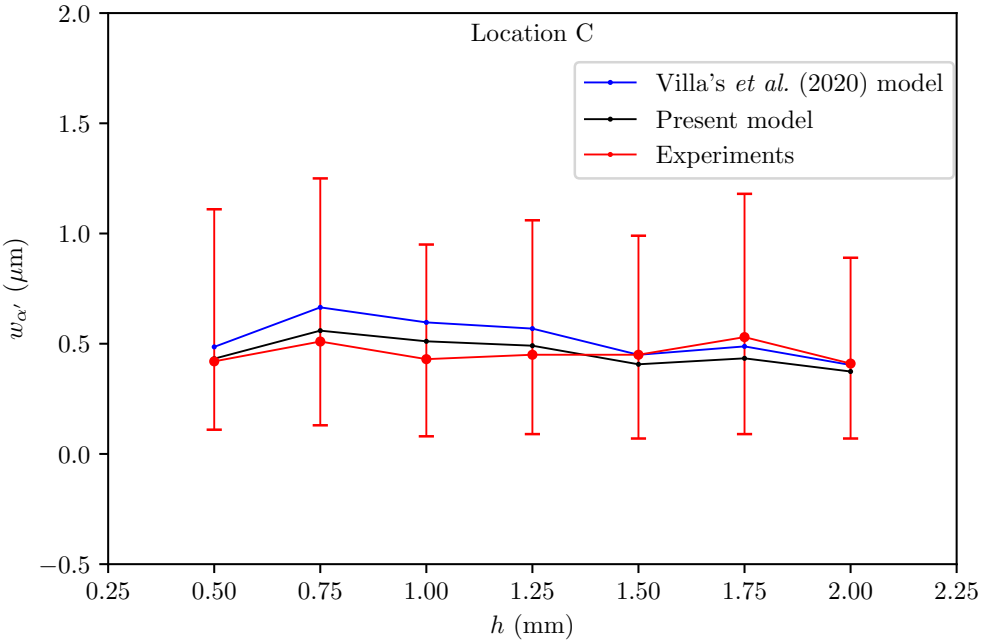

(a) Comparison between Villa *et al.* model (2020) [93, 94], experimental values and the model here proposed for α' martensite thickness in location C. The error bars indicates the lower and the upper quartile.

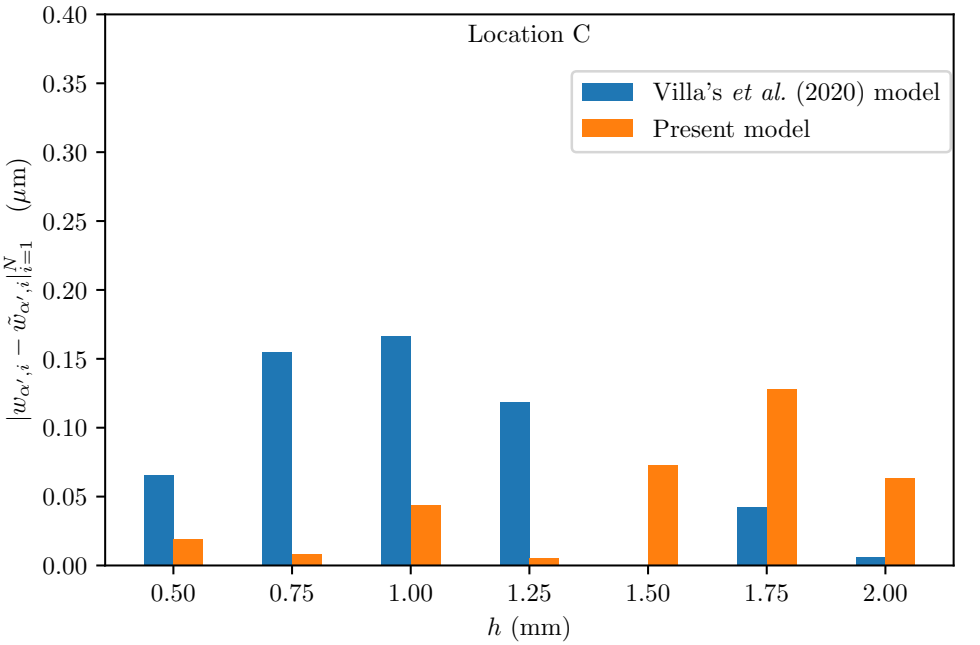

(b) Difference between experimental data and the two models, expressed in µm.

FIGURE 5.14: Comparison between Villa *et al.* model (2020) [93, 94], experimental values and the model here proposed for α' martensite thickness in location C.

	m (µm)			α (µm)		
h (mm)	A	B	C	A	B	C
0.50	0.46	0.36	0.42	0.55	0.43	0.65
0.75	0.44	0.48	0.51	0.63	0.48	0.54
1.00	0.52	0.37	0.43	0.39	0.51	0.31
1.25	0.59	0.51	0.45	0.25	0.37	0.40
1.50	0.44	0.50	0.45	0.45	0.39	0.09
1.75	0.49	0.46	0.53	0.31	0.62	0.50
2.00	0.51	0.33	0.41	0.86	0.20	0.51

TABLE 5.3: Experimental α' martensite thickness median value $w_{\alpha'}$ and standard deviation α for three locations in the melt pool (A, B, C), at different values of hatch spacing h.

5.2.2 Martensite volume fraction

The martensite volume fraction $V_{\alpha'}$ was measured from SEM using ImageJ software. This procedure has been completed for each point in the melt pool, repeated for three images acquired in each location, and for different values of hatch spacing. It should be emphasised that the value thus obtained is not exactly the fraction of volume, but only a fraction of area, because only a 2D surface was processed. However, this approximation was considered acceptable and from now on the two terms will be interchangeable.

In a first analysis, using a specific filter in ImageJ, only the area corresponding to the largest particles was taken into account, so as to approximately exclude all particles not immediately identifiable as the α' martensite. In a second analysis, the martensite volume fraction was measured by considering the area of all particles in the acquired images, thus calculating the total amount of the volume fraction, regardless of whether it was α', α'' and so on. Again, this is an approximation and more detailed studies are deferred to future work.

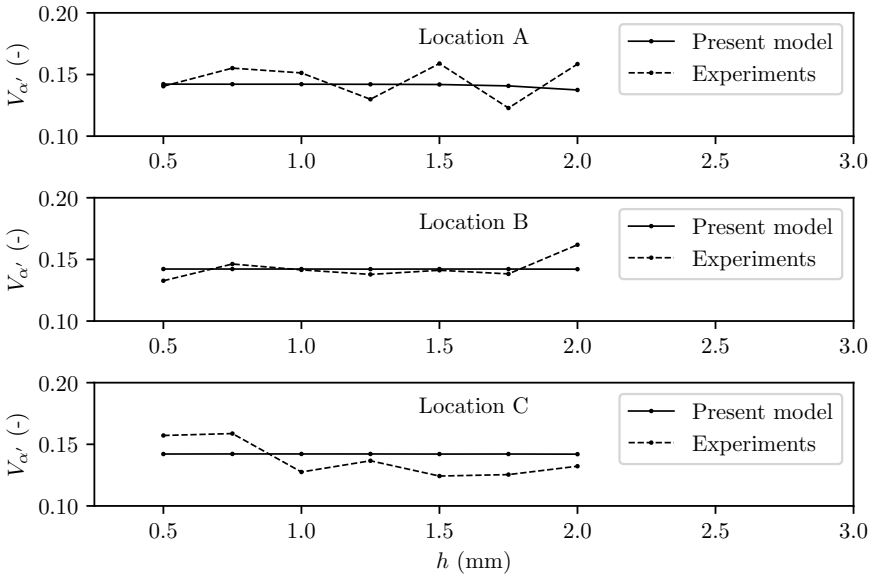

FIGURE 5.15: Martensite volume fraction model prediction for different hatch spacing values and different locations within the laser track (A, B, C), compared with experimental values.

Martensite α' volume fraction

The variation of the volume fraction with hatch spacing was found using the same iterative optimisation procedure already described. The equation was readjusted using the method of optimisation described by Equations (3.70) and (3.70), starting from the model given in Villa *et al.* (2020) [93, 94], where much higher values of martensite were found. Two constants were set equal to zero, obtaining the following function of the cooling rate:

$$V_{\alpha'}(\partial T/\partial t) = a \arctan\left(\frac{\partial T}{\partial t}\right), \tag{5.2}$$

where $a = 0.0905$. A near-zero residual has been reached after the optimisation ($R = -3.9 \times 10^{-14}$) and the new equation plotted together with the experimental data is represented in Figure 5.15.

Additionally, upon critically analysing the experiments performed it was observed that the different values of α' martensite volume fraction at room tempera-

ture fall near the expected value predicted by the Koistinen-Marburger model [99] with a coefficient $\chi = 0.0030$, as suggested in the literature [100, 101]. However, there is a little variation of the data around the expected behaviour, such that it is possible to define an upper and a lower bound, respectively obtained by setting $\chi = 0.0018$ and $\chi = 0.0040$. In terms of volume fraction at room temperature, if i is the generic measure of volume fraction in the entire series of experiments S, a minimum and a maximum value has been found, respectively:

$$\min\{V_{\alpha',i}\}_{i=1}^{N} \approx 0.1228; \tag{5.3a}$$

$$\max\{V_{\alpha',i}\}_{i=1}^{N} \approx 0.1619. \tag{5.3b}$$

On the other hand, the expected ideal value was $V_{\alpha'} \approx 0.1528$. Therefore, the evolution described by the Koistinen-Marburger [99] model can be considered quite accurate, provided one takes into account the fact that the values may fall within a specific range, identifiable with an upper and a lower bound. The predicted temperature evolution of the volume fraction is represented in Figure 5.16, together with the experimental points measured at room temperature, bounded by the two extreme curves representing the upper and lower bound. An enlarged scale of the region at room temperature can be viewed in Figure 5.18, where the data are represented with different colours according to the hatch spacing values.

The data obtained from the experiments can be further disaggregated to better clarify the underlying trend and see if other considerations can be extrapolated. In terms of the martensite volume fraction, in particular, the volume fraction obtained for lower values of hatch spacing ($h = 0.50$ mm and $h = 0.75$ mm) can be separated in two different plots from those obtained for higher hatch spacing values ($h = 1.75$ mm and $h = 2.00$ mm), as in the Figure 5.19 and 5.20. In addition, this means that data can be differentiated according to position within the melt pool, as represented in the Figures 5.21, 5.22, 5.23.

A number of useful considerations can be drawn from these analytical approaches. Firstly, the spread in the volume fraction prediction is larger when the

distance between the laser scans is higher and therefore the Koistinen-Marburger model works better for lower values of this distance. Secondly, the spread does not appear to depend on the position within the melt pool, so there is no single point within the laser track where the Koistinen-Marburger model performs best, although the spread is slightly lower at location B, at the centre of the intersections of the two melt pools.

An additional numerical study has been performed to better elucidate the martensite formation process within the melt pool during a single laser track, taking into account a time-dependent Koistinen-Marburger model [99], as already introduced in Equation (2.7). This was done by implementing the Koistinen-Marburger model for each time increment within a finite element model using a HETVAL subroutine. According to the results obtained, it was found that the α' martensite starts growing firstly at the interface between the melt pool and the solid material and as the heat source moves the solidification front advances and then the martensite starts forming, as shown in Figure 5.17. At the end of the process, the last position where the martensite grows is exactly at the middle of the melt pool. The formation of martensite is therefore a process that takes place from the outside inwards and this may explain, at least partially, the small differences between the outer and inner needles and the fact that they are rotated and not perpendicular to the laser source.

Martensite total volume fraction

In the present study, it was observed that the total volume fraction of the martensite is quite high, showing a sensible variation with the hatch spacing parameter. This susceptibility contrast with the almost flat behaviour just found for the α' particles. This means that increasing the hatch spacing distance produces a predominant finer microstructure., whose influence on mechanical behaviour needs to be assessed in future works.

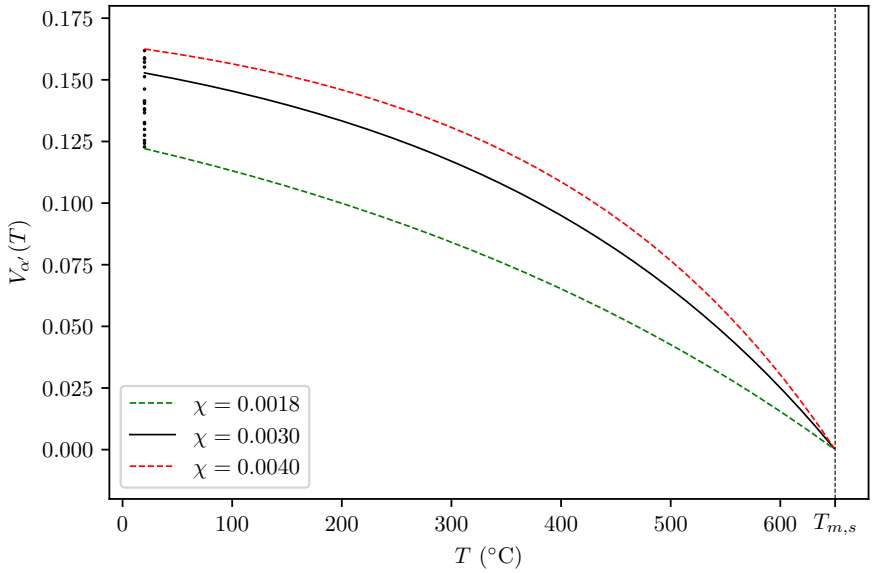

FIGURE 5.16: Martensite volume fraction $V_{\alpha'}(T)$ evolution with temperature according to the Koistinen-Marburger model and the experimental values measured at room temperature, for different locations within the laser track for different values of the hatch spacing, within the upper bound (red) and lower bound (green). The value $\chi = 0.003$ is estimated for Ti-6Al-4V in some studies as [100] (laser forming) and [101] (laser metal deposition), whereas in others $\chi = 0.005$ was proposed [102] (additive manufacturing).

5.2.3 Martensite needle spacing

Starting from the model proposed for the α' martensite thickness and the results obtained for the volume fraction, the spacing between two arbitrary martensite laths can now be calculated according to the Equations (3.65) and (3.69) and at the same time compared with experimental measurements.

Overall, it can firstly be observed that in most cases the first model predicts slightly higher martensite spacing values than experimental data suggests. On the other hand, the values predicted by the first model are always higher than those predicted by the second, so that the experimental data often lie between predictions from the two models. In relation to this fact, it can be said that a

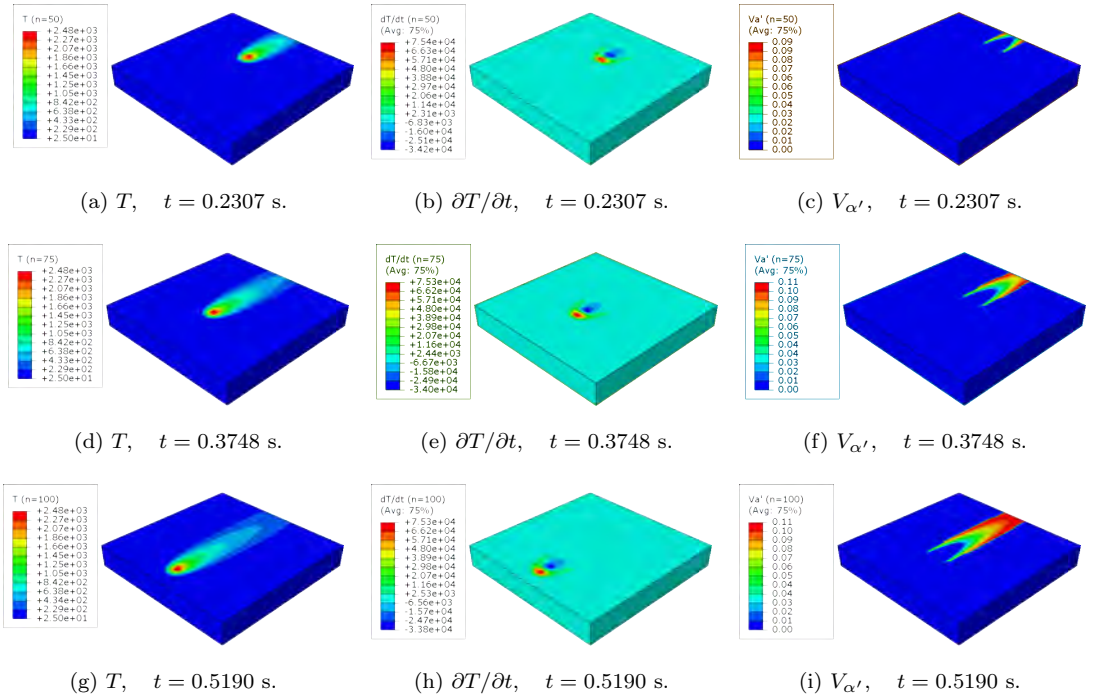

(a) T, $t = 0.2307$ s. (b) $\partial T/\partial t$, $t = 0.2307$ s. (c) $V_{\alpha'}$, $t = 0.2307$ s.

(d) T, $t = 0.3748$ s. (e) $\partial T/\partial t$, $t = 0.3748$ s. (f) $V_{\alpha'}$, $t = 0.3748$ s.

(g) T, $t = 0.5190$ s. (h) $\partial T/\partial t$, $t = 0.5190$ s. (i) $V_{\alpha'}$, $t = 0.5190$ s.

FIGURE 5.17: Numerical study of the martensite formation process during a single laser scan. Here is represented the temperature distribution (on the left, in °C), the temperature rate distribution (on the middle, in °C/s), and the α' martensite volume fraction distribution (on the right) on the surface of a Ti-6Al-4V volume element during the laser scan modelled as a travelling Gaussian heat source, at different time increments.

possible advantage of using the two models may be that they are complementary and they can offer a good upper and lower bound estimate of the real data. Nevertheless, it cannot be ignored that the first model is more accurate than the second one, especially because every value predicted by the first model is within the confidence interval demarcated by the percentiles of the skew Gaussian distribution. The finding that the first model is preferable to the second one is corroborated by observing Figures 5.24, 5.25, and 5.26 where the histograms show the absolute value of the difference between the theoretical and experimental value, *i.e.* $|d_{\alpha',i} - \tilde{d}_{\alpha',i}|$, where $\tilde{d}_{\alpha',i}$ is the i-th experimental value.

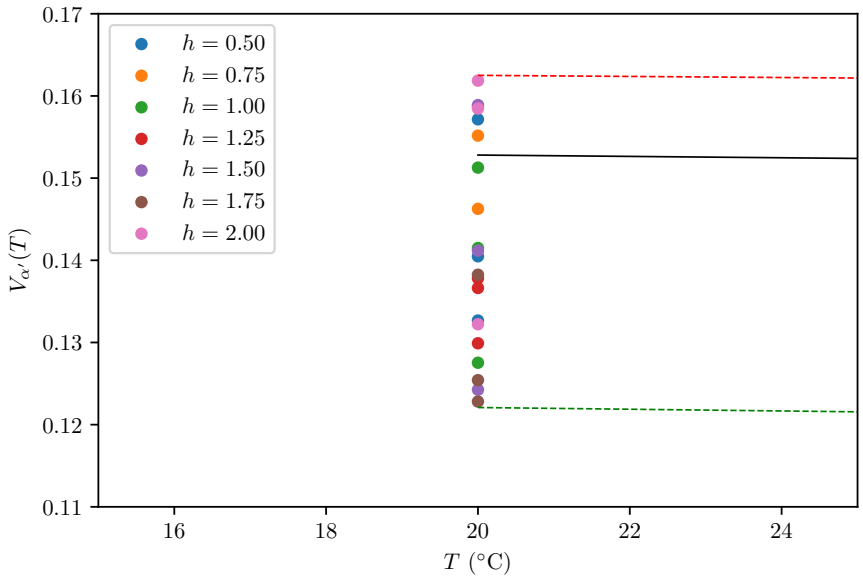

FIGURE 5.18: Martensite volume fraction $V_{\alpha'}(T)$ experimental measurements arranged by hatch spacing value h, measured at room temperature.

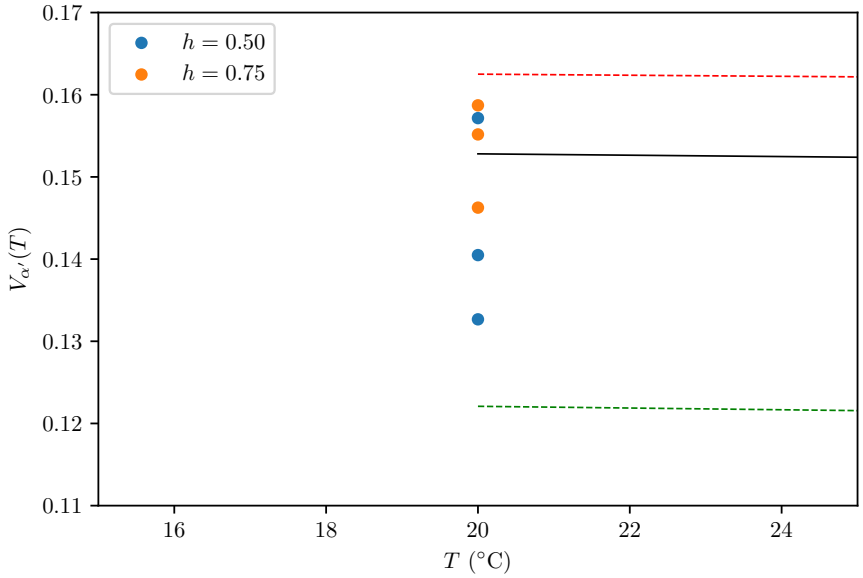

FIGURE 5.19: Martensite volume fraction $V_{\alpha'}(T)$ experimental measurements for lower values of hatch spacing h, measured at room temperature.

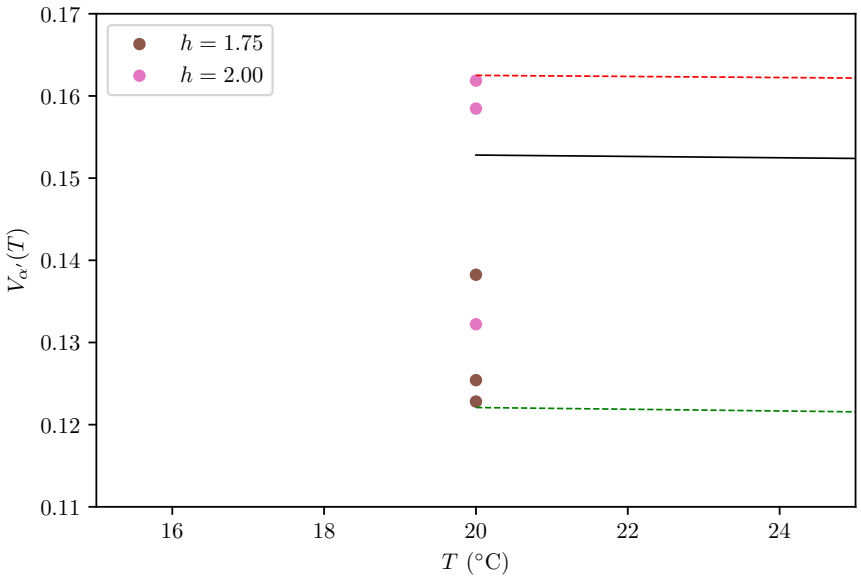

FIGURE 5.20: Martensite volume fraction $V_{\alpha'}(T)$ experimental measurements for higher values of hatch spacing h, measured at room temperature.

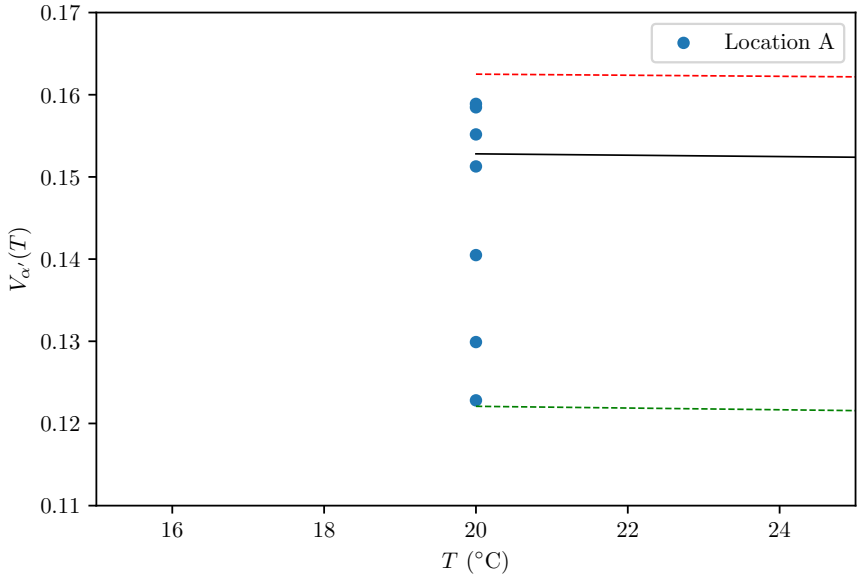

FIGURE 5.21: Martensite volume fraction $V_{\alpha'}(T)$ experimental measurements for the location A, measured at room temperature (different hatch spacing values are plotted).

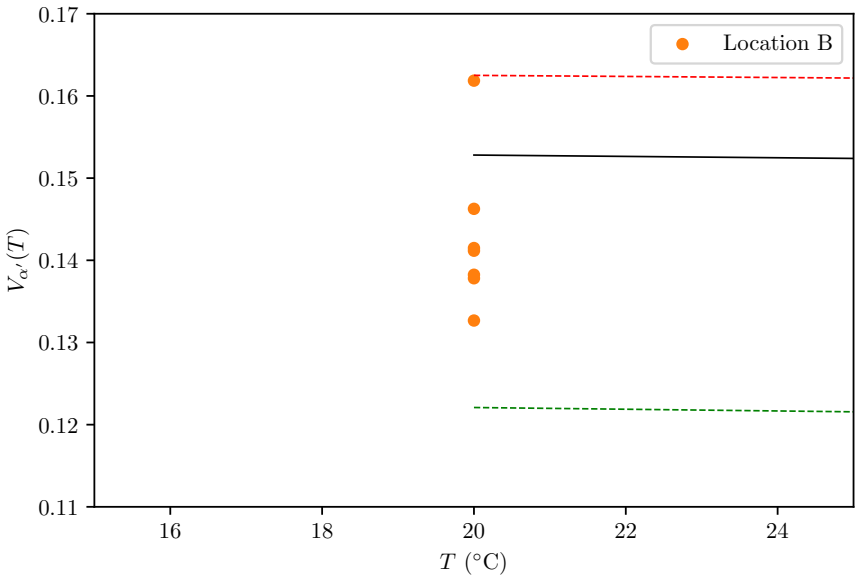

FIGURE 5.22: Martensite volume fraction $V_{\alpha'}(T)$ experimental measurements for the point B, measured at room temperature (different hatch spacing values are plotted).

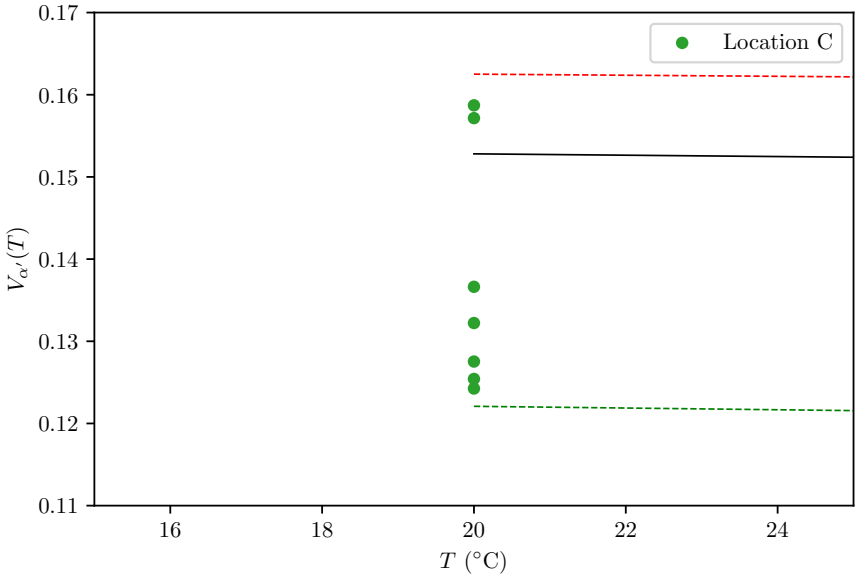

FIGURE 5.23: Martensite volume fraction $V_{\alpha'}(T)$ experimental measurements for the point C, measured at room temperature (different hatch spacing values are plotted).

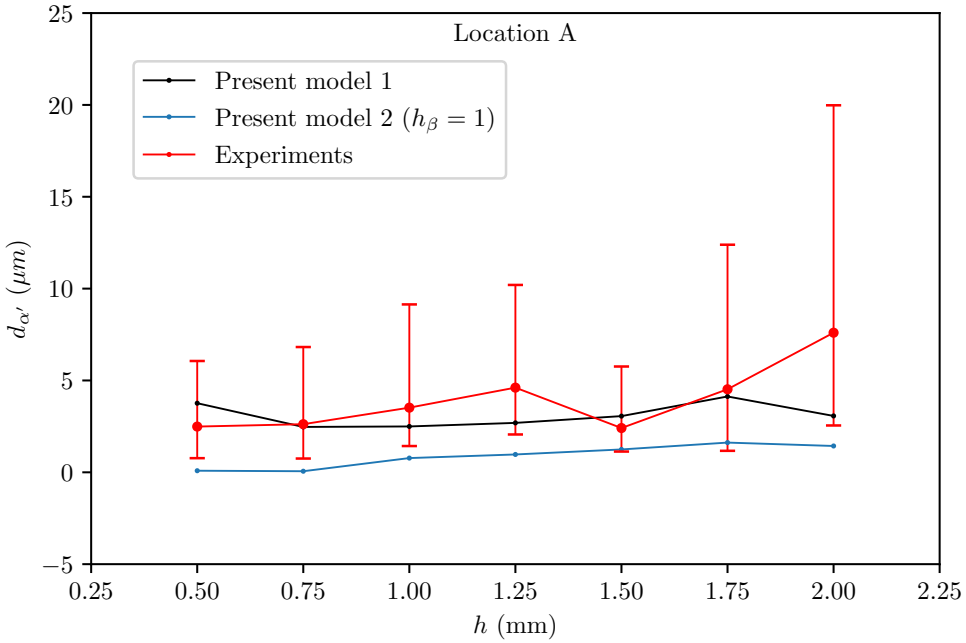

(a) Comparison between experimental values and the two models proposed in the present work for α' martensite spacing in location A. The error bars indicates the lower and the upper quartile.

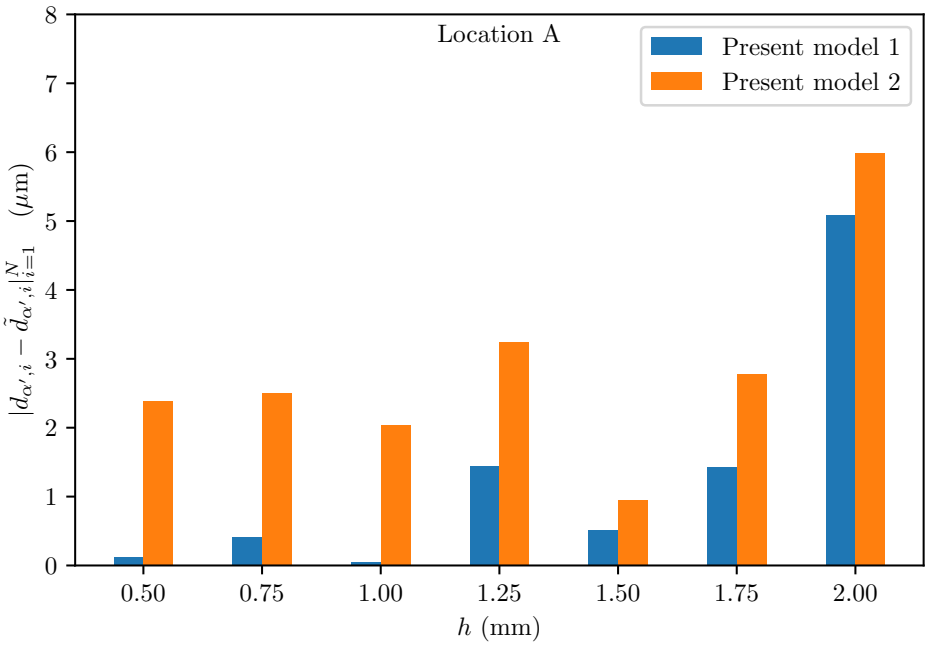

(b) Difference between experimental data and the two models, expressed in µm.

FIGURE 5.24: Comparison between experimental values and the two models proposed in the present work for α' martensite spacing in location A.

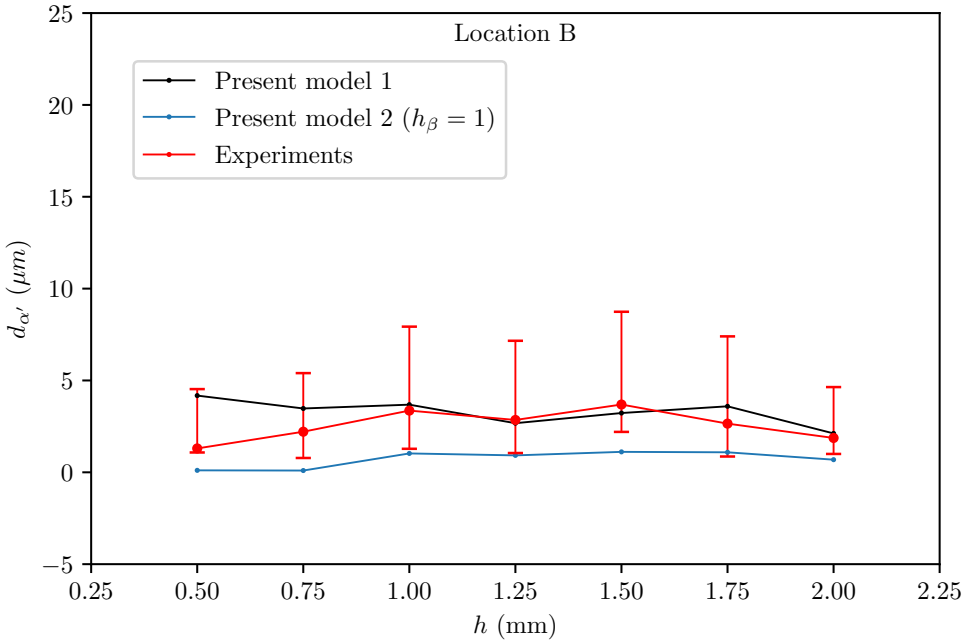

(a) Comparison between experimental values and the two models proposed in the present work for α' martensite spacing in location B. The error bars indicates the lower and the upper quartile.

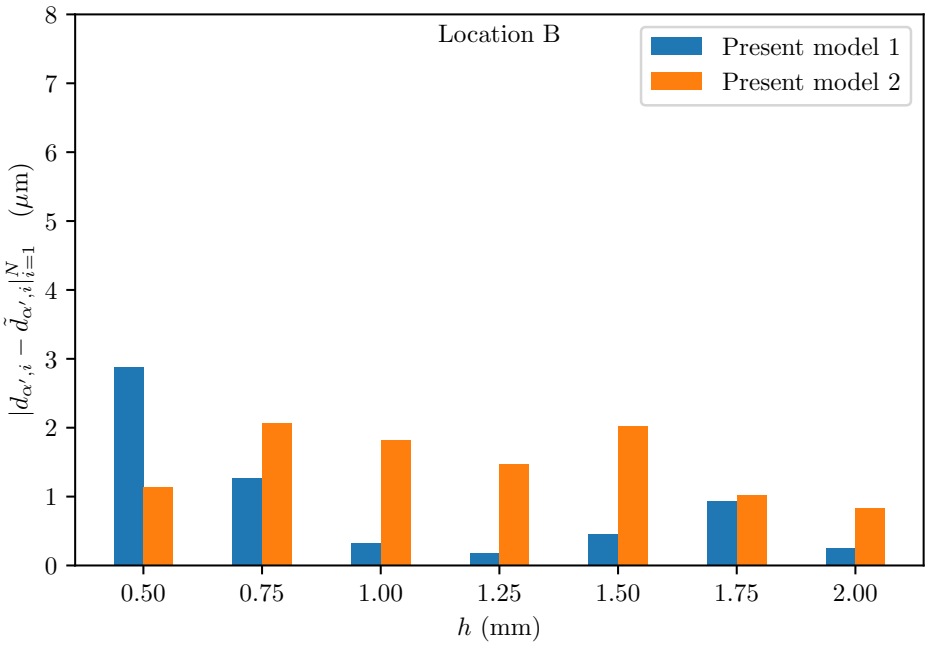

(b) Difference between experimental data and the two models, expressed in µm.

FIGURE 5.25: Comparison between experimental values and the two models proposed in the present work for α' martensite spacing in location B.

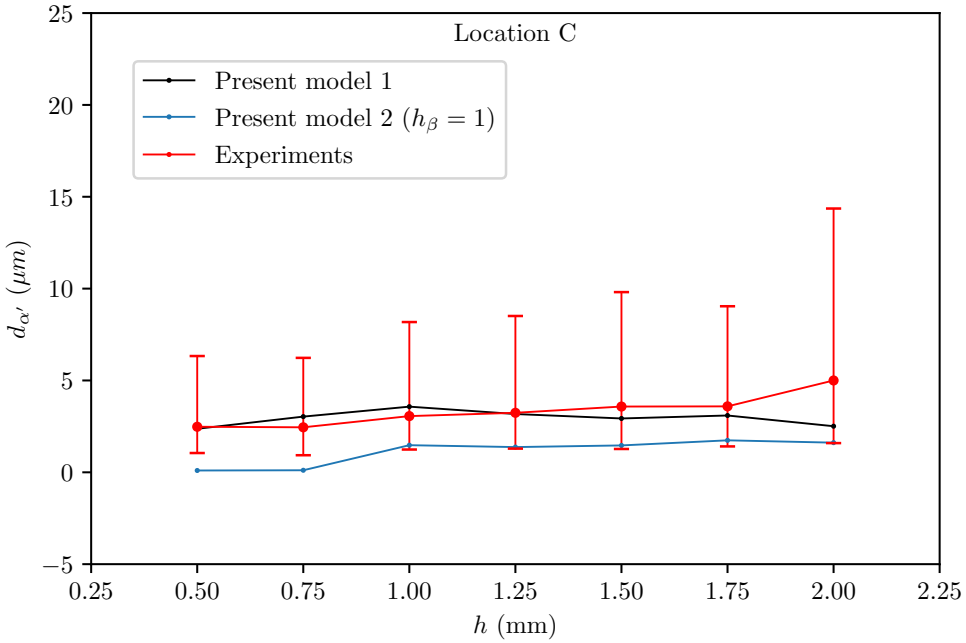

(a) Comparison between experimental values and the two models proposed in the present work for α' martensite spacing in location C. The error bars indicates the lower and the upper quartile.

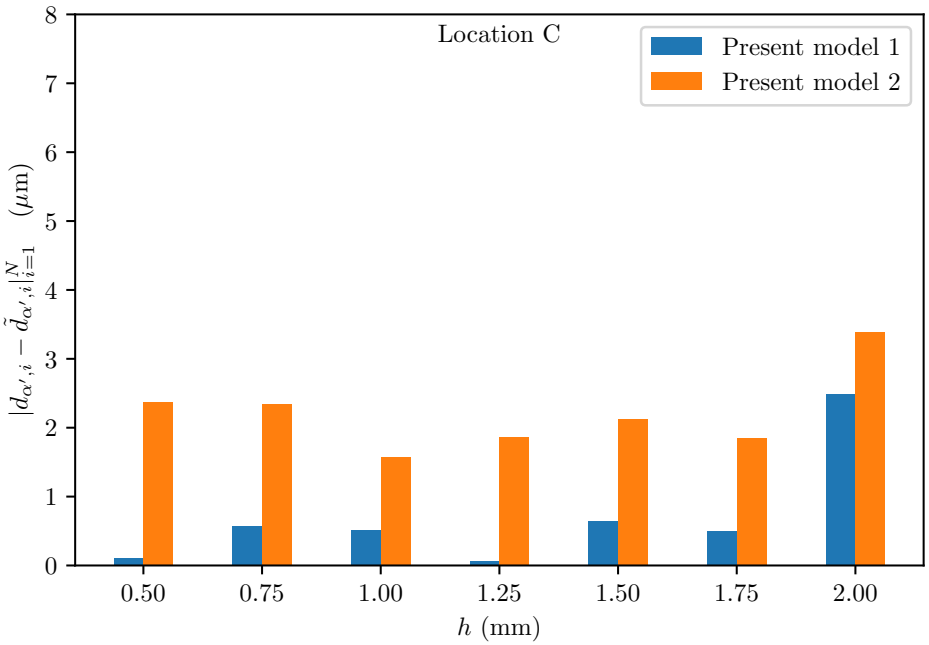

(b) Difference between experimental data and the two models, expressed in µm.

FIGURE 5.26: Comparison between experimental values and the two models proposed in the present work for α' martensite spacing in location C.

	m (µm)			α (µm)		
h (mm)	A	B	C	A	B	C
0.50	2.93	0.83	2.68	0.49	1.67	0.51
0.75	2.37	2.25	1.90	0.83	0.56	0.79
1.00	3.67	2.65	2.96	0.59	0.64	0.73
1.25	5.16	2.86	2.75	0.51	0.59	0.69
1.50	1.86	2.97	3.81	0.77	0.72	0.60
1.75	4.88	1.96	2.57	0.67	0.91	0.81
2.00	8.63	1.65	5.53	0.55	0.88	0.54

TABLE 5.4: Experimental α' martensite spacing median value m and standard deviation α for three locations in the melt pool (A, B, C), at different values of hatch spacing h in mm.

5.2.4 Initial dislocation density and residual stresses

In the light of the discussion in this study, the initial dislocation density formula given in [88] can be rewritten by including the new expressions for martensite thickness $w_{alfa'}$ and spacing $d_{alfa'}$, using the first model, given by the Equation (3.65):

$$\begin{aligned} \rho_0 &= \frac{12Ew_{\alpha'}}{(1+2\nu)\mu b}\frac{\epsilon_0}{{d_{\alpha'}}^2} \\ &= \frac{12E(a\log(\partial T/\partial t))}{(1+2\nu^2)\mu b}\frac{\epsilon_0}{(c\log(\partial T/\partial t))^2}, \end{aligned} \tag{5.4}$$

where $a \approx 5.64 \times 10^{-2}$ is the calibration constant found for $w_{\alpha'}$, and $c = [a(1 - V_{\alpha'})/V_{\alpha'}]$. Therefore, the initial dislocation density now explicitly depends solely on the cooling rate, and the modified formula becomes:

$$\rho_0 = \frac{k_c(p,s)E\epsilon_0}{(1+2\nu)\mu|b|\log(\partial T/\partial t)}, \tag{5.5}$$

where the cooling rate coefficient $k_c(p,s) = 12a/c^2$ just introduced is, in general, a function of the laser power p and on the laser speed s. For the conditions tested in this study ($p = 1000$ W, $s = 2000$ mm/min), assuming, for example,

as α' martensite volume fraction $V_{\alpha'} \approx 0.475$, this coefficient is $k_c \approx 175$. As a consequence, the formula for the initial dislocation density for Ti-6Al-4V no longer depends on the α' martensite shape and distribution, but only on the cooling rate. Since the cooling rate depends on the point where it is calculated within the material, this formula now allows to consider the spatial dependence of the initial dislocation density.

The constitutive model for Ti-6Al-4V with the modified formula for dislocation density dependent on the cooling rate has been used to evaluate the vertical residual stresses σ_{22} as function of the hatch spacing values, at different locations within the laser track. The results are plotted in Figure 5.29. As expected, the vertical residual stress σ_{22} values in location A and C does not differ too much from each other, whereas these obtained in location B (*i.e.* at the centre of the overlap area) are quite different from them. Indeed, the vertical residual stress (σ_{22}) is lower, indicating that within the overlap area the influence of the residual stress in the scanning direction and of that perpendicular to it, in the same plane, has a bigger impact. Moreover, it can be observed that the vertical residual stress is lower if the hatch spacing values are lower, so there is a small increase until the influence of the second melt pool becomes negligible.

Looking at the spatial profiles of residual stresses developed for different hatch spacing values, it can be observed the presence of a shift of the peak von Mises stress and a more jagged profile for the vertical residual stress as the hatch spacing increases (Figure 5.30). This jaggedness can also be due to the element size, which could be decreased as the hatch spacing value increases, in order to obtain more accuracy.

5.2.5 Other experimental observations

Additional microstructure findings were also obtained during the analysis of the SEM micrographies, such as the total α-martensite volume fraction, the marten-

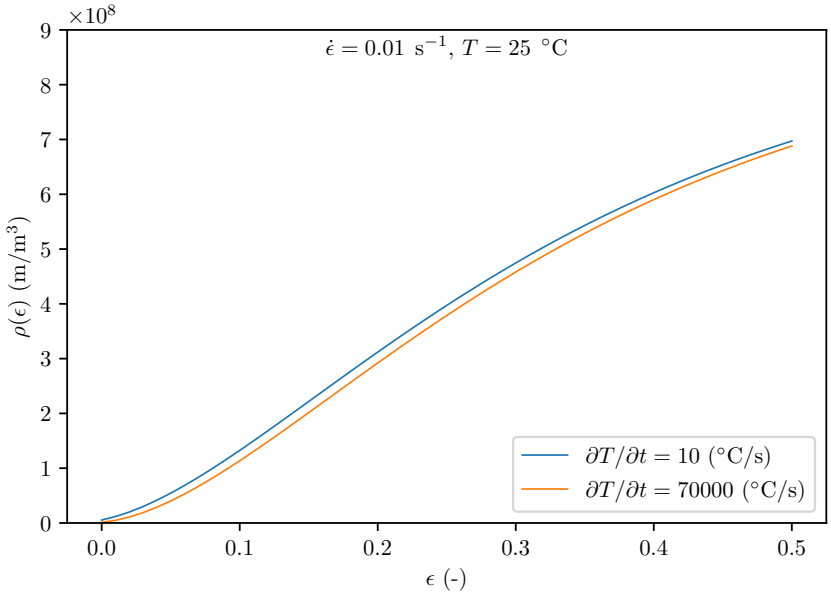

(a) Dislocation density evolution at different cooling rates and for low temperature.

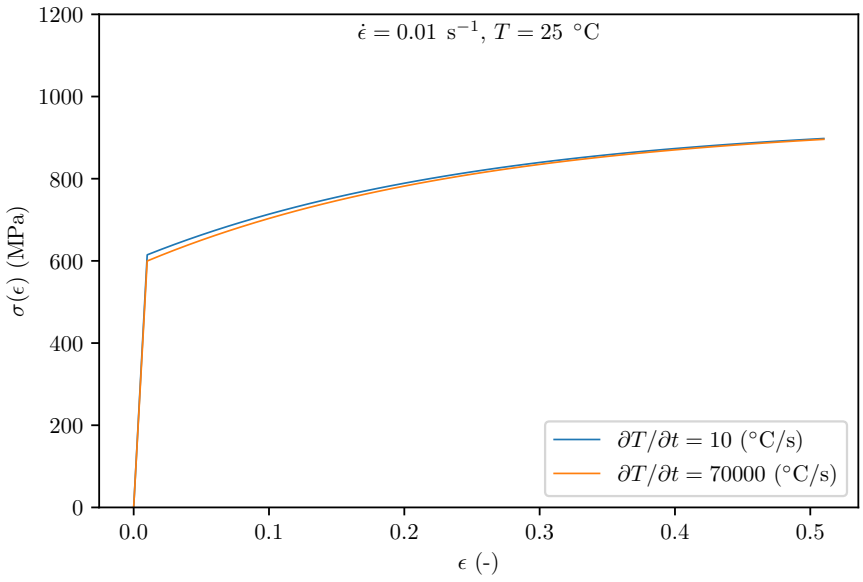

(b) Flow stress curves response in Ti-6Al-4V at different cooling rates and for low temperature.

FIGURE 5.27: Dislocation density evolution and associated flow stress curves response in Ti-6Al-4V at different cooling rates and for low temperature, according to Galindo-Fernández *et al.* (2018) constitutive model for Ti-6Al-4V (2018) with the new formula for the initial dislocation density introduced in this study.

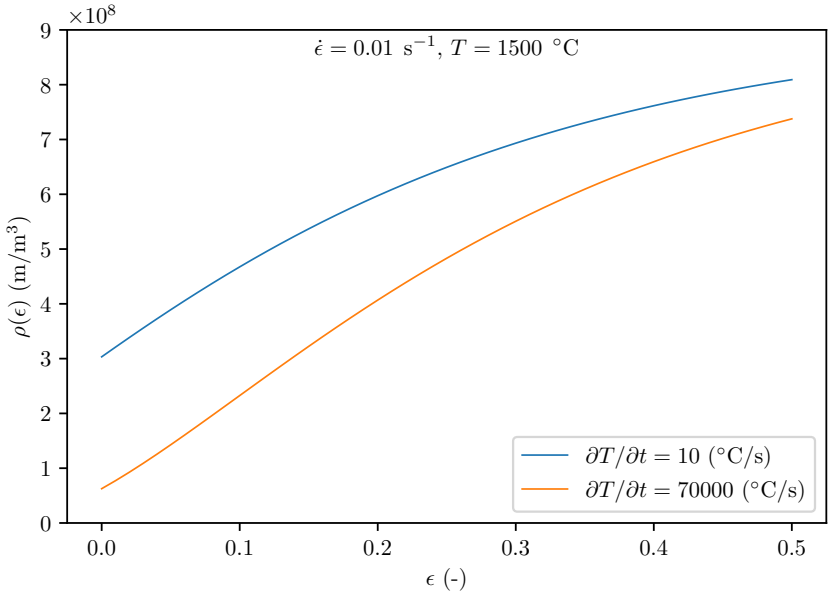

(a) Dislocation density evolution at different cooling rates and for high temperature.

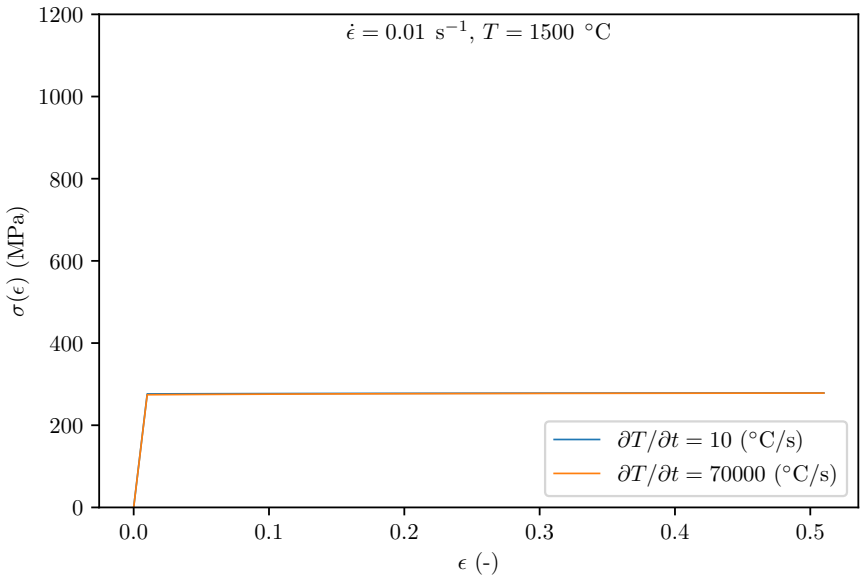

(b) Flow stress curves response in Ti-6Al-4V at different cooling rates and for high temperature.

FIGURE 5.28: Dislocation density evolution and associated flow stress curves response at different cooling rates and for high temperature, according to Galindo-Fernández *et al.* (2018) constitutive model for Ti-6Al-4V (2018) with the new formula for the initial dislocation density introduced in this study.

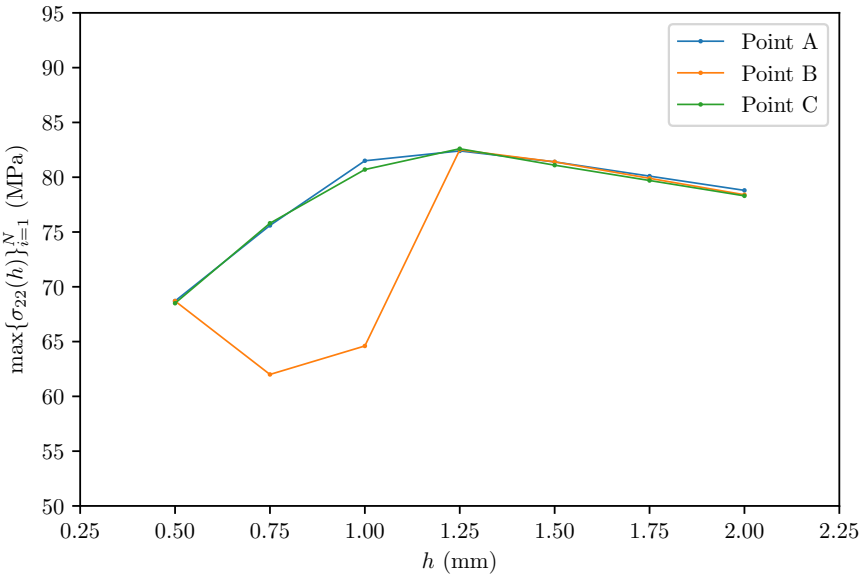

FIGURE 5.29: Maximum residual vertical stresses (σ_{22}) as functions of the hatch spacing at different points of the melt pool, obtained from a finite element model implementing the Galindo-Fernández *et al.* (2018) constitutive model for Ti-6Al-4V with the modified formula for the initial dislocation density introduced in this study.

site minor-axis and major-axis length, its angle of growth, and the hardness profiles along a section of the laser tracks. The convention for the geometric parameters is similar to that in Figure 5.11, provided that instead of α' one considers the generic α martensite lath, replacing its thickness $w_{\alpha'}$ with the minor-axis $d_{\alpha,1}$ and its major-axis with $d_{\alpha,2}$.

Total martensite volume fraction

As already reported in the previous section, the α' martensite volume fraction, approximated as the area fraction of the bidimensional image, does not vary significantly with the hatch spacing, for every location within the laser track. Accordingly, it has been also found that the total martensite volume fraction,

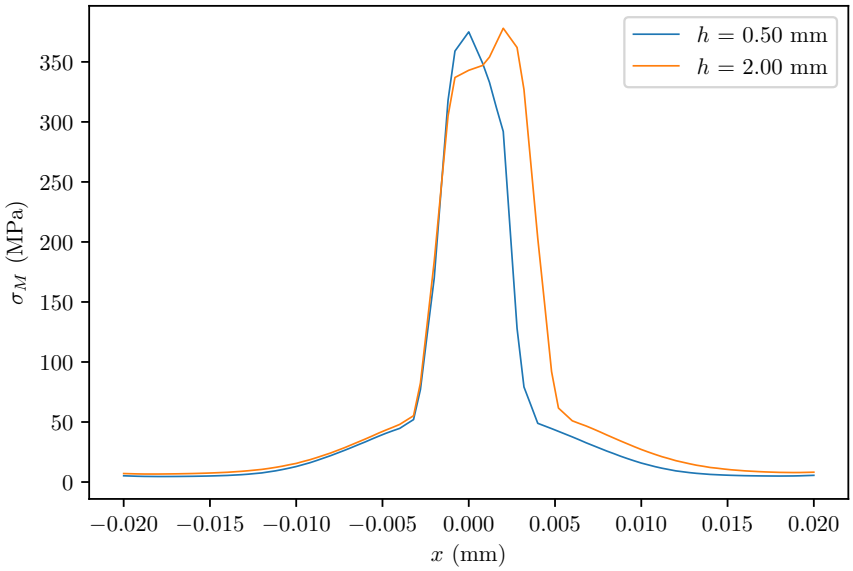

(a) Residual von Mises stress profile (σ_M) at the extreme values of hatch spacing adopted in this study.

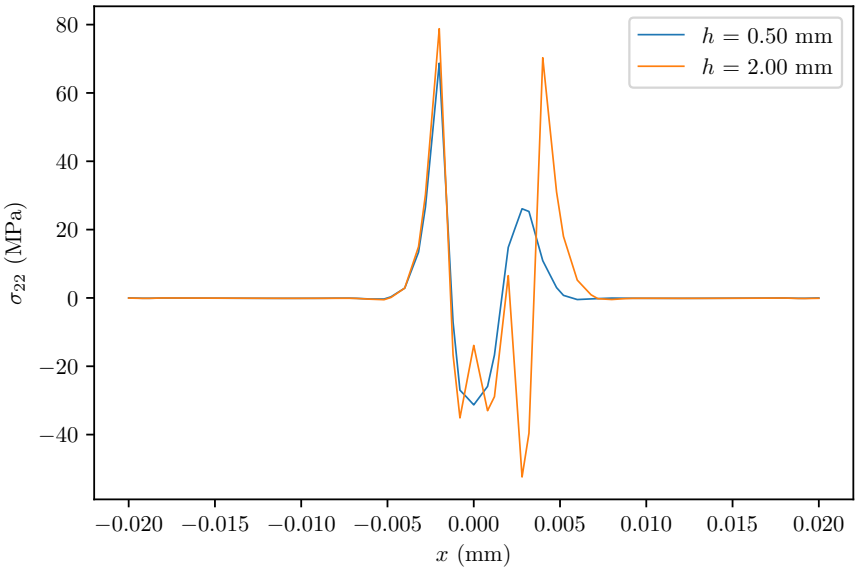

(b) Residual vertical stress profile (σ_{22}) at the extreme values of hatch spacing adopted in this study.

FIGURE 5.30: Residual von Mises (σ_M) and vertical stresses (σ_{22}) profiles at location A represented for the extreme values of hatch spacing adopted in this study, obtained from a finite element model implementing the Galindo-Fernández *et al.* (2018) constitutive model for Ti-6Al-4V with the new formula for the initial dislocation density introduced in this study.

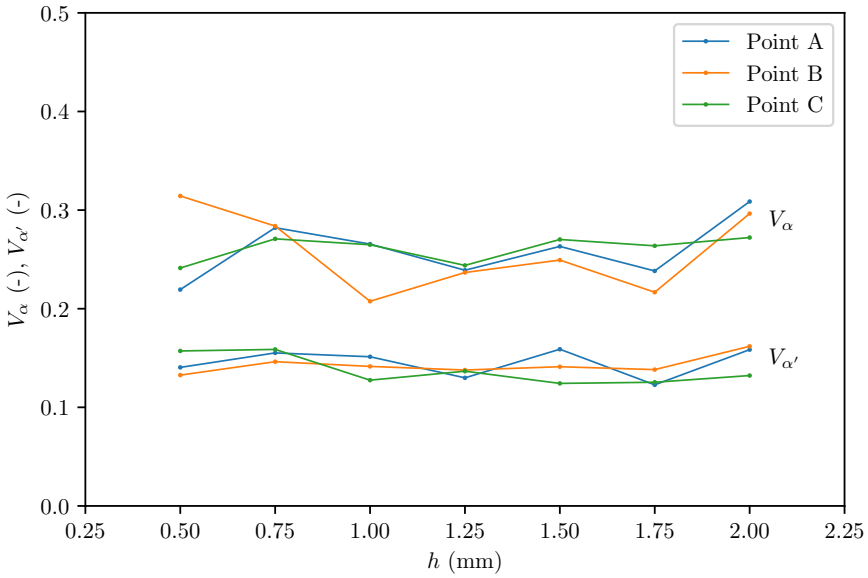

FIGURE 5.31: Martensite mean area fraction V_α compared to α' martensite area fraction $V_{\alpha'}$ for different hatch spacing values h and different points (A, B, C) within the laser track, measured at room temperature.

again approximated as the area fraction, exhibits a similar trend. Moreover, the total martensite volume fraction is approximately twice the value of the α' volume fraction, which means that the latter remains the most important from a quantitative point of view. These conclusions can be grasped immediately by looking at the graph in the Figure 5.31.

Martensite minor-axis and major-axis length

Martensite presents itself as a fine acicular structure with high aspect ratios [87]. Therefore, starting from the approximation of the martensite lath cross-section as an ellipse, as in Figure 5.11, it is possible to define its minor-axis and its major-axis length, respectively indicated as $d_{\alpha,1}$ and $d_{\alpha,2}$. From the experimental data it was observed that this dimension increases as the hatch spacing is increased in both directions. In particular, for the location A this increment is almost perfectly represented as a straight line. Therefore, for this point, the following

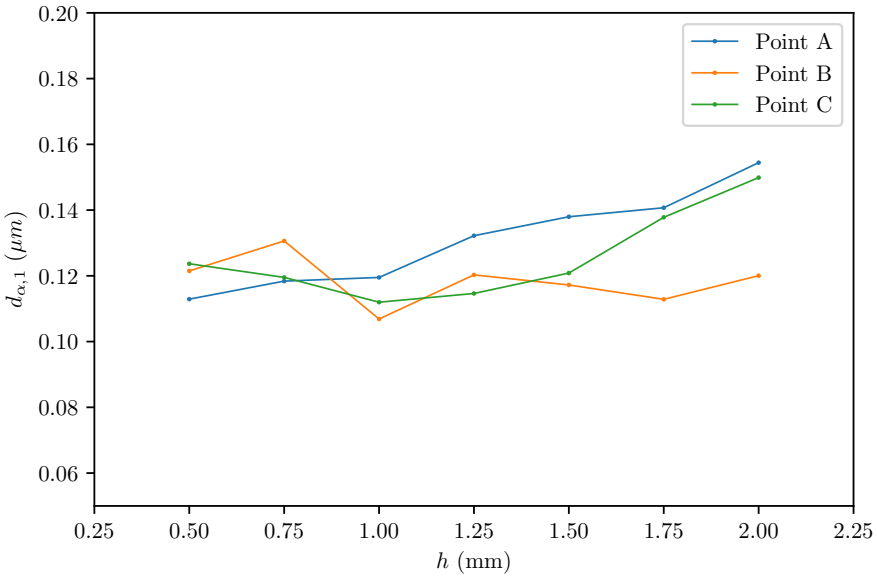

FIGURE 5.32: Martensite minor-axis length $d_{\alpha,1}$ for different hatch spacing values h at different points (A, B, C) within the laser track, measured at room temperature.

two linear fit equations for the relationship between major and minor-axis length and hatch spacing can be derived:

$$d_{\alpha,1}(h)|_A = 0.0973 + 0.0268h; \tag{5.6a}$$

$$d_{\alpha,2}(h)|_A = 0.1626 + 0.0867h. \tag{5.6b}$$

These last two Equations (5.6) are plotted against the experimental measurements in the Figure 5.34.

Martensite angle of growth

During the solidification process, the martensite lamellae, irrespective of their hierarchy, grow by elongating in a direction that is approximately indicated as 45° [87], calculated with respect to the vertical direction of the laser. However, in the present study, it has been observed that the mean angle formed between the vertical direction (direction of the laser beam) and the major-axis direction or axis of growth is always a little less than 45°. Moreover, it was found that the

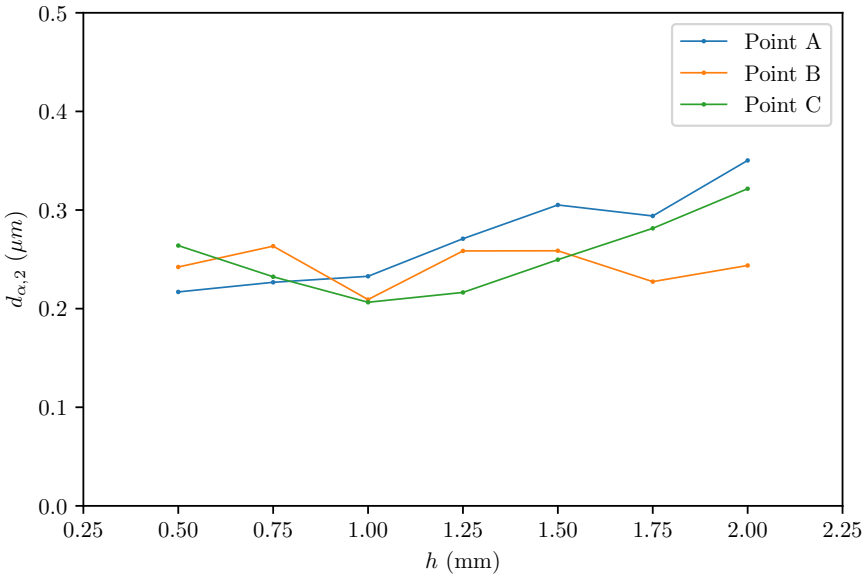

FIGURE 5.33: Martensite major-axis length $d_{\alpha,2}$ for different hatch spacing values h at different points (A, B, C) within the laser track, measured at room temperature.

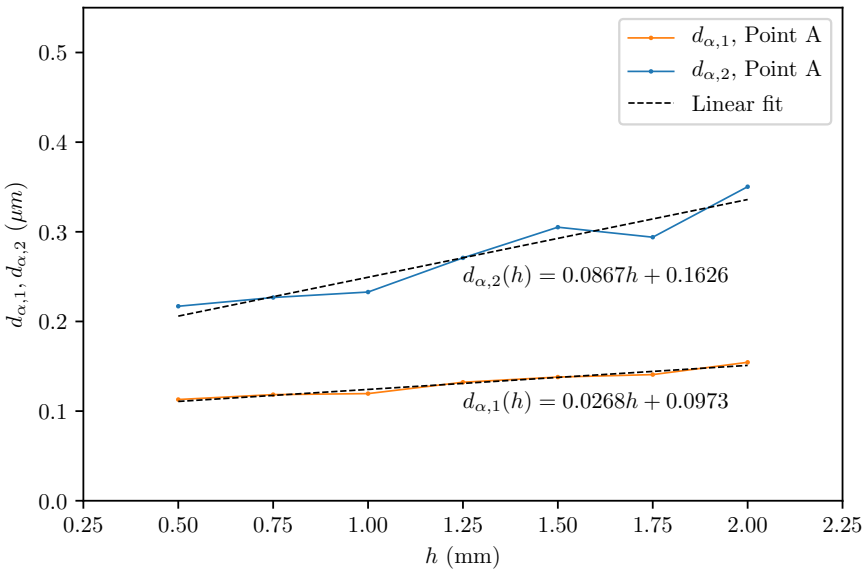

FIGURE 5.34: Martensite minor-axis and major-axis length variation, respectively indicated as $d_{\alpha,1}$ and $d_{\alpha,2}$, with the hatch spacing values h at location A (centre of the first melt pool) within the laser track, measured at room temperature.

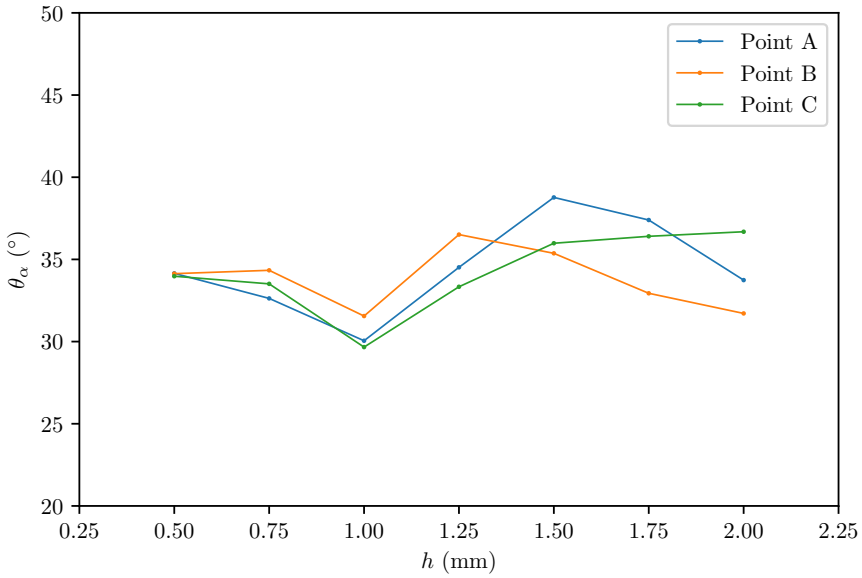

FIGURE 5.35: Martensite mean angle of growth, measured between the vertical direction (direction of the laser beam) and the major-axis direction, varying with the hatch spacing and for different points within the laser track, at room temperature.

angle variation has a minimum for $h = 1.00$ mm, which, in the present study, corresponds to the half of the melt pool width or to the beam radius. This suggests that for this specific hatch-spacing, value the martensite lath is more vertically oriented. Additionally, as the hatch spacing decreases, the orientations for all increases converge to a unique value, around 35°, as the hatch spacing is decreased. All these behaviours are well illustrated in the graph plotted in Figure 5.35.

A hypothesis from this study is that the martensite lath angle is important as a parameter in the correlation with the fracture behaviour. An indirect confirmation of that hypothesis could be the recent observation that during a deformation process the hatch spacing influences the propagation of cracks [257]. Therefore, since when the hatch spacing assumes an intermediate value the fracture strain is greater [257], this may potentially suggest that the angle of the martensite phase affects this response of the material, but this hypothesis needs to be confirmed

by further analysis and studies, which are beyond the scope of this study.

Hardness profiles

Another experimental outcome involved assessing the hardness profiles along a section of the laser tracks. The heat treatment typically influences the hardness value [25], thus leading to variations in the size of the indentation mark. With a 3 N force, the average diagonal indentation for Ti-6Al-4V was roughly 40 µm in the melted zone, resulting in an approximate Vickers hardness of $H_V \approx 412.37$. A hardness profile was experimentally acquired for each of the hatch spacing value conditions and the results for the two extreme hatch spacing values considered in this study, $h = 0.50$ and $h = 2.00$ mm, are shown in Figure 5.36b. From these results it can be immediately seen that the martensite presence has the effect of increasing the hardness of about 1/4 of the nominal value generally obtained for the material unaffected by the laser source. Moreover, from the plot of $h = 2.00$ mm, one can clearly distinguish that the hardness profile has a shape resembling that of the two melt pools. Analogously, the hardness profile obtained for $h = 0.50$ mm is more pronounced where there is a second laser pass, so it can be seen the superimposition effect of the two laser tracks. The complete hardness profiles for the hatch spacing values are shown together in the Figure 5.36a.

Hardness measure can be used as a predictive tool for the yield strength σ_y and for the ultimate tensile strength σ_u. Whilst general linear equations were already proposed in the literature, it is only recently that some scholars developed those equations for additively manufactured parts, and specifically for Ti-6Al-4V [258]:

$$\sigma_y = \frac{H_V}{3.60} - 90; \tag{5.7a}$$

$$\sigma_u = \frac{H_V}{3.34} - 56; \tag{5.7b}$$

where both stresses are expressed in MPa. By using the Equations 5.7 for the

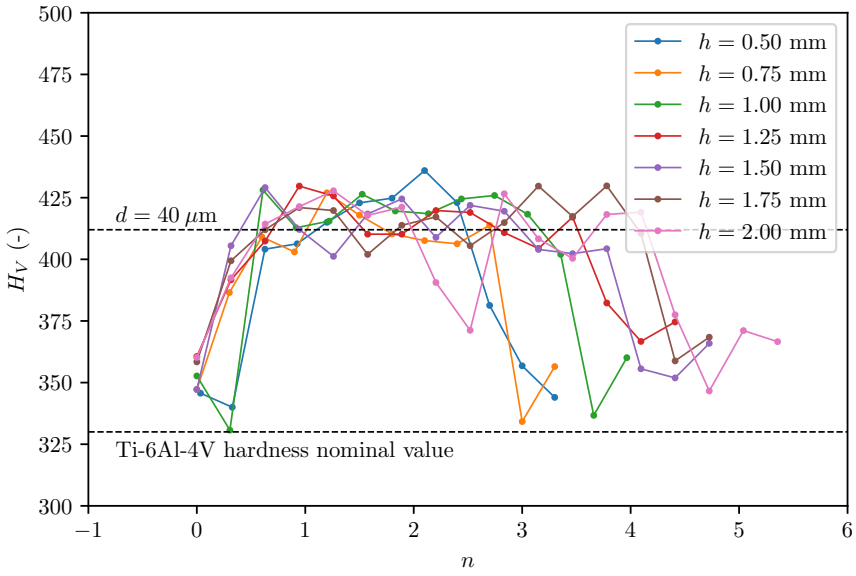

(a) Hardness profiles for the hatch spacing values considered in this study.

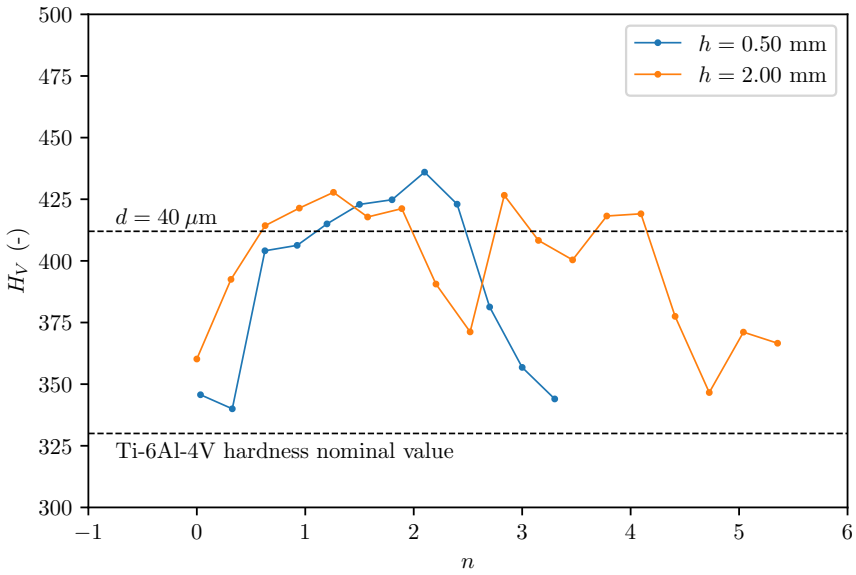

(b) Hardness profile obtained for the two extreme values of the hatch spacing considered in this study.

FIGURE 5.36: Hardness profiles along the melt pool for different hatch spacing values. It is indicated the hardness nominal value for Ti-6Al-4V as reported in the literature [25, p. 944] and the hardness value obtained with an average indentation diagonal of 40 µm.

hardness value previously estimated from the average indentation diagonal measure, the results for Ti-6Al-4V are $\sigma_y = 1033.32$ MPa and $\sigma_u = 1154.77$ MPa. On the other hand, the nominal values for Ti-6Al-4V are $\sigma_y = 892$ MPa and $\sigma_u = 961$ MPa [25, p. 944] (the values for the plates under analysis were, respectively, $\sigma_y = 958$ MPa and $\sigma_u = 986$ MPa). This confirms that the presence of martensite due to the thermal conditions achieved during the laser pass has a significant impact on the mechanical performance of the material. However, a better evaluation of the effect of martensite on these values would be desirable, but it is beyond the scope of this study.

5.3 Numerical studies

5.3.1 Initial speed benchmarks of the multi-pass finite element model

A set of numerical tests was preliminary conducted on both a non-optimised and an optimised multi-pass finite element model (Figures 5.37 and 5.37), in order to assess the impact of the mesh on the speed of the model. The speed of the model was evaluated as the ratio between the increment of time and the total running time, which was fixed as 30 minutes for each simulation. The total time after 30 minutes of running is not fully representative of the total simulation time, but it is possible to argue that this is a good indicator of the model behaviour during the whole simulation. Additionally, to have the most fair and objective results possible, and to avoid any possible variation of the model speed due any particular resource allocation management by the HPC supercomputer, a set of five simulations for each number of core and for each of the two models were performed.

The results of this analysis, summarised in Table 5.5, Table 5.6 and illustrated in Figure 5.39, highlight the following trends, relevant for further optimi-

sations. The initial mesh, represented in Figures 5.37a and 5.38a, characterised by 17024 nodes and 89094 ten-nodes tetrahedral elements (C3D10 elements in SIMULIA/Abaqus) were optimised to reduce the number of degrees of freedom. The final mesh, represented in Figures 5.37b and 5.38b, was then composed of 4465 nodes (about 26.22% of the initial number) and 21279 elements (about 23.88% of the initial number). The main considerations drawn from this analysis are therefore the followings:

- the mesh size plays an important role in the speed of complex finite element models;
- by reducing the element size by about 1/4, the model became about 3-4 times faster, which is a considerable achievement, especially considering the computational resource requirements; the numerical accuracy is compromised only locally, while the average of the nodal variable remains approximately the same;
- the simulation speed does not scale up proportionally with the number of cores used in the calculations. This means that there is not a huge impact on the speed by increasing the number of cores (by using 16 core, indeed, the model runs only two or three times faster and not sixteen times);
- better scalability can be achieved by optimising the mesh size, in the sense that an optimised mesh also allows full utilisation of increased hardware resources.

5.3.2 Mesh convergence study

Independently from the boundary conditions, the study confirmed a logarithmic trend in terms of computational time needed and mesh size, as in Figure 5.42b,

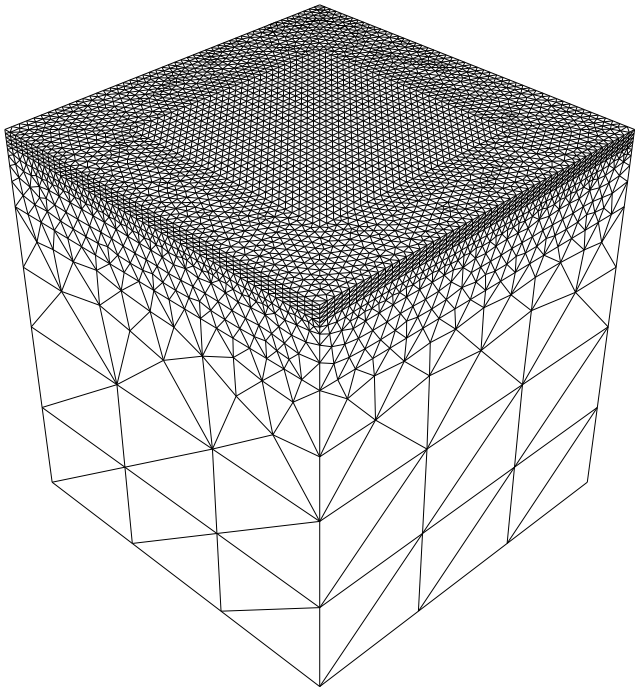

(a) Mesh before the optimisation (17024 nodes, 89094 elements).

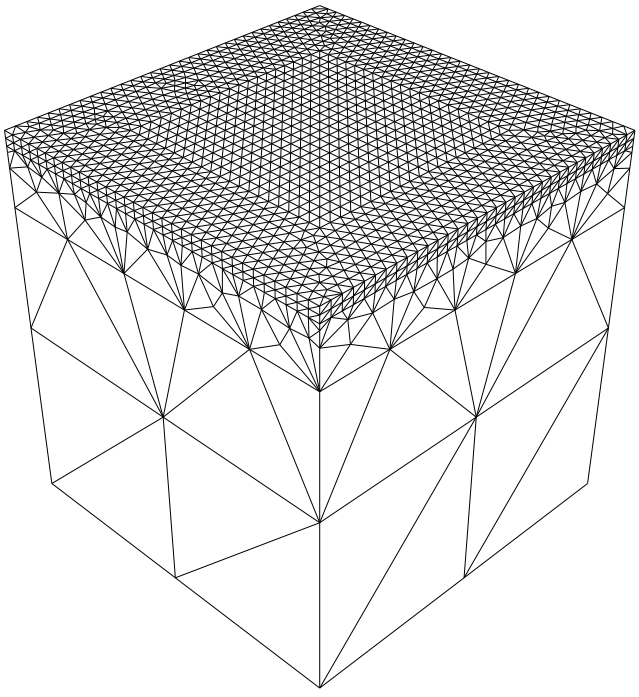

(b) Mesh after the optimisation (4465 nodes, 21279 elements).

FIGURE 5.37: Tridimensional view of the mesh adopted in the multi-pass finite element model before (a) and after (b) the optimisation.

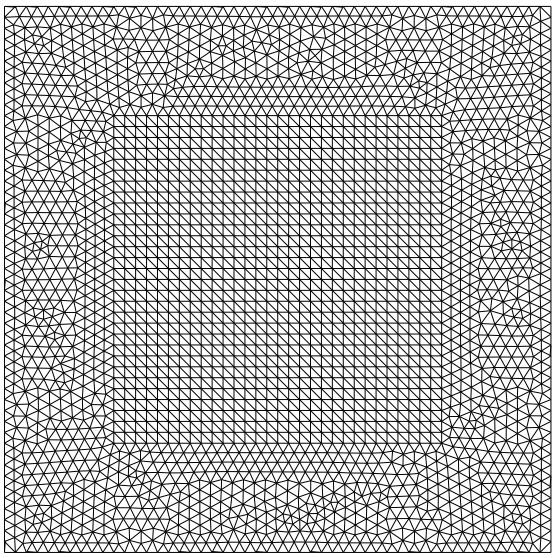

(a) Mesh before the optimisation (17024 nodes, 89094 elements).

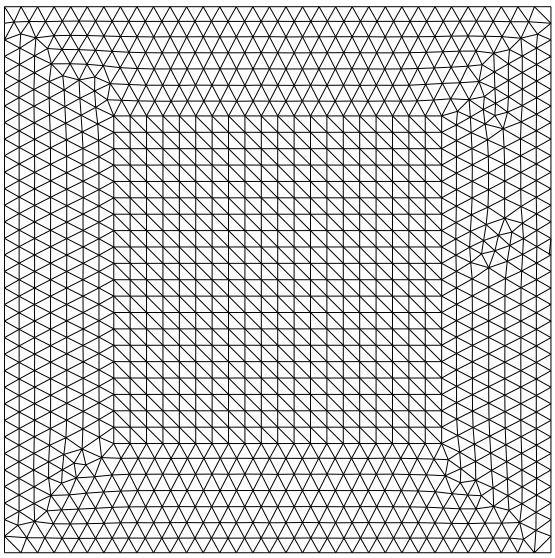

(b) Mesh after the optimisation (4465 nodes, 21279 elements).

FIGURE 5.38: Top view of the mesh adopted in the multi-pass finite element model before (a) and after (b) the optimisation.

Cores	Test no. 1	Test no. 2	Test no. 3	Test no. 4	Test no. 5	Average
1	5.36E-04	4.41E-04	5.36E-04	5.33E-04	5.29E-04	5.15E-04
2	7.31E-04	6.15E-04	8.01E-04	8.12E-04	7.27E-04	7.37E-04
3	9.31E-04	7.12E-04	9.25E-04	9.38E-04	8.50E-04	8.71E-04
4	1.05E-03	8.08E-04	7.95E-04	1.06E-03	9.69E-04	9.36E-04
5	1.16E-03	8.81E-04	8.77E-04	1.10E-03	8.76E-04	9.79E-04
6	9.19E-04	9.25E-04	9.25E-04	1.26E-03	1.23E-03	1.05E-03
7	9.19E-04	9.25E-04	9.62E-04	1.24E-03	1.17E-03	1.04E-03
8	1.05E-03	1.40E-03	1.01E-03	9.94E-04	1.08E-03	1.11E-03
9	1.45E-03	9.67E-04	9.75E-04	1.07E-03	1.26E-03	1.14E-03
10	1.50E-03	1.53E-03	1.06E-03	1.09E-03	1.16E-03	1.27E-03
11	1.08E-03	1.55E-03	1.05E-03	1.46E-03	1.16E-03	1.26E-03
12	1.11E-03	1.55E-03	1.10E-03	1.11E-03	1.39E-03	1.25E-03
13	1.32E-03	1.55E-03	1.15E-03	1.13E-03	1.24E-03	1.28E-03
14	1.13E-03	1.15E-03	1.15E-03	1.48E-03	1.37E-03	1.26E-03
15	1.27E-03	1.55E-03	1.18E-03	1.20E-03	1.46E-03	1.33E-03
16	1.16E-03	1.19E-03	1.17E-03	1.18E-03	1.21E-03	1.18E-03

TABLE 5.5: Simulation time in seconds after 30 minutes of calculations and its average value for different number of cores used for the model before the mesh optimisation.

Cores	Test no. 1	Test no. 2	Test no. 3	Test no. 4	Test no. 5	Average
1	1.37E-04	8.99E-05	8.61E-05	1.81E-04	1.48E-04	1.28E-04
2	2.16E-04	1.80E-04	1.68E-04	1.68E-04	2.45E-04	1.95E-04
3	2.17E-04	2.87E-04	1.93E-04	1.88E-04	2.62E-04	2.29E-04
4	3.20E-04	3.20E-04	2.44E-04	3.23E-04	2.43E-04	2.90E-04
5	3.50E-04	2.64E-04	2.59E-04	2.66E-04	3.47E-04	2.97E-04
6	3.80E-04	3.80E-04	2.62E-04	3.72E-04	3.73E-04	3.53E-04
7	4.02E-04	4.09E-04	2.94E-04	3.75E-04	3.38E-04	3.64E-04
8	3.08E-04	4.23E-04	2.92E-04	2.24E-04	4.29E-04	3.35E-04
9	3.11E-04	2.88E-04	3.13E-04	3.15E-04	3.54E-04	3.16E-04
10	3.16E-04	4.40E-04	3.26E-04	4.31E-04	3.64E-04	3.75E-04
11	3.32E-04	4.53E-04	3.33E-04	3.33E-04	3.75E-04	3.65E-04
12	4.22E-04	3.37E-04	3.42E-04	3.37E-04	3.94E-04	3.66E-04
13	3.39E-04	3.45E-04	3.50E-04	4.62E-04	4.12E-04	3.82E-04
14	3.45E-04	3.51E-04	3.54E-04	4.75E-04	4.67E-04	3.98E-04
15	3.54E-04	3.58E-04	3.70E-04	3.58E-04	4.75E-04	3.83E-04
16	4.35E-04	3.62E-04	3.72E-04	3.70E-04	4.79E-04	4.04E-04

TABLE 5.6: Simulation time in seconds after 30 minutes of calculations and its average value for different number of cores used for the model after the mesh optimisation.

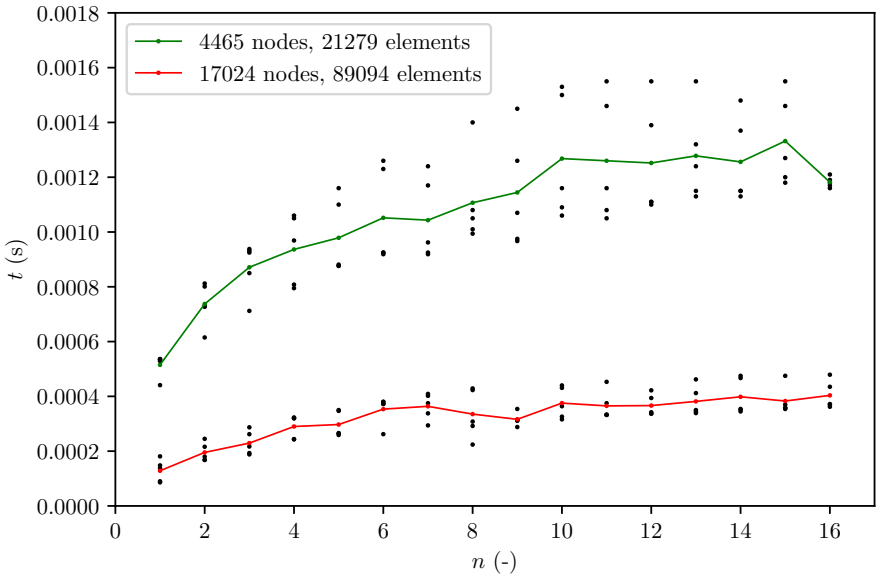

FIGURE 5.39: Speed benchmark of the multi-pass double-layer numerical simulations performed on the high-performance computing cluster during some numerical studies. In this graph is plotted the simulation time after 30 minutes t against n, the number of CPU cores. The red line represents the average behaviour of the finite element model with a higher number of elements and nodes, while the green one represents the average behaviour of the model after the mesh optimisation, and the dots are the values reported for any of the five numerical experiments for every CPU core number.

which can be described by the following two fitting equations:

$$t(n_e) = a \log(bt) + c, \tag{5.8}$$

where $a = 8.41$, $b = 4.28 \times 10^{-4}$, $c = -1.12 \times 10$ for the model with all bulk properties, and $a = 4.87$, $b = 6.47 \times 10^{-4}$, $c = -7.88$ for the model with powder-bulk properties.

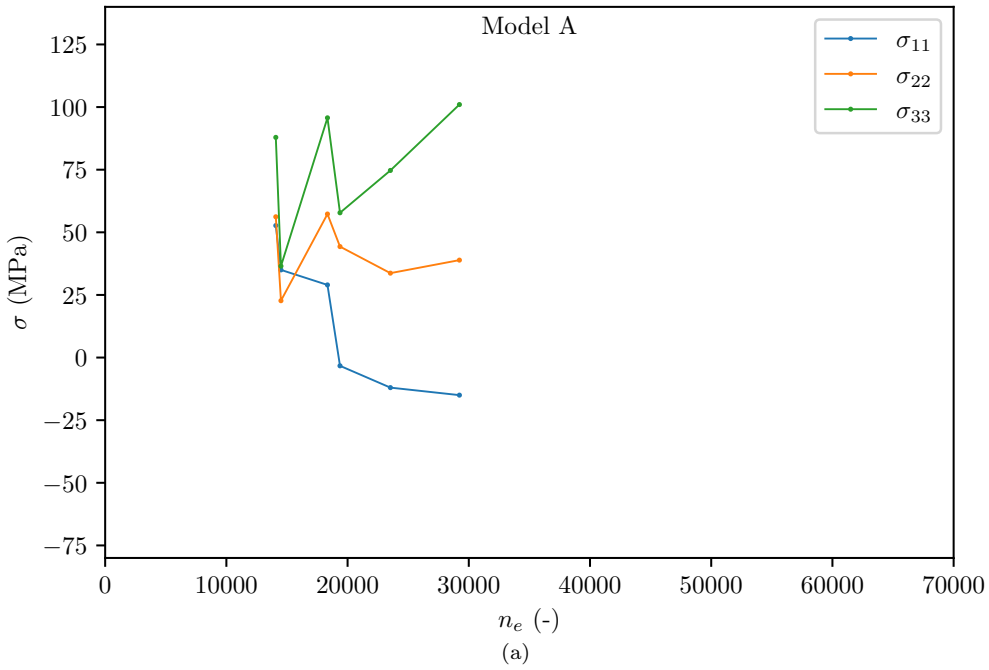

(a)

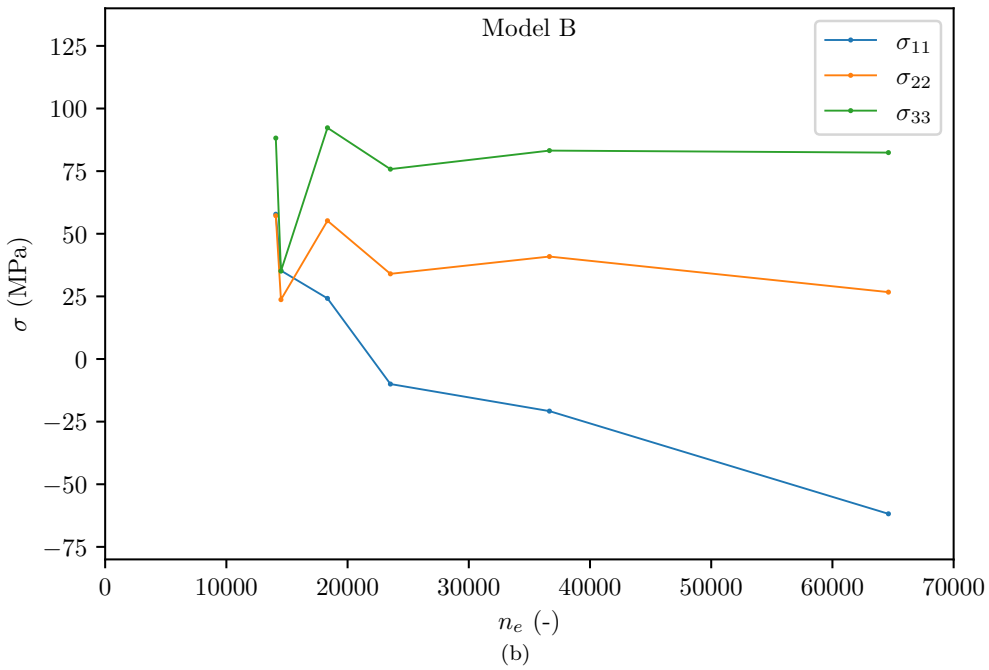

(b)

FIGURE 5.40: Results of the mesh convergence study (models A and B).

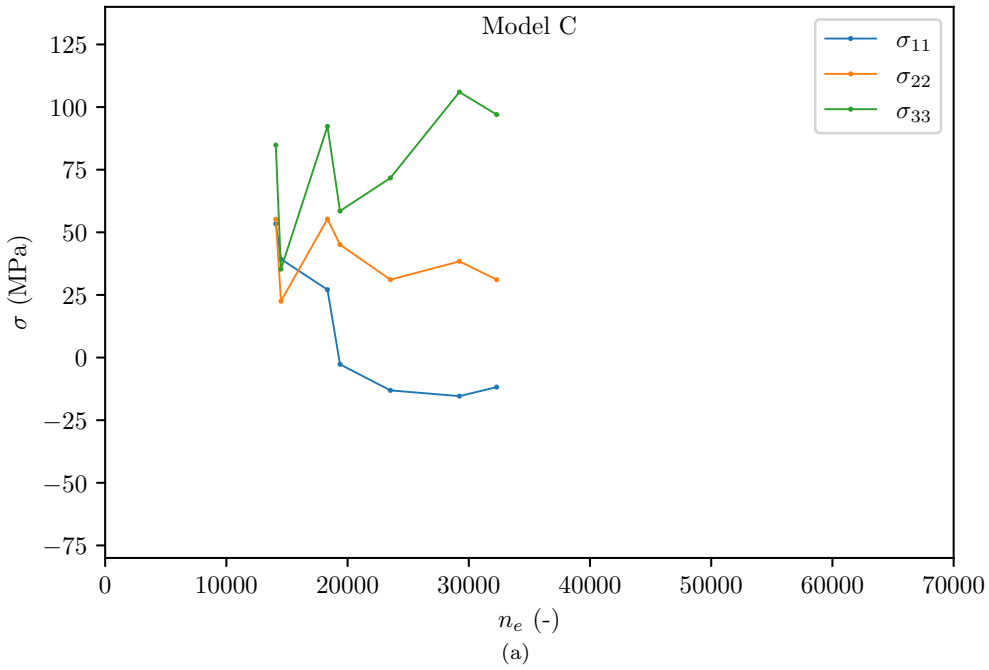

(a)

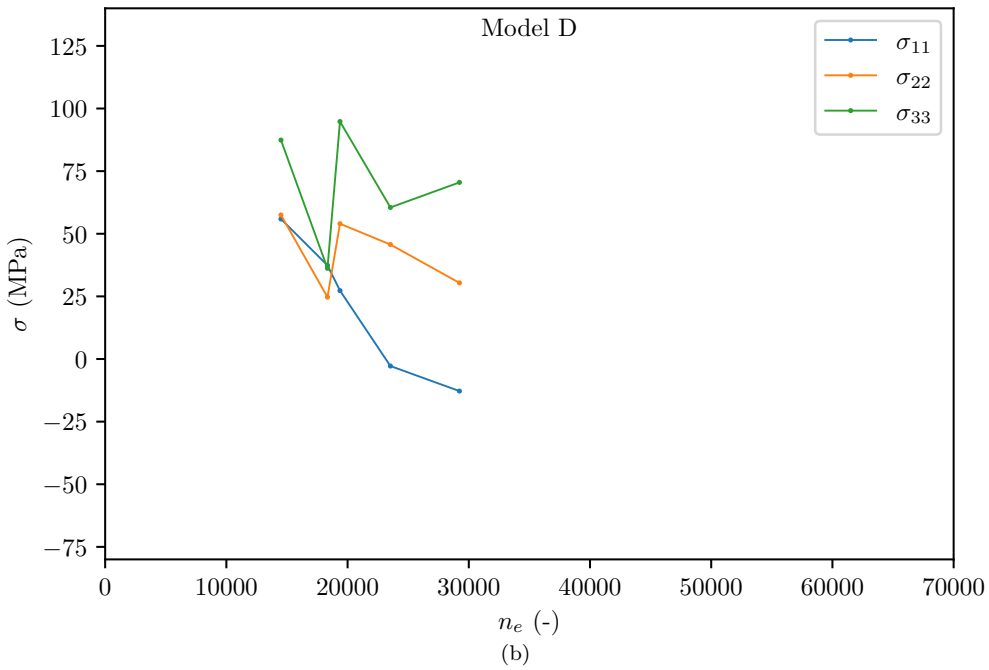

(b)

FIGURE 5.41: Results of the mesh convergence study (models C and D).

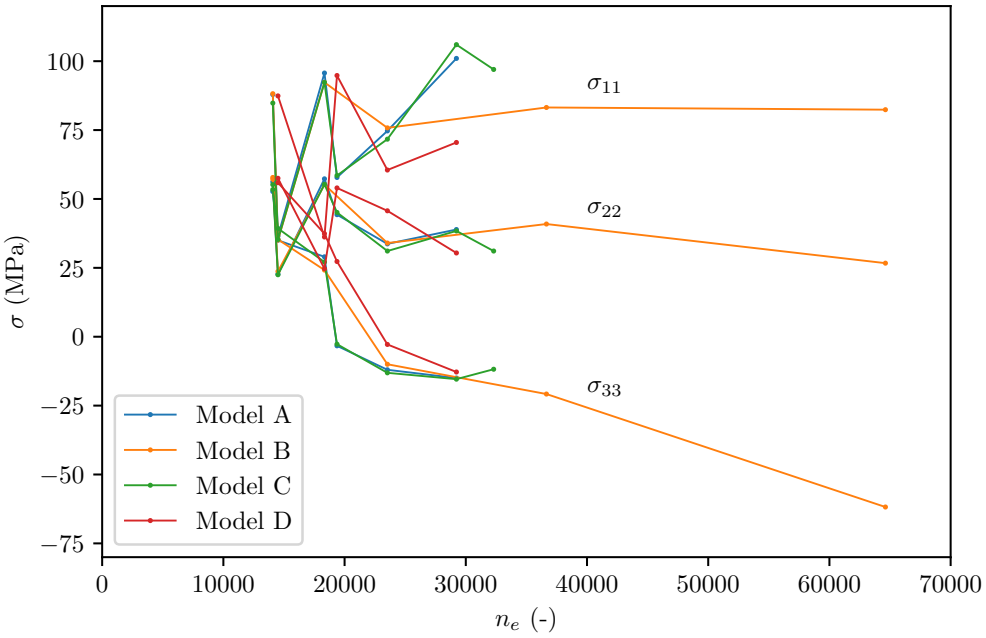

(a) Results of the mesh convergence study for all models and all stress components.

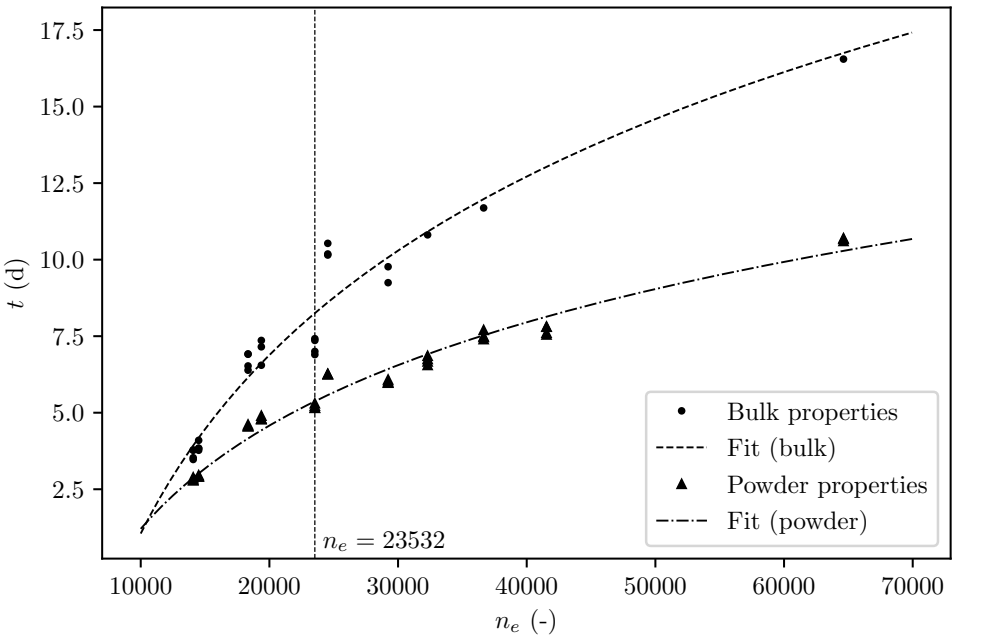

(b) Computational time needed to complete the single layer simulations for different mesh sizes.

FIGURE 5.42: Results of the mesh convergence study for all models and all stress components (a), and computational time needed to complete the single layer simulations for different mesh sizes (b).

5.4 Residual displacements, deformations, and stresses in a multiple-pass model

The multiple-pass single-layer and double-layer models allowed for the combined effect of the hatch spacing and laser speed parameters pair to be analysed in terms of distortions and residual stresses under the influence of a Gaussian heat source. In Figure 5.43 is represented the thermal field during the laser scan pass at different times. In addition, the distortions and residual stresses are clearly influenced also by the boundary conditions implemented. Therefore, with the aim to explore these relations, the results of some numerical simulations are briefly summarised here. Although the results presented in this section have not been validated in any direct way by experiments, but only partially, by referring to the available literature as will be clear in the next chapter, they constitute a first step towards a systematic, wide-ranging search for the best combinations of parameters, in order to optimise the final product built by additive manufacturing or influenced by any other laser technology. This allows some useful considerations to be made and to understand the magnitude and distribution of residual stress development in additive manufacturing. Furthermore, Figure 5.49 shows the impact of thermal fields on the formation of residual stresses during the laser scan, in the model using different properties for the substrate and the deposition layers, whilst Figure 5.49 depicts the development of residual stresses for three varying hatch spacing values.

5.4.1 Single-layer model

The outcomes presented here stem from the original calculations that utilised identical thermo-physical and constitutive model properties for both the substrate and the deposition layer. However, the next chapter will showcase the more

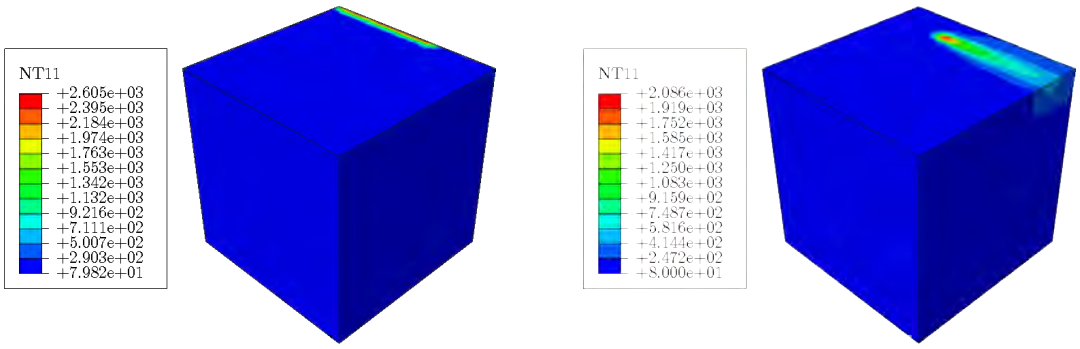

(a) $t = 8.1250 \times 10^{-4}$ s. (b) $t = 1.5844 \times 10^{-2}$ s.

FIGURE 5.43: Nodal temperature (NT11) distribution during the laser scan pass at different instant of time.

precise outcomes generated by the models considering differentiated properties. These more accurate results will be discussed in the context of fatigue analysis.

Since it is clear in this context that each of the variables mentioned is a residual variable, as residual displacements and residual stresses, the word *residual* will be sometimes omitted for simplicity. Moreover, a notation such as '800/60' will be used to indicate the laser speed $s = 800$ mm/s and the hatch spacing $h = 60$ µm, and so on. Based on numerical computations, the following statements can be made, independently from the scanning condition (laser speed and hatch spacing) and for every boundary condition tested:

- the average surface displacements along the scanning axis (u_{11}) is approximately about 1.5 µm for every scanning condition tested and for every boundary condition tested;
- the absolute value of the average displacement perpendicular to the layer plane (u_{22}) is always less than 1 µm for every scanning condition tested and for every boundary condition tested;
- the average surface displacement perpendicular to the layer plane (u_{22}) tends always to be outward with respect to the layer plane (except in rare cases), for every scanning condition tested and for every boundary condition

tested;

- the average displacement perpendicular to the scanning direction (u_{33}) is always less than 1 µm for every scanning condition tested and for every boundary condition tested;

- the average displacement perpendicular to the scanning direction (u_{33}) is always directed towards the layer.

These results are summarised in Figure 5.45, from which one can immediately observe the magnitude and the direction of the displacements at the end of the cooling process.

In terms of the scanning conditions, it was found that the absolute value of the average surface displacement along the scanning direction (u_{11}) is attained for the lowest speed tested, while the maximum was found for the highest speed, for every boundary condition tested. Moreover, this displacement decreases as the laser speed increases and this occurs for every fixed value of the hatch spacing.

The von Mises stress values vary in the range 170-230 MPa and the minimum is attained in most of the cases for the pair 800/60, while the maximum von Mises stress is observed for 1000/80. The values remain almost the same as the model becomes more constrained, *i.e.* moving from boundary condition no. 1 to no. 6.

Regarding the surface distribution of the displacements, it was found that for every scanning condition (laser speed and hatch spacing), and for every boundary condition tested, the maximum displacement is localised in an area near the end point of the scanning path, whereas the minimum is always attained near the starting point of the scanning path.

The residual strain shows a repeated pattern of high and low strain values, interspersed with each other, visually following and imitating the scanning path. This is partially reflected also in the distribution of von Mises residual stresses, which maintain a similar, albeit more dispersed, spatial distribution.

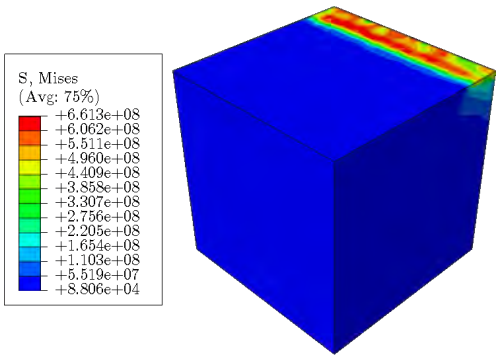

(a) $t = 1.2188 \times 10^{-2}$ s.

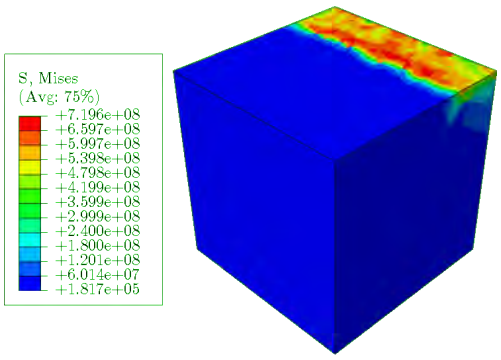

(b) $t = 2.4375 \times 10^{-2}$ s.

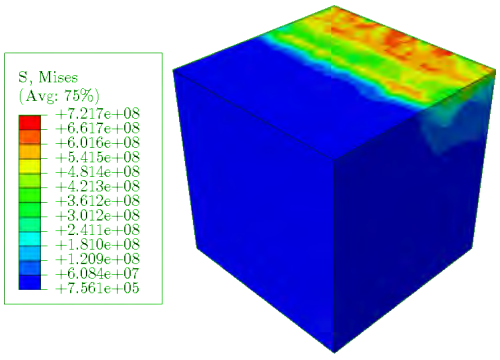

(c) $t = 3.6562 \times 10^{-2}$ s.

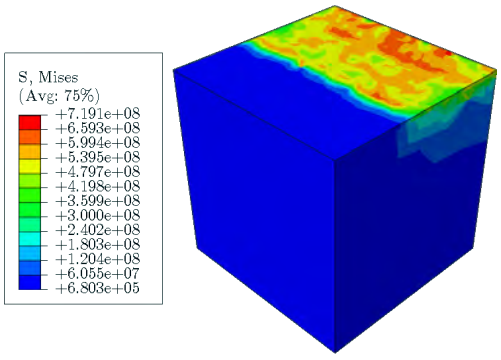

(d) $t = 4.8750 \times 10^{-2}$ s.

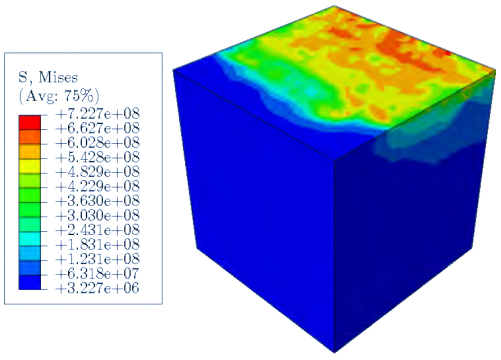

(e) $t = 6.0937 \times 10^{-2}$ s.

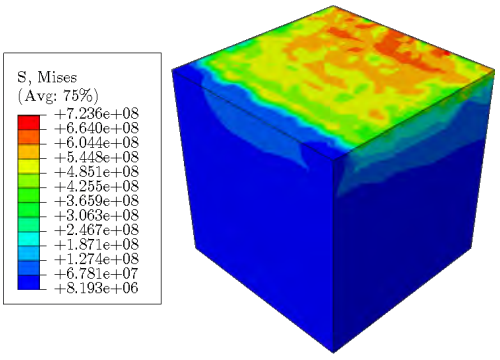

(f) $t = 7.3125 \times 10^{-2}$ s.

FIGURE 5.44: Simulated von Mises stress development during the laser scanning process at different time instants for a single-layer of Ti-6Al-4V. The stress value initially attained during the first few scans (A and B) is then almost equivalent to the final one and its magnitude is distributed according to the laser scan track.

5.4.2 Double-layer model

An extract of the results for a double-layer model is here presented. The same nomenclature and conventions used in the previous paragraph are here adopted. Comparing the numerical results, the following statements can be made, independently from the scanning condition (laser speed and hatch spacing) and for every boundary condition tested:

- the average surface displacements along the scanning axis (u_{11}) is approximately about 1.2 µm for every scanning condition tested and for every boundary condition tested;
- the absolute value of the average displacement perpendicular to the layer plane (u_{22}) is approximately 0.5 µm for every scanning condition tested and for every boundary condition tested;
- the average surface displacement perpendicular to the layer plane (u_{22}) is always directed outward with respect to the layer plane, for every scanning condition tested and for every boundary condition tested;
- the average displacement perpendicular to the scanning direction (u_{33}) is approximately about 1 µm for every scanning condition tested and for every boundary condition tested;
- the average displacement perpendicular to the scanning direction (u_{33}) is always directed towards the layer.

These results are summarised in Figure 5.45, where it is possible to immediately observe the magnitude and the direction of the displacements at the end of the cooling process.

As opposed to the model with only one layer, the absolute value of the average surface displacement along the scanning direction (u_{11}) is attained for the highest speed values, independently of the boundary conditions.

The peak von Mises stress varies from 220-280 MPa, thus showing an increment of roughly 50 MPa. Its minimum is always attained for the conditions 800/60, while the maximum is reached for 1100/80 and this does not depend on the boundary conditions.

The spatial distribution of the magnitude of the residual displacements for the condition BC1, *i.e.* in absence of constraints, is quite similar to that of the single layer model. However, as the model becomes constrained on one or more sides, the aspect of this distribution changes significantly, showing a central narrow strip in which the maximum values are attained. This strip is in the direction of the laser path adopted for the second layer and it expands on one side, where the displacements were bigger during the first layer scan.

The residual strain shows a similar repeated pattern as that found for the single-layer model. However, surprisingly as the model becomes constrained, that pattern appears to be rotated by 90°, following the new scanning path adopted for the second layer scan. Once again, this behaviour is also reflected in the distribution of the residual stresses, although it is not accentuated.

5.4.3 Summary of residual stresses results for the single-layer and double-layer simulations

As it was observed during the present study, a second layer introduces additional residual stresses, so as the model size increases vertically from one to two layers, the magnitude of residual stresses increases. This is true for the model that has similar properties between the substrate and the deposition layer, as illustrated in Figure 5.47, whilst the opposite holds true when considering different thermo-physical and material properties, as shown in Figure 6.12. This aspect needs a clarification in future studies. At the same time, both types of analyses confirmed that hatch spacing little impact in terms of residual stresses, having fixed speed and boundary conditions. It can be concluded that impact of hatch spacing on

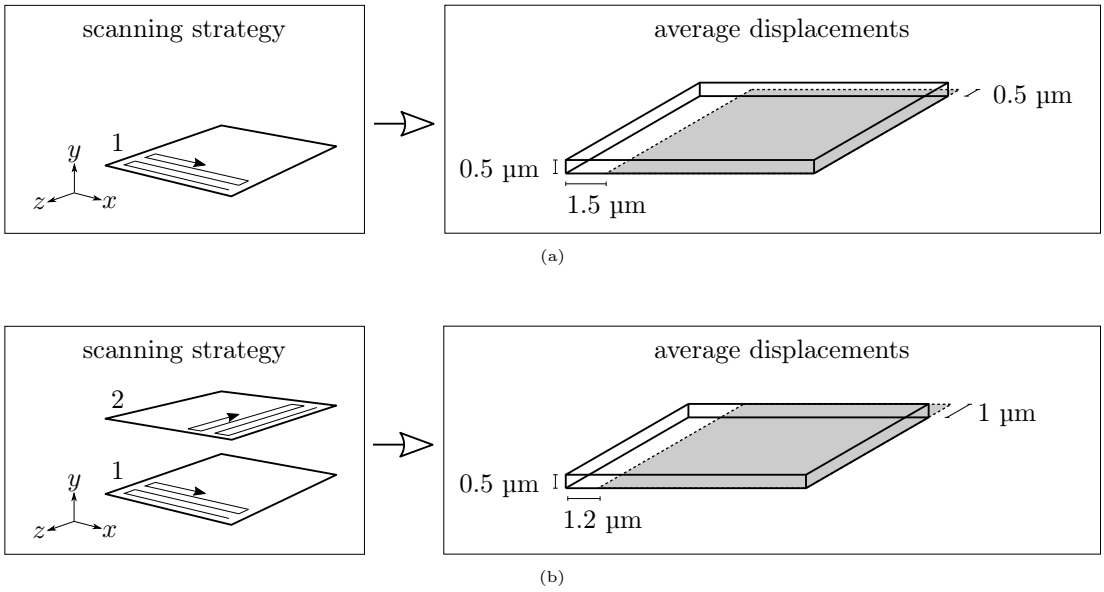

FIGURE 5.45: Schematic representation of the scanning strategy effect on the average residual displacements, independently from the boundary conditions and scanning parameters (hatch spacing and laser speed), as obtained for the single-layer model (a) and for the double-layer (b). The grey surface represents the layer surface before the laser scan. It can be observed that the maximum displacement is achieved along the first layer scanning direction.

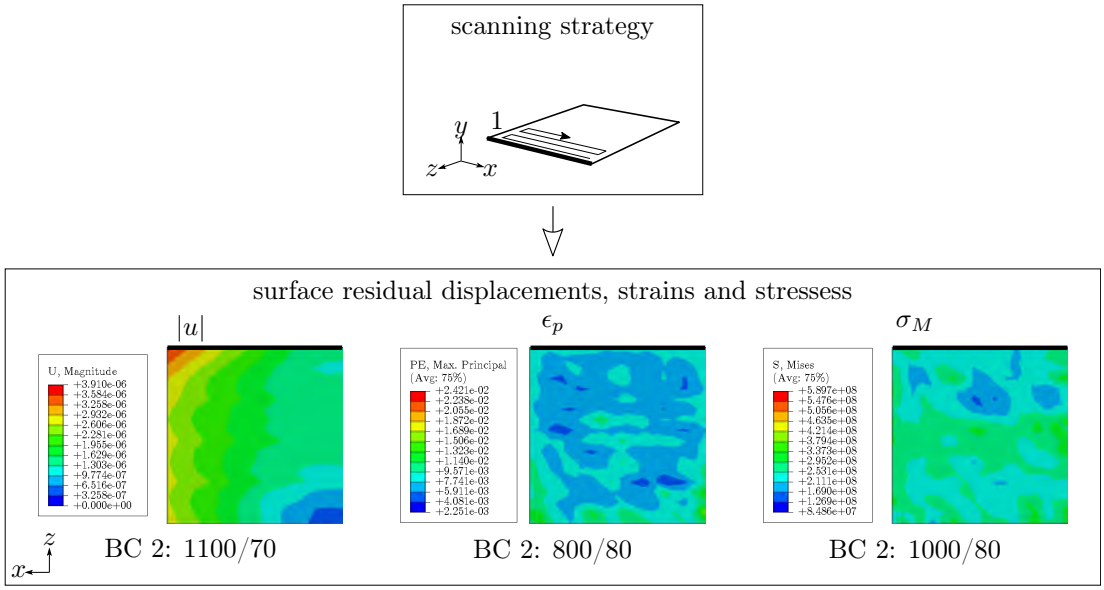

(a)

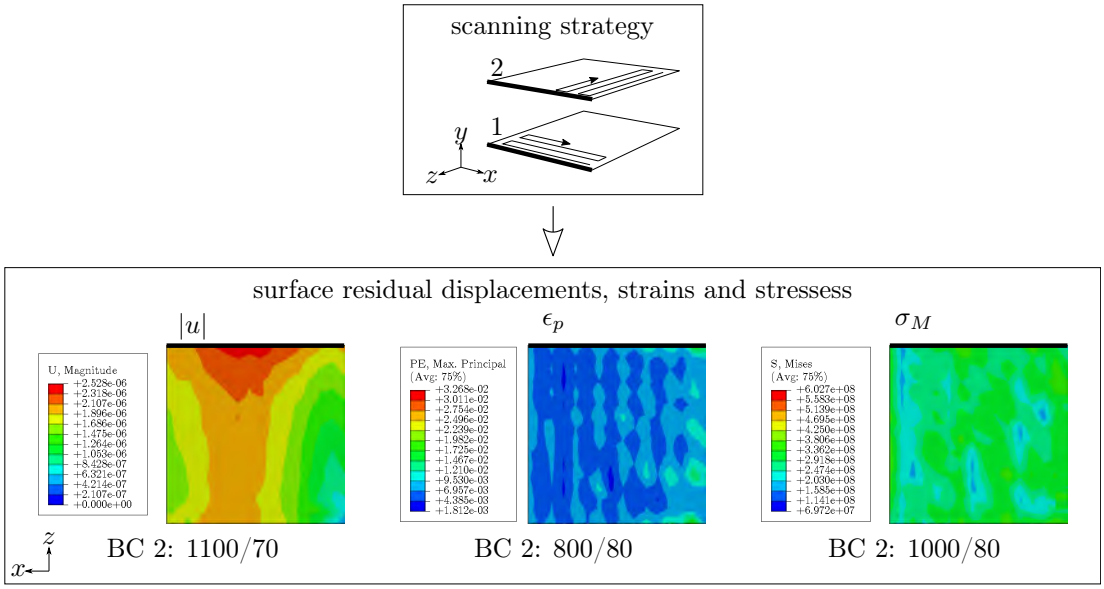

(b)

FIGURE 5.46: Schematic representation of the typical scanning strategy effect on the surface distribution of residual displacements, residual strains, and residual stresses, as obtained for the single-layer model (a) and for the double-layer (b).

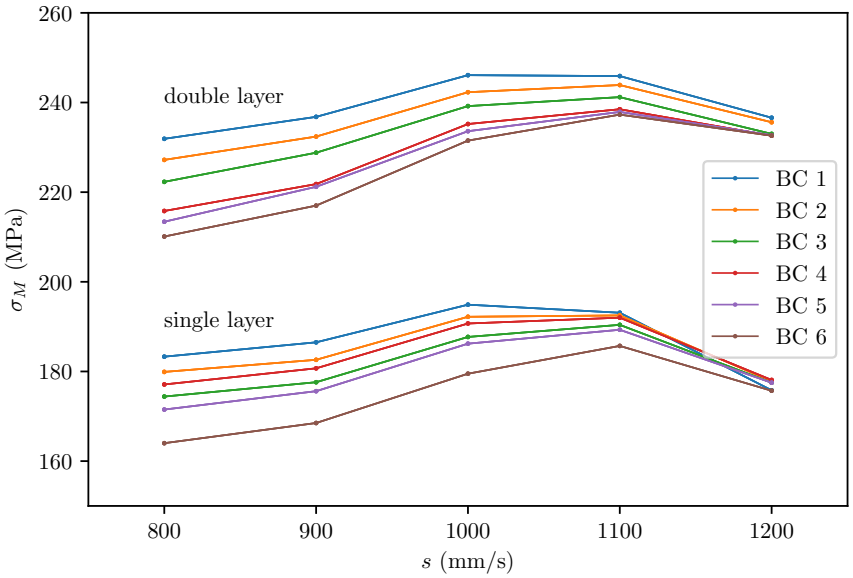

FIGURE 5.47: Von Mises residual stress magnitude according to the laser speed, for different hatch spacing values and boundary conditions.

residual stress magnitude is relatively small when compared to the influence of laser speed and boundary conditions. Nevertheless, the impact of hatch spacing on cooling rate, as shown in the double-pass simulations of the experimental program, needs to be acknowledged for its effect on residual stress distribution and surface quality.

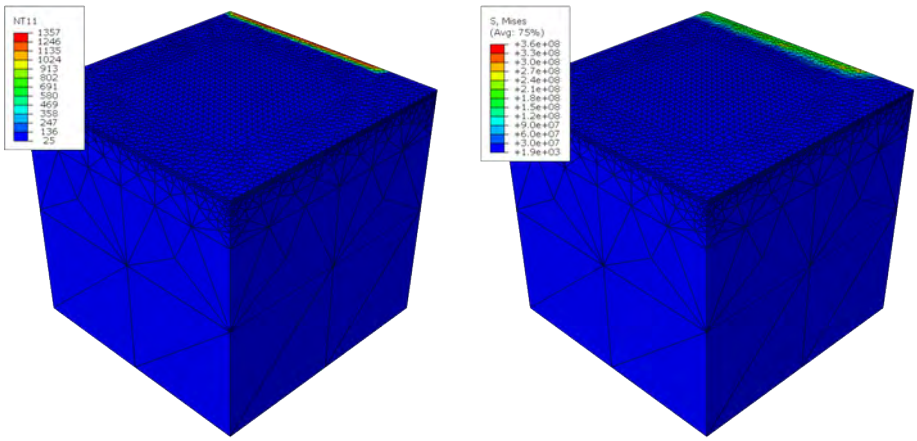

(a) $t = 7.6500 \times 10^{-4}$ s.

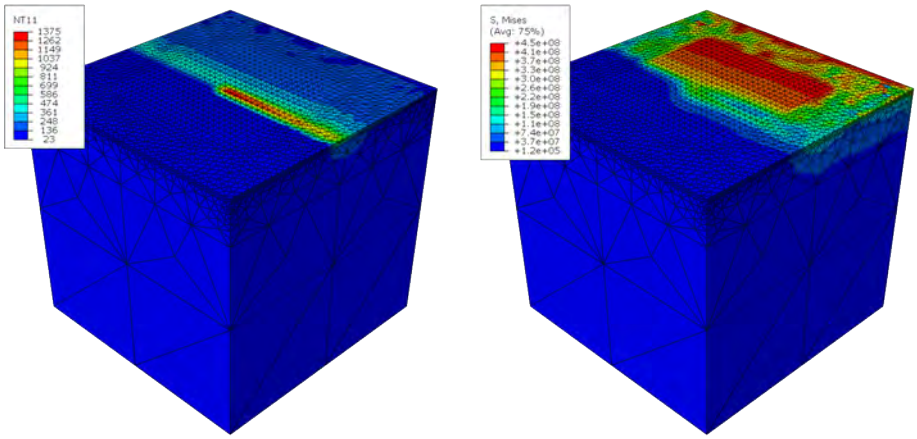

(b) $t = 2.652 \times 10^{-2}$ s.

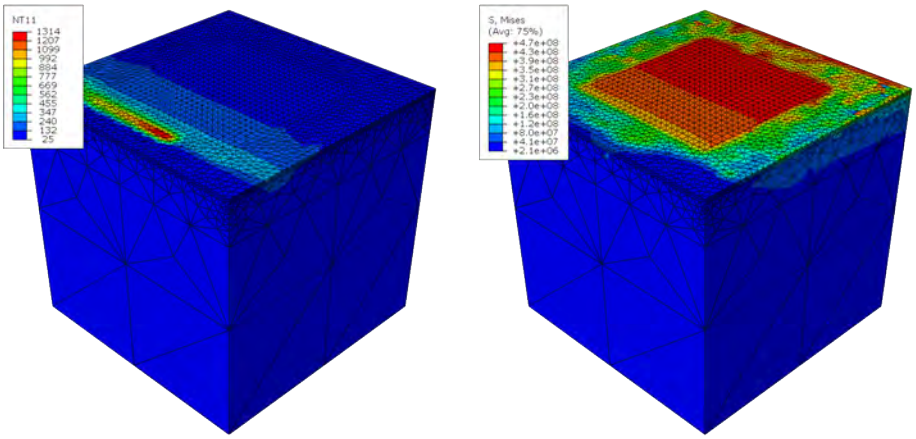

(c) $t = 4.462 \times 10^{-2}$ s.

FIGURE 5.48: Simulated von Mises stress development (on the right) during the temperature evolution (on the left) for a laser scanning process at different time instants.

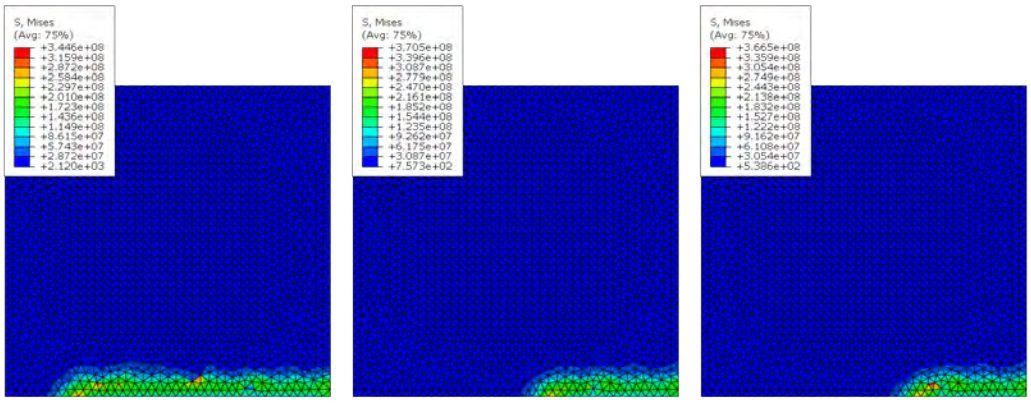

(a) $t = 7.6500 \times 10^{-4}$ s.

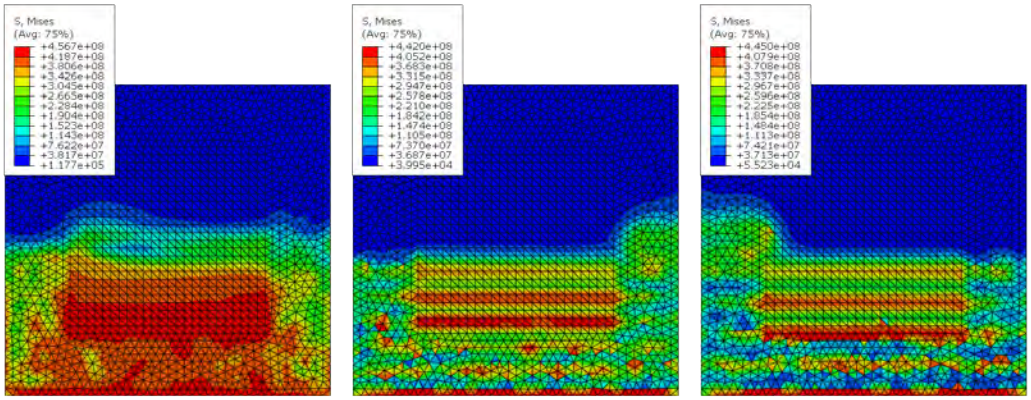

(b) $t = 2.4735 \times 10^{-2}$ s.

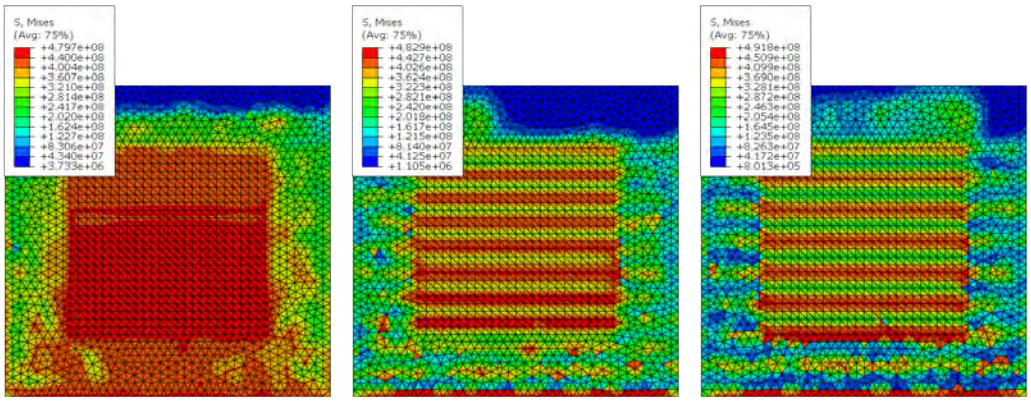

(c) $t = 4.5645 \times 10^{-2}$ s.

FIGURE 5.49: Simulated von Mises stress development for different hatch spacing values (40, 80, and 100 µm), at different time instants.

Chapter 6

Discussion

The initial hypothesis stated that additive manufacturing was assimilable to a multi-pass welding process. This hypothesis, which inspired and guided the present research work, was confirmed by some results already available in the literature on welding. This will be better elucidated out in detail in the current chapter. The study herewith was able to confirm and partially extend some of the ideas already presented in the available literature, as discussed herewith. However, some limitations are still applicable and they are mainly due to research path followed, with the progressive adjustment of the intermediate objectives. Nevertheless, once this methodology is extended in full, it will provide new insights for the benefit of both additive manufacturing and welding, by using both experiments and numerical simulations. Therefore, with this purpose in mind, in this chapter the work done will be summarised, discussed and compared with the available literature. Finally, some guidelines to mitigate the negative effects of residual stresses in additive manufacturing components subjected to fatigue will be outlined.

6.1 Laser source influence on the material

As seen in the previous chapters, the laser source is responsible for altering the microstructure and residual stresses, therefore a qualitative and quantitative description of those alterations is needed.

6.1.1 Qualitative analysis

An observation regarding the analogy between welding and additive manufacturing

The validity and limitation of the analogy between welding and additive is more clear when one looks at grain growth in Figure 5.1. Controlling epitaxial growth has been recognised as one of the fundamental methods to build or repair single crystal turbine blades, which permits better thermal performance by inhibiting the development of grain boundaries [259], but a better understanding is also useful in polycrystalline components. By looking at the epitaxial grain growth of the β-grains for $h = 0.50$ mm in Figure 5.1, compared with their radial distribution for $h = 2.00$ mm, it is possible to understand better the formation of the columnar microstructure in additive manufacturing (Figure 2.38), by imagining the rotation of the tilted grains towards the upward direction due to their remelting during the second laser scan. Therefore, the final columnar microstructure in bigger components can be thought as generated by a superimposition of several radial solidified melt-pools.

Material inhomogeneities due to the laser track

During the early stage of the experimental work, it was observed that the laser source effect is not exactly uniform, but there are some inhomogeneities that need to be pointed out. A first inhomogeneity was observed in the Trumpf® laser track

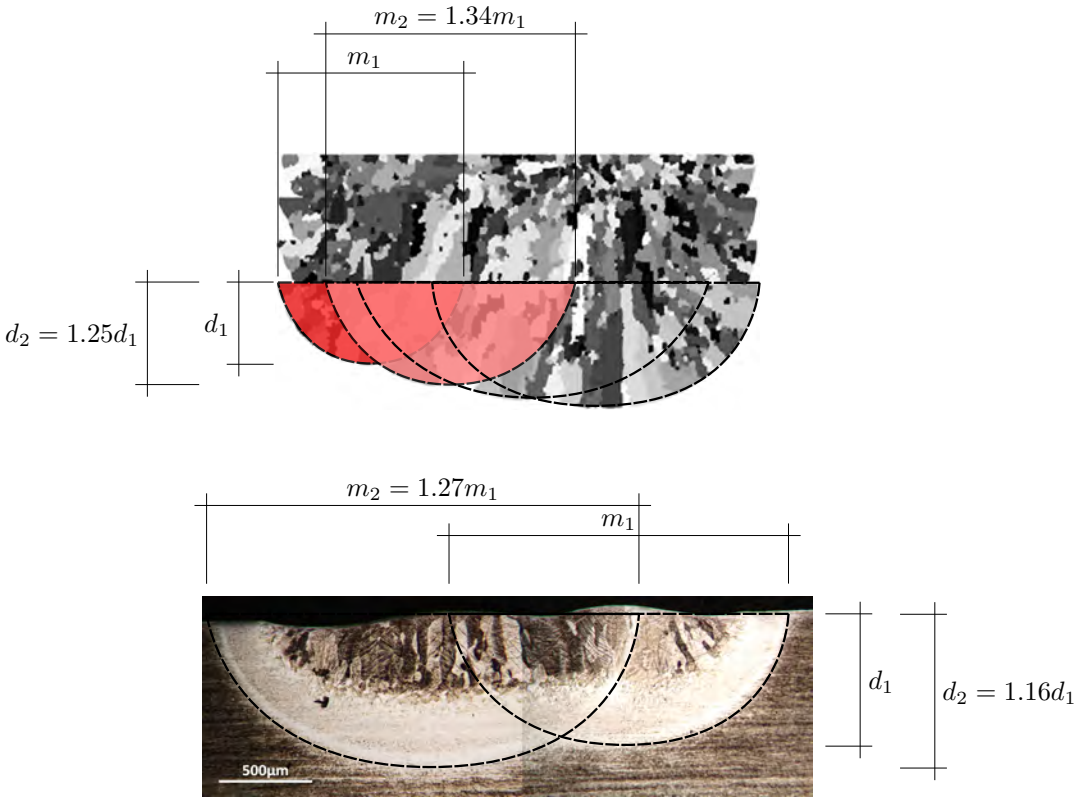

FIGURE 6.1: Microstructure prediction resulting from a grain-growth numerical simulation during additive manufacturing, where four unidirectional laser scans and four layers were used. The initial laser scan is on the left and the scans progressively advance towards right, producing a deeper track within the material. Image reproduced from [260, p. 11, fig. 11].

appearance when viewed from above, because the surface of the material where the laser starts is concave, while the end point is convex, as observed in Figure 5.3. This can potentially lead to different height of the material deposit on a substrate and can be explained, perhaps, as a result of the inhomogeneous laser beam source on the material. However, this aspect needs a better clarification, its effect on a final component needs to be investigated during metal deposition.

As remarked from the visual observations of the results of the experimental work done, it has been found that the second laser track shows a deeper penetration within the material if it is observed from the cross-section, as in Figure

5.1. A similar trend was already noticed in the recent literature, when performing numerical simulations for additive manufacturing of Inconel 718 (a precipitation-hardening nickel-chromium alloy), as visible in Figure 6.1 [260]. Those trends are also reflected into the hardness profile obtained for $h = 0.50$ mm, as represented in Figure 5.36b, where the higher value of the hardness is achieved during the second laser track. Since in the study it was just mentioned that metal powder was employed, whilst in the present work this was avoided. This particular correspondence, again, confirms that similar trends in additive manufacturing can be obtained despite the complete absence of powder metal particles. Therefore, the reason can be attributed to the thermal superimposition causing an increase in temperature during the second pass, whilst the first track is still above room temperature [260]. This found confirmation in the thermal cycles obtained numerically, because the second laser pass occurs when the material is not completely cooled to room temperature, as shown in Figures 5.8, 5.9, 5.10. It is here suggested that these inhomogeneities can be avoided by planning accurately the speed of the laser and, for vertical layer deposition, also the inter-layer cooling time.

6.1.2 Microstructure characterisation

Martensite characterisation in the present work include martensite volume fraction and its morphology, taking into account the different locations within the melt pool for varying hatch spacing values.

Martensite volume fraction

As observed from the experiments, and from the adaptation of a mathematical model described in Villa *et al.* (2020) [93, 94], the volume fraction of the martensite does not seem to be particularly affected by the hatch spacing variation (Figure 5.31). Recently, while investigating the martensite in stainless steel

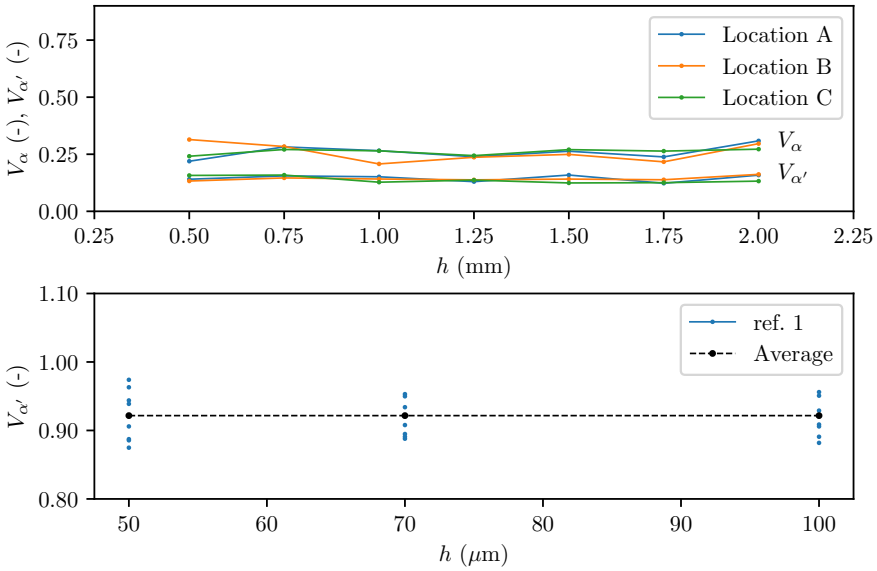

FIGURE 6.2: Visual comparison between the constant martensite volume fraction in Ti-6Al-4V (present work) and the constant martensite content in stainless steel fabricated by selective laser melting. In both cases the content variation with the hatch spacing is limited. The reference is the following: ref. 1 = [261, p. 5, fig. 4c].

fabricated by selective laser melting, it was also found that the hatch spacing has little impact on the martensite volume fraction for a fixed laser speed [261] (Figure 6.2). Indeed, since the martensite generation is a diffusionless process, it can be argued that it is created homogeneously in every point, provided that Equations (2.2) are respected.

Moreover, the implementation of the Koistinen-Marburger model [99] shows also that the volume fraction does not systematically vary with the hatch spacing. Indeed, it was found to be bound in a specific range if measured at room temperature. However, the aforementioned model can estimate well the volume fraction content of the martensite, which is much more accurate during the first stages of its formation, because the distance between the upper and lower bound is reduced, as represented in Figure 5.16.

Some scholars found also that in Ti-6Al-4V additively manufactured parts

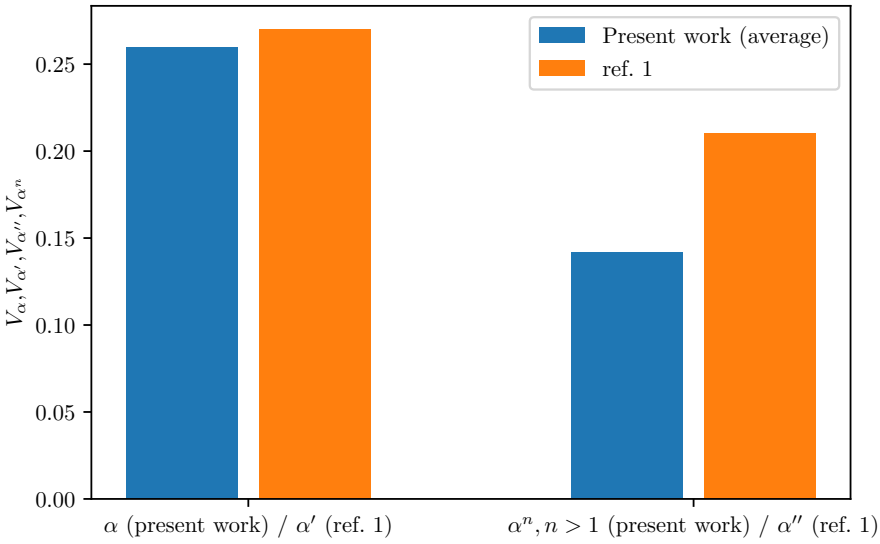

FIGURE 6.3: Sum of the primary and secondary martensite volume fraction in Ti-6Al-4V fabricated by selective laser melting at two different powers: the white bar represents the value obtained for 100 W and the grey bar represents that obtained for 175 W. The reference is the following: ref. 1 = [262, p. 118, fig. 4.3e].

using selective laser melting the volume fraction of primary martensite was higher than the volume fraction of the secondary martensite, as represented in Figure 6.3. This is exactly what was found in the present work, because the sum of all the martensite laths volume fractions ($V_\alpha \approx 0.25$, as can be inferred from Figure 5.31) is similar to the value found in the study just mentioned [262]. This trend, again, confirms the approach of looking only at the thermal fields, independently of the other parameters, ignoring also the role of the powder, in order to study the martensite formation.

Martensite morphology

Regarding the thickness and the spacing of the martensite, the trends already found in Villa *et al.* (2020) [93, 94], showing their dependency on the cooling rate, was supported by the findings of this study. However, the modified model

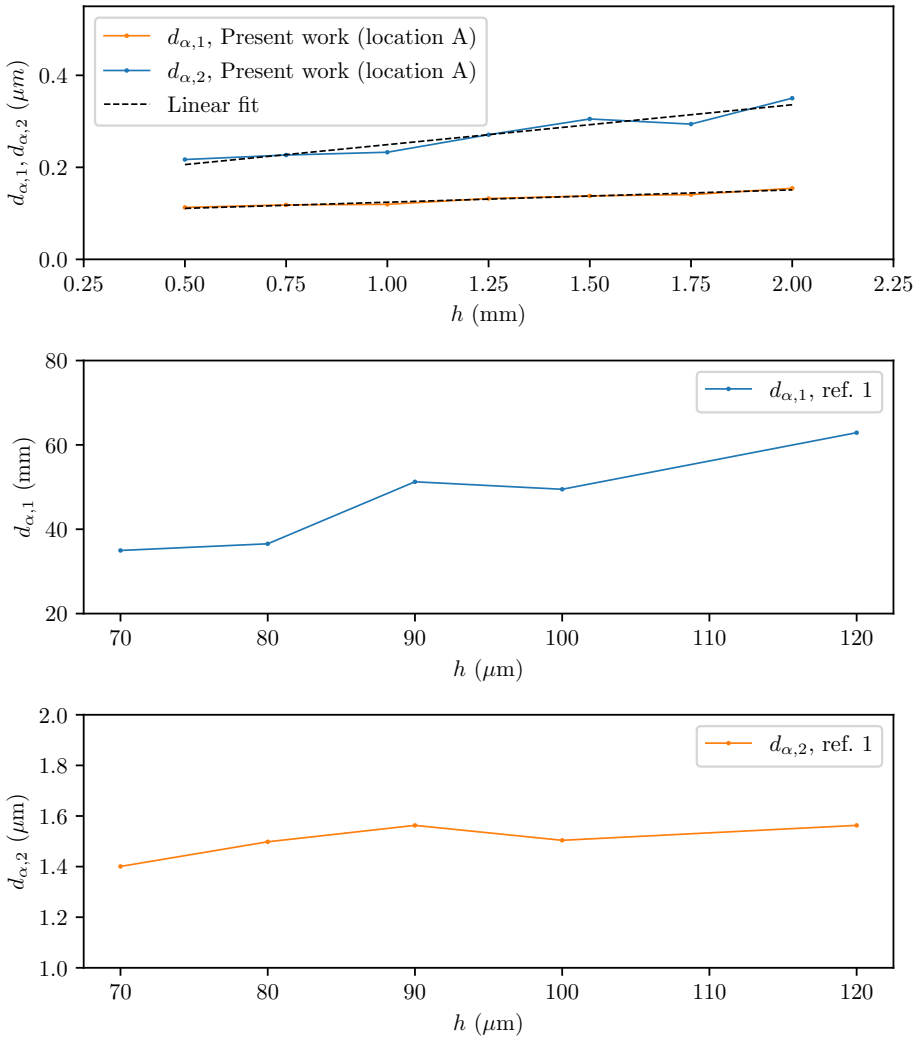

FIGURE 6.4: Lath martensite minor and major axes length and martensite aspect ratio in Ti-6Al-4V produced by selective laser melting. It can be observed how the major and the minor axes increase as the hatch spacing increases. Moreover, the major axis growth is more pronounced than that of the minor one, exactly as found in the present work (Figure 5.34). Image reproduced from [87, p. 317, fig. 11a].

presented in this study can better represent the overlapping effect. Indeed, the second laser pass overlapping the first one affects the cooling rate of the former and

the new model has a better agreement when the hatch spacing is lower, because it was explicitly calibrated on this condition. This situation is well illustrated in Figure 5.14, where the error between Villa *et al.* model (2020) [93, 94] is bigger as the hatch spacing is decreased (ALM condition) and it is smaller when it is increased (welding condition). Exactly the opposite occurs with the modified model presented in this study. This means that even if the trends are almost similar, the two conditions determined by the two processes, welding and additive manufacturing, are similar but not equal, due to the remelting of the material in the second one.

The width of the smaller martensite laths, in the present work, were found to increase as the hatch spacing increases (Figure 5.32 and 5.33). Moreover, exactly in the middle of the melt pool (location A in this study, Figure 5.34), the total martensite width (or minor-axis) showed an almost perfect linear increase. Even if the numerical values are different, because the minor axis was reported to be around 1.5 µm, while here is 0.10–0.15 µm, the linear trend already found during a deposition process by selective laser melting of Ti-6Al-4V [87] has been agreed with, as represented in Figure 6.4. The fact that all sizes increase can be explained by the proportional growth of grain with increasing of the hatch spacing, as, incidentally, pointed out in [87]. This could mean that each single lath is in some way bound to the grain size, even if this constraint is not so strict, because the martensite lath can potentially extend beyond the grain boundary.

Lath martensite thickness

According to the α' martensite lath characterisation expressed by the Equation (5.1) and represented in Figures 5.12a, 5.13a, 5.14a, its thickness does not vary sensibly within the melt pool. Therefore, since within the laser track the cooling rates are different, there is a small variation of the thickness with cooling rate, confirming the result of Villa *et al.* (2020) [93, 94] and extending this study to

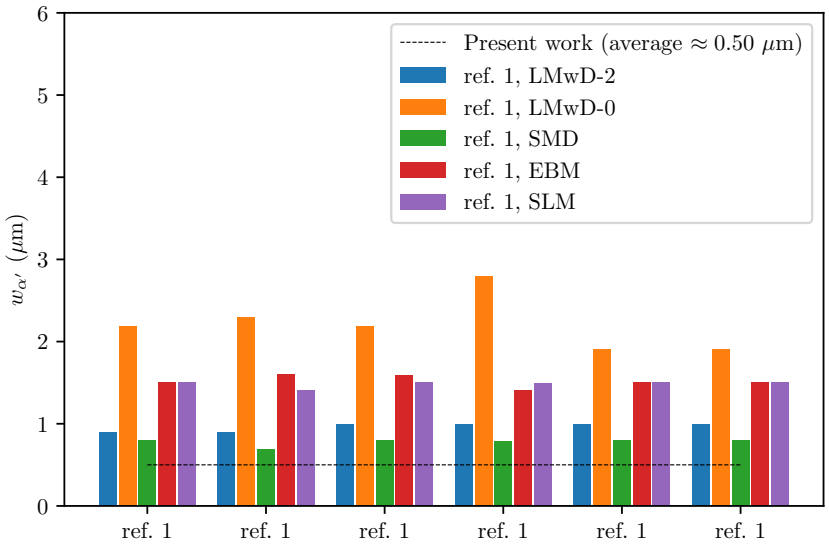

FIGURE 6.5: Lath martensite thickness in Ti-6Al-4V produced with different additive manufacturing processes. The reference is the following: ref. 1 = [263, p. 7, fig. 5].

two overlapped tracks. This characteristic of small variations matches the results obtained by Neikter *et al.* (2017) [263], who studied different additive manufacturing processes of Ti-6Al-4V. Indeed, it was found that lath martensite thickness remained almost constant during deposition and it did not vary sensibly with the point in which it was measured, as presented in Figure 6.5. The experimental measurements carried out in the present work lead approximately to the interval 0.25-1.25 µm for the lath martensite thickness and this roughly matches with the study just mentioned. The only exception is represented by the higher values of thickness measured for the process indicated as LMwD-0, but its average value is still less than 2 µm. In this process each layer was deposited continuously, whereas in the one called LMwD-2 a waiting time of two minutes between each layer was decided. Again, it seems reasonable to state that the dwell time plays an important role also in the growth of the laths.

Initial dislocation density

By using the Equation (5.1) for $w_{\alpha'}$ and Equation (3.65) for $d_{\alpha'}$ and comparing them with experimental findings (respectively, Figures 5.12a, 5.13a, 5.13a and 5.24a, 5.25a, 5.26a), in this study some of the gaps present in Table 2.10 were filled. This enabled to redefine the initial dislocation density of Ti-6Al-4V as inversely proportional to the cooling rate, as in Equation (5.5). This concept is not totally new, because reports have been found that in silicon the dislocation density decreases under a fast cooling process [264]. This was explained with the notion of *dwell time*, associated with the time needed to generate dislocations and this time decreases with a rapid cooling. However, for a different material (InP/Si) some scholars found in a previous study that the dislocation density was directly proportional to the cooling rate and they attributed this behaviour to the fact that a lower cooling rate induces a lower stress state, which is responsible for less dislocation generation [265]. Nevertheless, as seen for example in the flow stress model taken as reference in this study (Galindo-Fernández *et al.*, 2008), the stress state is determined starting from the dislocation density and not *vice versa* (Equations (2.56) and (2.57)). Since the cooling rate alone is not able to capture the initial dislocation density value, it is perhaps required a further extensive work in this direction. The objective there will be to clarify the relationship between the cooling rates in the martensite range and the dislocation density.

6.2 Residual stresses validation

Validation of predicted process-induced residual stresses is performed in the present work by using data acquired through destructive or non-destructive techniques and using the experimental data already available in the literature.

6.2.1 Adapted Carlsson-Larsson formulation

A non-destructive method was elaborated by Carlsson and Larsson in 2001 [266] and recently adapted for parts fabricated by selective laser melting and, in particular, for Ti-6Al-4V [266, 267]. According to this theory, the residual strain is correlated with the hardness value and the residual stress depends on the size of contact area of the material with the indenter. An initial hypothesis is that the indentation is related with the equi-biaxial plane stress state, which is defined as followings for a point $x \in \mathbb{R}^3$:

$$\sigma_{ij}(x) = \sigma(x), \quad i = j; \tag{6.1a}$$

$$\sigma_{ij}(x) = 0, \qquad i \neq j. \tag{6.1b}$$

Therefore, in order to use this method, it is necessary to check that the stresses on the surface S perpendicular to the vector representing the indentation force verify the following:

$$\sigma_{11}(x) \approx \sigma_{33}(x), \quad \forall x \in S. \tag{6.2}$$

In particular, if the validation pertains the maximum stresses calculated with finite element method, Equation (6.2) can be rewritten as an approximate condition:

$$\max_{i \in S_j}\{\sigma_{11,i}\} \approx \max_{i \in S_j}\{\sigma_{33,i}\}, \quad i = 1, \ldots, n, \tag{6.3}$$

where x_i is the i-th nodal coordinate where the stresses are calculated and n is the maximum number of nodes on the discretised surface S_j. By recurring to the notion of relative error, which in this particular case can be defined as

$$e_r^k = \frac{|\max_{i \in S_j}\{\sigma_{11,i}\} - \max_{i \in S_j}\{\sigma_{33,i}\}|}{\max_{i \in S_j}\{\sigma_{kk,i}\}}, \qquad k = 1, 2, \tag{6.4}$$

in Figure 6.12 is represented the approximate condition firstly stated in Equation (6.3), which holds with sufficient accuracy. For the double-pass simulations, the error for different hatch spacing values is represented in Figure 6.10a. It is maximum when there is a partial overlap between the two melt pools, but when there

is a complete remelting ($h = 0.5$ mm) the error is less than 20%. When considering the multi-pass simulations, the error is around 25% for higher speeds, but it is generally around 5–10% and it tends to decrease when adding up the second layer, as represented in Figure 6.10b. According to this, the modified Carlsson-Larsson method could be used to validate the simulations carried out in the present work, especially for lower speeds, but this was outside the present scope and it needs additional experiments. In the present work the method is used only to assess the validity of the thermo-physical and mechanical computational model to calculate residual stresses.

The second condition, represented by Equation (6.1b) is not satisfied, because the residual stress in the direction perpendicular to the surface of interest has a similar magnitude and is non-zero. However, it is possible to assume that the method is still valid and through its use check if this hypothesis is valid. Therefore, the following expression (valid for EBM and SLM) for calculating the residual stress can be implemented [267]:

$$\sigma_r(L_1, L_2, P) = \sigma_0 \left[\left(\frac{8P}{C\sigma_0 (L_1 + L_2)^2} \right) - \epsilon_r \right]^n \left[\exp\left(\frac{{c_0}^2}{0.32} \frac{8A_r}{(L_1 + L_2)^2} \right) - 1 \right], \tag{6.5}$$

where L_1, L_2 are the length of the two diagonals, P is the force, A_r is the contact area, C is a constant equal to 3 when a Vicker's indenter is used, $\epsilon_r = 0.08$ is a representative value of the strain, ${c_0}^2 = 1$, σ_0 and n are two constants which can be used to fit the stress-strain tensile curve of a material by using a power-law in the form $\sigma(\epsilon) = \sigma_0 \epsilon^n$. For Ti-6Al-4V produced with selective laser melting, the following values are suggested:

$$\sigma_0 = 1181.21 \text{ MPa}, \quad n = 0.1754. \tag{6.6}$$

The main assumption of the Carlsson-Larsson theory is that there exist a constant $C \in \mathbb{R}$ such that [267]:

$$H = C\sigma_y, \tag{6.7}$$

but, for a strain-hardening material, the Equation (6.7) can be replaced by the following [267]:

$$H = C\sigma(\epsilon_r). \tag{6.8}$$

Now, in order to use this methodology, it is also necessary to check that the value of the stress calculated using the power law, with the constants given in (6.6), is approximately the same as the value used by the constitutive model used in the thermo-mechanical model for calculating the residual stress. An overall immediate check of the comparison between this power law and the assumed material behaviour in the present work can be drawn by looking at the Figure 6.6, from which is evident that progressively become negligible as the strain increases. Moreover, the exact difference $\Delta\sigma(\epsilon_r)$ between the power law and the Galindo-Fernández *et al.* (2018) [88] model can be calculated taking into account that:

$$\text{Galindo-Fernández } \textit{et al.} \text{ (2018):} \quad \sigma(\epsilon_r) \approx 826\,\text{MPa}; \tag{6.9a}$$

$$\text{Wang and Chou (2005):} \quad \sigma(\epsilon_r) \approx 758\,\text{MPa}; \tag{6.9b}$$

from which it follows that $\Delta\sigma \approx 68$ MPa. From this, it can be deduced that the theory can be used to assess the validity of the residual stresses calculated in the present work with sufficient accuracy because this stress difference represent a small fraction of the predicted residual stresses. Further research into this discrepancy and its impact is postponed until the future.

In order to complete the description of the Equation (6.5), is now necessary to calculate the contact area. In Figure 6.8 are represented some sample images acquired during hardness measurement, showing the diagonals and the indentation areas for reference. Assuming that $L_1 = L_2$, if the depth of the indentation in unknown, it is possible to state that the real contact area A_r is equal to the area of the plane surface A before the indenter hits the surface (*nominal area* A) plus a portion of it, which, in absence of measurements, can be determined using the approximate estimate that follows. Considering the triangle formed by

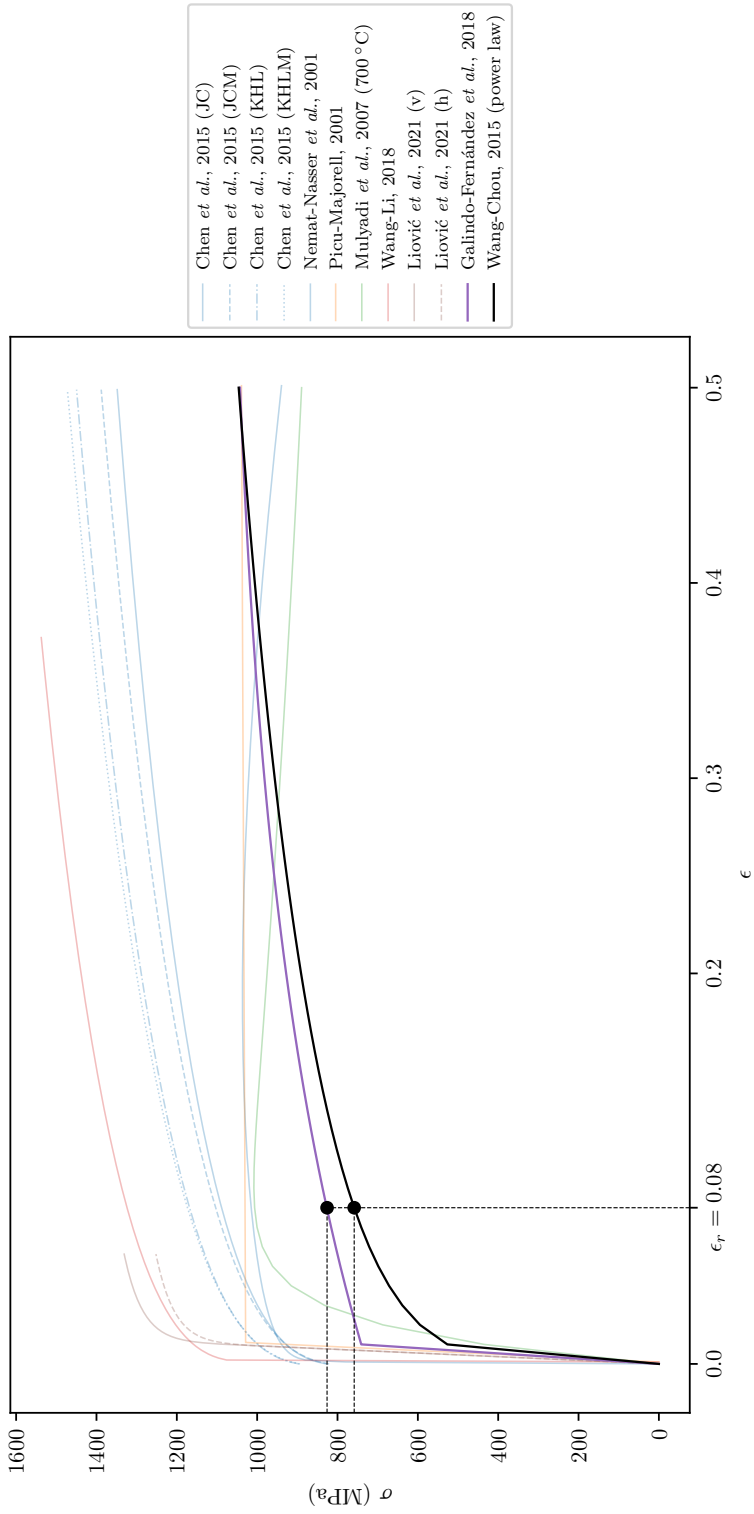

FIGURE 6.6: Comparison the power law for flow stress prediction of Ti-6Al-4V and the constitutive models investigated in this study ($T = 25$ °C, $\dot{\epsilon} = 0.001$ s^{-1}).

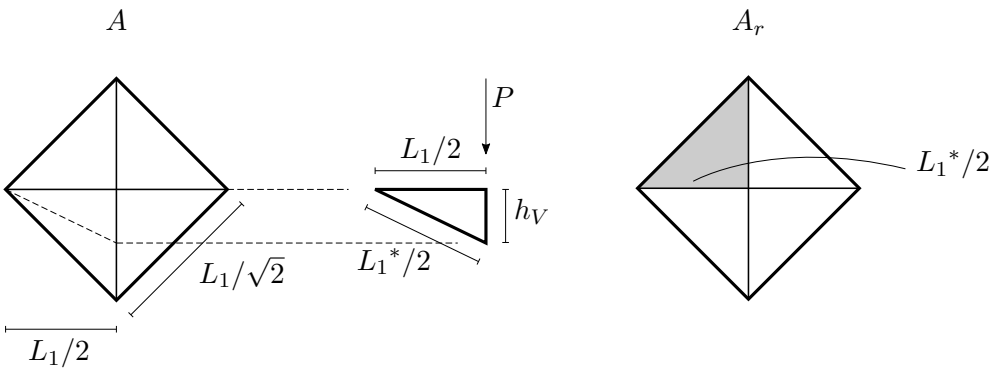

FIGURE 6.7: Dimensions useful to calculate the nominal and real indentation areas for a Vickers hardness test.

a half diagonal and the indentation depth h_V at the middle point of the indentation track and the half diagonal measured at the impressed surfaces ${L_1}^*/2$, as in Figure 6.7, it possible to use the following set of equations to approximate the contact area:

$$ {L_1}^* = 2\sqrt{\left(\frac{L_1}{2}\right)^2 + {h_V}^2}; \tag{6.10a} $$

$$ A_r = 4\left[\frac{1}{2}\left(\frac{{L_1}^*}{2}\right)^2\right] = \frac{1}{2}\left({L_1}^*\right)^2 \tag{6.10b} $$

From the data available in the literature [268], $h_V \in [0, 700]$ (in nm) when the indentation pressure is between 0 and 10 mN, and

$$ h_V = 200\,\text{nm} \tag{6.11} $$

is the maximum attained during plastic deformation regime [268]. Therefore, it is possible to assume the following maximum value in the plastic regime, a value which is however obtained for a lower force than that used in the present work (3 N). As a consequence, the contact area increment can be roughly estimated to be 0.01%, so:

$$ A_r \approx A + \frac{1}{10000}A = \frac{1}{2}L_1L_2 + \frac{1}{10000}\frac{1}{2}L_1L_2 \approx (1 + 10^{-5}){L_1}^2. \tag{6.12} $$

Since no exact data have been found, the estimate of residual stresses has been carried out assuming that $A_r = A + kA$, where k is an increment factor which has

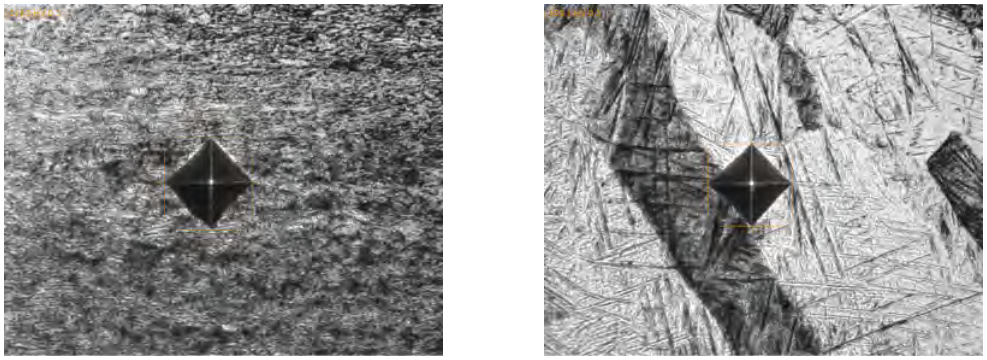

(a) Outside the laser-affected area: non-martensitic microstructure.

(b) Inside the melt-pool area: martensitic microstructure.

FIGURE 6.8: Vickers indentations at different points.

been evaluated in two different scenarios. Firstly, $k = 10^{-2}$, and then $k = 10^{-1}$, showing that an increment of 1% of the contact area is in line with what expected, while 10% is too high, as in Figure 6.11. Therefore, it should be pointed out that the assumption $A_r \approx A_n$ can also be used for simplicity, because it has been here shown that the variation of the ratio between the areas versus h_V is minimal, especially when h_V is small, as can be appreciated in Figure 6.9. However, in the present work Equation (6.12) is preserved and $k = 10^{-2}$ is assumed, although a more accurate estimate could be made taking into account the curved shape of the sides of the square and an in-depth experimental study to effectively refine the residual stress analysis, if necessary.

Finally, from the analyses carried out in the present work, it is possible to establish that the numerical model and procedures to approximate the coupled thermo-mechanical model for a single-pass simulation permit to predict with sufficient accuracy the magnitude of residual stresses. Indeed, when Equation (6.5) is used to calculate the stresses from the experimental data acquired in the present work, the values are found within an acceptable range, because this difference is less than 200 MPa when considering $\sigma_{r,22}$ and about 50 MPa when considering $\sigma_{r,11}$. A comparison between the predicted values and the values obtained through the adapted Carlsson-Larsson theory are shown in Figure 6.11.

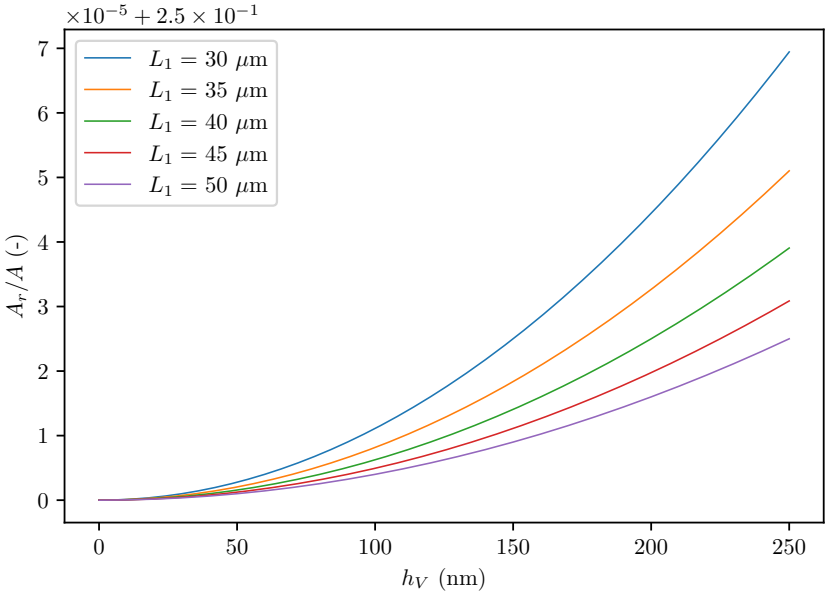

FIGURE 6.9: Ratio between the real contact area and the nominal contact area as function of the Vicker's hardness indentation depth for different values of the diagonal L_1.

6.2.2 Comparison with relevant literature

Since, as seen, the single-pass numerical thermo-mechanical model is able to predict residual stresses with sufficient accuracy (50–200 MPa), the same material thermo-mechanical properties can be used to extend the prediction to residual stresses for metal deposition in a multi-pass single-layer and multi-layer scenario. The results of the predicted residual stresses varying with laser speed is represented in Figure 6.12, where a comparison with values available in the literature is also made.

The results show that the maximum predicted residual stresses are in the range of approximately 300-1100 MPa and similar values are found for low speed processes (grouped by an ellipse in Figure 6.12), which usually consist in simultaneous melting and deposition of material (DLD, DMD, WAAM). On the other hand, the results show a good agreement with laser powder-bed fusion methods when they are validated through accurate destructive and non-destructive

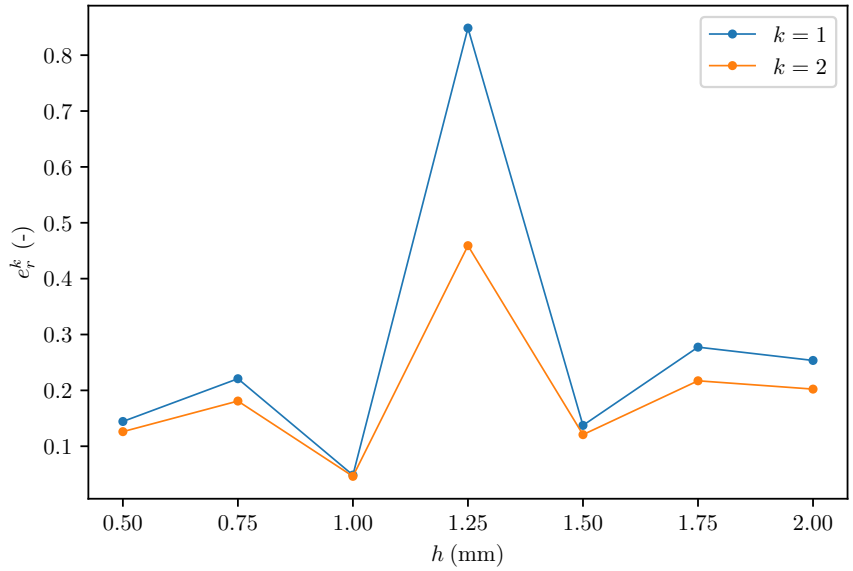

(a) Relative error for the equibiaxial stress state in finite element double-pass simulations for different hatch spacing values.

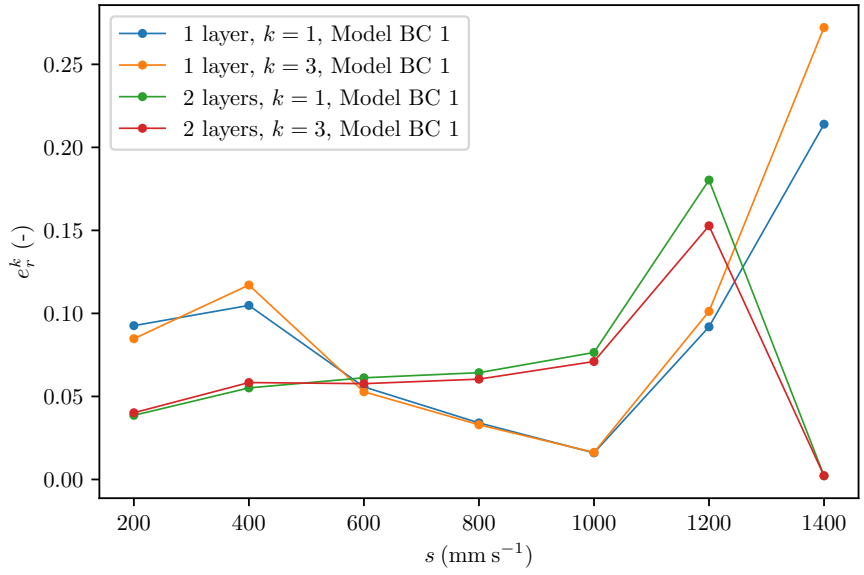

(b) Relative error for the equibiaxial stress state in finite element multi-pass single layer and double-layer simulations.

FIGURE 6.10

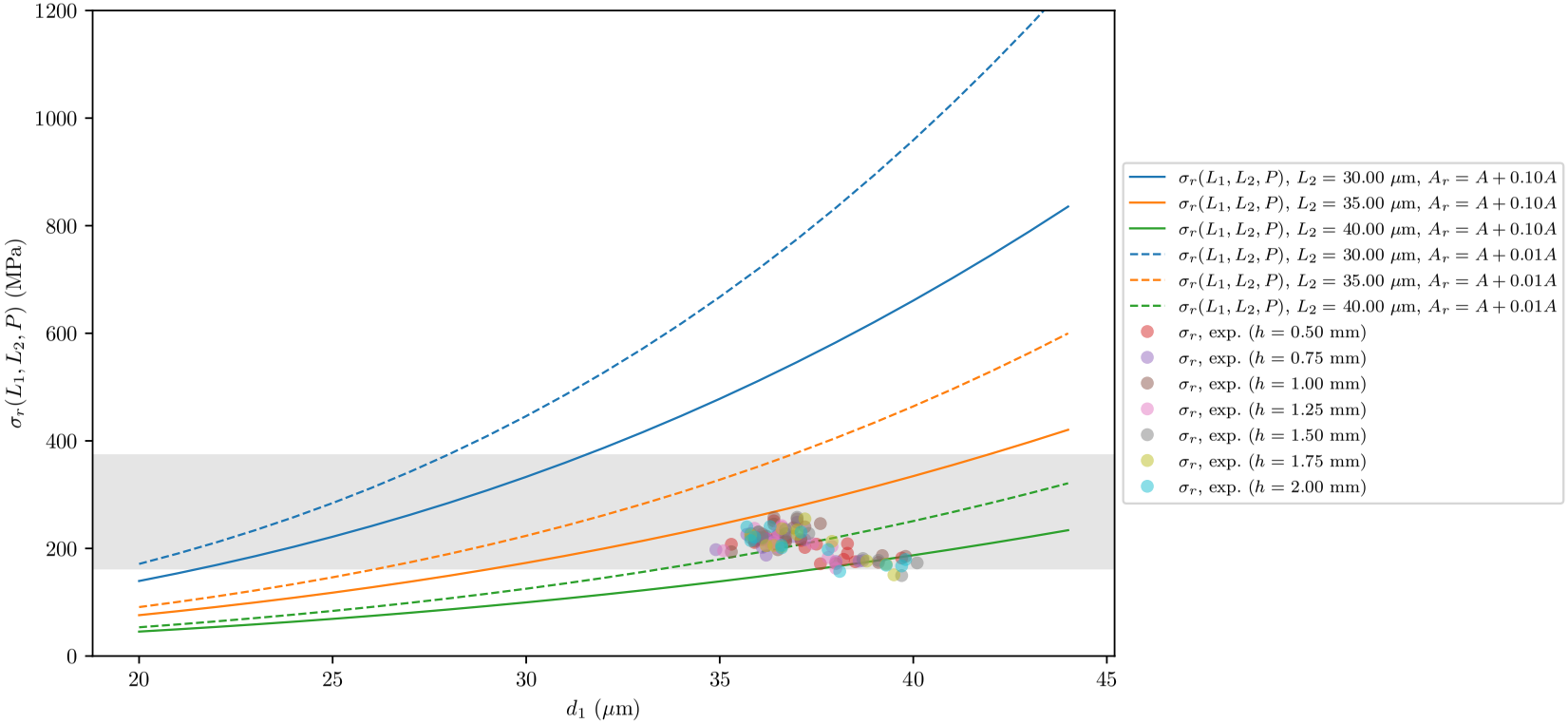

FIGURE 6.11: Comparison between the residual stresses calculated with finite element method and the estimated values, according to Carlsson-Larsson theory, obtained from the diagonals of the Vickers hardness tests for a double laser pass on Ti-6Al-4V plates ($P = 3$ N). The grey band indicates the range of values obtained by finite element analyses (149.57–257.85 MPa).

measurements techniques.

6.3 Stress-life fatigue curve of a Ti-6Al-4V additively-manufactured specimen

According to the formulation introduced in the literature review, a new methodology for taking into account the effect of the residual stresses on the fatigue-life behaviour was outlined in the present work. This permits to assess the combined impact of residual stresses, surface roughness, and microstructure on an additively-manufactured specimen of Ti-6Al-4V under a fatigue test. This is also the standard specimen test for fatigue recommended by ASTM E466-15 and used to evaluate Ti-6Al-4V parts behaviour for the turbine engine BLISKs testing [269].

One of the applications of the scanning strategies investigated in the present work for one and two layers, it is the possibility to define two different scenarios for a fatigue specimen, as represented in Figure 6.13. More generally, it is possible to determine the combined fatigue behaviour due to the surface roughness and residual stresses obtained for additive manufactured parts of Ti-6Al-4V, alongside some relevant literature data, as represented in Figure 6.15. The stress-life curve in presence of residual stresses is qualitatively similar to the one experimentally found and used within a new implemented standard in welding applications [270], where only the endurance stress is significantly influenced by the residual stresses. The equation to evaluate the fatigue behaviour for $n_f \in [n_{f,0}, n_{f,f}]$ is the following:

$$\sigma_a(n_f) = \sigma_{a,0} \left(\frac{n_f}{n_{f,0}} \right)^{\log(\sigma_e/\sigma_{a,0})/\log(n_{f,f}/n_{f,0})}, \tag{6.13}$$

where $n_{f,0} = 10^3$, $n_{f,f} = 10^7$, and

$$\sigma_{a,0} = \sigma(n_{f,0}) = \begin{cases} 893\,\text{MPa}, & \text{AB-1, AB-2;} \\ 952\,\text{MPa}, & \text{MA/Pol.} \end{cases} \tag{6.14}$$

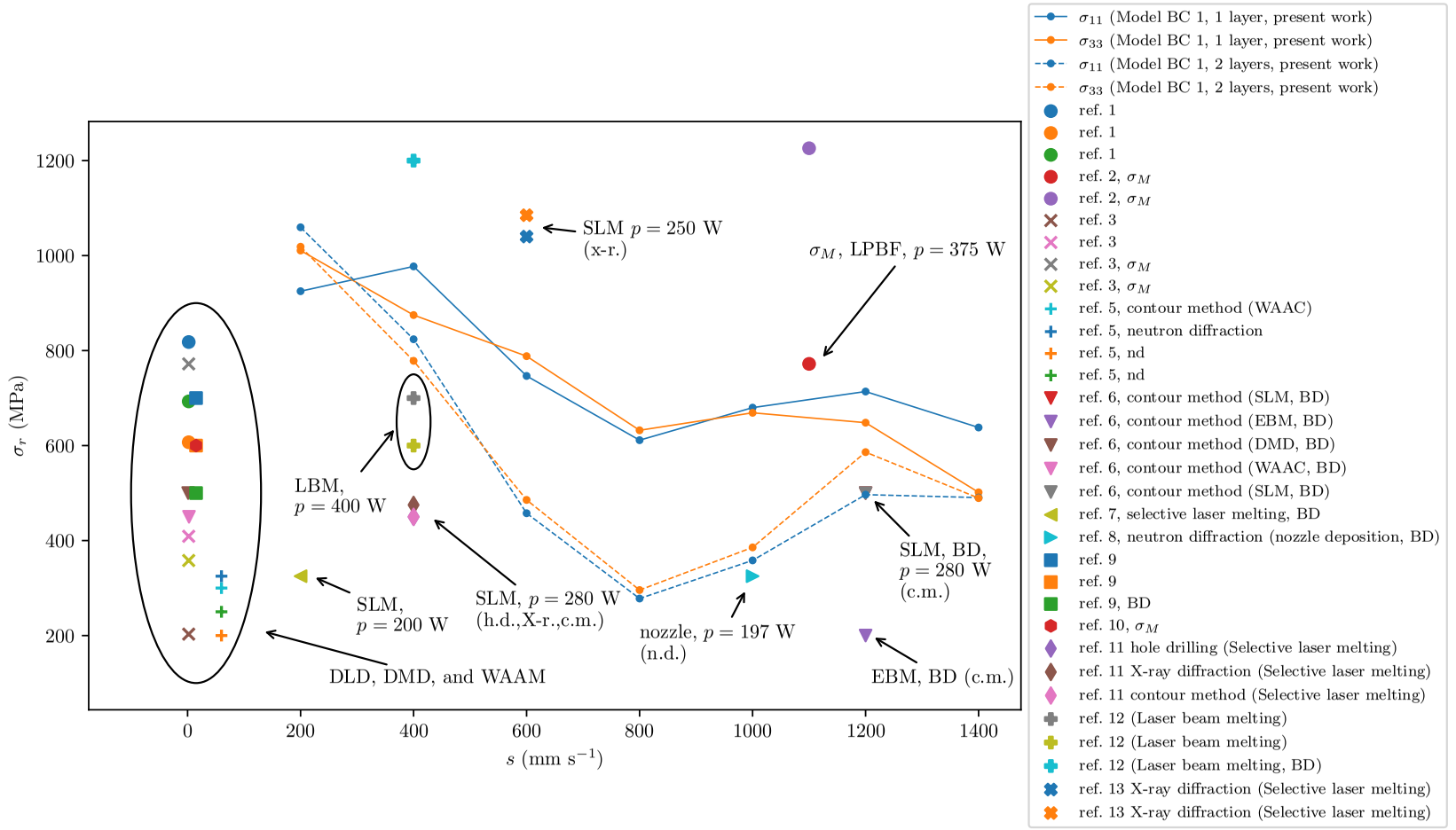

FIGURE 6.12: Comparison between the maximum residual stresses calculated with finite element method models for multi-pass single layer and double layer additive manufacturing models and data available in the literature. The references are the followings: ref. 1 = [165], ref. 2 = [166], ref. 3 = [150], ref. 4 = [160], ref. 5 = [167], ref. 6 = [161], ref. 7 = [168], ref. 8 = [169], ref. 9 = [170], ref. 10 = [171], ref. 11 = [172], ref. 12 = [173], ref. 13 = [174].

It is worth remembering that the surface parameters for AB-1, AB-2, and MA/Pol are reported in Table 2.13. Finally, the endurance stress can be calculated by using Equation (2.67). For the purpose of discussion, three different stages in fatigue life can be distinguished, as in Figures 6.14 and 6.15, according to the number of cycles:

- low cycles, $n_f < 10^4$;
- high cycles, $10^4 \leq n_f \leq 10^6$;
- very high cycles, $n_f > 10^6$.

The boundary between high and very high cycles lies approximately where there is a transition between internal and surface fracture. Since no data were found in the literature for this transition and especially for Ti-6Al-4V, the behaviour of 316L stainless steel was accepted as having a similar character, as shown in 6.14. Moreover, these steels show a similar behaviour in terms of fatigue life when compared with additively manufactured Ti-6Al-4V, as represented in Figure 6.14. Nevertheless, this aspect needs further clarification, especially because it has been reported that for very high cycles Ti-6Al-4V both subsurface and surface crack initiation were observed [271]. Moreover, the internal defects such as porosity play an important role in crack nucleation at high cycles [272]. Post-heat treatments like hot isostatic pressing are often suggested if the part will be subjected to high cycle regime, because of its capacity to consolidate the part and close pores [272].

The theoretical approach followed and developed in the present work permits to quantify effectively the effect of residual stresses on fatigue life in Ti-6Al-4V components by taking also into account the surface roughness and the martensitic α' thickness and some useful considerations can therefore be drawn. For low cycles, residual stresses have little influence on the stress amplitude, which can be quantified as lower than approximately 200 MPa for $n_f \approx 10^4$, when $\sigma_r = 400$ and $\sigma = 100$ MPa.

At high cycles, residual stress begin to have a higher influence, which can considerably reduce the fatigue life and this effect can be quantified as around 10^3 cycles for a fixed stress amplitude, when $\sigma_r = 400$ and $\sigma = 100$ MPa.

Finally, for very high cycles, it is possible to see a higher scatter on the data due to the different thermo-mechanical histories. At this regime, residual stresses have an extremely significant impact on the stress life and on the endurance stress, which corresponds to $n_f \approx 10^7$, a value confirmed also in multiple studies, as represented in Figure 6.15. However, compressive residual stresses act almost like a post-heat treatment, and permit to increase the endurance stress up to approximately 1 GPa for some conditions.

In summary, residual stresses arising from additive manufacturing can be negligible in fatigue when the number of cycles is below 10^4, or for high cycles when the stress amplitude is below 10^2 MPa, but this depends on the in-service applications of the component. Fatigue life can be extended much further $n_f > 10^7$ by recurring to heat treatments and a similar behaviour seem to be confirmed also where compressive residual stress are present. A discrepancy of about 100 MPa between the predicted behaviour for AB-1 when tensile residual stresses are present ($\sigma_r = 400$ MPa) and a value found in the literature for 316L stainless steel, for $\sigma_r = 300$ MPa is attributable to the different materials. However, examining the specimen AB-2, the predicted behaviour for $\sigma_r = 400$ MPa (tensile) is close to the value found in the literature for the same steel [270]. The conclusion is that when the surface conditions of Ti-6Al-4V are not particularly cared for, the fatigue strength is comparable to that of steel.

6.3.1 Post heat treatments and martensite influence on fatigue

As seen, the martensitic width can be incorporated into the calculation for the stress-life curve of additively manufactured specimens of Ti-6Al-4V. In general,

the martensitic structure shows significantly reduced fatigue strength compared to the globular microstructure, and this is another negative effect in addition to porosity [272].

It is now of interest to quantify the influence of this microstructural characteristic on the endurance stress. This can be achieved by evaluating the notch sensitivity factor in the Equation (2.65) respectively for $w_{\alpha'} = 0.5$ and $w_{\alpha'} = 4.0$ µm, and the result is presented in Figure 6.16. From the calculations an increment of about 20 MPa in σ_e when average martensitic width increases from 0.5 to 4.0 µm was found. This increase in martensitic width is usually found when using temperatures around 400–950 °C [107] and it is possible that the single lath starts to grow before being subjected to a perpendicular fracture as represented in Figure 2.8b. The fact that the martensite lath grows during heating could be related to the reduction in dislocation density, represented in Figure 2.7, because a finer microstructure can lead to accumulation of defects. Therefore, it can be convenient to achieve better performance by completely segregating the martensite laths, instead of tuning its geometry.

Predictions for various martensitic structures of polished specimens are not possible, because of the following limitation of the formulation and, in particular, in Equation (2.65) if $\overline{\rho}_{10}$ represent the period of an ideal sinusoidal profile:

$$\overline{\rho}_{10} \to +\infty \implies q \to 1, \tag{6.15}$$

from which it follows that the endurance stress is constant, namely $\sigma_e \approx 449.04$ MPa (similar to 450 found in [178]). This limitation may conceal a realistic behaviour, because the improved performance due to polishing may possibly reflect a real loss of influence of the martensite on the fatigue strength, but the interaction surface-microstructure needs to be clarified in future studies.

6.3.2 Limitations of the current formulation

Due to the interconnected and difficult nature of the problem here tackled, several limitations can affect the present formulation, which can be seen as an initial tentative of incorporating residual stresses, surface condition and microstructure into a unique approach. An important limitation of this approach lies in the fact that compressive residual stresses has to be bounded as

$$\sigma_r \leq \sigma_{r,l}, \tag{6.16}$$

where the stress limit $\sigma_{r,l}$ is 483.82 MPa for as-built specimens and 181.38 MPa for machined or polished specimens (values found numerically when $\sigma = 100$ MPa), cannot be incorporated into this formulation, otherwise the predicted fatigue curve shows an unrealistic and increasing trend according to which stress amplitude increases with an increased number of cycles. The maximum value for the as-built condition is represented by the horizontal line in Figures 6.14, 6.15, 6.16 and a few experimental points are effectively above this limit, as shown in Figures 6.15 and 6.16.

6.4 Guidelines for reducing residual stresses or minimise their negative impact on fatigue

In summary, based on the investigations carried out in the present study, the following strategies can be briefly outlined to reduce residual stresses or improve the mechanical properties of Ti-6Al-4V fabricated with additive manufacturing:

- set the pre-heating temperature in the range 100–500 °C to achieve better ductility, yield stress, and ultimate tensile stress; with 100 °C similar properties are obtained, so this particular temperature permits to save energy with equal final performance;

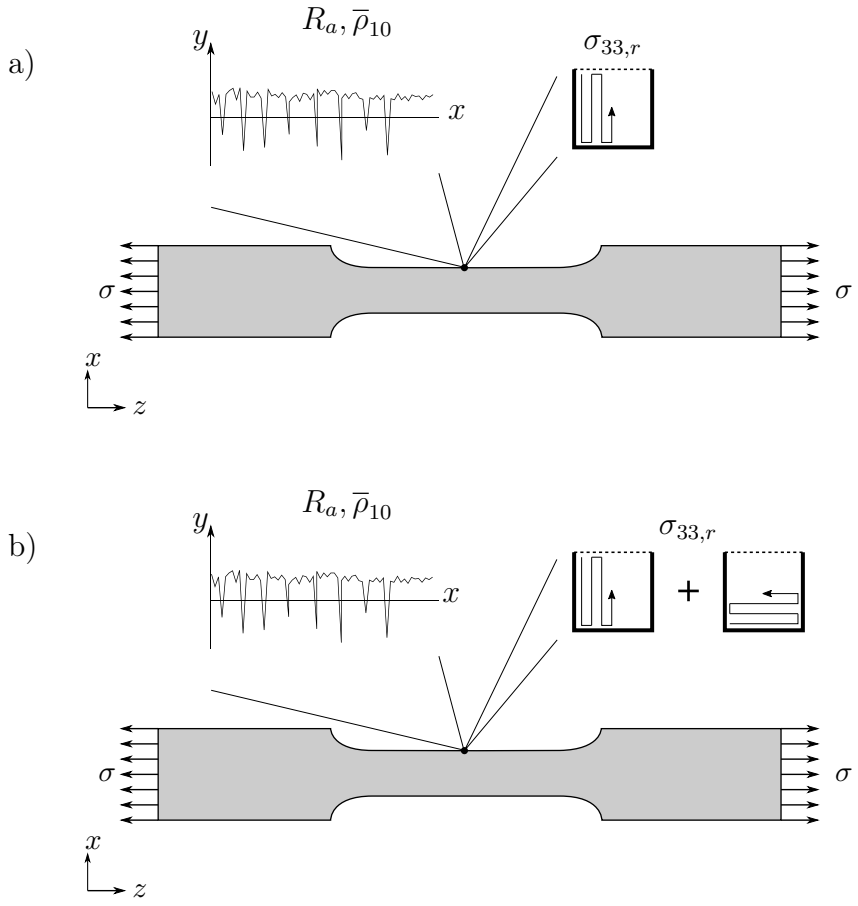

FIGURE 6.13: An additively-manufactured *dog-bone* specimen with surface roughness and subjected to fatigue under two different scenarios, under the same boundary conditions and with two different laser scanning strategies.

- set the substrate temperature in the range 100–500 °C to achieve better ductility, yield stress, and ultimate tensile stress; with 100 °C similar properties are obtained, so this temperature permits to save energy with equal final performance;
- use a laser speed of approximately 800 $\mathrm{mm\,s^{-1}}$ to reduce the maximum tensile residual stress from 1000 to 300–600 MPa.

Furthermore, for minimising the residual stress impact on fatigue life, the following recommendations can be outlined:

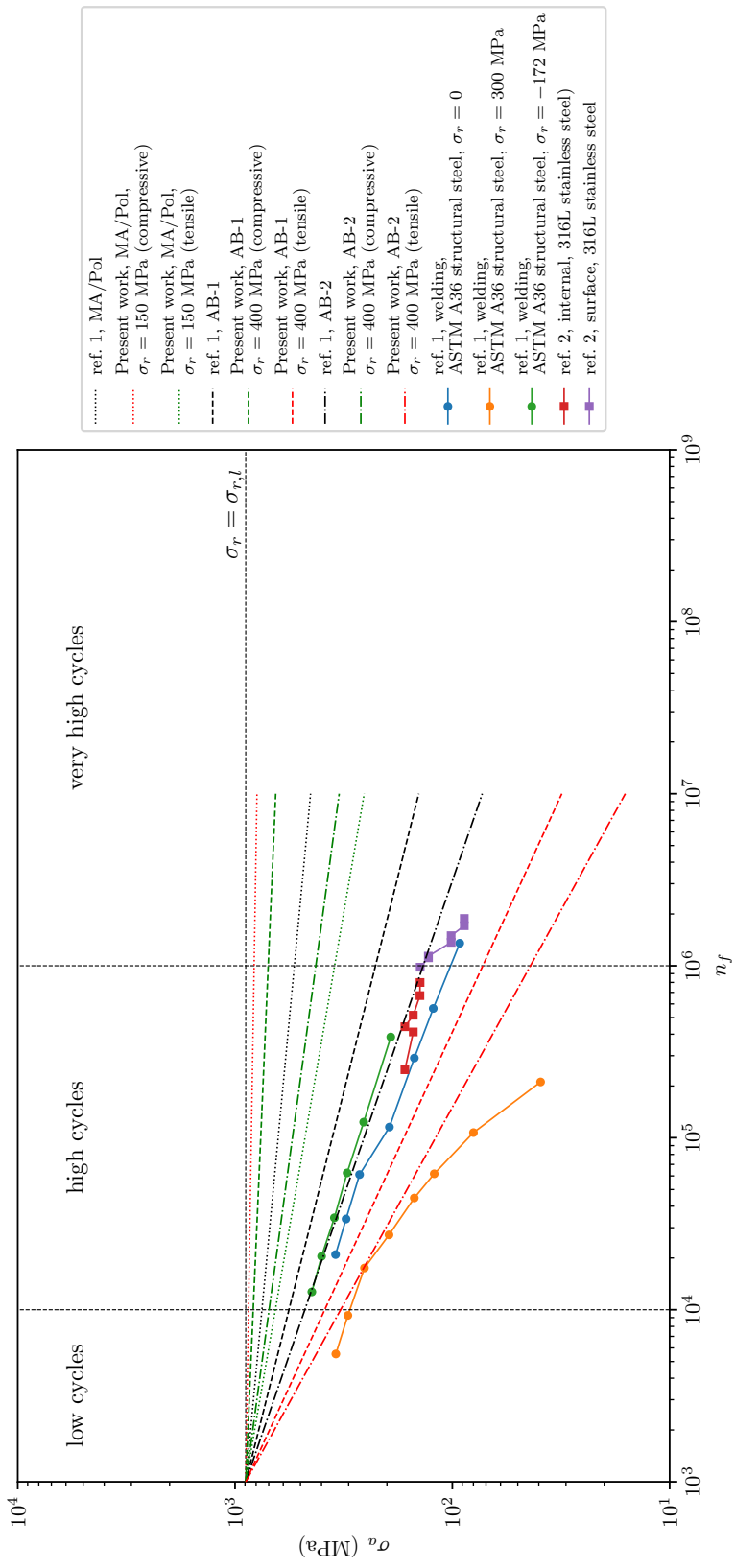

FIGURE 6.14: Stress-life fatigue of Ti-6Al-4V, incorporating surface roughness, average α' martensitic thickness, and residual stresses. In the present work $\overline{K}_f{}' = \overline{K}_f \pm \sigma_r/\sigma$ (negative sign for compressive residual stresses and positive sign for tensile residual stresses); the reference stress value is $\sigma = 100$ MPa. Comparison of fatigue life considering residual stresses from welding in steels. The references are the following: ref. 1 = [270, p. 79, fig. 5], ref. 2 = [177, p. 1955, fig. 10A]. The surface conditions for specimens MA/Pol, AB-1, and AB-2 are summarised in Table 2.13.

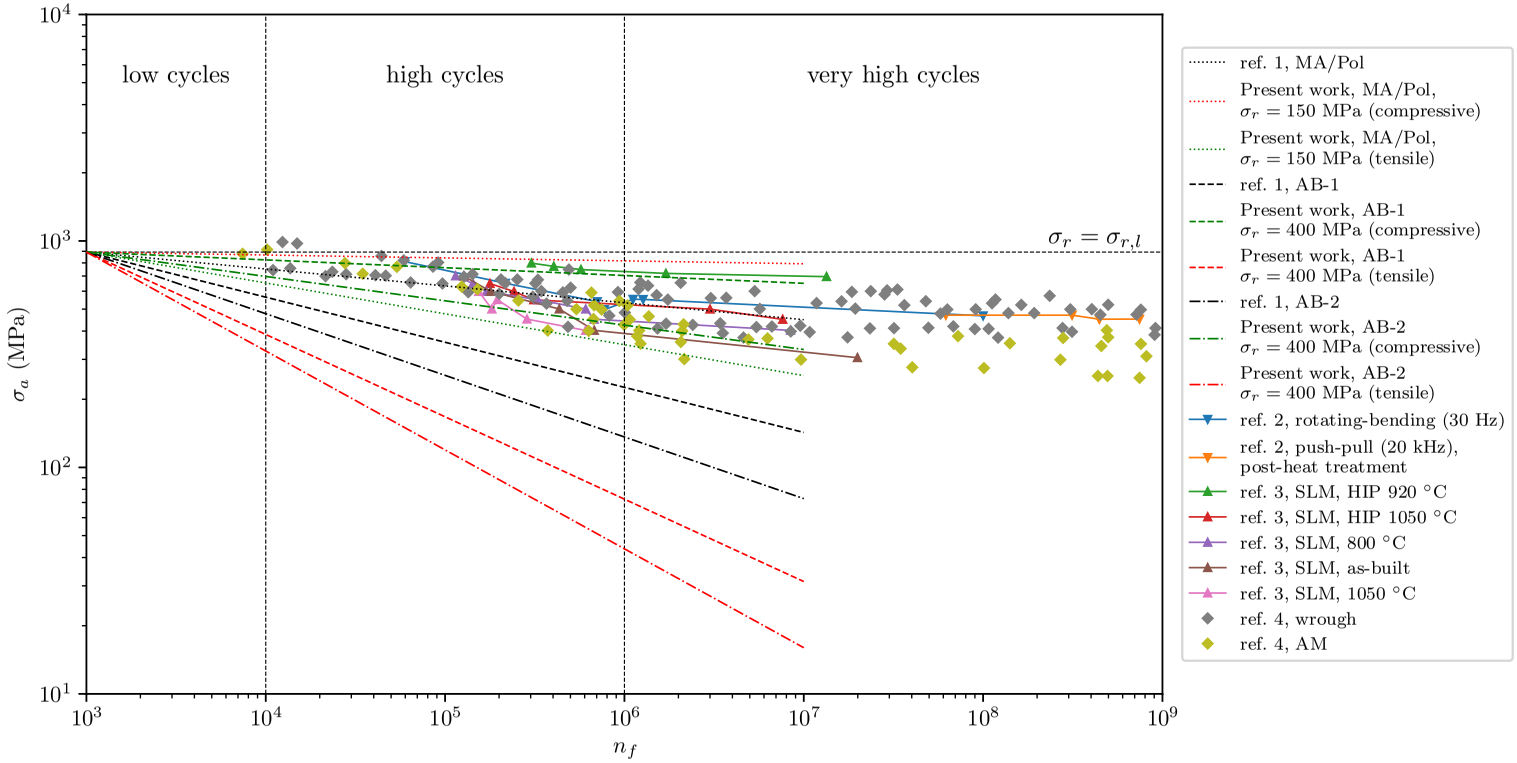

FIGURE 6.15: Stress-life fatigue of Ti-6Al-4V, incorporating surface roughness, average α' martensitic thickness, and residual stresses. In the present work $\overline{K_f}' = \overline{K}_f \pm \sigma_r/\sigma$ (negative sign for compressive residual stresses and positive sign for tensile residual stresses); the reference stress value is $\sigma = 100$ MPa. Comparison of fatigue life in Ti-6Al-4V fabricated with additive manufacturing. The references are the following: ref. 1 = [178, p. 79, fig. 5], ref. 2 = [271, fig. 2, p. 498], ref. 3 = [273, fig. 6a, p. 11], ref. 4 = [272, p. 2, fig. 1b]. The surface conditions for specimens MA/Pol, AB-1, and AB-2 are summarised in Table 2.13.

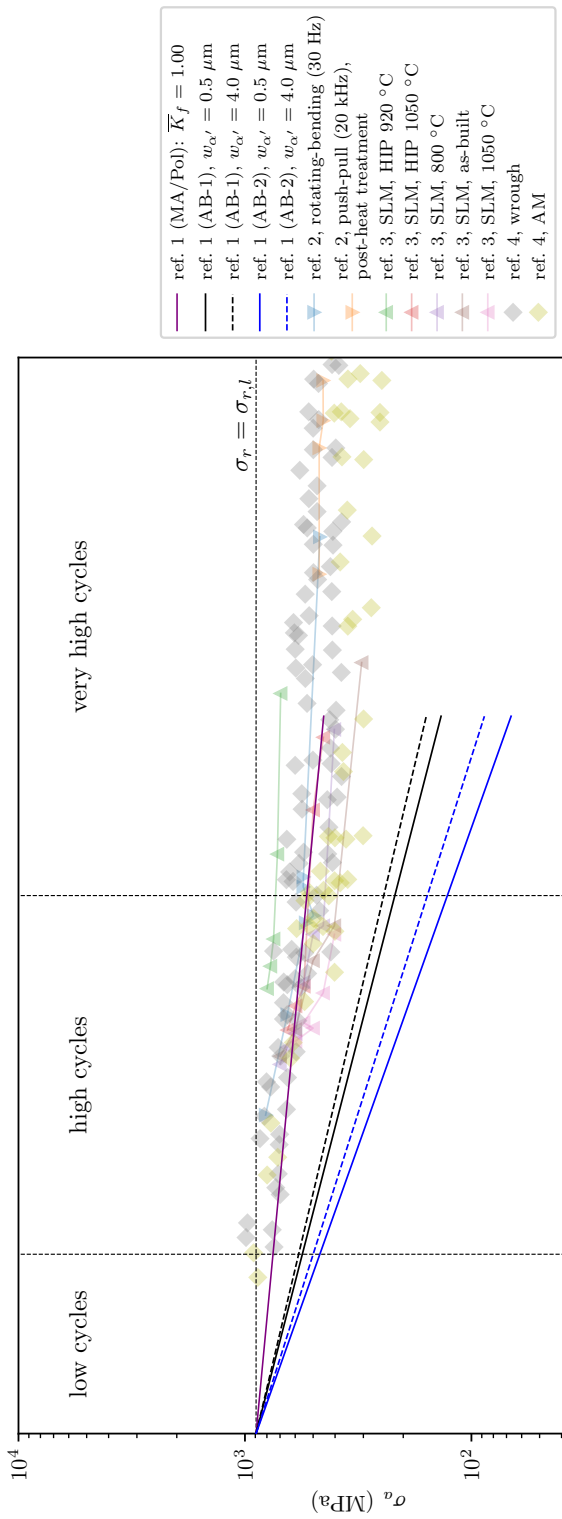

FIGURE 6.16: Prediction of stress-life fatigue of Ti-6Al-4V for different α' martensite width under different surface roughness and in absence of residual stresses. In the present work $\overline{K}_f{}' = \overline{K}_f \pm \sigma_r/\sigma$ (negative sign for compressive residual stresses and positive sign for tensile residual stresses); the reference stress value is $\sigma = 100$ MPa. The references are the following: ref. 1 = [178, p. 79, fig. 5], ref. 2 = [271, fig. 2, p. 498], ref. 3 = [273, fig. 6a, p. 11], ref. 4 = [272, p. 2, fig. 1b]. The surface conditions for specimens MA/Pol, AB-1, and AB-2 are summarised in Table 2.13.

- polishing the surface of the part, verifying that $R_a/\overline{\rho}_{10} \to 0$, can improve the endurance stress by approximately 100 MPa (for high cycles, both under shear and tension);
- a post-heat treatment can decompose the martensite laths and thus increase the endurance stress by approximately 100 MPa.

Finally, the following actions appear to be irrelevant or of little effect:

- hatch spacing control in the range 40–120 µm for residual stresses magnitude control;
- martensite width tailoring for fatigue life improvement.

Chapter 7

Conclusions and future work

The use of additive manufacturing is rapidly increasing with respect to traditional manufacturing techniques, thanks to the prospect of reducing material and energy waste, and shortening the time between the design and the manufacturing of a product, in an ever more rapidly changing world. However, traditional manufacturing technologies are still competitive, because they can benefit from the knowledge accumulated during decades of experience and so provide, for some aspects, a better finished product with better mechanical performance. It is only with the contribution of research that additive manufacturing can be driven to result in products with better features, by working on the process conditions, and so achieve the coveted objectives.

The processing route inevitably affect the manufactured component, but this is particularly true for those processes which involve the use of a laser. In additive manufacturing one of the most relevant causes of concern is the presence of residual stresses, which arise from the high temperatures and cooling rates reached from the material during laser scanning. Moreover, when manufacturing Ti-6Al-4V, this concern is mainly represented by the presence of the martensite, a phase generated during rapid cooling. Therefore, the objective of this study

was the study of the influence of laser pass on the material, in conditions that reproduce experimentally and numerically additive manufacturing. However, due to the complex physics involved in this new building technique, the objective has been partially pursued by recurring to the analogy between welding and additive manufacturing, which enabled to use some of the methodology and data available in this field. In particular, the martensite of Ti-6Al-4V has been studied and characterised, for the first time, in three different locations of two melt pools, with a variable hatch spacing. Whils primary martensite exhibited an almost constant trend, the other finer microstructure showed linear relationship with the hatch spacing values and this aspect need to be better clarified and, possibly, incorporated into a new constitutive model. Moreover, the role of microstructure and process parameters on residual stresses has been numerically investigated by using a process model based on finite element modelling and thanks to the possibilities offered by high-performance computing. Additionally, a potential approach was suggested to predict the fatigue life of Ti-6Al-4V components manufactured using additive manufacturing. This method allows for combining residual stresses, surface roughness, and lath martensite width in one formulation.

Shortening the distance between welding and additive manufacturing, balancing experiments with theoretical frameworks, linking the metallurgy of steel with that of a titanium alloy: these have been the fundamental steps in the attempted methodology to contribute to this research area. However, huge ambitions such as these must be always confronted with realistic possibilities, which, as is often the case in life, are conditioned by certain limitations. Those limitations naturally arise when pursuing something new and they should be accepted as part of our human nature. Nevertheless, the hope is that the present work can be useful and inspirational to the readers, who will certainly find more gaps and more limitations to overcome, than those overcame. According to the spirit of modern science, these limitations can be also seen as interesting opportunities for future

research.

7.1 Summary of the achievements and conclusions derived from the present study

In summary, the achievements can be summarised as the following:

- introduced a time-dependent Koistinen-Marburger model and used to assess the formation of martensite in Ti-6Al-4V (see Figure 5.17);
- presented an analysis of temperature-dependent thermal and mechanical parameters of Ti-6Al-4V for both bulk and powder material (see Paragraphs 3.1.6 and 3.1.7) and a comparison of constitutive models for Ti-6Al-4V (see Figure 2.26);
- introduced a versatile process model for additive manufacturing based on a numerical framework using finite element modelling and implementing thermo-dependent thermo-mechanical parameters and a thermo-viscoplastic constitutive model (see Figure 3.1);
- calibrated a fitting equation to describe the emissivity of a powder layer and implemented it in the finite element model (see Figure 3.19);
- numerically quantified the residual stresses for a single a double-layer multi-pass model of Ti-6Al-4V, in its common processing window;
- characterised the martensite content (volume fraction) and its morphology (thickness, spacing, major axis, minor axis, angle of growth, hardness) as a function of the hatch spacing for a double-pass laser scan;
- used the Vicker's hardness data to predict residual stresses in Ti-6Al-4V for a double-pass model, using the Carllson-Larsson theory and its most recent integrations (see Figure 6.11);

- predicted the fatigue life curves for parts realised in Ti-6Al-4V with additive manufacturing (laser-powder bed fusion) and taking into account the average α' martensite width, surface conditions, and compressive or tensile residual stresses (see Figures 6.14, 6.15, and 6.16).

Finally, from the present study, the following conclusions can be drawn:

- the hatch spacing has little influence on both martensite thickness (approximately less than 1 µm, see Figures 5.12, 5.13, 5.14), spacing (approximately less than 5 µm, see Figures 5.24, 5.25, 5.26), and volume fraction (approximately less than 0.05, see Figure 6.2), when it is increased from 0.50 to 2.00 mm;

- the hatch spacing has little influence on residual stresses (approximately less than 10 MPa), when it is varied in the range 40-120 µm;

- the α' martensite spacing increases from approximately 3 to 9 µm when the hatch spacing at the centre of the melt pool is increased from 0.50 to 2.00 mm, with smaller changes observed at other locations (see Table 5.4);

- the dimensions of martensite minor and major axes, as well as the aspect ratio, demonstrate a linear increase as the hatch spacing increases from 0.50 to 2.00 mm (see Figure 6.4 and Figure 5.34);

- laser speed of approximately 800 $\mathrm{mm\,s^{-1}}$ appears to result in reduced residual stresses (for both the single and double-layer models) from 1000 to 300–600 MPa (see Figure 6.12);

- the boundary conditions of the model can change the magnitude of residual stresses by approximately 20 MPa when considering only the bulk properties for the material (see Figure 5.47);

- the incorporation of recent integrations into Carlsson-Larsson theory enables accurate prediction of residual stresses in alignment with finite element analysis, showing a difference of around 200 MPa (see Figure 6.11);
- a drop of about 60 MPa in the stress amplitude for very high loading cycles (greater than 10^6) is attained when tensile residual stresses of 400 MPa are present in the mechanical part (see Figure 6.14);
- a rise of about 275 MPa in the stress amplitude for very high loading cycles (greater than 10^6) is attained when compressive residual stresses of 400 MPa are present in the mechanical part (see Figure 6.14).

7.2 Future work

Although the methodology outlined in the present work highlights multiple possibilities for optimising the metallurgical process of additive manufacturing, this is only the first step in a broader process of integration between the design phase and the component manufacturing phase. Indeed, it is desirable to increasingly integrate the product design phase and the production phase, the so-called *digital twin* methodology, so that there is a mutual exchange of ideas and knowledge between the two worlds. In this way, mathematical models will be informed and guided by metallurgical practice which, in turn, will exploit the predictive capabilities of the models. Below are some of the possible improvements: these should also be read partly as a possible constructive self-criticism of the work done.

1. **Experimental programmes: residual stresses and martensite**

   Accurate residual stresses measurements can be conducted through neutron diffraction using the same numerical parameters presented in this study to build samples, in order to complete the validation of the predictions reported in this study. Furthermore, metal powder could not be used in this

study and only the effect of the laser source on a plate could be studied. Therefore, a natural extension of the analyses presented here would require the deposition of layers of material, in order to extend the study of martensite morphology. Furthermore, a comprehensive approach should also take laser speed into account, so the work presented could be expanded in this direction. The term $k_c(p, s)$ introduced in this study within the Equation (5.5), used for calculating the initial dislocation density, can be evaluated for different values of laser power p and laser speed s, completing the mathematical description of the initial dislocation density as a function of the cooling rate.

2. **Gaussian heat source model extension**

   The preliminary numerical analyses confirmed that the Gaussian heat source model defined as in the Equation (3.48) is able to capture the shape of the melt pool created by the Trumpf® machine, as observed in Figure 5.2, with sufficient accuracy. Therefore, this numerical model can be used as a good approximation. However, the Gaussian heat source needs to be accurately described taking into account different parameters, such as power and laser speed. It is therefore desirable to find a single mathematical expression that reflects these parameters.

3. **Constitutive model**

   The Galindo-Fernández *et al.* (2018) [88] constitutive model adopted in this study can be refined and extended in different ways, and this has been partially completed in more recent times [274]. However, a constitutive model able to capture the micro-stresses can be based on crystal plasticity theory, whose capabilities have been investigated only on a preliminary basis during the preliminary stages of the present work. This will also permit to calculate the type II residual stresses, which are on the grain boundaries.

Any extension in this direction should find a balance between accurate description and computational time, because crystal plasticity for studying additive manufacturing for polycrystalline alloys is computationally expensive [275].

4. **Model refinement and further extensions**

   One of the limitations of the thermal parameters used here in finite element models is that they do not consider the difference between the physical parameters of the bulk and the packed spherical powder during simulations of the deposition process. In fact, some of these parameters are significantly different, such as the density of the powder, which is less than half, and its thermal conductivity, which is not only lower than that of the bulk material, but does not even increase excessively with increasing temperature. Therefore, a suggested approach for future works will take into account this variability, as some scholars recently did, in 2021 [232].

   Another extension could take into account direct laser deposition processes, starting from an implementation of wire and arc additive manufacturing, which can be modelled thanks to the 'element activation' functionality in SIMULIA/Abaqus and using the double ellipsoid heat source model proposed by Goldak *et al.* (1984) [137], as suggested recently [17].

5. **Determination of porosity and powder agglomeration and aggregation**

   Porosity was introduced to determine the powder agglomeration and aggregation and, in particular, to model the thermal response of the powder deposition layer. However, an extension would take into account more realistic models for determination of powder agglomeration and aggregation. On the other hand, one of the primary objectives to achieve a better mechanical response in additive manufacturing is the control of *porosity* [276] and study

of porosity is also relevant for the fatigue analysis. More specifically, it has been shown that all the tensile properties (ultimate tensile stress, yield stress, elongation and ductility) are greater in the location where porosity is lower [276, 277]. Therefore, since porosity is commonly present in additively manufactured parts, it can be viewed as a process-induced defect [277]. The internal porosity $p \in (0, 1)$ can be at first instance quantified with the following formula:

$$p = \left(1 - \frac{m}{\rho_t V}\right), \tag{7.1}$$

where m is the weight of the specimen, ρ_t is the theoretical mass density of the alloy and V is the volume of the specimen. The density of the specimen can be evaluated by referring to the Archimedes' principle, according to ASTM B311–13 [106]. However, since this method can be quite inaccurate and not satisfactory [276, p. 56], especially for materials containing more than two percent porosity, some more advanced experimental techniques, mainly based on X-rays, have been developed to overcome this limitation and to obtain more precise information also regarding their spatial distribution [278, 277]. Finally, in terms of mechanical behaviour it has primarily been reported that the mechanical properties (Young's modulus, yield strength and ultimate tensile strength) show a linear dependency on porosity [279] (the values of the constants for such relationships, relative to the SLM processing of Ti-6Al-4V, are given in [279, p. 375]).

6. **Uncertainty analysis**

The results obtained in the present study are derived from several assumptions on the material behaviour and thus quantifying the variability of the 'output', which is the residual stresses magnitude in this case, due to the variability of the 'input', which are the model parameters, could be beneficial to assess the error in the model calculations.

Bibliography

[1] Witzel J., Schrage J., Gasser A., Kelbassa I. 'Additive manufacturing of a blade-integrated disk by laser metal deposition'. *ICALEO* 208, 2011, 250–256.

[2] McAndrew A. R., Colegrove P. A., Bühr C., Flipo B. C. D., Vairis A. 'A literature review of Ti-6Al-4V linear friction welding'. *Progress in Materials Science* 92, 2018, 225–257.

[3] Yuan J., Scarpa F., Allegri G., Titurus B., Patsias S., Rajasekaran R. 'Efficient computational techniques for mistuning analysis of bladed discs: A review'. *Mechanical Systems and Signal Processing* 87, 2017, 71–90.

[4] Williams J. C., Rodney R. B. 'Opportunities and Issues in the Application of Titanium Alloys for Aerospace Components'. *Metals* 10 (6), 2020, 1–22.

[5] Inagaki I., Takechi T., Ariyasu Y. S. N. 'Application and Features of Titanium for the Aerospace Industry'. In: 2014.

[6] Kanishka K., Acherjee B. 'A systematic review of additive manufacturing-based remanufacturing techniques for component repair and restoration'. *Journal of Manufacturing Processes* 89, 2023, 220–283.

[7] Berbente S., Andrei I., Stroe G., Mihaela C. 'Topical Issues in Aircraft Health Management with Applications to Jet Engines'. *INCAS BULLETIN* 12, Mar. 2020, 13–26.

[8] Grilli M. L., Valerini D., Slobozeanu A. E., Postolnyi B. O., Baloš S., Rizzo A., Piticescu R. R. 'Critical Raw Materials Saving by Protective

Coatings under Extreme Conditions: A Review of Last Trends in Alloys and Coatings for Aerospace Engine Applications'. *Materials* 14, 2021.

[9] Liu S., Shin Y. C. 'Additive manufacturing of Ti6Al4V alloy: A review'. *Materials & Design* 164, 2019, 107552.

[10] Nagalingam A. P., Gopasetty S. K., Wang J., Yuvaraj H. K., Gopinath A., Yeo S. H. 'Comparative fatigue analysis of wrought and laser powder bed fused Ti-6Al-4V for aerospace repairs: Academic and industrial insights'. *International Journal of Fatigue* 176, 2023, 107879–1–16.

[11] Chen C., Wang X., Wang Y., Yang D., Yao F., Zhang W., Wang B., Sewvandi G. A., Yang D., Hu D. 'Additive Manufacturing of Piezoelectric Materials'. *Advanced Functional Materials* 30 (52), 2020, 1–29.

[12] Wong K. V., Hernandez A. 'A Review of Additive Manufacturing'. *International Scholarly Research Network Mechanical Engineering*, 2012, 1–10.

[13] Campbell T., Williams C., Ivanova O., Garrett B. *Could 3D Printing Change the World?: Technologies, Potential, and Implications of Additive Manufacturing*. Tech. rep. Atlantic Council, 2011.

[14] Béchet E., Cuilliere J.-C., Trochua F. 'Generation of a finite element MESH from stereolithography (STL) files'. *Computer-Aided Design* 34 (1), 2002, 1–17.

[15] Satish Prakash K., Nancharaih T., Subba Rao V. V. 'Additive Manufacturing Techniques in Manufacturing - An Overview'. *Materials Today: Proceedings* 5 (2, Part 1), 2018, 3873–3882.

[16] Herzog D., Seyda V., Wycisk E., Emmelmann C. 'Additive manufacturing of metals'. *Acta Materialia* 117, 2016, 371–392.

[17] Sampaio R. F. V., Pragana J. P. M., Bragança I. M. F., Silva C. M. A., Nielsen C. V., Martins P. A. F. 'Modelling of wire-arc additive manufacturing – A review'. *Advances in Industrial and Manufacturing Engineering* 6, 2023, 100121.

[18] Trevisan F., Calignano F., Lorusso M., Pakkanen J., Aversa A., Ambrosio E. P., Lombardi M., Fino P., Manfredi D. 'On the Selective Laser Melting (SLM) of the AlSi10Mg Alloy: Process, Microstructure, and Mechanical Properties'. *Materials* 10, 2017, 1–23.

[19] Chen S.-g., Gao H.-j., Zhang Y.-d., Wu Q., Gao Z.-h., Zhou X. 'Review on residual stresses in metal additive manufacturing: formation mechanisms, parameter dependencies, prediction and control approaches'. *Journal of Materials Research and Technology* 17, 2022, 2950–2974.

[20] Wysocki B., Maj P., Sitek R., Buhagiar J., Kurzydłowski K. J., Święszkowski W. 'Laser and Electron Beam Additive Manufacturing Methods of Fabricating Titanium Bone Implants'. *Applied Sciences* 7 (7), 2017.

[21] Cao S., Zou Y., Lim C. V. S., Wu X. 'Review of laser powder bed fusion (LPBF) fabricated Ti-6Al-4V: process, post-process treatment, microstructure, and property'. *Light: Advanced Manufacturing* 2 (20), 2021, 1–20.

[22] Azarmi F., Sevostianov I. 'Evaluation of the residual stresses in metallic materials produced by additive manufacturing technology: effect of microstructure'. *Current Opinion in Chemical Engineering* 28, 2020. Materials Engineering - Separations Engineering, 21–27.

[23] Mosallanejad M. H., Niroumand B., Aversa A., Saboori A. 'In-situ alloying in laser-based additive manufacturing processes: A critical review'. *Journal of Alloys and Compounds* 872, 2021, 159567.

[24] Obilanade D., Dordlofva C., Törlind P. 'Surface Roughness Considerations in Design for Additive Manufacturing - A Literature Review'. *Proceedings of the Design Society* 1, 2021, 2841–2850.

[25] Boyer R., Welsch G., Collings E. W. *Materials Properties Handbook: Titanium Alloys*. ASM International, 1994.

[26] Cotton F. A., Wilkinson G., Murillo C. A., Bochmann M. *Advanced Inorganic Chemistry*. John Wiley & Sons, 1999.

[27] Froes F. H. *Titanium - Physical Metallurgy, Processing, and Applications*. ASM International, 2015.

[28] Russell A. 'The Rev. William Gregor (1761-1817), discoverer of titanium'. *Mineralogical Magazine and Journal of the Mineralogical Society* 30 (229), 1955, 617–624.

[29] Kroll W. 'The Production of Ductile Titanium'. *Journal of the Electrochemical Society* 78 (1), 1940, 35–47.

[30] Voort G. V. 'Metallographic Preparation of Titanium and its Alloys'. *Buehler* 3 (3), 2015, 1–5.

[31] Chang R., Overby J. *Chemistry*. 13th ed. New York: McGraw-Hill, 2019.

[32] Mouritz A. P. *Introduction to aerospace materials*. Woodhead Publishing Limited, 2012.

[33] Schwab H., Bönisch M., Giebeler L., Gustmann T., Eckert J., Kühn U. 'Processing of Ti-5553 with improved mechanical properties via an in-situ heat treatment combining selective laser melting and substrate plate heating'. *Materials and Design* 130, 2017, 83–89.

[34] Moiseyev V. N. *Titanium Alloys: Russian Aircraft and Aerospace Applications*. CRC Press, 2005.

[35] Shreir L. L., Jarman R. A., Burstein G. T., eds. *Corrosion*. 3rd ed. Oxford: Butterworth-Heinemann, 1994.

[36] Donachie M. J. *Titanium: A Technical Guide*. Second edition. ASM International: The materials Information Society, 2000.

[37] Polmear I. J. *Light Alloys: Metallurgy of the Light Metals*. Metallurgy and Materials Science Series. Edward Arnold, 2000.

[38] Boyer R. R., Williams J. C. 'Developments in Research and Applications in the Titanium Industry in the USA'. *Proceedings of the 12th World Conference on Titanium* 1, 2012, 10–19.

[39] Semlitsch M. 'Titanium alloys for hip joint replacements'. *Clinical Materials* 2 (1), 1987, 1–13.

[40] Nicholson J. V. 'Titanium Alloys for Dental Implants: A Review'. *Prosthesis* 2 (2), 2020, 100–116.

[41] Long M., Rack H. J. 'Titanium alloys in total joint replacement—a materials science perspective'. *Biomaterials* 19 (18), 1998, 1621—1639.

[42] Junkar I., Kulkarni M., Benčina M., Kovač J., Mrak-Poljšak K., Lakota K., Sodin-Šemrl S., Mozetič M., Iglič A. 'Titanium Dioxide Nanotube Arrays for Cardiovascular Stent Applications'. *ACM Omega* 5 (13), 2020, 7280–7289.

[43] Zhong C., Liu J., Zhao T., Schopphoven T., Fu J., Gasser A., Schleifenbaum J. H. 'Laser Metal Deposition of Ti6Al4V—A Brief Review'. *Applied Sciences* 10 (3), 2020, 1–12.

[44] Emminghaus N., Bernhard R., Kaierle J. H. S. 'Laser-based powder bed fusion of Ti-6Al-4V powder modified with SiO_2 nanoparticles'. *The International Journal of Advanced Manufacturing Technology* 122, 2022, 1679–1694.

[45] Wei H. L., Mukherjee T., Zhang W., Zuback J. S., Knapp G. L., De A., DebRoy T. 'Mechanistic models for additive manufacturing of metallic components'. *Progress in Materials Science* 116, 2021, 100703.

[46] Neikov O. D. 'Chapter 13 - Powders for Additive Manufacturing Processing'. In: *Handbook of Non-Ferrous Metal Powders (Second Edition)*. Ed. by Neikov O. D., Naboychenko S. S., Yefimov N. A. Second Edition. Oxford: Elsevier, 2019, 373–399.

[47] Lui E. W., Medvedev A. E., Edwards D., Qian M., Leary M., Brandt M. 'Microstructure modification of additive manufactured Ti-6Al-4V plates for improved ballistic performance properties'. *Journal of Materials Processing Technology* 301, 2022, 117436.

[48] Bartolomeu F., Gasik M., Silva F. S., Miranda G. 'Mechanical Properties of Ti6Al4V Fabricated by Laser Powder Bed Fusion: A Review Focused on the Processing and Microstructural Parameters Influence on the Final Properties'. *Metals* 12 (6), 2022.

[49] Yang F., Chen C., Zhou Q., Gong Y., Li R., Li C., Klämpfl F., Freund S., Wu X., Sun Y., Li X., Schmidt M., Yu D. M. Y. 'Laser beam melting 3D printing of Ti6Al4V based porous structured dental implants: fabrication, biocompatibility analysis and photoelastic study'. *Scientific Reports* 7, 2017, 1–12.

[50] Nahr F., Rasch M., Burkhardt C., Renner J., Baumgärtner B., Hausotte T., Körner C., Steinmann P., Mergheim J., Schmidt M., Markl M. 'Geometrical Influence on Material Properties for Ti6Al4V Parts in Powder Bed Fusion'. *Journal of Manufacturing and Materials Processing* 7 (3), 2023.

[51] Ahuja B., Schaub A., Karg M., Lechner M., Merklein M., Schmidt M. 'Developing LBM Process Parameters for Ti-6Al-4V Thin Wall Structures and Determining the Corresponding Mechanical Characteristics'. *Physics Procedia* 56, 2014. 8th International Conference on Laser Assisted Net Shape Engineering LANE 2014, 90–98.

[52] Segurajauregi U., Vázquez A. Álvarez, Muñiz-Calvente M., Urresti k., Naveiras H. 'Fatigue Assessment of Selective Laser Melted Ti-6Al-4V: Influence of Speed Manufacturing and Porosity'. *Metals* 11 (7), 2021.

[53] Zhao X., Li S., Zhang M., Liu Y., Sercombe T. B., Wang S., Hao Y., Yang R., Murr L. E. 'Comparison of the microstructures and mechanical properties of Ti–6Al–4V fabricated by selective laser melting and electron beam melting'. *Materials & Design* 95, 2016, 21–31.

[54] Chen Z., Wu X., Tomus D., Davies C. H. J. 'Surface roughness of Selective Laser Melted Ti-6Al-4V alloy components'. *Additive Manufacturing* 21, 2018, 91–103.

[55] Soylemez E. 'High deposition rate approach of selective laser melting through defocused single bead experiments and thermal finite element analysis for Ti-6Al-4V'. *Additive Manufacturing* 31, 2020, 100984.

[56] Zhechao F., Hongwei F. 'Study on selective laser melting and heat treatment of Ti-6Al-4V alloy'. *Results in Physics* 10, 2018, 660–664.

[57] Nandhakumar R., Venkatesan K. 'A process parameters review on selective laser melting-based additive manufacturing of single and multi-material: Microstructure, physical properties, tribological, and surface roughness'. *Materials Today Communications* 35, 2023, 105538.

[58] Wang J., Lin X., Wang J., Yang H., Zhou Y., Wang C., Li Q., Huang W. 'Grain morphology evolution and texture characterization of wire and arc additive manufactured Ti-6Al-4V'. *Journal of Alloys and Compounds* 768, 2018, 97–113.

[59] Ramosena L. A., Dzogbewu T. C., Preez W. du. 'Direct Metal Laser Sintering of the Ti6Al4V Alloy from a Powder Blend'. *Materials* 15 (22), 2022, 1–21.

[60] Zenani A., Dzogbewu T., Preez W. du, Yadroitsev I. 'Optimum Process Parameters for Direct Metal Laser Sintering of Ti6Al Powder Blend'. *Universal Journal of Mechanical Engineering* 8, June 2020, 170–182.

[61] Bertol L., Silva F., Junior W. 'Design and health care: A study of virtual design and direct metal laser sintering of titanium alloy for the production of customized facial implants'. *Australasian Medical Journal* 2, Nov. 2009.

[62] Miura H. 'Direct Laser Forming of Titanium Alloy Powders for Medical and Aerospace Applications'. *KONA Powder and Particle Journal* 32, 2015, 253–263.

[63] Calderón L. A. Ávila, Graf B., Rehmer B., Petrat T., Skrotzki B., Rethmeier M. 'Characterization of Ti–6Al–4V Fabricated by Multilayer Laser Powder-Based Directed Energy Deposition'. *Advanced Engineering Materials* 24 (6), 2022, 2101333.

[64] Schneider-Maunoury C., Weiss L., Acquier P., Boisselier D., Laheurte P. 'Functionally graded Ti6Al4V-Mo alloy manufactured with DED-CLAD® process'. *Additive Manufacturing* 17, 2017, 55–66.

[65] Cheng D., Zhang J., Shi T., Li G., Shi J., Lu L., Fu G. 'Microstructure and mechanical properties of additive manufactured Ti-6Al-4V components by annular laser metal deposition in a semi-open environment'. *Optics & Laser Technology* 135, 2021, 106640.

[66] Zhai Y., Lados D. A., Brown E. J., Vigilante G. N. 'Fatigue crack growth behavior and microstructural mechanisms in Ti-6Al-4V manufactured by laser engineered net shaping'. *International Journal of Fatigue* 93, 2016, 51–63.

[67] Zhai Y., Lados D. A., Brown E. J., Vigilante G. N. 'Understanding the microstructure and mechanical properties of Ti-6Al-4V and Inconel 718 alloys manufactured by Laser Engineered Net Shaping'. *Additive Manufacturing* 27, 2019, 334–344.

[68] Buciumeanu M., Bagheri A., Shamsaei N., Thompson S. M., Silva F. S., Henriques B. 'Tribocorrosion behavior of additive manufactured Ti-6Al-4V biomedical alloy'. *Tribology International* 119, 2018, 381–388.

[69] Sahoo S., Joshi A., Balla V. K., Das M., Roy S. 'Site-specific microstructure, porosity and mechanical properties of LENS™ processed Ti–6Al–4V alloy'. *Materials Science and Engineering: A* 820, 2021, 141494.

[70] Wolff S., Lee T., Faierson E., Ehmann K., Cao J. 'Anisotropic properties of directed energy deposition (DED)-processed Ti–6Al–4V'. *Journal of Manufacturing Processes* 24, 2016. SI: NAMRC, 397–405.

[71] Park C. W., Adomako N. K., Lee M. G., Kim J. H., Kim J. H. 'Interfacial structure and pore formation mechanism during laser cladding of pure vanadium on Ti-6Al-4V alloy'. *International Journal of Refractory Metals and Hard Materials* 101, 2021, 105671.

[72] Xu J., Zhu J., Fan J., Zhou Q., Peng Y., Guo S. 'Microstructure and mechanical properties of Ti–6Al–4V alloy fabricated using electron beam freeform fabrication'. *Vacuum* 167, 2019, 364–373.

[73] Yan W., Yue Z., Zhang J. 'Study on the residual stress and warping of stiffened panel produced by electron beam freeform fabrication'. *Materials & Design* 89, 2016, 1205–1212.

[74] Li X., Yao Z., Tao X., Yao M., Zhang S. 'Developing Cu modified Ti6Al4V alloys with a combination of high strength and ductility by electron beam freeform fabrication'. *Vacuum* 194, 2021, 110638.

[75] Zhou Y., Qin G., Li L., Lu X., Jing R., Xing X., Yang Q. 'Formability, microstructure and mechanical properties of Ti-6Al-4V deposited by wire and arc additive manufacturing with different deposition paths'. *Materials Science and Engineering: A* 772, 2020, 138654.

[76] Gou J., Wang Z., Hu S., Shen J., Liu Z., Yang C., Bai Y., Lu W. F. 'Effect of cold metal transfer mode on the microstructure and machinability of Ti–6Al–4V alloy fabricated by wire and arc additive manufacturing in ultra-precision machining'. *Journal of Materials Research and Technology* 21, 2022, 1581–1594.

[77] Wang J., Lin X., Li J., Xue A., Liu F., Huang W., Liang E. 'A study on obtaining equiaxed prior-β grains of wire and arc additive manufactured Ti–6Al–4V'. *Materials Science and Engineering: A* 772, 2020, 138703.

[78] Wang J., Lin X., Wang M., Li J., Wang C., Huang W. 'Effects of subtransus heat treatments on microstructure features and mechanical properties of wire and arc additive manufactured Ti–6Al–4V alloy'. *Materials Science and Engineering: A* 776, 2020, 139020.

[79] Tian Y., Shen J., Hu S., Wang Z., Gou J. 'Microstructure and mechanical properties of wire and arc additive manufactured Ti-6Al-4V and AlSi5 dissimilar alloys using cold metal transfer welding'. *Journal of Manufacturing Processes* 46, 2019, 337–344.

[80] Ward A. A., Zhang Y., Cordero Z. C. 'Junction growth in ultrasonic spot welding and ultrasonic additive manufacturing'. *Acta Materialia* 158, 2018, 393–406.

[81] Gujba A. K., Medraj M. 'Power Ultrasonic Additive Manufacturing: Process Parameters, Microstructure, and Mechanical Properties'. *Advances in Materials Science and Engineering* 2020, 2020, 1–17.

[82] Portella P. D., Helmerich R. 'Adolf Martens and his contribution to materials engineering'. *Engineering Failure Analysis* 43, 2014, 2—10.

[83] Fan Y., Tian W., Guo Y., Sun Z., Xu J. 'Relationships among the Microstructure, Mechanical Properties, and Fatigue Behavior in Thin Ti6Al4V'. *Advances in Materials Science and Engineering* 1, 2016, 1–9.

[84] Motyka M. 'Martensite Formation and Decomposition during Traditional and AM Processing of Two-Phase Titanium Alloys—An Overview'. *Metals* 11, 3 2021, 1–17.

[85] Zafari A., Xia K. 'High Ductility in a fully martensitic microstructure: a paradox in a Ti alloy produced by selective laser melting'. *Materials Research Letters* 6 (11), 2018, 627–633.

[86] Zafari A., Barati M. R., Xia K. 'Controlling martensitic decomposition during selective laser melting to achieve best ductility in high strength Ti-6Al-4V'. *Materials Science and Engineering: A* 744, 2019, 445–455.

[87] Yang J., Yu H., Yin J., Gao M., Wang Z., Zeng X. 'Formation and control of martensite in Ti-6Al-4V alloy produced by selective laser melting'. *Materials & Design* 108, 2016, 308—318.

[88] Galindo-Fernández M. A., Mumtaz K., Castillo P. E. J. R.-D. del, Galindo-Nava E. I., Ghadbeigi H. 'A microstructure sensitive model for deformation of Ti-6Al-4V describing Cast-and-Wrought and Additive Manufacturing morphologies'. *Materials & Design* 160, 2018, 350–362.

[89] Rogoff E., Antony M., Markle P. 'Calculating Ti-6Al-4V β Transus Through a Chemistry-Based Equation Derived from Combined Element Binary Phase Diagrams'. *Journal of Materials Engineering and Performance* 27 (10), 2018, 5227–5235.

[90] Boivineau M., Cagran C., Doytier D., Eyraud V., Nadal M.-H., Wilthan B., Pottlacher G. 'Thermophysical Properties of Solid and Liquid Ti-6Al-4V (TA6V) Alloy'. *International Journal of Thermophysics* 27, 2 2006, 507—529.

[91] Zhang G., Chen J., Zheng M., Yan Z., Lu X., Lin X., Huang W. 'Element Vaporization of Ti-6Al-4V Alloy during Selective Laser Melting'. *Metals* 10 (4), 2020, 1—14.

[92] Bignon M., Bertrand E., Castillo P. E. J. Rivera-Díaz-del, Tancret F. 'Martensite formation in titanium alloys: Crystallographic and compositional effects'. *Journal of Alloys and Compounds* 872, 2021, 1—16.

[93] Villa M., Brooks J. W., Turner R., Ward R. M. 'Microstructural Modeling of Thermally-Driven β Grain Growth, Lamellae & Martensite in Ti-6Al-4V'. *Modeling and Numerical Simulation of Material Science* 10, 2020, 55–73.

[94] Villa M., Brooks J. W., Turner R., Boitout F., Ward R. M. 'Metallurgical modelling of Ti-6Al-4V for welding applications'. *Metals* 11 (6), 2021, 1–20.

[95] Lu Y., Turner R., Brooks J., Basoalto H. 'Microstructural characteristics and computational investigation on electron beam welded Ti-6Al-4V alloy'. *Journal of Materials Processing Technology* 288, 2021, 1–10.

[96] Ahmed T., Rack H. J. 'Phase transformations during cooling in $\alpha+\beta$ titanium alloys'. *Materials Science and Engineering: A* 243 (1), 1998, 206–211.

[97] Neelakantana S., Castillo P. E. J. Rivera-Díaz-del, Zwaag S. van der. 'Prediction of the martensite start temperature for β titanium alloys as a function of composition'. *Scripta Materialia* 60 (8), 2009, 611–614.

[98] Dharmendra C., Hadadzadeh A., Amirkhiz B. S., Lloyd A., Mohammadi M. 'Deformation mechanisms and fracture of electron beam melted Ti–6Al–4V'. *Materials Science and Engineering: A* 771, 2020, 138652.

[99] Koistinen D., Marburger R. 'A General Equation Prescribing the Extent of the Austenite-Martensite Transformation in Pure Iron-Carbon Alloys and Plain Carbon Steels'. *Acta Metallurgica* 7, 1959, 59—60.

[100] Fan Y., Cheng P., Yao Y. L., Yang Z., Egland K. 'Effect of phase transformations on laser forming of Ti–6Al–4V alloy'. *Journal of Applied Physics* 98 (1), 2005, 013518–1–013518–10.

[101] Suárez A., Tobar M. J., Yáñez A., Pérez I., Sampedro J., Amigó V., Candel J. J. 'Modeling of phase transformations of Ti6Al4V during laser metal deposition'. *Physics Procedia* 12, 2011. Lasers in Manufacturing 2011 - Proceedings of the Sixth International WLT Conference on Lasers in Manufacturing, 666–673.

[102] Salsi E., Chiumenti M., Cervera M. 'Modeling of Microstructure Evolution of Ti6Al4V for Additive Manufacturing'. *Metals* 8 (8), 2018.

[103] Picu R. C., Majorell A. 'Mechanical behavior of Ti–6Al–4V at high and moderate temperatures—Part II: constitutive modeling'. *Materials Science and Engineering: A* 326 (2), 2002, 306–316.

[104] Semiatin S. L., Knisley S. L., Fagin P. N., Zhang D. R., Barker F. 'Microstructure evolution during alpha-beta heat treatment of Ti-6Al-4V'. *Metallurgical and Materials Transactions A* 34, 2003, 2377–2386.

[105] Moridi A., Demir A. G., Caprio L., Hart A. J., Previtali B., Colosimo B. M. 'Deformation and failure mechanisms of Ti–6Al–4V as built by selective laser melting'. *Materials Science and Engineering: A* 768, 2019, 138456.

[106] Ter Haar G. M., Becker T. H. 'Selective Laser Melting Produced Ti-6Al-4V: Post-Process Heat Treatments to Achieve Superior Tensile Properties'. *Materials* 11 (1), 2018, 1–15.

[107] Johnsen A. R., Petersen J. E., Pedersen M. M., Yildirim H. C. 'Factors affecting the fatigue strength of additively manufactured Ti-6Al-4V parts'. *Welding in the World* 68, 2024, 361–409.

[108] Muiruri A., Maringa M., du Preez W. 'Evaluation of Dislocation Densities in Various Microstructures of Additively Manufactured Ti6Al4V (Eli) by the Method of X-ray Diffraction'. *Materials* 13 (23), 2020, 1–23.

[109] Roters F., Eisenlohr P., Hantcherli L., Tjahjanto D. D., Bieler T. R., Raabe D. 'Overview of constitutive laws, kinematics, homogenization and multiscale methods in crystal plasticity finite-element modeling: Theory, experiments, applications'. *Acta Materialia* 58 (4), 2010, 1152–1211.

[110] Johnson G. R., Cook W. H. 'A Constitutive Model and Data for Metals Subjected to Large Strains, High Strain Rates, and High Temperatures'. *Proceedings 7th International Symposium on Ballistics, The Hague*, 1983, 541–547.

[111] Promoppatum P., Rollett A. D. 'Physics-based and phenomenological plasticity models for thermomechanical simulation in laser powder bed fusion additive manufacturing: A comprehensive numerical comparison'. *Materials & Design* 204, 2021, 109658.

[112] Chen Z., Jiang Y., Shao Y.-T., Holtz M. E., Odstrčil M., Guizar-Sicairos M., Hanke I., Ganschow S., Schlom D. G., Muller D. A. 'Electron ptychography achieves atomic-resolution limits set by lattice vibrations'. *Science* 372 (6544), 2021, 826–831.

[113] Castany P., Pettinari-Sturmel F., Crestou J., Douin J., Coujou A. 'Experimental study of dislocation mobility in a Ti–6Al–4V alloy'. *Acta Materialia* 55 (18), 2007, 6284–6291.

[114] Hirth J. P. 'A Brief History of Dislocation Theory'. *Metallurgical Transactions A* 16 (12), 1985, 2085–2090.

[115] Hirth J. P., Lothe J. *Theory of dislocations*. Second edition. New York: John Wiley & Sons, 1982.

[116] Han W., Reddy B. D. *Plasticity : Mathematical Theory and Numerical Analysis*. 2nd ed. New York: Springer, 2012.

[117] Lubliner J. *Plasticity Theory*. Mineola: Dover Publications, 2008.

[118] Frost H. J., Ashby M. F. *Deformation-mechanism maps: The Plasticity and Creeps of Metals and Ceramics*. 1st ed. Oxford: Pergamon Press, 1982.

[119] Honeycombe R. W. K. *The Plastic Deformation of Metals*. Maidenhead: Edward Arnold, 1968.

[120] Lainé S. J., Knowles K. M., Rugg D. 'Very high strain rate deformation twinning behaviour of Ti–6Al–4V'. *Materialia* 12, 2020, 100762.

[121] Zheng Z., Balint D. S., Dunne F. P. E. 'Rate sensitivity in discrete dislocation plasticity in hexagonal close-packed crystals'. *Acta Materialia* 107, 2016, 17–26.

[122] Umezawa O., Morita M., Yuasa T., Morooka S., Ono Y., Yuri T., Ogata T. 'Analyses of heterogeneous deformation and subsurface fatigue crack generation in alpha titanium alloy at low temperature'. In: *Advances in Cryogenic Engineering: Transactions of the International Cryogenic Materials Conference ICMC Volume 60*. Vol. 1574. American Institute of Physics Conference Series. Jan. 2014, 34–41.

[123] Chen G., Ren C., Qin X., Lia J. 'Temperature dependent work hardening in Ti–6Al–4V alloy over large temperature and strain rate ranges: Experiments and constitutive modeling'. *Materials & Design* 83, 2015, 598–610.

[124] Khan A. S., Liang R. 'Behaviors of three BCC metal over a wide range of strain rates and temperatures: experiments and modeling'. *International Journal of Plasticity* 15, 1999, 1089–1109.

[125] Nemat-Nasser S., Guo W.-G., Nesterenko V. F., Indrakanti S. S., Gu Y.-B. 'Dynamic response of conventional and hot isostatically pressed Ti–6Al–4V alloys: experiments and modeling'. *Mechanics of Materials* 33 (8), 2001, 425–439.

[126] Majorell A., Srivatsa S., Picu R. C. 'Mechanical behavior of Ti–6Al–4V at high and moderate temperatures—Part I: Experimental results'. *Materials Science and Engineering: A* 326 (2), 2002, 297–305.

[127] Mecking H., Kocks U. F. 'Kinetics of flow and strain-hardening'. *Acta Metallurgica* 29 (11), 1981, 1865–1875.

[128] Mulyadi M., Rist M., Edwards L., Brooks J. W., Wilson A. F. 'A hot deformation model for two-phase titanium alloys based on an internal state-variable approach'. *Ti-2007 Science and Technology* 1, 2007, 315–318.

[129] Mulyadi M. 'Hot Compression Behaviour of Two-Phase Ti-6Al-4V: Experiments and State-Variable Modelling'. PhD thesis. The Open University, 2007.

[130] Blackwell P. L., Brooks J. W., Bate P. S. 'Development of microstructure in isothermally forged Nimonic alloy AP1'. *Materials Science and Technology* 14 (11), 1998, 1181–1188.

[131] Wang Z., Li P. 'Characterisation and constitutive model of tensile properties of selective laser melted Ti-6Al-4V struts for microlattice structures'. *Materials Science and Engineering: A* 725, 2018, 350–358.

[132] Liović D., Franulović M., Kozak D. 'Material models and mechanical properties of titanium alloys produced by selective laser melting'. *Procedia Structural Integrity* 31, 2021. 4th International Conference on Structural Integrity and Durability, ICSID 2020, 86–91.

[133] Ramberg W., Osgood W. R. *Description of stress–strain curves by three parameters*. Tech. rep. Technical Note No. 902, National Advisory Committee For Aeronautics, 1943.

[134] Galindo-Nava E. I., Castillo P. E. J. R.-D. del. 'A model for the microstructure behaviour and strength evolution in lath martensite'. *Acta Materialia* 98, 2015, 81–93.

[135] Cottrell A. H., Bilby B. A. 'Dislocation Theory of Yielding and Strain Ageing of Iron'. *Proceedings of the Physical Society A* 62 (1), Jan. 1949, 49–62.

[136] Smallman R. E., Bishop R. J. *Modern Physical Metallurgy and Materials Engineering: Science, process, applications*. VI. Butterworth-Heinemann, 1999.

[137] Goldak J., Chakravarti A., Bibby M. 'A new finite element model for welding heat sources'. *Metallurgical Transactions B* 15, 1984, 299–305.

[138] Rosenthal D. 'The Theory of Moving Sources of Heat and Its Application to Metal Treatments'. *Transactions ASME* 46, 1946, 849–866.

[139] Milberg J., Sigl M. 'Electron beam sintering of metal powder'. *Production Engineering - Research and Development* 2, 2008, 117–122.

[140] Schillinger D. E., Betz I. G., Markus H. 'Simplified Determination of Thermal Experience in Fusion Welding'. *Welding Research Supplement*, 1970, 410s–418s.

[141] Eagar T., Tsai N. 'Temperature Fields Produced by Traveling Distributed Heat Sources'. *Welding Journal* 62, 1983, 346–355.

[142] Kiran A., Li Y., Hodek J., Brázda M., Urbánek M., Džugan J. 'Heat Source Modeling and Residual Stress Analysis for Metal Directed Energy Deposition Additive Manufacturing'. *Materials* 15 (7), 2022.

[143] Li T., Zhang L., Chang C., Wei L. 'A Uniform-Gaussian distributed heat source model for analysis of residual stress field of S355 steel T welding'. *Advances in Engineering Software* 126, 2018, 1–8.

[144] Rossini N. S., Dassisti M., Benyounis K. Y., Olabi A. G. 'Methods of measuring residual stresses in components'. *Materials and Design* 35, 2012, 572–588.

[145] Nasir N. S. M., Razab M. K. A. A., Mamat S., Ahmad M. I. 'Review on welding residual stress'. *ARPN Journal of Engineering and Applied Sciences* 11 (9), 2016, 6166–6175.

[146] Hosford W. F. *Mechanical Behavior of Materials*. Cambridge: Cambridge University Press, 2005.

[147] Li C., Liu Z. Y., Fang X. Y., Guo Y. B. 'Residual Stress in Metal Additive Manufacturing'. *Procedia CIRP* 71, 2018, 348–353.

[148] Azarniya A., Colera X. G., Mirzaali M. J., Sovizi S., Bartolomeu F., Weglowski M. S., Wits W. W., Yap C. Y., Ahn J., Miranda G., Silva F. S., Hosseini H. R. M., Ramakrishna S., Zadpoor A. A. 'Additive manufacturing of Ti-6Al-4V parts through laser metal deposition (LMD): Process, microstructure, and mechanical properties'. *Journal of Alloys and Compounds* 804, 2019, 163–191.

[149] Azizi H., Ghiaasiaan R., Prager R., Ghoncheh M. H., Samk K. A., Lausic A., Byleveld W., Phillion A. B. 'Metallurgical and mechanical assessment of hybrid additively-manufactured maraging tool steels via selective laser melting'. *Additive Manufacturing* 27, 2019, 389–397.

[150] Liu H.-L., Sparks T., Liou F., Dietrich D. M. 'Residual Stress and Deformation Modelling for Metal Additive Manufacturing Processes'. In: *Proceedings of the World Congress on Mechanical, Chemical, and Material Engineering (MCM 2015)*. Barcelona, Spain, 2015, 245–1–245–9.

[151] Guo C., Li G., Li S., Hu X., Lu H., Li X., Xu Z., Chen Y., Li Q., Lu J., Zhu Q. 'Additive manufacturing of Ni-based superalloys: Residual stress, mechanisms of crack formation and strategies for crack inhibition'. *Nano Materials Science* 5 (1), 2023, 53–77.

[152] Xie D., Lv F., Yang Y., Shen L., Tian Z., Shuai C., Chen B., Zhao J. 'A Review on Distortion and Residual Stress in Additive Manufacturing'. *Chinese Journal of Mechanical Engineering: Additive Manufacturing Frontiers* 1 (3), 2022, 1–11.

[153] Acevedo R., Kantarowska K., Santos E., Fredel M. 'Residual stress measurement techniques for Ti6Al4V parts fabricated using selective laser melting: state of the art review'. *Rapid Prototyping Journal* ahead-of-print, July 2020, 1549–1564.

[154] Yakout M., Elbestawi M. A., Veldhuis S. C. 'A study of the relationship between thermal expansion and residual stresses in selective laser melting of Ti-6Al-4V'. *Journal of Manufacturing Processes* 52, 2020, 181–192.

[155] Wan Y., Jiang W., Song M., Huang Y., Li J., Sun G., Shi Y., Zhai X., Zhao X., Ren L. 'Distribution and formation mechanism of residual stress in duplex stainless steel weld joint by neutron diffraction and electron backscatter diffraction'. *Materials & Design* 181, 2019, 108086.

[156] Elmer J. W., Palmer T. A., Babu S. S., Specht E. D. 'In situ observations of lattice expansion and transformation rates of α and β phases in Ti–6Al–4V'. *Materials Science and Engineering: A* 391 (1), 2005, 104–113.

[157] Kruth J. P., Deckers J. H., Yasa E., Wauthlé R. 'Assessing and comparing influencing factors of residual stresses in selective laser melting using a novel analysis method'. *Proceedings of the Institution of Mechanical Engineers, Part B: Journal of Engineering Manufacture* 226, 2012, 980 –991.

[158] Pauzon C., Mishurova T., Evsevleev S., Dubiez-Le Goff S., Murugesan S., Bruno G., Hryha E. 'Residual stresses and porosity in Ti-6Al-4V produced by laser powder bed fusion as a function of process atmosphere and component design'. *Additive Manufacturing* 47, 2021, 102340.

[159] Zhan Y., Liu C., Zhang J., Mo G., Liu C. 'Measurement of residual stress in laser additive manufacturing TC4 titanium alloy with the laser ultrasonic technique'. *Materials Science and Engineering: A* 762, 2019, 138093.

[160] Pant P., Sjöström S., Simonsson K., Moverare J., Proper S., Hosseini S., Luzin V., Peng R. 'A Simplified Layer-by-Layer Model for Prediction of Residual Stress Distribution in Additively Manufactured Parts'. *Metals* 11 (6), 2021.

[161] Cottam R., Palanisamy S., Avdeev M., Jarvis T., Henry C., Cuiuri D., Balogh L., Abdul Rahman Rashid R. 'Diffraction Line Profile Analysis of 3D Wedge Samples of Ti-6Al-4V Fabricated Using Four Different Additive Manufacturing Processes'. *Metals* 9 (1), 2019, 1–13.

[162] Clausen B., D'Elia C. R., Prime M. B., Hill M. R., Bishop J. E., Johnson K. L., Jared B. H., Allen K. M., Balch D. K., Roach R. A., Brown D. W. 'Complementary Measurements of Residual Stresses Before and After Base Plate Removal in an Intricate Additively-Manufactured Stainless-Steel Valve Housing'. *Additive Manufacturing* 36, 2020, 101555.

[163] Kim I., Park S. C., Kim Y. I., Kim D.-K., Lee K.-A., Oh S. J., Lee B. 'Surface residual stress analysis of additive manufactured AlSi10Mg alloys'. *Journal of Alloys and Compounds* 945, 2023, 1–14.

[164] Fang Z.-C., Wu Z.-L., Huang C.-G., Wu C.-W. 'Review on residual stress in selective laser melting additive manufacturing of alloy parts'. *Optics & Laser Technology* 129, 2020, 106283.

[165] Zhou J., Barrett R. A., Leen S. B. 'Three-dimensional finite element modelling for additive manufacturing of Ti-6Al-4V components: Effect of scanning strategies on temperature history and residual stress'. *Journal of Advanced Joining Processes* 5, 2022, 100106.

[166] Jimenez Abarca M., Darabi R., Sa J. C. de, Parente M., Reis A. 'Multi-scale modeling for prediction of residual stress and distortion in Ti–6Al–4V semi-circular thin-walled parts additively manufactured by laser powder bed fusion (LPBF)'. *Thin-Walled Structures* 182, 2023, 1–15.

[167] Hönnige J. R., Colegrove P. A., Ahmad B., Fitzpatrick M. E., Ganguly S., Lee T. L., Williams S. W. 'Residual stress and texture control in Ti-6Al-4V wire + arc additively manufactured intersections by stress relief and rolling'. *Materials & Design* 150, 2018, 193–205.

[168] Sun X., Zhao Y., Yang W., Li W., Liu D. Y. H. 'Novel Strategy for Reducing Residual Stress in Titanium Alloy Parts Obtained via Additive Manufacturing'. *Metals and Materials International* 28, 2022, 3057–3067.

[169] Megahed M., Mindt H.-W., N'Dri N., Duan H., Desmaison O. 'Metal additive-manufacturing process and residual stress modeling'. *Integrating Materials and Manufacturing Innovation* 5, 2016, 61–93.

[170] Mukherjee T., Zhang W., DebRoy T. 'An improved prediction of residual stresses and distortion in additive manufacturing'. *Computational Materials Science* 126, 2017, 360–372.

[171] Lu X., Cervera M., Chiumenti M., Lin X. 'Residual Stresses Control in Additive Manufacturing'. *Journal of Manufacturing and Materials Processing* 5 (4), 2021, 1–12.

[172] Levkulich N. C., Semiatin S. L., Gockel J. E., Middendorf J. R., DeWald A. T., Klingbeil N. W. 'The effect of process parameters on residual stress evolution and distortion in the laser powder bed fusion of Ti-6Al-4V'. *Additive Manufacturing* 28, 2019, 475–484.

[173] Germain A., Thüngen I., Piellard M., Metton C. 'An innovative method to assess and manage residual stresses in additively manufactured titanium'. *MATEC Web of Conferences* 321 (03030), Jan. 2020, 1–7.

[174] Yakout M. E. M. A. V. S. C., Nangle-Smith S. 'Influence of thermal properties on residual stresses in SLM of aerospace alloys'. *Rapid Prototyping Journal* 26 (1), 2020, 213–222.

[175] Murr L. 'Metallurgy of Additive Manufacturing: Examples from Electron Beam Melting'. *Additive Manufacturing* 5, Dec. 2014.

[176] Sneddon S., Xu Y., Dixon M., Rugg D., Li P., Mulvihill D. M. 'Sensitivity of material failure to surface roughness: A study on titanium alloys Ti64 and Ti407'. *Materials & Design* 200 (109438), 2021, 1–14.

[177] Tridello A., Boursier Niutta C., Berto F., Qian G., Paolino D. S. 'Fatigue failures from defects in additive manufactured components: A statistical methodology for the analysis of the experimental results'. *Fatigue & Fracture of Engineering Materials & Structures* 44 (7), 2021, 1944–1960.

[178] Pegues J. W., Shamsaei N., Roach M. D., Williamson R. S. 'Fatigue life estimation of additive manufactured parts in the as-built surface condition'. *Material design & processing communications* 1 (3), 2019.

[179] Arola D., Williams C. L. 'Estimating the fatigue stress concentration factor of machined surfaces'. *International Journal of Fatigue* 24 (9), 2002, 923–930.

[180] Jiang J., Zhao M. 'Influence of residual stress on stress concentration factor for high strength steel welded joints'. *Journal of Constructional Steel Research* 72, 2012, 20–28.

[181] *ABAQUS/Standard User's Manual*. version 6.3. Pawtucket (U.S.A.): Hibbitt, Karlsson & Sorensen, 2002.

[182] Zubelewicz A. 'Century-long Taylor-Quinney interpretation of plasticity-induced heating reexamined'. *Scientific Reports* 9088, 2019, 1–7.

[183] Sovani Y., Basoalto H. *ALM_ Thermal_ Deposition v.1.0*. CASIM2 Research Group, University of Birmingham. Rolls-Royce Point of contact: Nunzio Palumbo, Ben Saunders. Feb. 2016.

[184] Huang H., Ma N., Chen J., Feng Z., Murakawa H. 'Toward large-scale simulation of residual stress and distortion in wire and arc additive manufacturing'. *Additive Manufacturing* 34, 2020, 1–13.

[185] Ockendon J., Howison S., Lacey A., Movchan A. *Applied Partial Differential Equations*. Oxford: Oxford University Press, 1999.

[186] Young E. C. *Partial Differential Equations: An Introduction*. Boston: Allyn and Bacon, Inc., 1972.

[187] Koshlyakov N. S., Smirnov M. M., Gliner E. B. *Differential equations of mathematical physics*. Amsterdam: North-Holland Publishing Company, 1964.

[188] Noll I., Bartel T., Menzel A. 'A computational phase transformation model for selective laser melting processes'. *Computational Mechanics* 66, 2020, 1321–1342.

[189] Finlayson B. A. 'Variational Principles for Heat Transfer'. In: *Numerical Properties and Methodologies in Heat Transfer: Proceedings of the Second National Symposium*. Ed. by Shih T. M. Washington - New York - London: Hemisphere Publishing Corporation, 1983, 17–31.

[190] Thomée V. *Galerkin Finite Element Methods for Parabolic Problems*. 2nd. Springer Series in Computational Mathematics. Berlin, Heidelberg (Germany): Springer-Verlag, 2006.

[191] *Abaqus. Getting started with Abaqus. Interactive edition, v. 6.8*. Dassault Systèmes, 2008.

[192] Harewood F. J., McHugh P. E. 'Comparison of the implicit and explicit finite element methods using crystal plasticity'. *Computational Materials Science* 39 (2), 2007, 481–494.

[193] Prior A. M. 'Applications of implicit and explicit finite element techniques to metal forming'. *Journal of Materials Processing Technology* 45 (1), 1994, 649–656.

[194] Naghibi Beidokhti H., Janssen D., Khoshgoftar M., Sprengers A., Perdahcioglu E. S., Boogaard T. Van den, Verdonschot N. 'A comparison between dynamic implicit and explicit finite element simulations of the native knee joint'. *Medical Engineering & Physics* 38 (10), 2016, 1123–1130.

[195] Galati M., Iuliano L. 'A literature review of powder-based electron beam melting focusing on numerical simulations'. *Additive Manufacturing* 19, 2018, 1–20.

[196] Sun J. S., Lee K. H., Lee H. P. 'Comparison of implicit and explicit finite element methods for dynamic problems'. *Journal of Materials Processing Technology* 105 (1), 2000, 110–118.

[197] *Abaqus 6.10. Analysis User's Manual*. Vol. IV: Elements. Simulia, 2010.

[198] Kim S., Sohn D., Im S. 'Construction of polyhedral finite element meshes based upon marching cube algorithm'. *Advances in Engineering Software* 128, 2019, 98–112.

[199] Zienkiewicz O. C., Taylor R. L., Zhu J. Z. *The Finite Element Method: Its Basis and Fundamentals*. Seventh. Vol. I. Oxford: Butterworth-Heinemann, 2013.

[200] Saunders N., Guo Z., Li X., Miodownik A. P., Schillé J.-P. 'Using JMatPro to Model Materials Properties and Behavior'. *The Journal of The Minerals, Metals & Materials Society (TMS)* 55 (12), 2003, 60–65.

[201] Saunders N., Li X., Miodownik A. P., Schille J.-P. 'An Integrated Approach To The Calculation Of Materials Properties For Ti-Alloys'. In: *Ti-2003: Proc 10th World Conference on Titanium, July 13-18, Hamburg, Germany*. 2003.

[202] Bewick V., Cheek L., Ball J. 'Statistics review 7: Correlation and regression'. *Critical care* 7 (6), 2003, 451–459.

[203] Colin Cameron A., Windmeijer F. A. G. 'An R-squared measure of goodness of fit for some common nonlinear regression models'. *Journal of Econometrics* 77 (2), 1997, 329–342.

[204] Mills K. C. *Recommended Values of Thermophysical Properties for Selected Commercial Alloys*. Abington Hall, Abington, Cambridge (England): Woodhead Publishing, 2002.

[205] Li J. J. Z., Johnson W. L., Rhim W.-K. 'Thermal expansion of liquid Ti–6Al–4V measured by electrostatic levitation'. *Applied Physics Letters* 89 (11), 2006, 111913–111913–2.

[206] Nikam S. H., Jain N. K. 'Finite Element Simulation of Pre-Heating Effect on Melt Pool Size During Micro-Plasma Transferred Arc Deposition Process'. *IOP Conference Series: Materials Science and Engineering* 389, July 2018, 012006.

[207] Park H. S., Ansari M. J. 'Numerical investigation and an effective predicting system on the Selective Laser Melting (SLM) process with Ti6Al4V alloy'. *IOP Conference Series: Materials Science and Engineering* 400, Sept. 2018, 1–13.

[208] Sim M. S., Lee C. M. 'Determination of optimal laser power according to the tool path inclination angle of a titanium alloy workpiece in laser-assisted machining'. *The International Journal of Advanced Manufacturing Technology* 83, 2016, 1717–1724.

[209] Fonda P., Wang Z., Yamazaki K., Akutsu Y. 'A fundamental study on Ti–6Al–4V's thermal and electricalproperties and their relation to EDM productivity'. *Journal of Materials Processing Technology* 202, 2008, 583–589.

[210] Nouari M., Makich H. 'On the Physics of Machining Titanium Alloys: Interactions between Cutting Parameters, Microstructure and Tool Wear'. *Metals* 4 (3), 2014, 335–358.

[211] D'Ostuni S., Leo P., Casalino G. 'FEM Simulation of Dissimilar Aluminum TitaniumFiber Laser Welding Using 2D and 3D GaussianHeat Sources'. *Metals* 7 (307), 2017, 1–15.

[212] Mertens A., Reginster S., Paydas H., Contrepois Q., Dormal T., Lemaire O., Lecomte-Beckers J. 'Mechanical properties of alloy Ti–6Al–4V and of stainless steel 316L processed by selective laser melting: influence of out-of-equilibrium microstructures'. *Powder Metallurgy* 57 (3), 2014, 184–189.

[213] Golovin P. A., Vildanov A. M., Babkin K. D., Ivanov S. Y., Topalov I. K. 'Distortion prevention of axisymmetric parts during laser metal deposition'. *Journal of Physics: Conference Series* 1109 (012065), 2018, 1–8.

[214] Xie P., Zhao H. Y., Wu B., Gong S.-L. 'Using Finite Element and Contour Method to Evaluate Residual Stress in Thick Ti-6Al-4V Alloy Welded by Electron Beam Welding'. *Acta Metallurgica Sinica (English Letters)* 28 (7), 2015, 922–930.

[215] Nibennaoune Z., George D., Ahzi S., Ruch D., Remond Y., Gracio J. J. 'Numerical simulation of residual stresses in diamond coating on Ti-6Al-4V substrate'. *Thin Solid Films* 518 (12), 2010, 3260–3266.

[216] Pengfei T., Shen F., Li B., Zhou K. 'A thermo-metallurgical-mechanical model for selective laser melting of Ti6Al4V'. *Materials & Design* 168, 2019, 1–13.

[217] Fukuhara M., Sanpei A. 'Elastic moduli and internal frictions of Inconel 718 and Ti-6Al-4V as a function of temperature'. *Journal of Materials Science Letters* 12, 1993, 1122–1124.

[218] Zhang J., Nyilas A., Obst B. 'New technique for measuring the dynamic Young's modulus between 295 and 6 K'. *Cryogenics* 31 (10), 1991, 884–889.

[219] Zhang S., Lane B., Whiting J., Chou K. 'An Investigation into Metallic Powder Thermal Conductivity in Laser Powder Bed Fusion Additive Manufacturing'. *Solid Freeform Fabrication 2018: Proceedings of the 29th Annual InternationalSolid Freeform Fabrication Symposium – An Additive Manufacturing Conference*, 2018, 1796–1807.

[220] Chua B.-L., Lee H.-J., Ahn D.-G. 'Estimation of Effective Thermal Conductivity of Ti-6Al-4V Powders for a Powder Bed Fusion Process Using Finite Element Analysis'. *International Journal of Precision Engineering and Manufacturing* 19, 2018, pages257–264.

[221] Galati M., Snis A., Iuliano L. 'Powder bed properties modelling and 3D thermo-mechanical simulation of the additive manufacturing Electron Beam Melting process'. *Additive Manufacturing* 30, 2019, 1–9.

[222] Akwaboa S., Zeng C., Amoafo-Yeboah N., Ibekwe S., Mensah P. 'Thermophysical Properties of Laser Powder Bed Fused Ti-6Al-4V and AlSi10Mg Alloys Made with Varying Laser Parameters'. *Materials* 16 (14), 2023.

[223] Bartsch K., Herzog D., Bossen B., Emmelmann C. 'Material modeling of Ti–6Al–4V alloy processed by laser powder bed fusion for application in macroscale process simulation'. *Materials Science and Engineering: A* 814 (141237), 2021, 1–20.

[224] Vastola G., Pei Q. X., Zhang Y.-W. 'Predictive model for porosity in powder-bed fusion additive manufacturing at high beam energy regime'. *Additive Manufacturing* 22, 2018, 817–822.

[225] Rahman M. S., Schilling P. J., Herrington P. D., Chakravarty U. K. 'A Comparison of the Thermo-Fluid Properties of Ti-6Al-4V Melt Pools Formed by Laser and Electron-Beam Powder-Bed Fusion Processes'. *Journal of Engineering Materials and Technology* 143 (2), Oct. 2021, 021003–1–021003–13.

[226] Strumza E., Landau P., Kimmel G., Ganor Y. I., Yeheskel O., Hayun S. 'Thermophysical properties of Ti-6Al-4V fabricated by powder bed fusion methods'. *Additive Manufacturing* 58, 2022, 1–12.

[227] Olleak A., Xi Z. 'Finite Element Modeling of the Selective Laser Melting Process for Ti-6Al-4V'. In: *Solid Freeform Fabrication 2018: Proceedings of the 29th Annual International*. Solid Freeform Fabrication Symposium – An Additive Manufacturing Conference. 2018, 1710–1720.

[228] Gu H., Gong H., Dilip J., Pal D., Hicks A., Doak H., Stucker B. 'Effects of Powder Variation on the Microstructure and Tensile Strength of Ti6Al4V Parts Fabricated by Selective Laser Melting'. In: Aug. 2014, 470–483.

[229] Zherebtsov S., Salishchev G., Galeyev R. 'Dynamic Recrystallization of Titanium and Ti-6Al-4V Alloy'. In: *Proceedings of the First Joint International Conference*. Ed. by Gottstein G., Molodov D. A. Springer-Verlag, Aug. 2001, 961–966.

[230] Yan W., Lu Y., Jones K., Yang Z., Fox J., Witherell P., Wagner G., Liu W. K. 'Data-driven characterization of thermal models for powder-bed-fusion additive manufacturing'. *Additive Manufacturing* 36, 2020, 101503.

[231] Venkatkumar D., Ravindran D. 'Effect of Boundary Conditions on Residual Stresses and Distortion in 316 Stainless Steel Butt Welded Plate'. *High Temperature Materials and Processes* 38 (2019), 2019, 827–836.

[232] Hocine S., Van Swygenhoven H., Van Petegem S. 'Verification of selective laser melting heat source models with operando X-ray diffraction data'. *Additive Manufacturing* 37, 2021, 101747.

[233] Yang J., Sun S., Brandt M., Yan W. 'Experimental investigation and 3D finite element prediction of the heat affected zone during laser assisted machining of Ti6Al4V alloy'. *Journal of Materials Processing Technology* 210 (15), 2010, 2215–2222.

[234] Coppa P., Consorti A. 'Normal emissivity of samples surrounded by surfaces at diverse temperatures'. *Measurement* 38 (2), 2005, 124–131.

[235] Mohr G., Nowakowski S., Altenburg S. J., Maierhofer C., Hilgenberg K. 'Experimental Determination of the Emissivity of Powder Layers and Bulk Material in Laser Powder Bed Fusion Using Infrared Thermography and Thermocouples'. *Metals* 10 (11), 2020, 1–26.

[236] Zhang T., Li H., Liu S., Shen S., Xie H., Shi W., Zhang G., Shen B., Chen L., Xiao B., Wei M. 'Evolution of molten pool during selective laser melting of Ti–6Al–4V'. *Journal of Physics D: Applied Physics* 52 (5), 2019, 1–10.

[237] Babu B., Lundbäck A., Lindgren L. E. 'Simulation of Ti-6Al-4V Additive Manufacturing Using Coupled Physically Based Flow Stress and Metallurgical Model'. *Materials* 12 (23), 2019, 1–16.

[238] Tan J.L. T. C. W. C. H. 'A Computational Study on Porosity Evolution in Parts Produced by Selective Laser Melting'. *Metallurgical and Materials Transactions A* 49A, 2018, 3663–3673.

[239] Palmeri D., Pollara G., Licari R., Micari F. 'Finite Element Method in L-PBF of Ti-6Al-4V: Influence of Laser Power and Scan Speed on Residual Stress and Part Distortion'. *Metals* 13 (11), 2023.

[240] Lu X., Cervera M., Chiumenti M., Zhang J. L. X. J. andGuohao, Lin X. 'Modeling of the Effect of the Building Strategy on the Thermomechanical Response of Ti-6Al-4V Rectangular Parts Manufactured by Laser Directed Energy Deposition'. English. *Metals* 10 (12), 2020, 1–18.

[241] Li C., Gouge M. F., Denlinger E. R., Irwin J. E., Michaleris P. 'Estimation of part-to-powder heat losses as surface convection in laser powder bed fusion'. *Additive Manufacturing* 26, 2019, 258–269.

[242] Masoomi M., Pegues J. W., Thompson S. M., Shamsaei N. 'A numerical and experimental investigation of convective heat transfer during laser-powder bed fusion'. *Additive Manufacturing* 22, 2018, 729–745.

[243] Yang X., Gibbons G. J., Tanner D. A., Li Z., Wilson P., Williams M. A., Kotadia H. R. 'Scan strategy induced microstructure and consolidation variation in the laser-powder bed fusion (L-PBF) additive manufacturing of low alloy 20MnCr5 steel'. *Materials & Design* 232, 2023, 1–15.

[244] Vrancken B., Thijs L., Kruth J.-P., Van Humbeeck J. 'Heat treatment of Ti6Al4V produced by Selective Laser Melting: Microstructure and mechanical properties'. *Journal of Alloys and Compounds* 541, 2012, 177–185.

[245] Pedrazzini S., Pek M. E., Ackerman A. K., Cheng Q., Ali H., Ghadbeigi H., Mumtaz K., Dessolier T., Britton T. B., Bajaj P., Jägle E., Gault B., London A. J., Galindo-Nava E. 'Effect of Substrate Bed Temperature on Solute Segregation and Mechanical Properties in Ti–6Al–4V Produced by Laser Powder Bed Fusion'. *Metallurgical and Materials Transactions A* 54, 2023, 3069–3085.

[246] Fu H., Xu B., Xiao Q. H., Li S., Zhang X., Bian S., Kang T. 'Effect of preheating temperature on post-weld residual stress of dissimilar steel plates'. *Metalurgija* 59, 2020, 150–152.

[247] Lin Y. C., Lee K. H. 'Effect of preheating on the residual stress in type 304 stainless steel weldment'. *Journal of Materials Processing Technology* 63 (1), 1997, 797–801.

[248] Ali H., Ma L., Ghadbeigi H., Mumtaz K. 'In-situ residual stress reduction, martensitic decomposition and mechanical properties enhancement through high temperature powder bed pre-heating of Selective Laser Melted Ti6Al4V'. *Materials Science and Engineering: A* 695, 2017, 211–220.

[249] Du Y., You X., Qiao F., Guo L., Liu Z. 'A model for predicting the temperature field during selective laser melting'. *Results in Physics* 12, 2019, 52–60.

[250] Vallabh C. K. P., Zhao X. 'Melt pool temperature measurement and monitoring during laser powder bed fusion based additive manufacturing via single-

camera two-wavelength imaging pyrometry (STWIP)'. *Journal of Manufacturing Processes* 79, 2022, 486–500.

[251] Basoalto H. *Microstructure modelling Ti-6-4*. Tech. rep. M2i2 Report 2022, 2022.

[252] 'Trumpf develops 3D printers for metal parts'. *Metal Powder Report* 71 (1), 2016, 55.

[253] *Metallic materials - Vickers hardness test -Part 1: Test method (ISO 6507-1:2018)*. Tech. rep. European Standard, 2018.

[254] Nádai L., Katona B., Terdik A., Bognár E. 'Chemical etching of titanium samples'. *Periodica Polytechnica Mechanical Engineering* 57 (2), 2013, 53–57.

[255] Radzikowska J. M. 'Application of Color Metallographic Techniques to Study the Microstructure of Titanium Alloys'. In: 2016, 922–932.

[256] Childs P. R. N., Greenwood J. R., Long C. A. 'Review of temperature measurement'. *Review of Scientific Instruments* 71 (8), 2000, 2959–2978.

[257] Feng B., Wang C., Zhang Q., Ren Y., Cui L., Yang Q., Hao S. 'Effect of laser hatch spacing on the pore defects, phase transformation and properties of selective laser melting fabricated NiTi shape memory alloys'. *Materials Science and Engineering: A* 840, 2022, 142965, 1–9.

[258] Keist J. S., Palmer T. A. 'Development of strength-hardness relationships in additively manufactured titanium alloys'. *Materials Science and Engineering: A* 693, 2017, 214–224.

[259] Liu B., Ding Y., Xu J., Gao Y., Chu C., Hu Y., Chen D. 'Grain boundary engineering activated by residual stress during the laser powder bed fusion of Inconel 718 and the electrochemical corrosion performance'. *Materials Characterization* 204, 2023, 113160.

[260] Attard B., Cruchley S., Beetz C., Megahed M., Chiu Y. L., Attallah M. M. 'Microstructural control during laser powder fusion to create graded microstructure Ni-superalloy components'. *Additive Manufacturing* 36, 2020, 101432.

[261] Hsu T.-H., Huang P.-C., Lee M.-Y., Chang K.-C., Lee C.-C., Li M.-Y., Chen C.-P., Jen K.-K., Yeh A.-C. 'Effect of processing parameters on the fractions of martensite in 17-4 PH stainless steel fabricated by selective laser melting'. *Journal of Alloys and Compounds* 859, 2021, 157758.

[262] Cho J. 'Characterization of the α'-martensite phase and its decomposition in Ti-6Al-4V additively manufactured by selective laser melting'. PhD thesis. RMIT University, 2018.

[263] Neikter M., Åkerfeldt P., Pederson R., Antti M.-L. 'Microstructure characterisation of Ti-6Al-4V from different additive manufacturing processes'. *IOP Conference Series: Materials Science and Engineering* 258, Oct. 2017, 012007.

[264] Nakano S., Chen X. J., Gao B., Kakimoto K. 'Numerical analysis of cooling rate dependence on dislocation density in multicrystalline silicon for solar cells'. *Journal of Crystal Growth* 318 (1), 2011. The 16th International Conference on Crystal Growth (ICCG16)/The 14th International Conference on Vapor Growth and Epitaxy (ICVGE14), 280–282.

[265] Tachikawa M., Mori H. 'Cooling rate dependence of dislocation density in InP/Si from growth temperature to room temperature'. In: *Conference Proceedings. 1998 International Conference on Indium Phosphide and Related Materials (Cat. No.98CH36129)*. 1998, 116–118.

[266] Carlsson S., Larsson P.-L. 'On the determination of residual stress and strain fields by sharp indentation testing.: Part I: theoretical and numerical analysis'. *Acta Materialia* 49 (12), 2001, 2179–2191.

[267] Wang X., Chou Y. K. 'A Method to Estimate Residual Stress in Metal Parts Made by Selective Laser Melting'. In: vol. Volume 2A: Advanced Manufacturing.

ASME International Mechanical Engineering Congress and Exposition. Nov. 2015, V02AT02A015.

[268] Yazdi R., Ghasemi H. M., Abedini M., Wang C., Neville A. 'Oxygen Diffusion Layer on Ti–6Al–4V Alloy: Scratch and Dry Wear Resistance'. *Tribology Letters* 67 (101), 2019, 1–15.

[269] Rajan S., Wanjara P., Gholipour J., Kabir A. S. 'Fatigue Behavior of Linear Friction Welded Ti-6Al-4V and Ti-6Al-2Sn-4Zr-2Mo-0.1Si Dissimilar Welds'. *Materials* 14 (11), 2021, 1–19.

[270] Sedmak S., Jovicic R., Sedmak A., Aranđelović M., Djordjevic B. 'Influence of multiple defects in welded joints subjected to fatigue loading according to sist EN ISO 5817:2014'. *Structural Integrity and Life (1451-3749)* 18, Feb. 2018, 77–81.

[271] Janeček M., Novy F., Harcuba P., Stráský J., Trško L., Mhaede M., Wagner L. 'The Very High Cycle Fatigue Behaviour of Ti-6Al-4V Alloy'. *Acta Physica Polonica A* 128, Oct. 2015, 497–503.

[272] Rao J. H., Stanford N. 'A survey of fatigue properties from wrought and additively manufactured Ti-6Al-4V'. *Materials Letters* 283, 2021, 128800.

[273] Molaei R., Fatemi A. 'Fatigue Design with Additive Manufactured Metals: Issues to Consider and Perspective for Future Research'. *Procedia Engineering* 213, 2018. 7th International Conference on Fatigue Design, Fatigue Design 2017, 29-30 November 2017, Senlis, France, 5–16.

[274] Yang X., Barrett R. A., Harrison N. M., Leen S. B. 'A physically-based structure-property model for additively manufactured Ti-6Al-4V'. *Materials & Design* 205, 2021, 109709.

[275] Lyu X., Weber F., Gebhardt C., Chen G., Broeckmann C. 'Crystal plasticity enhanced direct cyclic analysis of cyclic behaviour of LPBF-manufactured AISI 316L'. *Materials & Design* 240, 2024, 112864.

[276] Galarraga H., Lados D. A., Dehoff R. R., Kirka M. M., Nandwana P. 'Effects of the microstructure and porosity on properties of Ti-6Al-4V ELI alloy fabricated by electron beam melting (EBM)'. *Additive Manufacturing* 10, 2016, 47–57.

[277] Carroll B. E., Palmer T. A., Beese A. M. 'Anisotropic tensile behavior of Ti–6Al–4V components fabricated with directed energy deposition additive manufacturing'. *Acta Materialia* 87, 2015, 309–320.

[278] Slotwinski J. A., Garboczi E. J., Hebenstreit K. M. 'Porosity Measurements and Analysis for Metal Additive Manufacturing Process Control'. *Journal of Research of the National Institute of Standards and Technology* 119, 2014, 494–528.

[279] Fousová M., Vojtěch D., Kubásek J., Jablonská E., Fojt J. 'Promising characteristics of gradient porosity Ti-6Al-4V alloy prepared by SLM process'. *Journal of the Mechanical Behavior of Biomedical Materials* 69, 2017, 368–376.

[280] Brown B. F. 'A Preface to the Problem of Stress Corrosion Cracking'. In: *Stress Corrosion Cracking of Metals - A State of the Art*. Ed. by Craig H. L. Vol. 518, Special Technical Publication. ASTM International, 1972, 3–15.

[281] Lynch S. P., Moutsos S. 'A Brief History of Fractography'. *Journal of Failure Analysis and Prevention* 6 (6), 2006, 54–69.

[282] Feige N. G., Covington L. C. 'Overview of Corrosion Cracking of Titanium Alloys'. In: *Stress Corrosion Cracking of Metals - A State of the Art*. Ed. by Craig H. L. Vol. 518, Special Technical Publication. ASTM International, 1972, 119–130.

[283] Wanhill R. J. H., Byrnes R. T., Smith C. L. 'Stress corrosion cracking (SCC) in aerospace vehicles'. In: *Stress corrosion cracking: Theory and practice*. Ed. by Raja, V. S.; Shoji, T. Woodhead Publishing, 2011, 608–650.

[284] Andresen P. L., Ford F. P. 'Prediction of stress corrosion cracking (SCC) in nuclear power systems'. In: *Stress corrosion cracking: Theory and practice*. Ed. by Raja V. S., Shoji T. Woodhead Publishing, 2011, 651–713.

[285] LaQue F. L. 'Electrochemistry and Corrosion'. *Journal of Electrochemical Society* 116 (2), 1969, 73C–77C.

[286] Lynch S. P. 'Mechanistic and fractographic aspects of stress-corrosion cracking (SCC)'. In: *Stress corrosion cracking: Theory and practice*. Ed. by Raja V. S., Shoji T. Woodhead Publishing, 2011, 3–89.

[287] Brettle J., Orman S. 'Laboratory testing for stress corrosion cracking'. *Anti-Corrosion Methods and Materials* 20 (9), 1973, 3–10.

[288] Kain V. 'Stress corrosion cracking (SCC) in stainless steels'. In: *Stress corrosion cracking: Theory and practice*. Ed. by Raja V. S., Shoji T. Woodhead Publishing, 2011, 199–243.

[289] Ketcham S. J. 'Testing Methods for Stress Corrosion Cracking'. In: *Stress Corrosion Cracking of Metals - A State of the Art*. Ed. by Craig H. L. Vol. 518, Special Technical Publication. ASTM International, 1972, 79–86.

[290] Scully J. C., Powell D. T. 'The stress corrosion cracking mechanism of α-titanium alloys at room temperature'. *Corrosion Science* 10, 1970, 719–733.

[291] Dietzel W., Srinivasan P. B., Atrens A. 'Testing and evaluation methods for stress corrosion cracking (SCC) in metals'. In: *Stress corrosion cracking: Theory and practice*. Ed. by Raja V. S., Shoji T. Woodhead Publishing, 2011, 133–166.

[292] Scully J. C. 'The mechanical parameters of stress-corrosion cracking'. *Corrosion Science* 8 (10), 1968, 759–769.

[293] Scully J. C. 'The theory of stress corrosion cracking in alloys'. *Anti-Corrosion Methods and Materials* 19 (9), 1972, 5–10.

[294] Qian L., Atrens A. 'A critical review of the influence of hydrogen on the mechanical properties of medium-strength steels'. *Corrosion Reviews* 31 (3-6), 2013, 85–103.

[295] Lynch S. P. 'Hydrogen embrittlement (HE) phenomena and mechanisms'. In: *Stress corrosion cracking: Theory and practice*. Ed. by Raja V. S., Shoji T. Woodhead Publishing, 2011, 90–130.

[296] Griffith A. A. 'The Phenomena of Rupture and Flow in Solids'. *Philosophical Transactions of the Royal Society of London* 221 (A), 1920, 163–198.

[297] Gross D. 'The History of Theoretical, Material and Computational Mechanics - Mathematics Meets Mechanics and Engineering'. In: *The History of Theoretical, Material and Computational Mechanics*. Ed. by Stein E. Vol. 1. Berlin, Heidelberg: Springer, 2014, 195–209.

[298] Sih G. C., Macdonald B. 'Fracture mechanics applied to engineering problems-strain energy density fracture criterion'. *Engineering Fracture Mechanics* 6 (2), 1974, 361–386.

[299] Oh H., Lee J., Kim J. G., Kim S. 'Effect of defects on environment-assisted fracture (EAF) behavior of Ti–6Al–4V alloy fabricated by direct energy deposition (DED)'. *Journal of Materials Research and Technology* 20, 2022, 4365–4377.

[300] Dai N., Zhang L.-C., Zhang J., Chen Q., Wu M. 'Corrosion behavior of selective laser melted Ti-6Al-4V alloy in NaCl solution'. *Corrosion Science* 102, 2016, 484–489.

[301] Dai N., Zhang L.-C., Zhang J., Zhang X., Ni Q., Chen Y., Wu M., Yang C. 'Distinction in corrosion resistance of selective laser melted Ti-6Al-4V alloy on different planes'. *Corrosion Science* 111, 2016, 703–710.

[302] Dai N., Zhang J., Chen Y., Zhang L.-C. 'Heat Treatment Degrading the Corrosion Resistance of Selective Laser Melted Ti-6Al-4V Alloy'. *Journal of The Electrochemical Society* 164 (7), 2017, C428.

[303] Huang R., Han Y. 'The effect of SMAT-induced grain refinement and dislocations on the corrosion behavior of Ti–25Nb–3Mo–3Zr–2Sn alloy'. *Materials Science and Engineering: C* 33 (4), 2013, 2353–2359.

[304] Lisagor W. B., Manning C. R. *Stress-corrosion cracking of Ti-6Al-4V titanium alloy in nitrogen tetroxide*. Tech. rep. NASA, 1968.

Appendix A

Stress corrosion cracking

Initially called *season cracking*, because of its periodic occurrence, the problem of stress corrosion cracking has been investigated from its discovery during the second half of 19th century, but even nowadays it is classified as a extremely complex engineering problem, mainly for the interaction between different factors. The study of this problem is therefore justified by the evidence of the impossibility to find effective inhibitors for stress corrosion cracking propagation.

Brief historical notes

Stress corrosion cracking were firstly reported in the second half of 19th century in the cold drawn brass cartridge case exposed to the moist ammonia (NH_3) atmosphere and it was called *season cracking*, due to its periodical manifestation associated with the environment [280, 281]. It has become a widespread problem during the 1930s, when the stainless steel were employed in several industries and for military aircrafts. It was also observed in titanium alloys in contact with nitric acid (HNO_3) or methanol (CH_3OH) during the following decades [280, p. 5]. In particular, in 1964 B. F. Brown showed that an highly promising titanium alloy for aircraft was subjected to stress corrosion cracking and this caused a dramatic reduction in load carrying ability and in 1966 there was a failure of a titanium alloy tank with an explosion that caused a loss of expensive aerospace components

[282, p. 120].

Today, stress corrosion cracking is a relevant problem and an interesting challenge in several industries, such as in aerospace industry, because it can occur in all major alloy systems used in the construction of aircraft, but also in nuclear power production, where it can be detected, for example, in boiling water reactors or in storage tanks containing radioactive waste [283, 284].

Overview of the problem

As pointed out by LaQue in 1969, most corrosion processes are electrochemical in nature [285]. A metal subject to corrosion, as a consequence of its interaction with the environment at which it is exposed, can partially or totally lose its resistance to the external mechanical actions, because the corrosion causes its irreversible destruction. In addition to purely electrochemical phenomena, there are the chemical-mechanical types, which include the stress corrosion cracking and the corrosion fatigue.

The stress corrosion cracking is the brittle fracture of a material exposed to the environment and subject to a certain traction stress level. Typically, it occurs at low stress levels, which are frequently constant stresses and which are widely below the stresses that lead the material to the macroscopic yielding. The fracture appears to be macroscopically brittle and, because of that, this phenomenon give cause for concern in the engineering world and it could be extremely dangerous if unexpected failures take place during service conditions. The mean velocity of crack propagation is extremely variable, varying from 10^{-2} m/s to 10^{-11} m/s, which is less than 0.3 mm/year, and it depends on several aspects [286, p. 3].

There are three important factors that sinergically contribute to stress corrosion cracking, namely the environment, the material and the stress, to which correspond three different scientific fields: chemistry, metallurgy, and mechanics. It is exactly the involvement of these three factors that determine the difficulty

of the problem and the interaction between experts in these three disciplines is frequently required to fully understand it. Another crucial element is time, often seen as a lesser factor, yet it still plays a critical part in determining failure. Some alloys, such as stainless steel, are protected from oxidation by a passive film and this layer has the important property that to self-repair if it is damaged: this property goes under the name of *repassivation*. If this film is damaged and it is not able to quickly reconstitute itself, stress corrosion cracking may occur. Since stress corrosion cracking takes place with almost constant loads, the rate of this process of rebuilding, and so the time, is thus an important parameter. This time dependent behaviour is known under the name of *repassivation kinetics*. It should be noted that this is only one of the different mechanisms proposed that can lead to stress corrosion cracking and it is more relevant for some specific combinations of alloy and environment.

Firstly, with regards to the role of environment, which can be liquid or gaseous, the main sensitive feature is that stress corrosion cracking can occur often when the alloy is inert to the environment, so that an environment can be apparently innocuous to a specific alloy. Conversely, when an environment seems to be aggressive towards the alloy, this phenomenon does not take place [280, p. 5]. This means that if a metal corrodes, most of the time this is not a premonitory factor [280]. In addition, it was observed that only few chemical species are responsible for stress corrosion cracking and they act by initiating or promoting the fracture. The environment is also responsible for the rate at which the fracture grows, indeed low levels of pH (acidic solutions) or high levels of oxygen accelerate the process of cracking [287]. The chemical species that cause stress corrosion cracking need not to be much high, neither unimportant in concentrations [280, p. 6]. Since is the acidic nature of the environment to cause stress corrosion cracking in several alloys, it is nearly impossible to find an inhibitor for the crack propagation, which is generally a compound that can decrease the corrosion rate

of a material by isolating the metal from the environment [280, p. 14]. Another essential parameter to be considered in the environment setting is temperature. In general, increasing temperature accelerate chemical reactions, but stress corrosion cracking was observed also at room or near ambient temperatures [288, p. 207] and at elevated temperature [280, p. 5].

Secondly, it seems obvious that different materials react in a different way to the same environment. It was observed that the stress corrosion cracking occurs only in alloys and hardly in pure elements [280]. However, the study of stress corrosion cracking in pure metals is mainly interesting only for the investigation of the mechanisms and it is in general unsubstantial for practical engineering applications [286, p. 11]. Some metals can be subject to a quicker repassivation, and the metallurgical phases, which are controlled by the production processes or subsequent treatments, can alter the time of failure.

Finally, traction stresses can be service stresses or also residual stresses, due to manufacturing processes. The stresses have shown an impact on the time of failure and also on the path of crack propagation. Residual stresses are in general associated with a general decrease in resistance to the stress corrosion cracking [289, p. 83]. Indeed, wherever the stresses are service stresses can be absent a crack branching. The crack propagates always perpendicular to the tensile axis, although there are some extraordinary observations, in fact, for a specific combination of alloy and environment were detected a propagation at 45° to the load direction [290, p. 728]. Although it was not proved, it seems to exists a threshold value for stress, under which stress corrosion cracking does not initiate [280, p. 8].

Laboratory testing methods for stress corrosion cracking

A test laboratory is supposed to be replicable and thus all the variables during an experiment need to be exactly measured. It should be noted that the repro-

ducibility is also a feature of experiments that give at all times invalid results [285, 289]. Due to the substantially complex nature of some scientific phenomena, it seems very difficult to take into account all its aspects and so the standardization of the laboratory testing needs much effort to be defined. This is particularly true in the field of stress corrosion cracking experimental analysis, where the environment and the material play an important role.

Since time is a fundamental variable in stress corrosion cracking, there exist two problems related to the determination of the exact instant of time when a sample should be considered cracked:

1. the advent of the first crack is usually determined by a visual inspection (or with a low magnification factor [289, p. 84], such as 10–15), so there is some arbitrariness in establishing exactly the time of the first crack appearing;

2. if the crack is not appeared in the past, there is no guarantee about its future occurrence, so this requires to test a sample for the same duration of the service life and this is not always feasible, because laboratory testing rarely simulates the precise conditions in service [286, p. 6].

Another difficulty in stress corrosion cracking tests arises from the necessity to pay a particular attention to the galvanic corrosion of the specimen. It can be caused by the simple contact of the sample with the testing apparatus and it should be avoided. An important role is also played by the form of the specimen, in fact if the specimen has a rectangular cross section, a fracture preferably starts from one edge and this situation sometimes is not realistic, if compared to a specific component. Also the surface treatments can alter the initiation of fracture and they should be related to the specific nature of the application [291, p. 135]. Indeed, roughness of the surface has a significant effect on stress corrosion cracking initiation [288, p. 227]. Surface preparation of the specimen is another variable which is difficult to reproduce correctly from one laboratory to another one, and

a very general guideline suggest that care must be taken to do not overheat the surface during this process [289].

In order to correctly define the execution, the American Society for Testing and Materials has prepared a standardisation for the stress corrosion cracking tests, including the definition of the environment [289, p. 85]. During recent times significant efforts were made by other organisations, such as the *International Organization for Standardization and the National Association of Corrosion Engineers* [291], and this exactly reflects the modern interest in this problem and its complexity.

Following the distinction written in [287], there are three main categories of cracking tests: constant strain (also called constant displacement test), constant stress (also called constant load test) and constant strain rate test. The latter is a dynamic test and so there is the possibility to conduct a test in static or in dynamic rate [291, p. 136].

Constant strain specimens are compact and cheap, and they are also suitable for long term exposure tests, but there are some disadvantages, such as that stresses are not know accurately and the crack growth is, in general, more slow than in the constant stress test. On the contrary, whilst in constant stress test the stresses are know, this test is performed by using a more complicated apparatus and a set of four specimen is suggested to be tested at each stress level [289, p. 85]. Furthermore, there is a category of pre-cracked specimens, firstly introduced by B. F. Brown and which are advantageous for testing materials with high strength, but with a limited ductility. The main advantage is that the crack propagation is directly comparable to in-service conditions, while one of the main disadvantages is the possibility to investigate only the crack propagation and not its initiation. A typical pre-cracked test is carried out with a notched cantilever beam with a constant dead weight, in which the damaged zone is exposed to a specific environment. Since stress corrosion cracking testing is usually a long process, testing is

usually performed by accelerating the entire process, selecting a more aggressive environment than what the alloy will encounter under service conditions. Although this appears to be a valid method for achieving quick results, its validity is questionable [287, p. 7].

Microstructure and stress corrosion cracking

One of the most useful technique in fracture problems observation is fractography, which is the study of fracture surfaces topographies, and its object is a better understanding of the causes and mechanisms. The term *fractography* was used for the first time in 1945 by C. A. Zapffe and M. Clogg. The evolution of instruments adopted in this research field from the use of naked eye and magnifying glass has led to detailed fractographic images, now obtained by scanning electron microscopy (SEM) and transmission electron microscopy (TEM). At microscale, the mode of failure due to stress corrosion cracking can be intergranular (crack propagating along the grain boundaries), transgranular (crack propagates through grains), or it can be exhibited in a mixed mode of cracking [288, p. 203]. In the experiment conducted by B. F. Brown in November 1964 for a titanium alloy exposed to sea-water, for example, a transgranular cleavage was detected.

The evidence of fractographic observations shows that stress corrosion cracking is a macroscopically brittle fracture that occurs also in generally ductile metals [280, p. 5]. One of the main causes is the recognized effect of the hydrogen propagation inside the microstructure of the material, although stress corrosion cracking mechanisms can be different and more complex [292, p. 764]. This phenomenon is called *hydrogen embrittlement* and was experimentally shown that it macroscopically may cause a reduction in ductility [290, p. 731]. Hydrogen embrittlement can be considered a different phenomenon and is sometimes distinguished from the stress corrosion cracking, but it seems to be no reason for this differentiation in nomenclature [293, p. 10].

Hydrogen embrittlement was observed by W. H. Johnson in 1874 and it was also reported by B. F. Brown in the aforementioned experiment [294] [290, p. 721]. In a series of investigations Johnson discovered an exceptional decrease in toughness and breaking-strain of iron and steel immersed for few minutes in hydrochloric (HCl) and sulphuric acids (H_2SO_4). The most extraordinary phenomenon is the production of bubbles of gas from the whole surface of the fracture, which was caused by a release of previously absorbed hydrogen. Moreover, he noticed that the reduction of the physical properties was only temporary, the specimens gradually regained their original toughness and strength after being removed from the acids.

Hydrogen embrittlement can be framed more generally as a hydrogen degradation process, or occasionally referred as *hydrogen-assisted cracking* [294, 295]. It can be divided into two types, depending on the source of this chemical element and it can be an internal hydrogen embrittlement, if the pre-existing hydrogen is already inside the metal, or hydrogen environment embrittlement, if it is initially present only in the environment.

The main effect of the hydrogen interaction with the microstructure is the hydride (H^-) nucleation on an operative slip plane, which restricts the ductility of the grain [290, p. 721]. During recent times, some different explanations for the mechanism which regulates the hydrogen embrittlement inside the microstructure were also proposed. In summary, they briefly state that hydrogen is responsible to enhancement of voids, or to the degradation of atomic bonds, or to the degradation of fracture stress by a surface free energy decrease, or to the enhancement of dislocation mobility [294, p. 89]. A significant reduction in ductility on the macroscale for several different steels, although sometimes the fracture surface did not show stress corrosion cracking features and some steels exhibited a good resistance to hydrogen embrittlement, was observed [294, p. 90]. In some cases an increasing in strength was also experienced. More specifically, an increasing

in hardening due to hydrogen and this was explained by hydrogen-dislocation interaction, because the hydrogen can inhibit the moving of a dislocation or it can impeding cross slip. The microstructure can be a potential trap source for the hydrogen and the traps, for example, depend on the dislocations and grains (attractive traps) and also on the grain boundaries and voids (physical traps).

As already mentioned, although the mechanism of hydrogen embrittlement seems well supported by experimental analysis and observations, this is not the unique mechanism in stress corrosion cracking, because hydrogen is not the only chemical specie that may cause stress corrosion cracking. Stress corrosion cracking was indeed detected in several different environments, such as those in which was present chlorine (Cl_2), which was responsible for the destruction of the protective film, and not hydrogen [290, p. 728]. The research for a single general mechanism to explain stress corrosion cracking in all systems is still difficult and it seems also improbable [280, p. 14].

Fracture mechanics and stress corrosion cracking

In 1920 A. A. Griffith published his work entitled *The Phenomena of Rupture and Flow in Solids* proposing a theoretical criterion of rupture based on a competition between elastic and fracture energy and, for this reason, he is often regarded as the father of the fracture mechanics [296]. A fracture can be classified as brittle or ductile and the latter is characterised by evident large deformations before the rupture of the material. Materials are so often classified as brittle or ductile based on their mechanical response to the fracture. However, such categorisation is not totally correct, because the same material, subject to different physical conditions, may reveal a distinct behaviour. Moreover, it was observed by Bertram Hopkinson (1874–1918) that a ductile fracture exhibits a hardening behaviour near the crack tip, so that the material becomes locally brittle [297, p. 206]. This can be due to the fact that a clear separation between brittle and ductile fracture does not

exist.

Despite stress corrosion cracking manifests itself as a brittle fracture, the application of Griffith's theory for crack propagation, is not correct, because locally the process always involves a plastic deformation and the Griffith's theory describes only the brittle fracture of a material [292, p. 765]. Stress corrosion cracking is indeed a slow process and fracture propagation is thus particularly influenced by plastic properties of the material in the region around the crack tip. Nevertheless, if the plastic zone is located only in a neighbourhood of the crack tip and the rest of the body is elastic, it is still possible to apply this theory, which is frequently referred as *linear elastic fracture mechanics*. This kind of analysis is performed in order to study only the elastic stress field associated with the existent crack [280, p. 9]. It seems also opportune, in this context, to remember that it is impossible to define a pre-existing crack path for a given set of conditions, because this path simply does not exist [293, p. 9].

In linear elastic fracture mechanics, the main parameter that completely characterize the stress field in the elastic region is the stress intensity factor K ($\mathrm{MPa}\sqrt{\mathrm{m}}$), which is associated with one of the three fracture opening modes. Mode I is referred as *opening mode*, mode II as *sliding mode* and mode III as *tearing mode*, so it is possible to identify three factors K_I, K_{II}, K_{III}. It was proposed that fracture propagates when the value of K reaches a critical value denominated *fracture toughness* and respectively denoted by K_{Ic}, K_{IIc}, K_{IIIc} [298].

A good macroscopic parameter for numerically evaluating the effect of stress corrosion cracking, specific for each combination of alloy and corrodent, is commonly designated, for a plain strain condition, by $K_{I\mathrm{SCC}}$ [292, 280]. This stress corrosion cracking threshold value represents the fracture toughness below which the crack growth has not been observed, but is observed above it [280, p. 10]. Therefore, since $K_{I\mathrm{SCC}} < K_{Ic}$, the effect of stress corrosion cracking can be seen

as the reduction of fracture toughness. Moreover, it was observed [280, p. 10], in the field of the studies in stress corrosion cracking kinetics, that the crack growth rate is approximately an exponential function of the stress intensity factor. In any case, it should be noted that care must be taken in defining this parameter for a given set of alloy and environment, because the crack can occur also at much lower values and so the value assumed for it can be too large [280, p. 13].

Titanium alloys and the effect of martensite on stress corrosion cracking

As already mentioned, titanium alloys have good corrosion resistance and perform better than high-strength aluminium alloys against the problem of stress corrosion cracking [32, p. 206]. However, some exceptions are represented by some specific environments, such as those composed by pure methanol and red, fuming nitric acid [35, p. 5:45]. Nevertheless, in both environments a presence of 2% of water is sufficient to inhibit cracking [35, p. 5:38], whilst the behaviour with methanol is aggravated by the presence of bromine or iodine [35, p. 5:38].

As shown in Figure 7.1, Ti-6Al-4V is susceptible to stress corrosion cracking. Additionally, the formation of martensite, as consequence of additive manufacturing, has been observed as one of the negative factors for corrosion resistance in Ti-6Al-4V [299]. Martensite is indeed metastable and in 'higher energy state' with regard to corrosion [300]. Moreover, the oxide film of β phase is more stable than the TiO_2 film on the α phase [301, 300].

Heat treatments dissolve the martensite and thus they seem to be beneficial against corrosion. However, this does not happen, especially when the material has been heated above the β-transus temperature. This is due to an increasing grain size, which has been correlated with lower corrosion resistance, because higher segregation or impurity precipitation at grain boundaries is observed [302, 303] and it was also associated with an increased surface roughness, which influ-

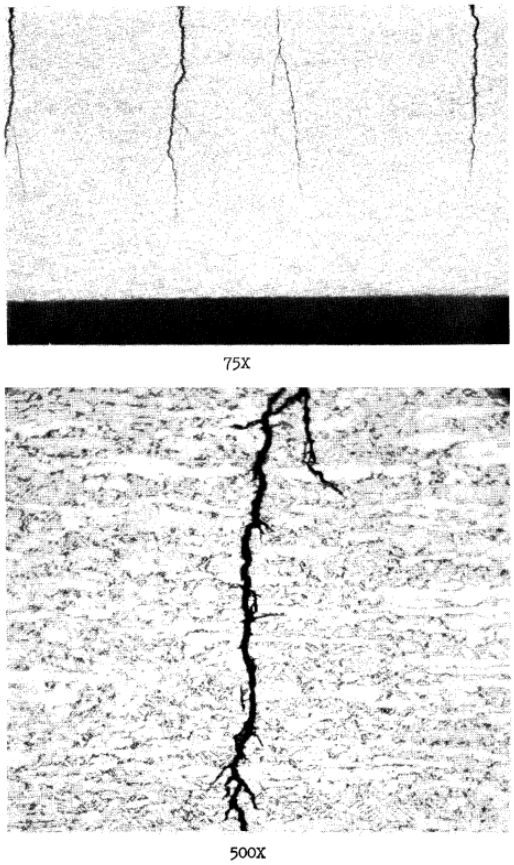

FIGURE 7.1: Stress corrosion cracking of Ti-6Al-4V. Image reproduced from [304, p. 27, fig. 13].

ences negatively the corrosion resistance [303].

Appendix B

SEM micrographies

In this Appendix B some images of the microstructure, captured with the scanning electron microscope (SEM) and analysed afterwards to quantitatively describe the martensite, are collected and made available for further investigations. This is done in the hope that they may be useful for further analysis, avoiding, or at least minimising, the need of replication of the same experiments. They are grouped firstly according to the hatch spacing ($h = 0.50$ mm and $h = 2.00$ mm) and then to the location A, B, C where they were acquired.

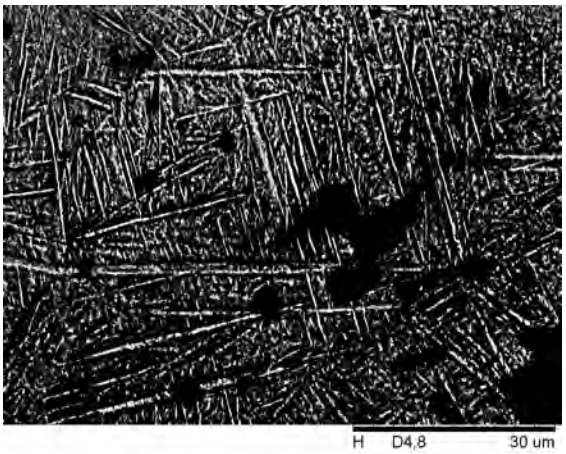

(a) Location A.

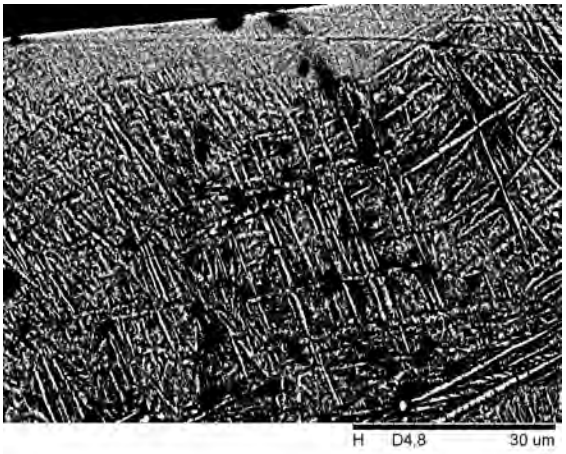

(b) Location B.

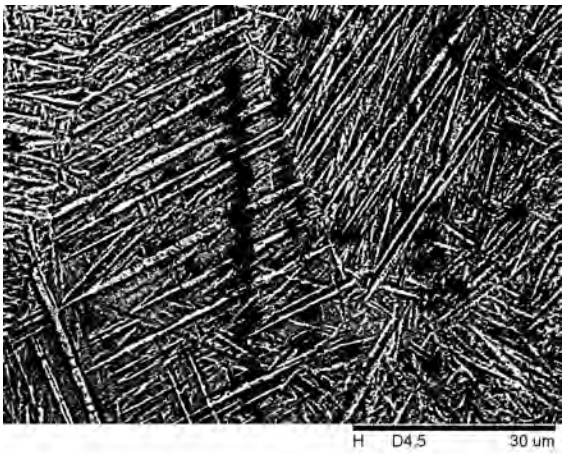

(c) Location C.

FIGURE 7.2: SEM mickrographs at location A, B, C (hatch spacing $h = 0.50$).

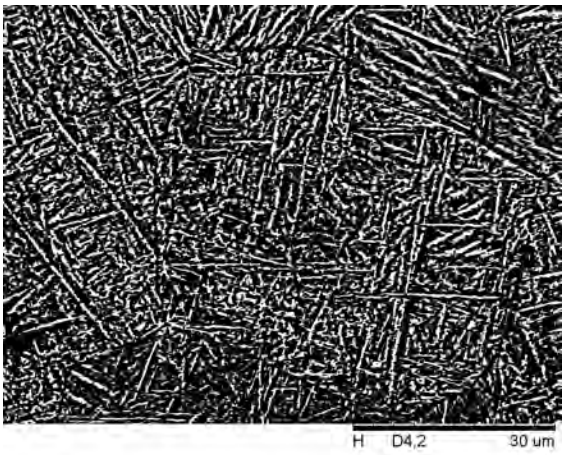

(a) Location A.

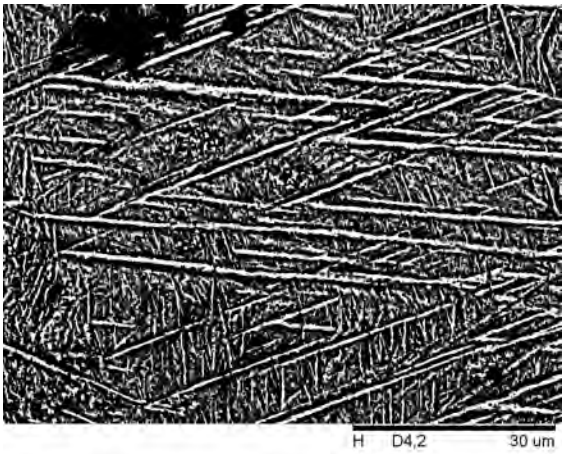

(b) Location B.

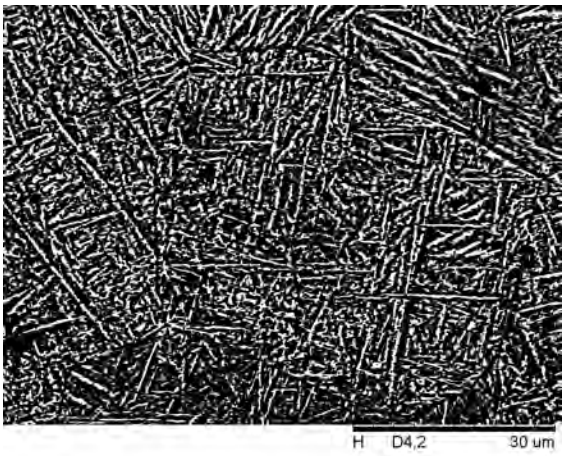

(c) Location C.

FIGURE 7.3: SEM micrographs at location A, B, C (hatch spacing $h = 2.00$).

Appendix C

In this Appendix C, the statistical information related to the martensite α' thickness $w_{\alpha'}$ measurements, obtained from the SEM images and subsequently processed, are reported. The results are subdivided into the skew-normal distributions, interpolated and reported from the measurements performed in each point within the cross-section of the laser track, and then into the cumulative distribution functions. For each group of measurement and thus for each skew-normal distribution, the numerical values of location ξ, scale ω, and shape α are also given. In addition, the median value m is also indicated, together with the 25th and 75th percentiles, denoted as t_{25} and t_{75} respectively. The latter values have been used for plotting the interquartile range (*i.e.* the spread of the middle half of data distribution) in the comparison between experimental data and models.

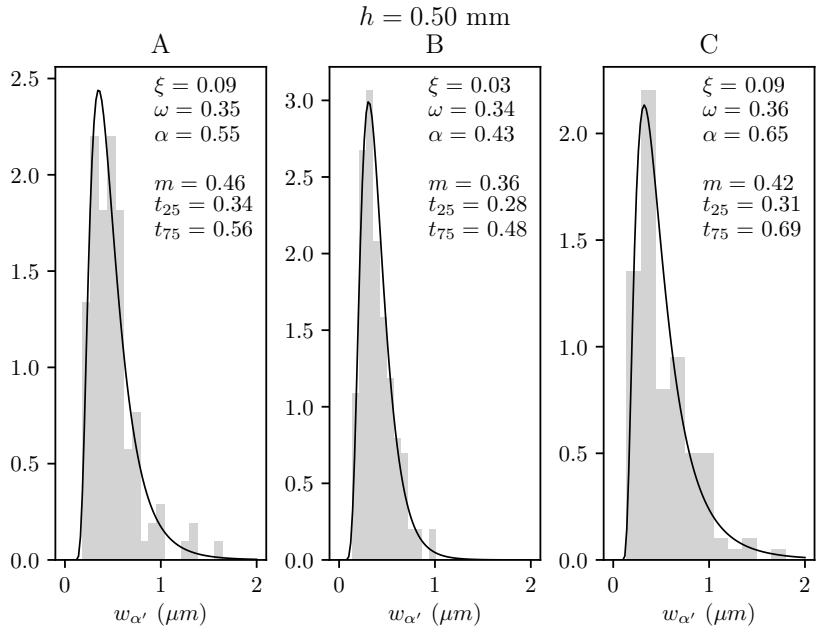

(a) Martensite α' thickness $w_{\alpha'}$ experimental data distribution for different locations in the melt pool (A, B, C) and for a hatch spacing value of $h = 0.50$ (parameters are: ξ location, ω scale, α shape, m median, t_{25} 25th-percentile, t_{75} 75th-percentile).

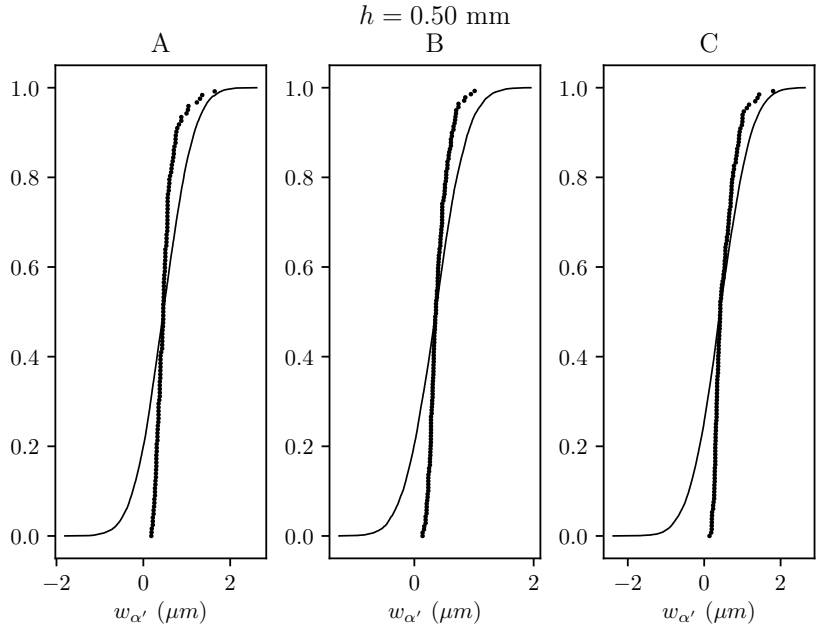

(b) Martensite α' thickness $w_{\alpha'}$ experimental cumulative distribution function for different locations in the melt pool (A, B, C) and for a hatch spacing value of $h = 0.50$.

FIGURE 7.4: Martensite thickness experimental data distributions for different locations in the melt pool (A, B, C), hatch spacing $h = 0.50$.

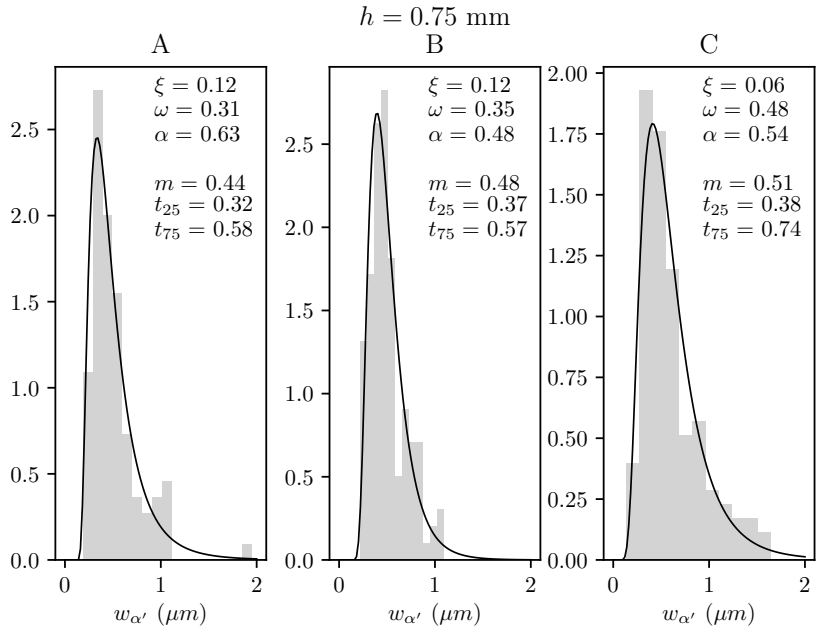

(a) Martensite α' thickness $w_{\alpha'}$ experimental data distribution for different locations in the melt pool (A, B, C) and for a hatch spacing value of $h = 0.75$ (parameters are: ξ location, ω scale, α shape, m median, t_{25} 25th-percentile, t_{75} 75th-percentile).

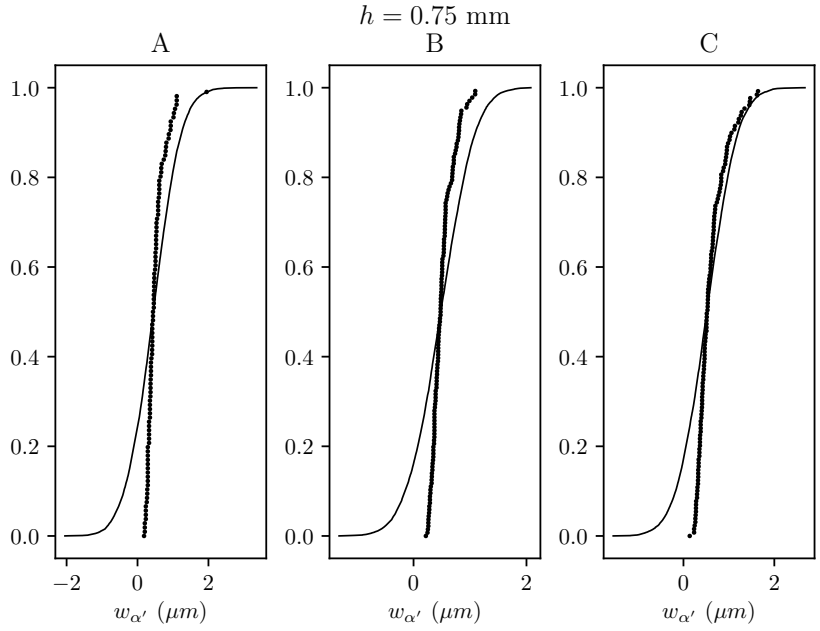

(b) Martensite α' thickness $w_{\alpha'}$ experimental cumulative distribution function for different locations in the melt pool (A, B, C) and for a hatch spacing value of $h = 0.75$.

FIGURE 7.5: Martensite thickness experimental data distributions for different locations in the melt pool (A, B, C), hatch spacing $h = 0.75$.

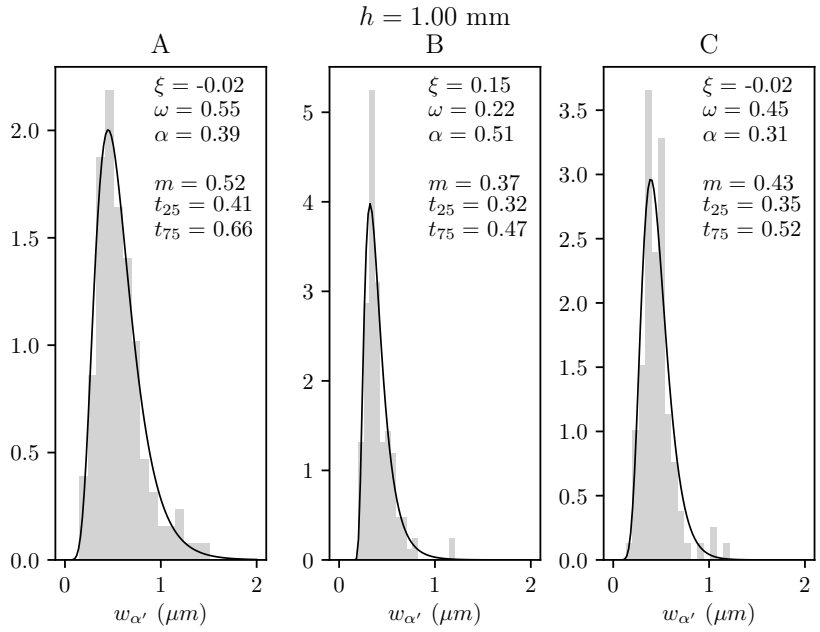

(a) Martensite α' thickness $w_{\alpha'}$ experimental data distribution for different locations in the melt pool (A, B, C) and for a hatch spacing value of $h = 1.00$ (parameters are: ξ location, ω scale, α shape, m median, t_{25} 25th-percentile, t_{75} 75th-percentile).

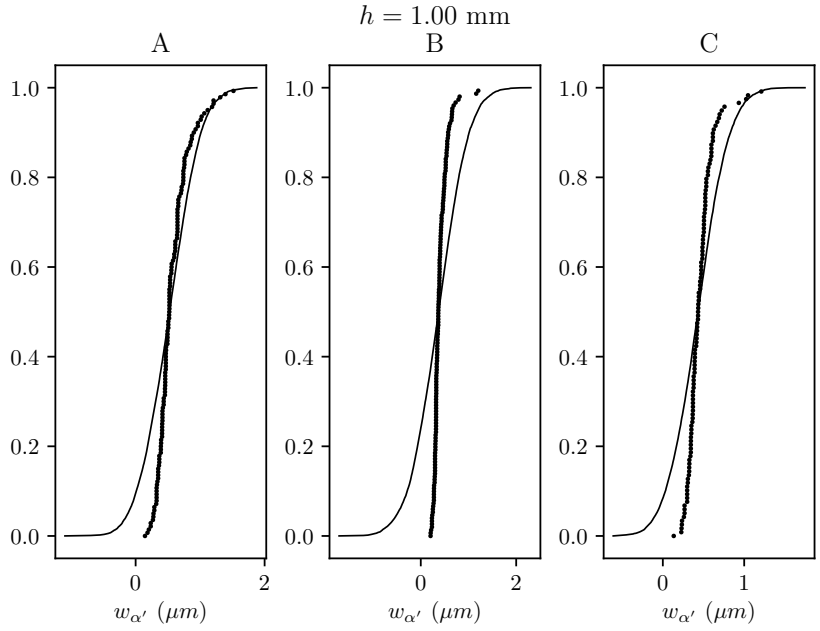

(b) Martensite α' thickness $w_{\alpha'}$ experimental cumulative distribution function for different locations in the melt pool (A, B, C) and for a hatch spacing value of $h = 1.00$.

FIGURE 7.6: Martensite thickness experimental data distributions for different locations in the melt pool (A, B, C), hatch spacing $h = 1.00$.

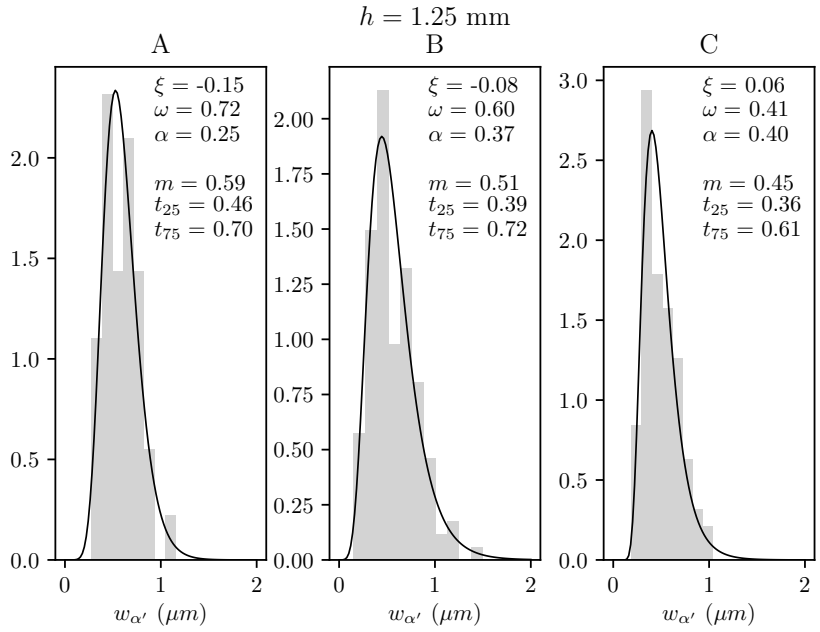

(a) Martensite α' thickness $w_{\alpha'}$ experimental data distribution for different locations in the melt pool (A, B, C) and for a hatch spacing value of $h = 1.25$ (parameters are: ξ location, ω scale, α shape, m median, t_{25} 25th-percentile, t_{75} 75th-percentile).

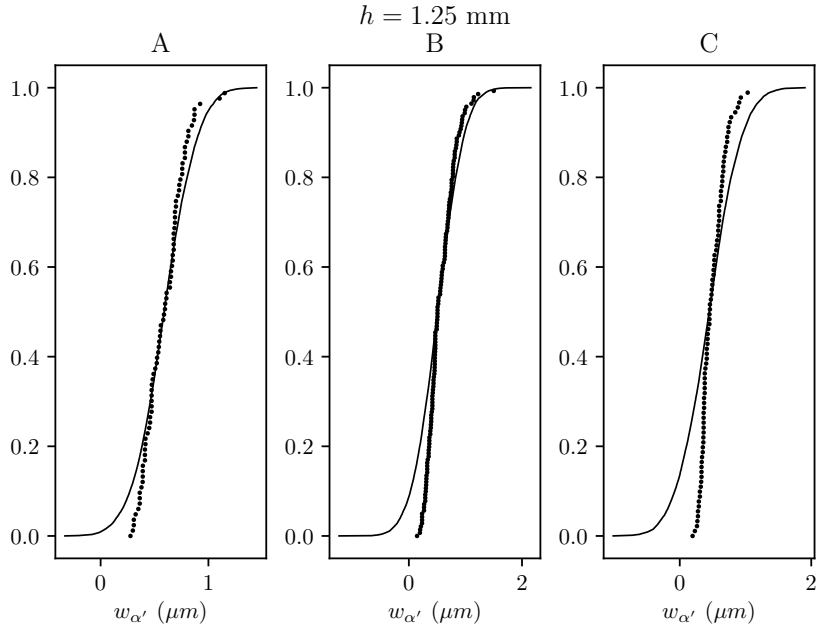

(b) Martensite α' thickness $w_{\alpha'}$ experimental cumulative distribution function for different locations in the melt pool (A, B, C) and for a hatch spacing value of $h = 1.25$.

FIGURE 7.7: Martensite thickness experimental data distributions for different locations in the melt pool (A, B, C), hatch spacing $h = 1.25$.

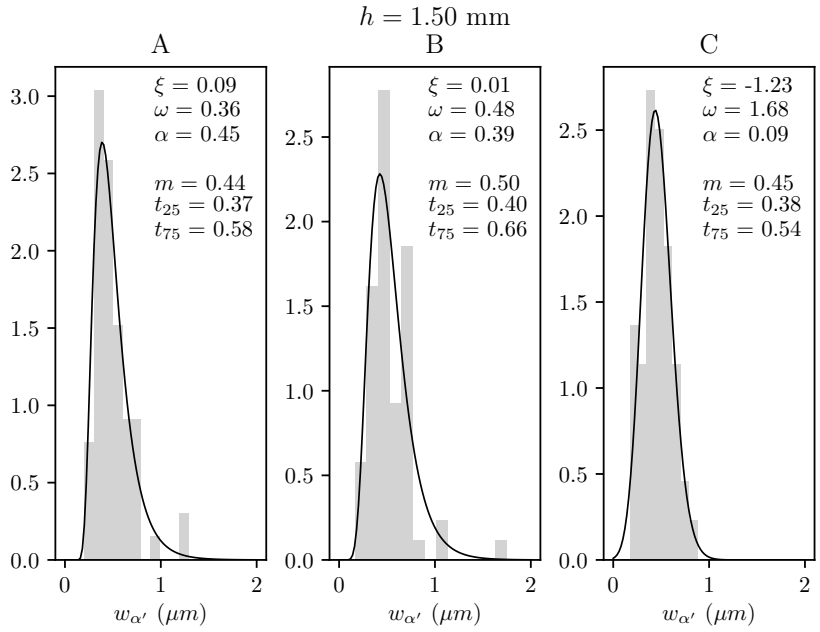

(a) Martensite α' thickness $w_{\alpha'}$ experimental data distribution for different locations in the melt pool (A, B, C) and for a hatch spacing value of $h = 1.50$ (parameters are: ξ location, ω scale, α shape, m median, t_{25} 25th-percentile, t_{75} 75th-percentile).

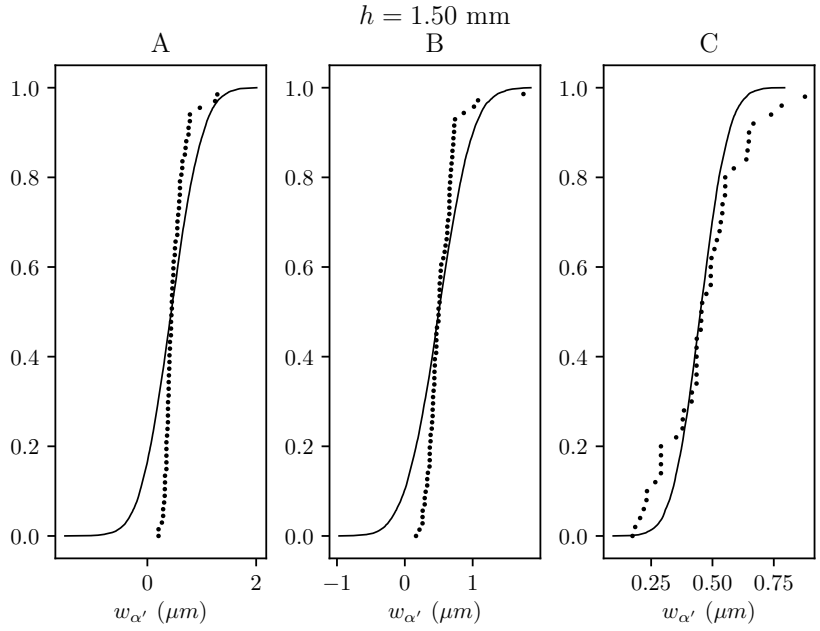

(b) Martensite α' thickness $w_{\alpha'}$ experimental cumulative distribution function for different locations in the melt pool (A, B, C) and for a hatch spacing value of $h = 1.50$.

FIGURE 7.8: Martensite thickness experimental data distributions for different locations in the melt pool (A, B, C), hatch spacing $h = 1.50$.

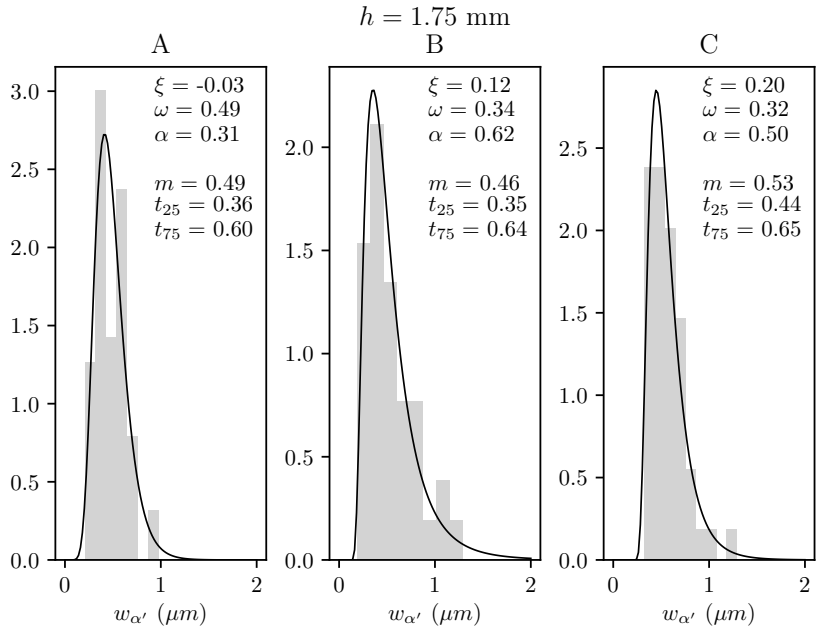

(a) Martensite α' thickness $w_{\alpha'}$ experimental data distribution for different locations in the melt pool (A, B, C) and for a hatch spacing value of $h = 1.75$ (parameters are: ξ location, ω scale, α shape, m median, t_{25} 25th-percentile, t_{75} 75th-percentile).

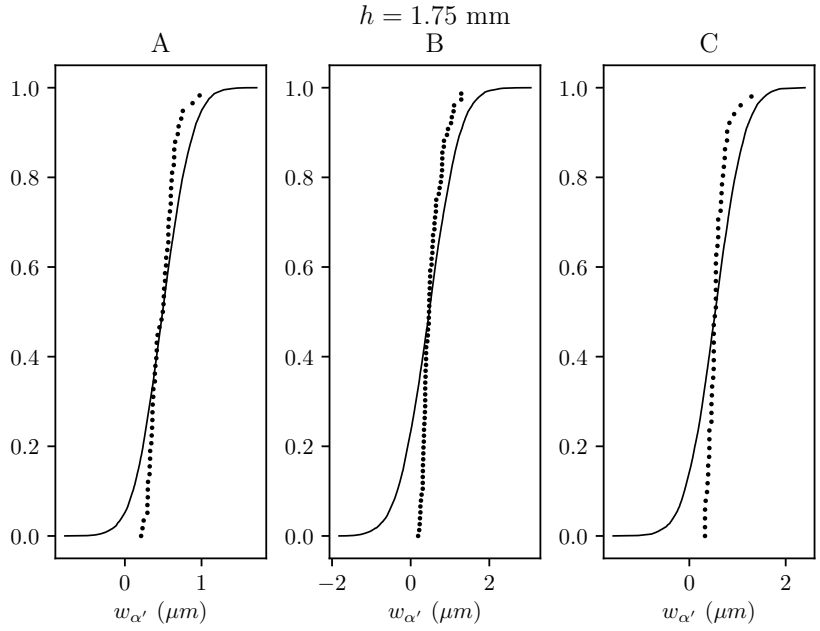

(b) Martensite α' thickness $w_{\alpha'}$ experimental cumulative distribution function for different locations in the melt pool (A, B, C) and for a hatch spacing value of $h = 1.75$.

FIGURE 7.9: Martensite thickness experimental data distributions for different locations in the melt pool (A, B, C), hatch spacing $h = 1.75$.

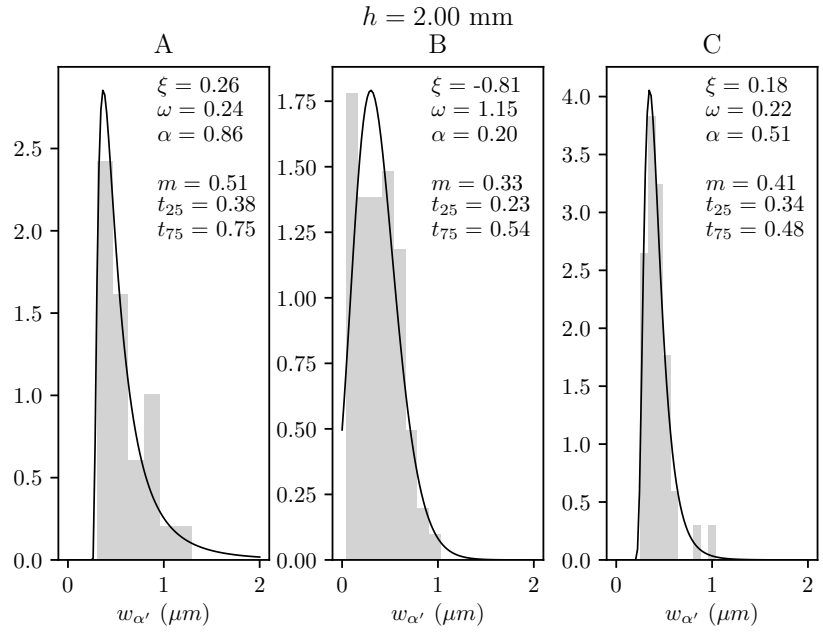

(a) Martensite α' thickness $w_{\alpha'}$ experimental data distribution for different locations in the melt pool (A, B, C) and for a hatch spacing value of $h = 2.00$ (parameters are: ξ location, ω scale, α shape, m median, t_{25} 25th-percentile, t_{75} 75th-percentile).

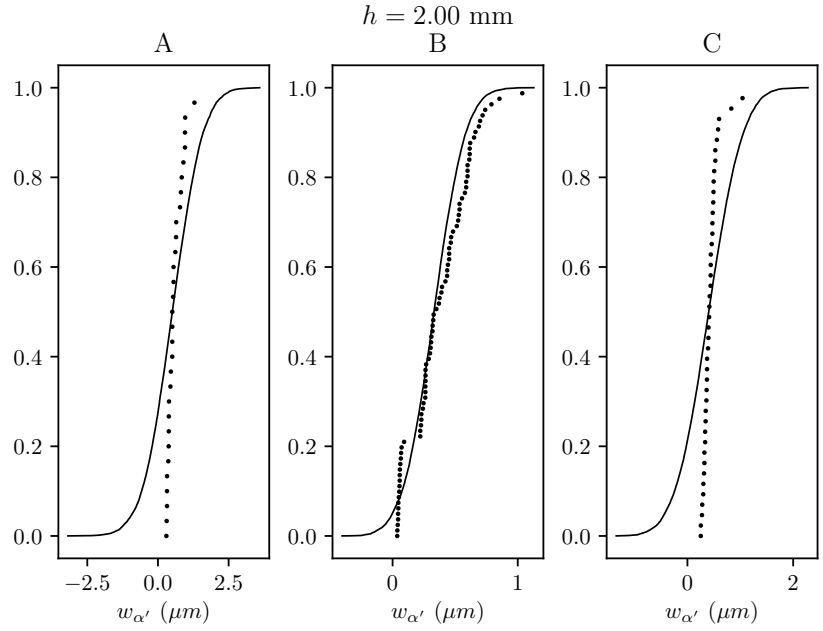

(b) Martensite α' thickness $w_{\alpha'}$ experimental cumulative distribution function for different locations in the melt pool (A, B, C) and for a hatch spacing value of $h = 2.00$.

FIGURE 7.10: Martensite thickness experimental data distributions for different locations in the melt pool (A, B, C), hatch spacing $h = 2.00$.

Appendix D

In this Appendix D, the statistical information related to the martensite α' spacing $d_{\alpha'}$ measurements, obtained from the SEM images and subsequently processed, are reported. The results are subdivided into the skew-normal distributions, interpolated and reported from the measurements performed in each point within the cross-section of the laser track, and then into the cumulative distribution functions. For each group of measurement and thus for each skew-normal distribution, the numerical values of location ξ, scale ω, and shape α are also given. In addition, the median value m is also indicated, together with the 25th and 75th percentiles, denoted as t_{25} and t_{75} respectively. The latter values have been used for plotting the interquartile range, which is the spread of the middle half of data distribution, in the comparison between experimental data and models.

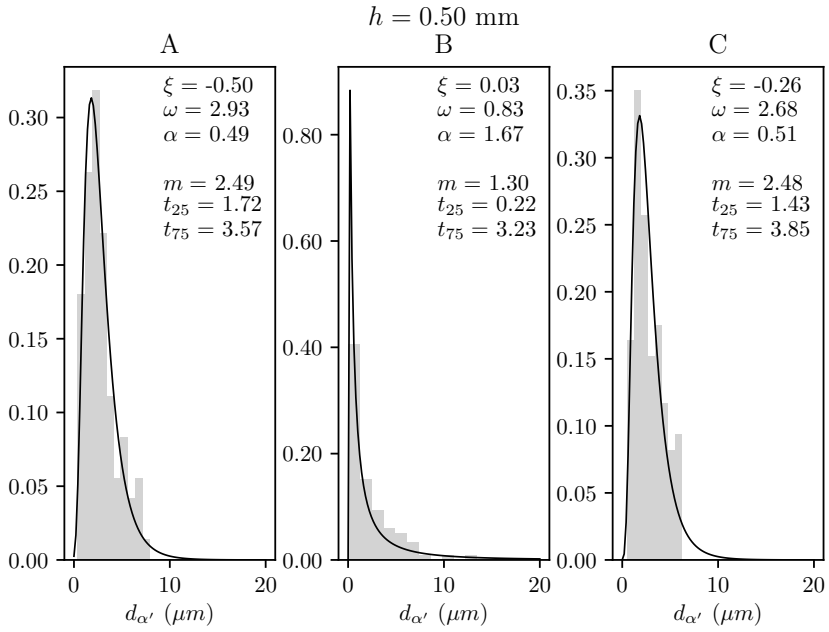

(a) Martensite α' needle spacing $d_{\alpha'}$ experimental data distribution for different locations in the melt pool (A, B, C) and for a hatch spacing value of $h = 0.50$ (parameters are: ξ location, ω scale, α shape, m median, t_{25} 25th-percentile, t_{75} 75th-percentile).

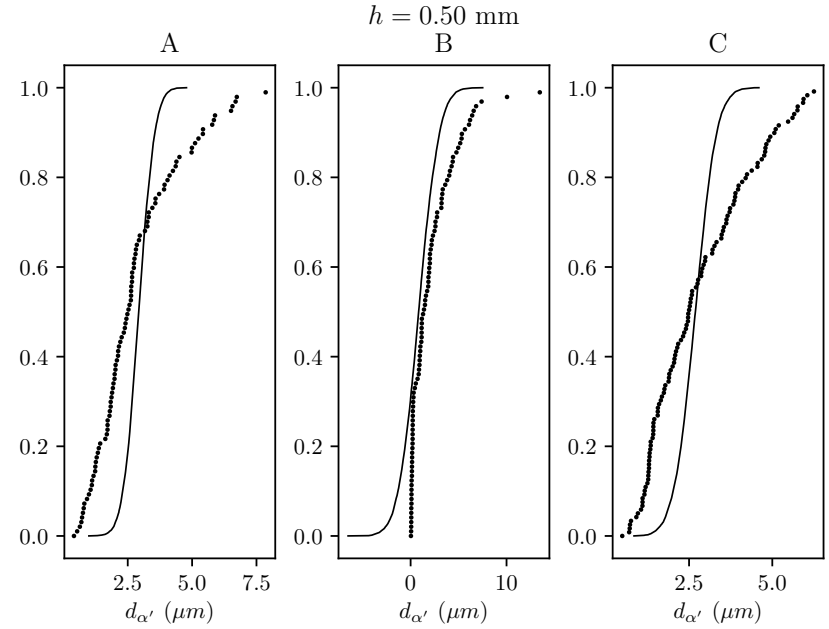

(b) Martensite α' needle spacing $d_{\alpha'}$ experimental cumulative distribution function for different locations in the melt pool (A, B, C) and for a hatch spacing value of $h = 0.50$ mm.

FIGURE 7.11: Martensite spacing experimental data distributions for different locations in the melt pool (A, B, C), hatch spacing $h = 0.50$ mm.

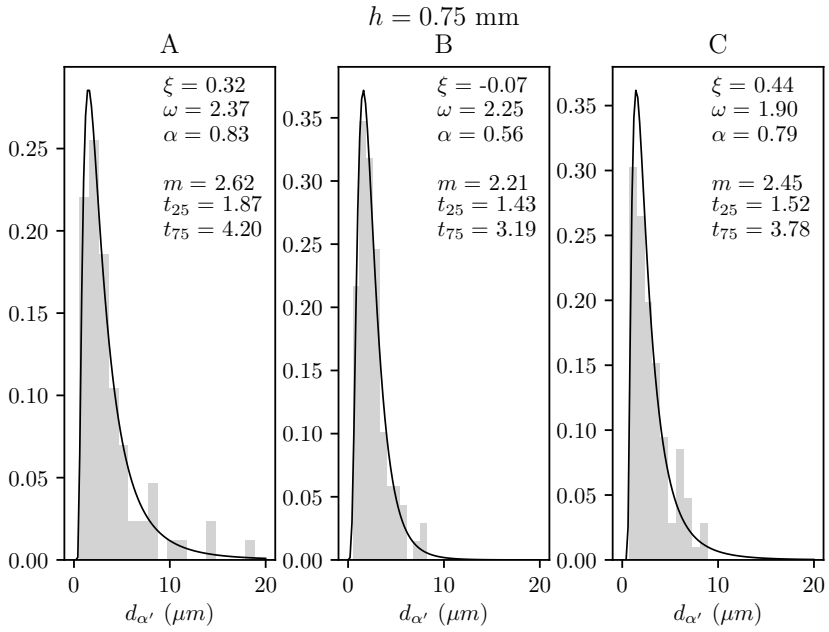

(a) Martensite α' needle spacing $d_{\alpha'}$ experimental data distribution for different locations in the melt pool (A, B, C) and for a hatch spacing value of $h = 0.75$ (parameters are: ξ location, ω scale, α shape, m median, t_{25} 25th-percentile, t_{75} 75th-percentile).

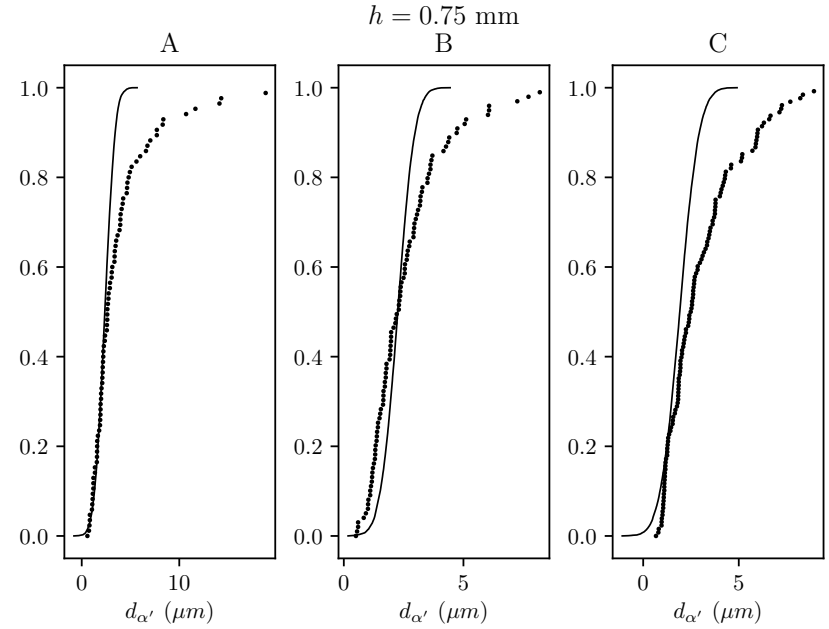

(b) Martensite α' needle spacing $d_{\alpha'}$ experimental cumulative distribution function for different locations in the melt pool (A, B, C) and for a hatch spacing value of $h = 0.75$ mm.

FIGURE 7.12: Martensite spacing experimental data distributions for different locations in the melt pool (A, B, C), hatch spacing $h = 0.75$ mm.

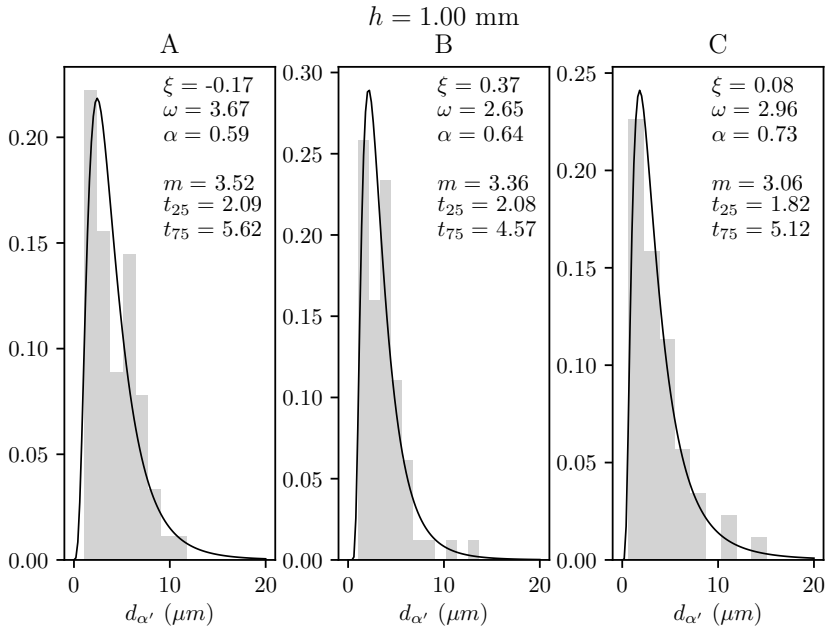

(a) Martensite α' needle spacing $d_{\alpha'}$ experimental data distribution for different locations in the melt pool (A, B, C) and for a hatch spacing value of $h = 1.00$ (parameters are: ξ location, ω scale, α shape, m median, t_{25} 25th-percentile, t_{75} 75th-percentile).

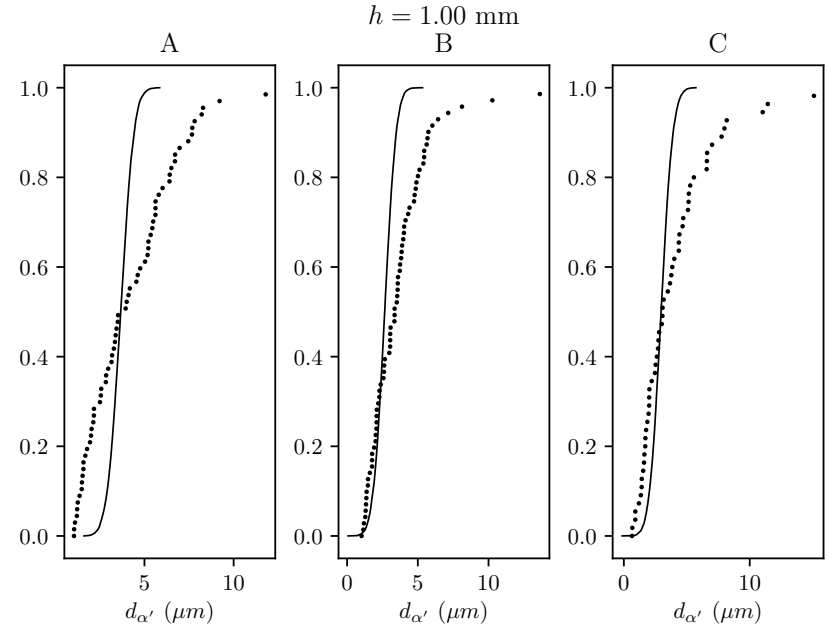

(b) Martensite α' needle spacing $d_{\alpha'}$ experimental cumulative distribution function for different locations in the melt pool (A, B, C) and for a hatch spacing value of $h = 1.00$.

FIGURE 7.13: Martensite spacing experimental data distributions for different locations in the melt pool (A, B, C), hatch spacing $h = 1.00$ mm.

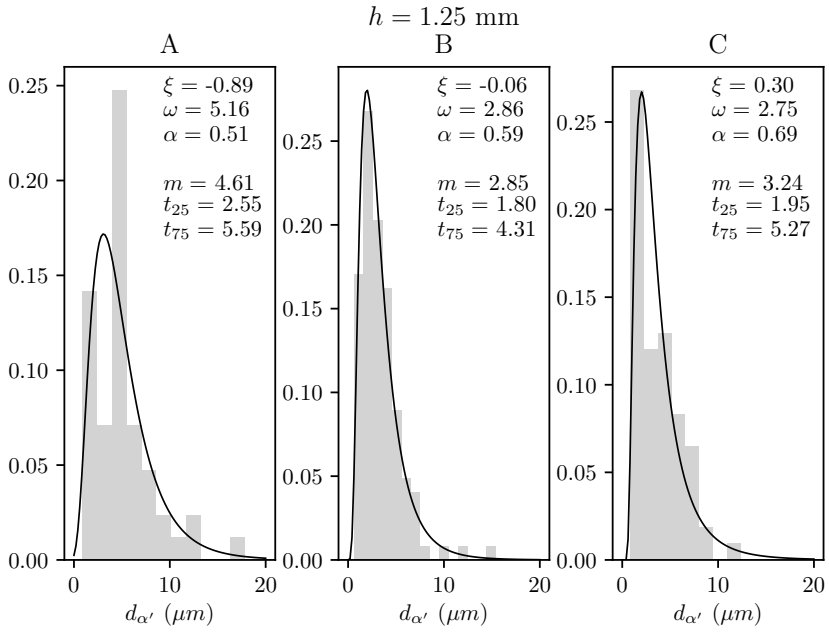

(a) Martensite α' needle spacing $d_{\alpha'}$ experimental data distribution for different locations in the melt pool (A, B, C) and for a hatch spacing value of $h = 1.25$ (parameters are: ξ location, ω scale, α shape, m median, t_{25} 25th-percentile, t_{75} 75th-percentile).

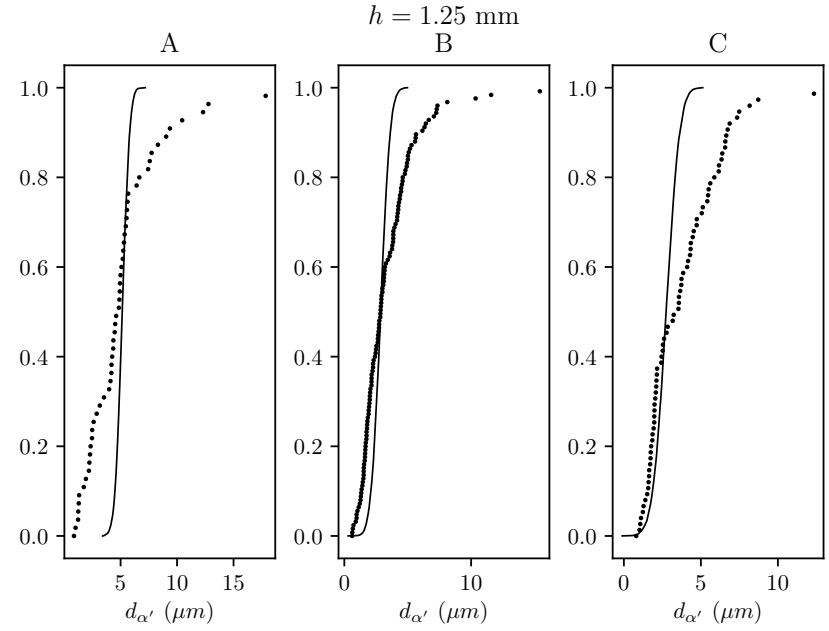

(b) Martensite α' needle spacing $d_{\alpha'}$ experimental cumulative distribution function for different locations in the melt pool (A, B, C) and for a hatch spacing value of $h = 1.25$ mm.

FIGURE 7.14: Martensite spacing experimental data distributions for different locations in the melt pool (A, B, C), hatch spacing $h = 1.25$ mm.

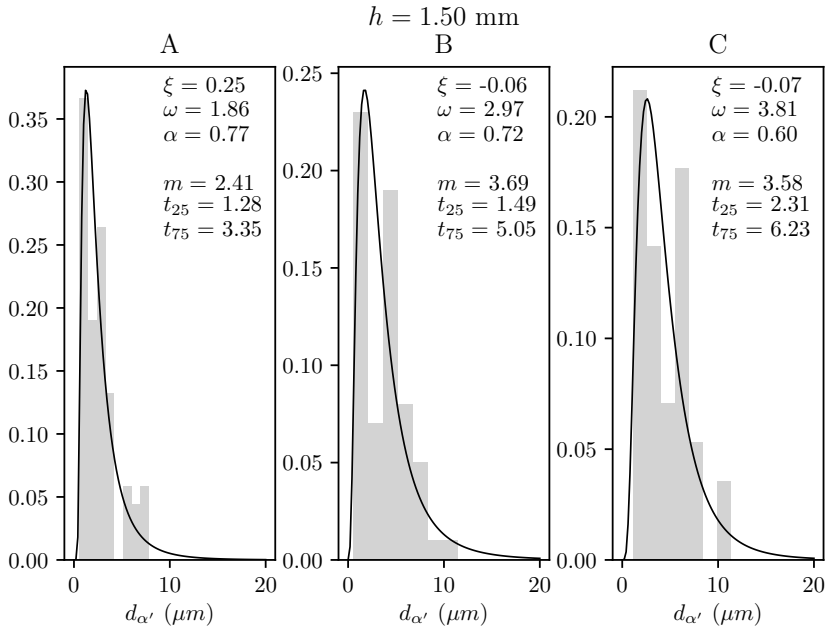

(a) Martensite α' needle spacing $d_{\alpha'}$ experimental data distribution for different locations in the melt pool (A, B, C) and for a hatch spacing value of $h = 1.50$ (parameters are: ξ location, ω scale, α shape, m median, t_{25} 25th-percentile, t_{75} 75th-percentile).

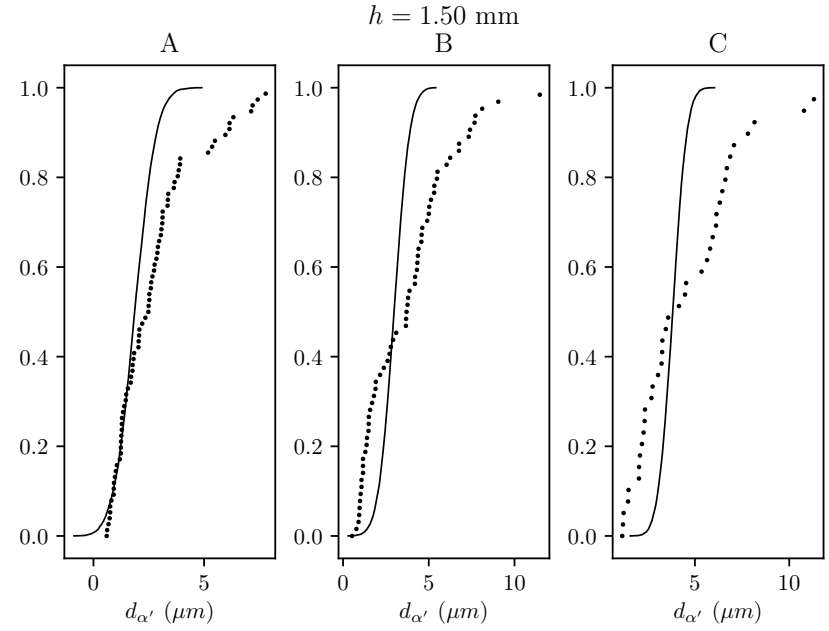

(b) Martensite α' needle spacing $d_{\alpha'}$ experimental cumulative distribution function for different locations in the melt pool (A, B, C) and for a hatch spacing value of $h = 1.50$ mm.

FIGURE 7.15: Martensite spacing experimental data distributions for different locations in the melt pool (A, B, C), hatch spacing $h = 1.50$ mm.

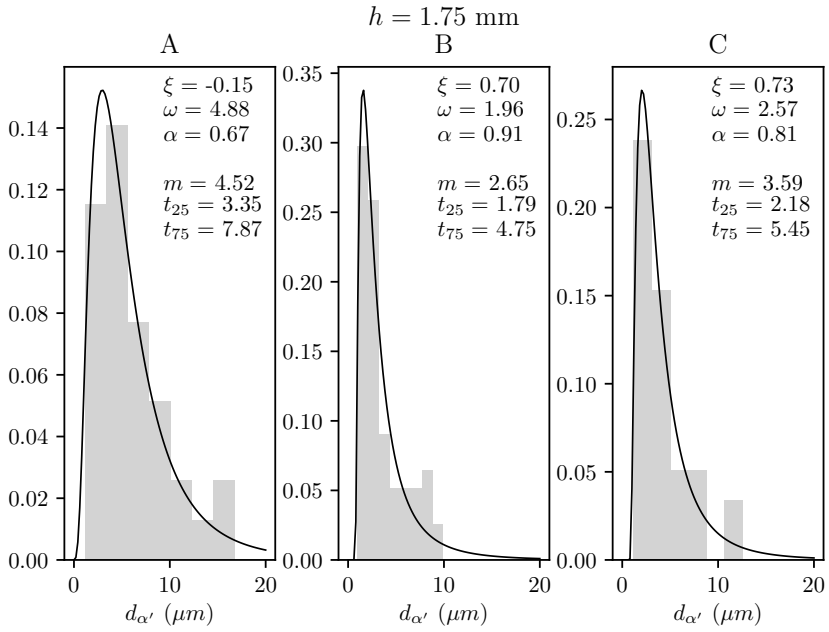

(a) Martensite α' needle spacing $d_{\alpha'}$ experimental data distribution for different locations in the melt pool (A, B, C) and for a hatch spacing value of $h = 1.75$ (parameters are: ξ location, ω scale, α shape, m median, t_{25} 25th-percentile, t_{75} 75th-percentile).

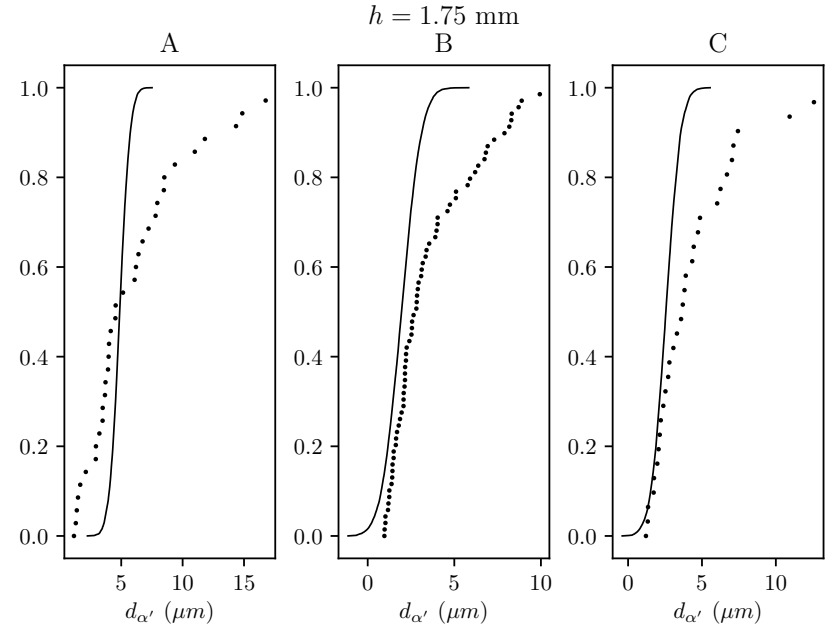

(b) Martensite α' needle spacing $d_{\alpha'}$ experimental cumulative distribution function for different locations in the melt pool (A, B, C) and for a hatch spacing value of $h = 1.75$ mm.

FIGURE 7.16: Martensite spacing experimental data distributions for different locations in the melt pool (A, B, C), hatch spacing $h = 1.75$ mm.

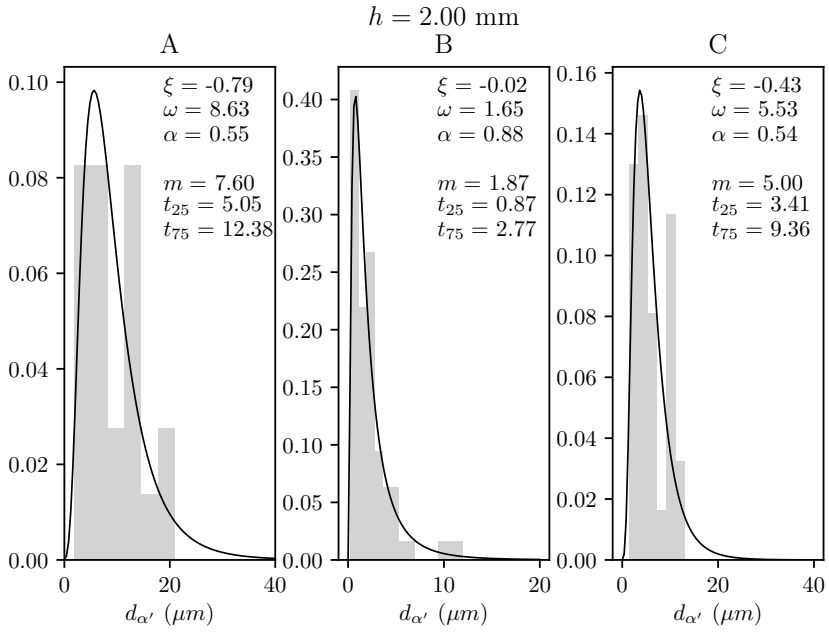

(a) Martensite α' needle spacing $d_{\alpha'}$ experimental data distribution for different locations in the melt pool (A, B, C) and for a hatch spacing value of $h = 2.00$ (parameters are: ξ location, ω scale, α shape, m median, t_{25} 25th-percentile, t_{75} 75th-percentile).

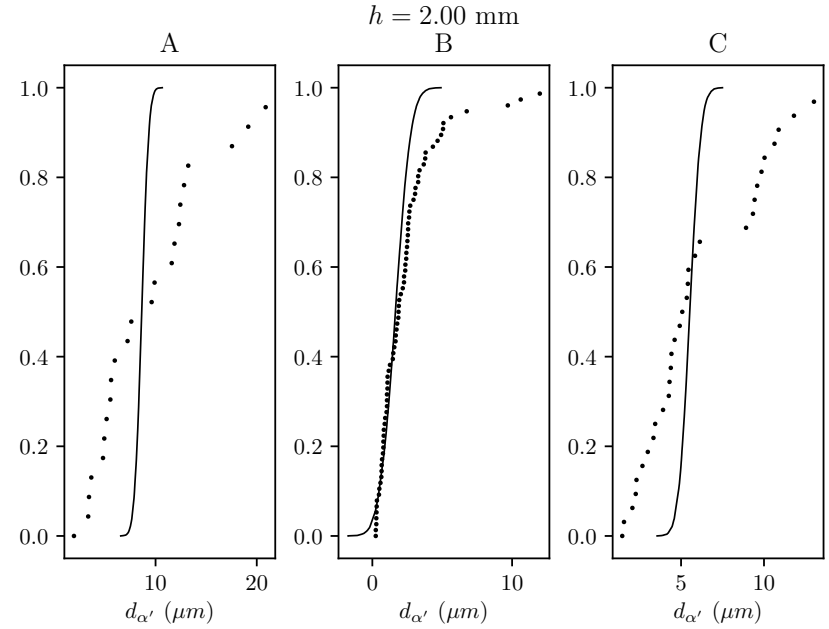

(b) Martensite α' needle spacing $d_{\alpha'}$ experimental cumulative distribution function for different locations in the melt pool (A, B, C) and for a hatch spacing value of $h = 2.00$ mm.

FIGURE 7.17: Martensite spacing experimental data distributions for different locations in the melt pool (A, B, C), hatch spacing $h = 2.00$ mm.